TABLE OF CONTENTS

INTRODUCTION

1.1 Overview

The flow over cavities or holes of various shapes and sizes is applicable to the aerodynamics of aircraft and automobiles as well as to the hydrodynamics of watercraft. The applications of cavity flows to aircraft aerodynamics have been the driving force of this type of research in the past, due to the fact that many features found on aircraft and automobiles can be adequately approximated by models of simple geometry such as holes of rectangular or circular planform.

Some examples of such features on aircraft include landing gear wheel wells, recessed windows, flap recesses, weapons bays and fueling points (Friesing, 1936). For automobiles, applicable features include sun roofs and door gaps (Milbank, 2004) and, more recently, these flows have also been studied to optimize the cooling of heat sensitive electronics such as microprocessors (Kuo and Huang, 2003).

Another driving force for the study of flow over rectangular cavities was the observation that a stationary, captive vortex is often found inside these features (Roshko, 1955) providing a rare opportunity to investigate and develop a greater understanding of vortices in general by measuring such a stable, captive vortex.

Although it has been shown that flow inside features such as rectangular cut-outs of finite width display three dimensional flow behaviour (Maull and East, 1963), flow related to cavities of circular planform are inherently more complex due to the curvilinear nature of their boundaries. Due to the more complex geometry of these holes, the flow inside these features is also more difficult to visualize intuitively.

Of the few investigations that have dealt with cavities of circular planform, most have limited their study to the effect of cavity depth and external flow conditions on drag (Friesing, 1936, Wieghardt, 1942, Tillman, 1951), however, recently some have carried out measurements aiding in the understanding of the flow inside and behind such cavities through the use of mean surface pressure

measurements (Hiwada et. al., 1983, Savory et. al., 1996), surface oil-flow investigations (Gaudet and Winter, 1971, Hiwada et. al., 1983), and traversed hot-wire measurements in the cavity wake (Hiwada et. al., 1983, Savory et. al., 1996). Literature resulting from these and other previous investigations of the flow over cavities is treated in the following chapter.

Previous investigations of the flow over circular cavities have revealed a stable captive vortex inside the cavity at most depth configurations (Gaudet and Winter, 1971, Hiwada et. al., 1983), however in all cases the mean flow pattern is strongly three dimensional. The flow inside the cavity has been observed to change radically for a cavity depth equal to approximately half of the cavity diameter ($h/D \cong 0.5$) such that vortices are shed from the cavity into the external flow resulting in a marked increase in the cavity drag (Gaudet and Winter, 1971).

The greatest contributions to flow visualization inside circular cavities have come from the analysis of surface oil-flow investigations (Gaudet and Winter, 1971, Hiwada et. al., 1983) which have given a glimpse of the mean velocity field for the flow along cavity surfaces.

1.2 Gaps in Research to Date

Since only a few investigators have ever studied the flow over cavities of circular planform, many gaps in the research remain.

In terms of measurements, mean pressure fields on the cavity surfaces and along the outer rim have been well researched, but to this point, no surface pressure fields have been published in the cavity wake beyond a radial distance of 0.32D from the cavity centre and no RMS surface pressure fields have been published on any cavity surfaces.

As well, although single span-wise lines of hot-wire measurements have been published outlining the presence of mean stream-wise velocity defects and peaks in turbulence intensity in the cavity wake (Hiwada et. al., 1983, Savory et. al., 1996), a

full plane of such measurements in multiple components should further elucidate the flow structure in the cavity wake.

Though turbulence intensity measurements of the flow in the cavity wake have been published, very little information is available regarding the frequencies of oscillations in and behind the cavity as has been studied in depth for rectangular cavities (Rockwell and Naudascher, 1978, Heller et. al., 1971, Disimile et. al., 2000, Hardin and Pope, 1995, Hardin and Mason, 1977, Elder et. al., 1982, Howe, 1997, Gharib and Roshko, 1987, Lin and Rockwell, 2001, Knisely and Rockwell, 1982). From one investigation in particular, a strong relationship was observed between cavity oscillation and resulting drag for rectangular cavities (Hardin and Mason, 1977), and thus a study of such oscillations for circular cavities is required.

No flow visualization measurements have been done inside the cavity, other than at the cavity surface (Gaudet and Winter, 1971, Hiwada et. al., 1983), and thus no three-dimensional visualization of the flow inside the cavity exists. Although knowledge of the mean flow patterns along the cavity surfaces allows some inferences to be made of the mean flow elsewhere in the cavity, a three-dimensional investigation of this flow would truly benefit the understanding of the flow inside circular cavities.

A series of three flow regimes has been proposed for the flow over circular cavities relating to the stability of the flow at varying depth (Hiwada et. al., 1983), but these regimes have yet to be confirmed by other investigators.

Finally, many results have been published which demonstrate the flow asymmetry observed for the cavity configuration of h/D = 0.47 (Friesing, 1936 and later investigators), along with the fact that the side on which this asymmetry is observed can be switched by introducing a disturbance to the flow (Gaudet and Winter, 1971, Hiwada et. al., 1983), but no publications have clearly described what type of disturbance is required to cause this asymmetry to switch. As well, no research

has been done to investigate whether or not this forced switch is repeatable or controllable.

To date, no theory has been proposed for why this flow asymmetry and resulting high drag is observed at h/D ≈ 0.5 and not for other cavity depth configurations.

1.3 Aim of Thesis

The main objective of this thesis is to fill in some of the aforementioned gaps that remain in the research relating to turbulent boundary layer flow over surface-mounted circular cavities with a focus on deepening the understanding of the flow related to the cavity depth configuration of h/D ≈ 0.5.

The following gaps in the research that were chosen as objectives for the current investigation were:

1. To search for a link between flow along cavity surfaces and the flow in the cavity wake.
2. To understand the causes for flow asymmetry and otherwise aberrant flow behaviour at h/D ≈ 0.5.
3. To probe for a link between the flow patterns in circular cavity flows and their frequency signatures.
4. To find the relationship between mean and fluctuating pressure patterns on all cavity surfaces.
5. To simplify circular cavity flow visualization for future investigators.
6. To confirm the existence of flow regimes proposed by Hiwada et. al. (1983).

Other fundamental objectives of this thesis were:

1. Adaptation of available flow facility to allow cavity measurements to be conducted.

2. Obtaining and integrating models and apparatus required for proposed measurements.
3. Thorough flow-field analysis of measurement facility to render it usable by future experimenters.

1.4 Approach

This study has sought to achieve the above listed objectives through an experimental investigation of turbulent boundary layer flow over a surface mounted circular cavity model with depth varied between h/D = 0.20, 0.47 and 0.70, measured in a low-speed closed loop wind tunnel with U_0 = 27 m/s. A brief study was also done for h/D = 0.37. Measurements were carried out at a constant Reynolds' number of 1.3×10^5, based on cavity diameter, and a boundary layer thickness of 55 mm was used.

The three types of measurements that were used for this investigation were:

- pressure transducer measurement of model surface mounted pressure taps
- model surface mounted microphone measurements
- traversed two-component hot-wire measurement in the cavity wake.

Each of these measurements was captured in a 30 second time series with appropriate sample frequency allowing for frequency analyses to be carried out in post-processing. Mean and RMS pressure patterns were created from pressure transducer and microphone measurements at points carefully located about the cavity base, sidewall and far into the cavity wake. The cavity wake flow switch for h/D ≈ 0.5 was studied in depth by monitoring the pressure transducer time series during a specially designed experiment to encourage wake flow switching and similar pressure transducer measurements were made in an attempt to confirm the Hiwada flow-regime proposal (Hiwada et. al., 1983). A traversed two-component hot-wire system was used to measure velocities in a plane perpendicular to the free-stream direction, downstream of the cavity.

Finally, visualization of the measured cavity flows was greatly aided by similar analyses by Hunt. et. al. (1978) and primarily by Gaudet and Winter (1971).

In addition to the experiments carried out for this thesis, a great deal of work was done by the author to design and build an appropriate wind tunnel roof, to design the experimental cavity models, to specify, acquire and integrate new measurement equipment and to program measurement acquisition and analysis software among other tasks.

1.5 Summary

A brief survey of research done in the flow over circular cavities revealed gaps in the understanding of oscillations and their relationship to measured mean surface pressures and wake velocities, along with a lack of understanding of the mean flow structure in the cavity wake and also of the reasons for the asymmetric flow observed at $h/D \approx 0.5$.

The objectives selected for the present investigation focus on many of these gaps along with other unexplored facets of the flow over circular cavities. Research done in this area of study is explained in greater detail in the following Literature Review section.

2 LITERATURE REVIEW

2.1 Overview

In this section, background is provided on previous developments in the area of flow over cavities and related developments aiding in the understanding of the results of this thesis.

Research in this area has been primarily concentrated on the flow over rectangular cavities or other two dimensional geometries such as forward and rearward-facing steps (see Fig. 2-1) and many developments resulting from investigations of rectangular cavity flow in particular have been used in the study of flow over circular cavities.

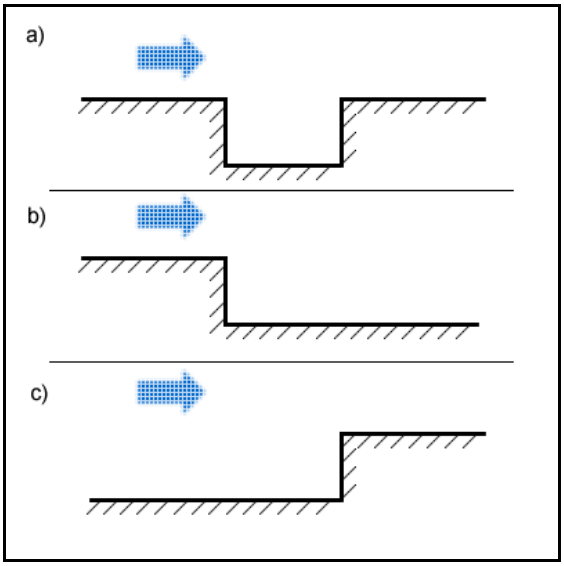

Figure 2-1 – Side views of commonly studied 2-D flow geometries a) 2-D rectangular cavity, b) rearward facing step and c) forward facing step

The present chapter should provide the reader with a comprehensive review of the study of cavity flow as related to this thesis and should prepare the reader for the discussion of results of the present work.

2.2 Developments from the Study of Flow over Rectangular Cavities

2.2.1 Open and Closed Flow Regimes

In an initial investigation of the flow over rectangular cavities, (Roshko, 1955) the analysis of a series of experimental results yielded cavity flow classifications now called "open" and "closed" flow regimes. In these classifications, a flow situation that results in the separated boundary layer reattaching onto the cavity base is deemed "closed", whereas a separated boundary layer that reattaches onto a point on the downstream cavity wall is called "open". "Open" flows were noted to be likely to cause a single stable vortex to be trapped in the cavity interior. Figures 2-2 a) and b) further illustrate this concept below:

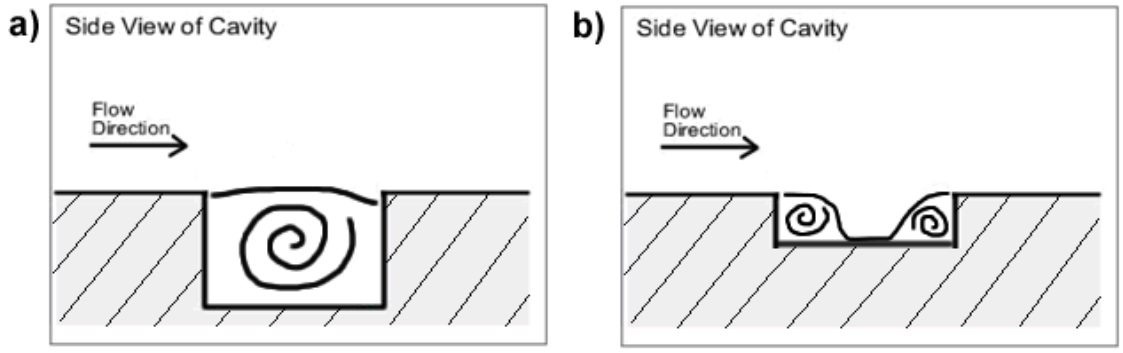

Figure 2-2 – Showing the difference between open (a) and closed (b) cavity flows.

Roshko noted that the cause of this single trapped vortex observed at some cavity configurations is due to the "deflection of part of the separated boundary layer into the cavity … at the downstream edge and creating a relatively high pressure on the cavity wall in that vicinity. (Roshko, 1955)". Closed flows are only observed for shallow cavities such that the cavity depth to length ratio (h/l) is less than 0.1 (Roshko, 1955).

2.2.2 Feedback Resonance

Another consequence of shear layer reattachment near the downstream lip of the cavity for open flows is the production of sound due to excitation by fluctuations

in the shear flow (Rossiter, 1964). This is a very important concept in the flow over cavities called feedback resonance, illustrated in Figure 2-3, (Rossiter, 1964) in which pressure pulses in rectangular cavity flows are produced when a vortex is shed from the upstream lip of the cavity and is convected downstream (Figure 2-3, Frame 1) to the downstream lip where it impinges (Frame 2). By impinging, a stagnation pressure is created at this lip and results in an acoustic pulse (Frame 3) which travels upstream to disturb the shear layer at the upstream lip (Frame 4), once again causing another vortex to be shed downstream (Frame 5) and thus closing the feedback loop. A necessary condition for this vortex shedding at the upstream lip is that the shear layer must be unstable. As this mechanism is repeated, a discrete tone acoustic wave is produced at the downstream lip.

An equation (shown below), known as Rossiter's formula (Rossiter, 1964), has been derived to predict the frequency of the discrete tone produced via this mechanism.

$$\boxed{\frac{fl}{U_0} = \frac{m - \gamma}{M + 1/\kappa}}$$

Where f is the frequency of the tone produced by the cavity, l is the stream-wise length of the cavity, U_0 is the velocity of the free-stream, m is an integer, M is the Mach number, κ is the ratio of convection velocity of vortices to the free-stream velocity, γ is a factor to account for the lag time between the passing of a vortex and the emission of a sound pulse at the downstream cavity lip. By setting γ = 0.25 and $1/\kappa$ = 1.75, good agreement has been found between the predictions of this formula and experimental results (Rossiter, 1964).

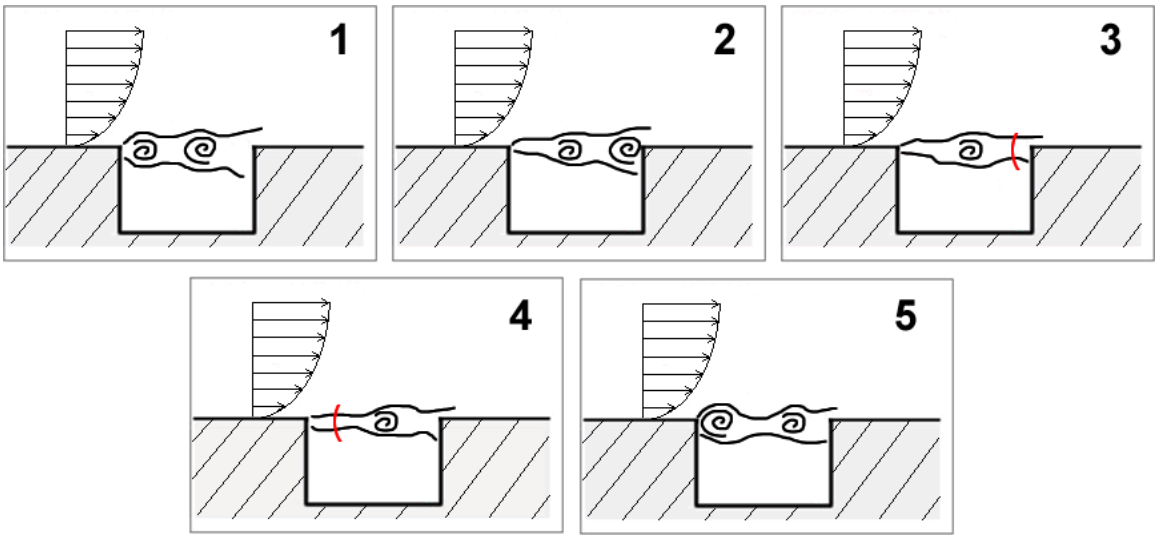

Figure 2-3 – A series of diagrams showing the feedback resonance mechanism at various points in time (elapsed time increases with increasing frame number).

One discovery that demonstrated the importance of this described cavity feedback resonance was made by McGregor and White (McGregor and White, 1970) in their investigation of the effect of resonance on cavity drag. The investigators found that when a cavity was undergoing acoustic resonance in a flow, the drag due to the cavity increased 250% as compared to a cavity under similar conditions not undergoing resonance.

2.2.3 Classification of Cavity Oscillations

Cavity-related oscillations can be classified into three categories: fluid-dynamic oscillations, fluid-resonant oscillations, and fluid-elastic oscillations (Rockwell and Naudascher, 1978). Fluid-dynamic oscillations are related to the vortex-acoustic pulse interaction described by the aforementioned feedback mechanism described in the previous sub-section. Fluid-resonant oscillations are usually high frequency oscillations which occur when a self-sustaining oscillation is of the same order as either the cavity length or depth such that a resonance occurs

within the cavity and amplifies the original oscillation. Fluid-elastic oscillations are caused when a cavity surface itself is forced into oscillation.

2.3 Developments from the Study of the Flow over Elliptical Cavities

Very little research has dealt with the flow over elliptical cavities, of which circular cavity flow is a subset. Most early publications in this field of study examined the flow over many different types of cavity and excrescences (a feature which protrudes into the external flow). The first study of the flow over cavities with elliptical planform (Friesing, 1936) was an investigation of the flow over cavities of both rectangular and elliptical planform.

2.3.1 Comparing Drag due to Elliptical and Rectangular Cavities

In the area of flow over elliptical cavities, Friesing found that, in general, the trends traced by the cavity-induced drag in relation to the cavity depth, matched reasonably well with results from rectangular cavity flow measurements (see Fig. 2-4). This modest match held for most elliptical configurations except for the case when the aspect ratio of the elliptical planform of the cavity was 1; the case of a circular planform. For this case there was a large peak in the drag centred at $h/D \cong 0/5$ not observed at other aspect ratios.

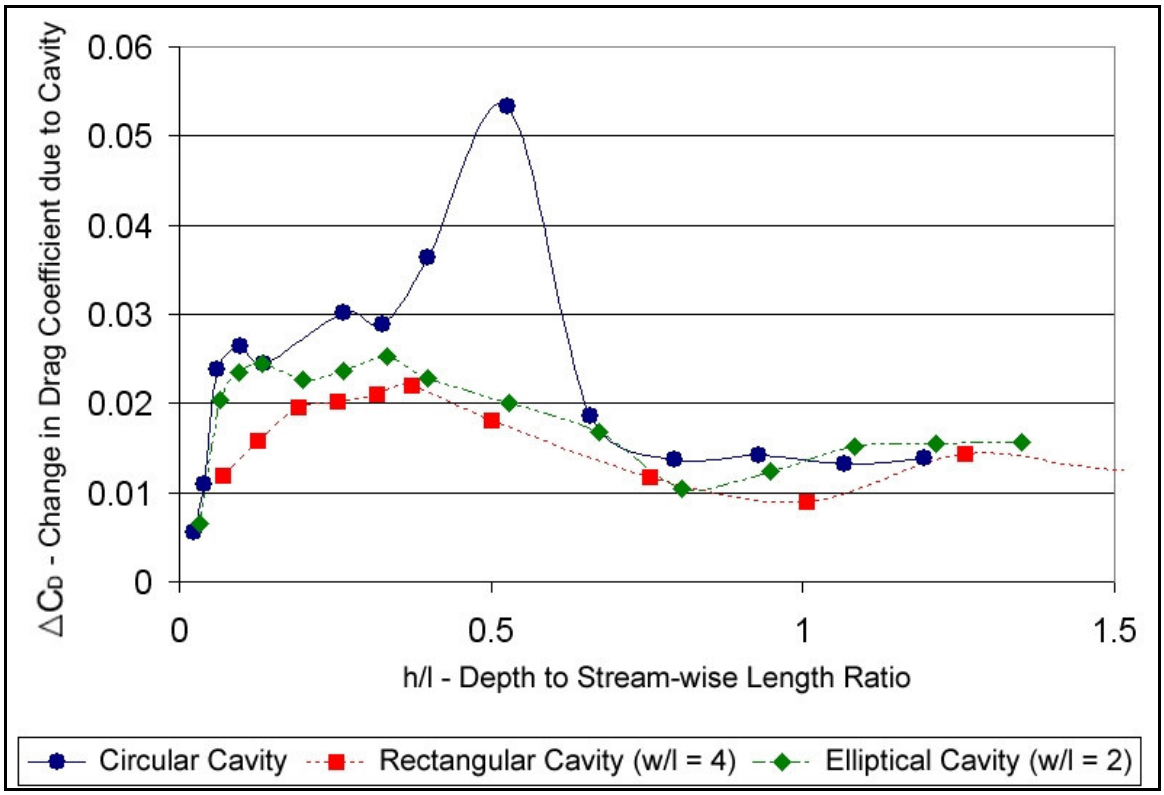

Figure 2-4 – Data recovered from Friesing's investigation showing typical cavity-related drag trends for cavities of rectangular, elliptical and circular planform. w in legend is span-wise width of cavity such that w/l is an effective aspect ratio for the cavities.

2.3.2 Developments in Study of Flow over Circular Cavities

Friesing also noted a substantial change in flow characteristics when varying the depth to diameter ratio (h/D) of the circular cavity and for the case of h/D=0.567 (see Fig. 2-5), the pressure distribution on the rim of the cavity displayed a noticeable asymmetry about the stream-wise axis not observed for other much shallower or deeper cavity configurations.

This apparent flow asymmetry shown in his results for h/D=0.567 was evidence that this particular geometrical depth to diameter condition stimulated the unexpected result of an asymmetric mean pressure distribution along the cavity rim about the cavity downstream centre line as seen in Fig. 2-5.

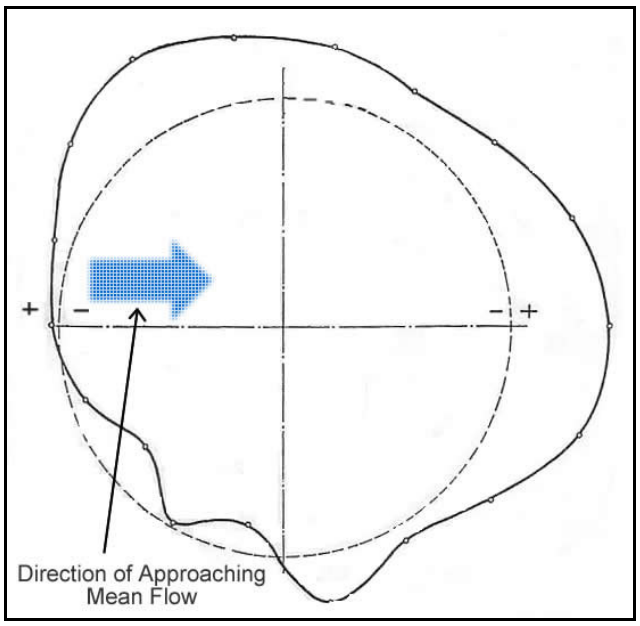

Figure 2-5 – Mean pressure measurements along the cavity rim for h/D = 0.567 (Friesing, 1936).

In subsequent work in the investigation of the flow over circular holes, the German military commissioned a series of drag balance measurements using wind tunnel mounted cavity models (Wieghardt, 1942). The main result of this work, as related to the present project, was the discovery of periodic pressure fluctuations inside the cavity at some h/D ratios due to a single stable large vortex in the cavity chamber.

A later study by Tillman (1951) resulted in the investigator combining his own results with previous data and confirmed the peak drag phenomenon for h/D = 0.5. Local drag maxima were also identified for h/D = 0.1 and h/D = 1.1 and it was inferred that circular cavity drag was a periodic function of h/D.

A vast improvement on earlier related works was published in the early 1970's (Gaudet and Winter, 1971) in the form of an investigation which was the first to have a more deliberate focus on cavities with circular planform. This investigation combined an analysis of previous results with a set of drag measurements using a drag balance allowing the direct measurement of horizontal forces acting on the

experimental cavity model, as well as a flow visualization in the form of a surface oil-film pattern study.

In the analysis of previous results, the investigators reasoned that at all depth conditions the flow inside the hole must somehow be driven by the shear stresses across the open face of the cavity and that these shear stresses must be related to those found in the boundary layer upstream of the cavity model.

Using this reasoning, the following relation was introduced:

$$\frac{\Delta C_D}{c_f} = \frac{\tau' - \tau}{\tau} = \frac{\tau'}{\tau} - 1$$

Where ΔC_D is the incremental drag coefficient due to the presence of the cavity, c_f is the local skin friction coefficient of the approaching boundary layer, τ is the wall shear stress of the approaching boundary layer and τ' is the shear stress across the mouth of the cavity. In this way $\tau' - \tau$ can be thought of as the effective shear stress provided by the presence of the cavity.

Hence, by using this quantity $\Delta C_D / c_f$, the drag data of any particular investigation can theoretically be made independent of the character of the upstream boundary layer used in the experiment, making it possible to fairly compare the results of previous investigations with widely varying boundary layer characteristics. The analysis of this quantity $\Delta C_D / c_f$ is now a standard way of comparing results of this type of measurement to previous work.

This investigation also introduced the following equation to fit experimental results for $\Delta C_D / c_f$ to a trend:

$$\frac{\Delta C_D}{c_f} = A\left(\frac{u_* D}{\nu}\right)^B$$

Where A is a function of h/D and Mach number, B is constant for a given Mach number, u_* is the friction velocity and ν is the kinematic viscosity of the fluid.

As can be seen from Figure 2-6 and 2-7 below, this fit causes results of varying external flow conditions to collapse quite well to a single trendline (Figure 2-7) much better than the graph for ΔC_D (Figure 2-6).

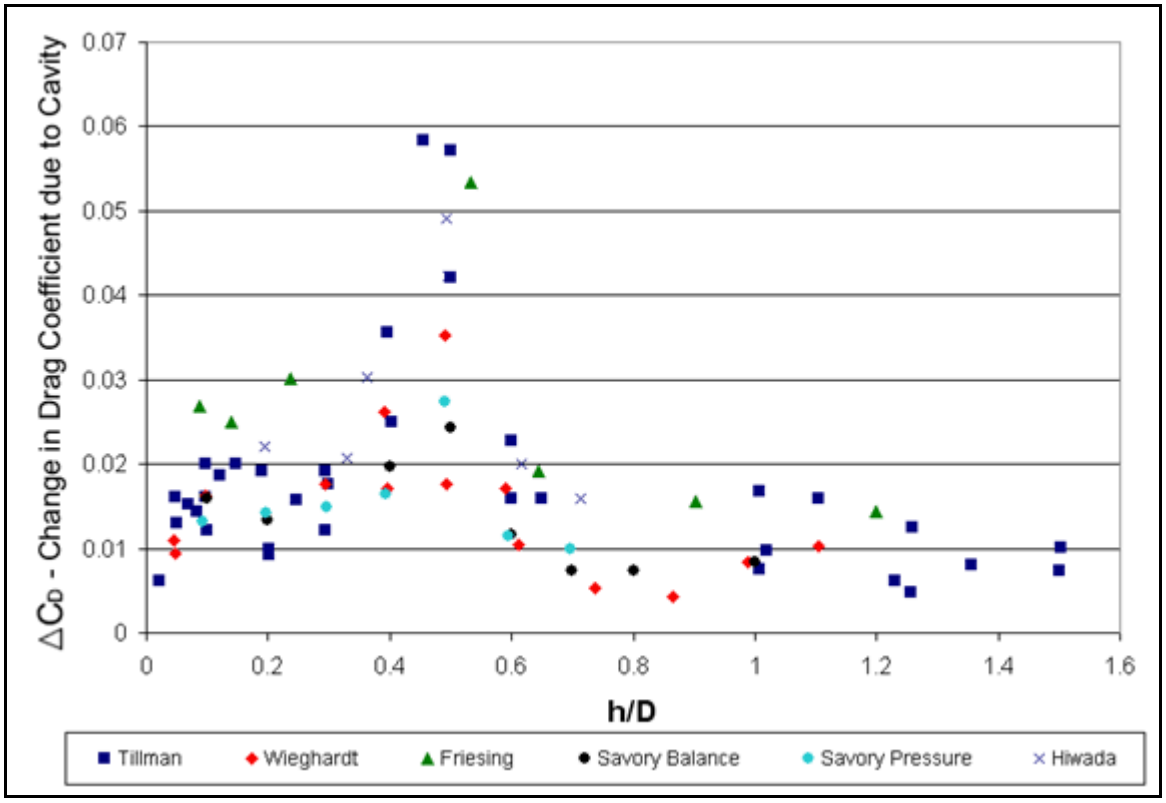

Figure 2-6 – Collapsing drag data from previous results using Gaudet and Winter's incremental drag coefficient ΔC_D.

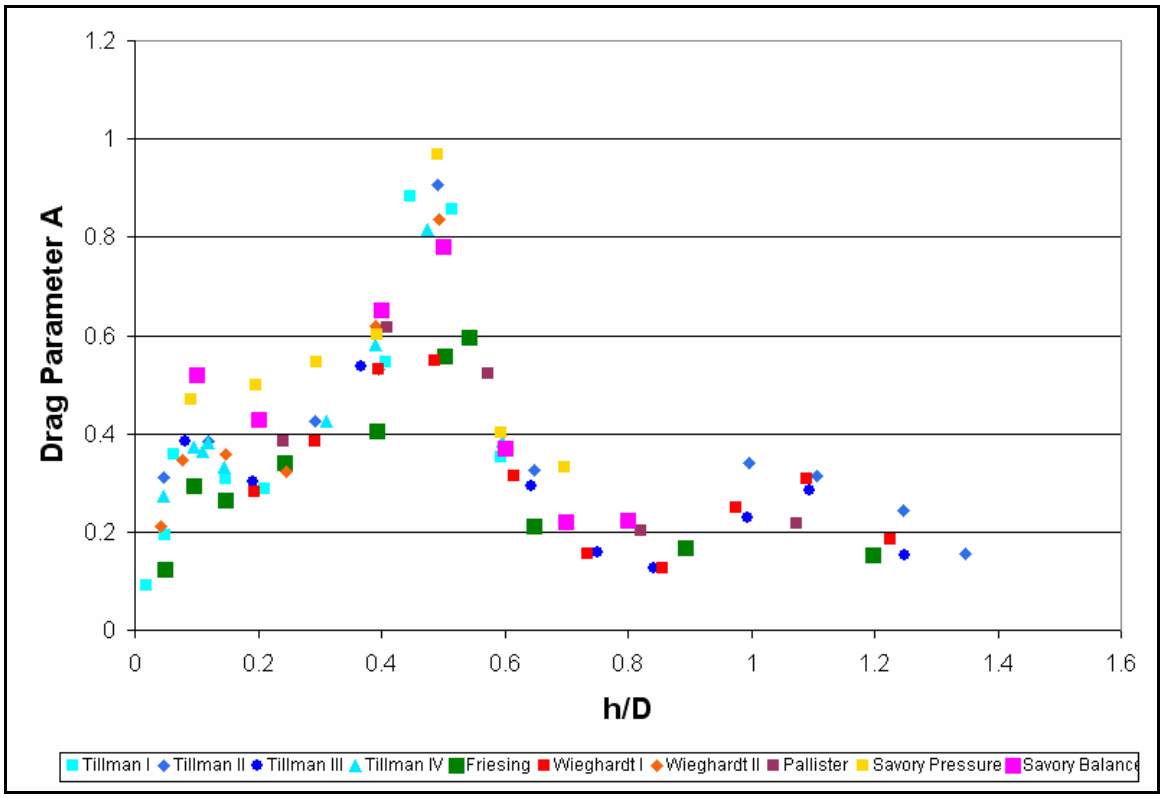

Figure 2-7 – Collapsing drag data from previous results using Gaudet and Winter's drag parameter A (Young and Patterson, 1981).

The investigators also commented on the apparent lack of dependence of the cavity drag on the thickness of the approaching boundary layer.

Using the surface oil-film flow pattern technique, Gaudet and Winter were able to visualize the mean movement of suspended particles on the cavity base as well as on the vertical cavity walls which, among other things, allowed direct observations of the asymmetric flow at h/D ≅ 0.5. More precisely, at a cavity geometry of h/D = 0.47, a strong asymmetry in the flow pattern was observed which was not noticed for other values of h/D (see Fig. 2-8).

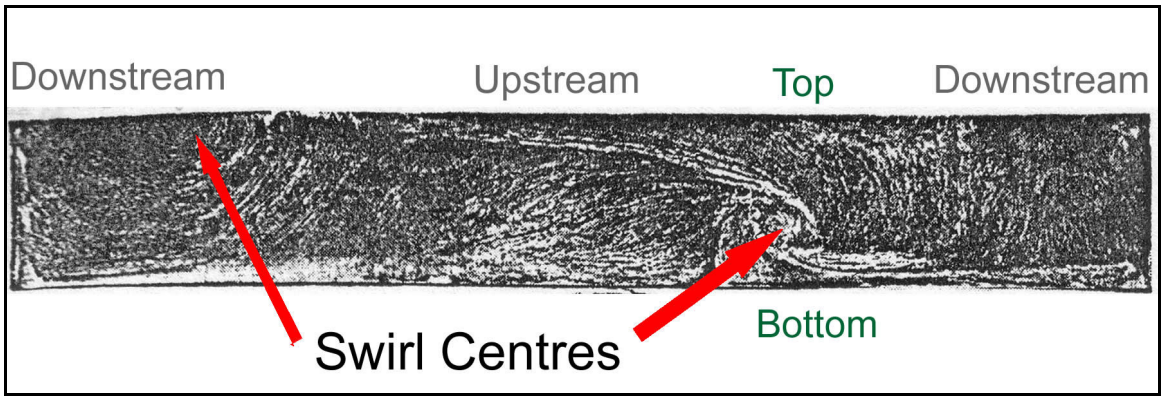

Figure 2-8 – "Unwrapped" oil flow visualization of cavity sidewall for h/D = 0.47 showing asymmetry of the cavity's main vortex centres (Gaudet and Winter, 1971).

This "unique character" (Gaudet and Winter, 1971), though asymmetric about the centre line of the cavity parallel to the direction of free stream flow, exhibited a certain degree of local symmetry about an axis 60 degrees to the free stream flow direction (Gaudet and Winter actually refer to this angle being "about 45 degrees" to the free stream flow, but drawing a line perpendicular to the mean flow lines on the cavity base points to an angle closer to 60 degrees to the free stream axis), this axis is labeled in Figure 2-9.

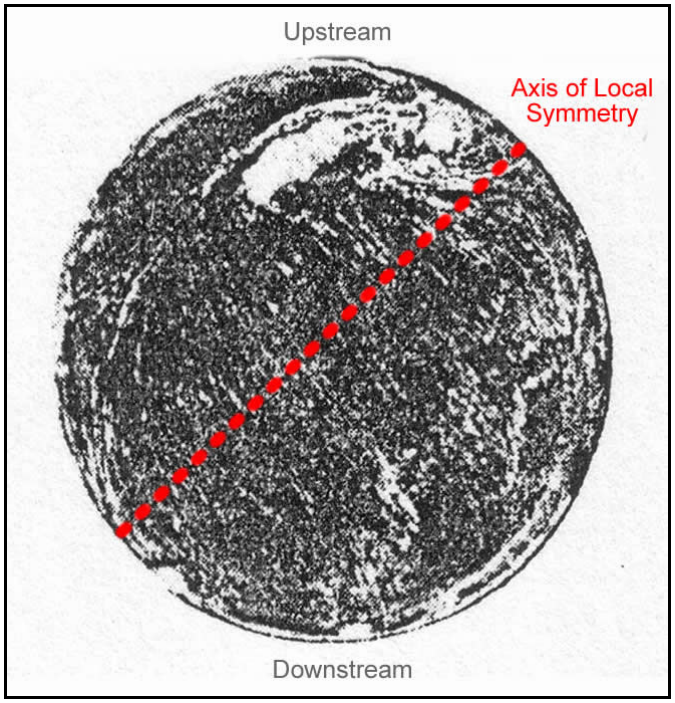

Figure 2-9 – Oil flow visualization on cavity base for h/D = 0.47 showing axis of local symmetry at about 60 degrees to free stream (perpendicular to flow lines on cavity base). (Gaudet and Winter, 1971).

The investigators implied the existence of a coiled vortex sheet intersecting the cavity surface at points in the visualization where there was centre of rotation (labeled in Figure 2-8). Such a coiled sheet was thus implied across the cavity at an angle of 60 degrees to the free stream direction and at an angle to the cavity base such that the tube extended from the upstream sidewall to outside the cavity at the downstream lip. The investigators reasoned that this exposed vortex tube was responsible for sweeping more fluid into the cavity, thus explaining the peak in cavity drag for this geometric configuration.

The flow structure at this configuration is made more complex by the presence of another noticeable swirl in the oil-film pattern on the cavity base near the outer edge at θ = 30° (see Figure 2-12c). Gaudet and Winter consequently reasoned that there must exist a second coiled vortex sheet that is rooted to the cavity bottom at this point which merges with the aforementioned main vortex tube (coiled sheet).

Another particularly interesting observation made by these researchers was the fact that the 60 degree local axis of symmetry visible in the oil-flow patterns at h/D=0.47 tended to one particular side of the cavity (Gaudet and Winter, 1971). However, this tendency was not completely consistent and occasionally the axis of local symmetry was reflected across the stream-wise cavity centreline.

A review of all previous cavity flow research was carried out by Young and Paterson (1981) which added some new hypotheses to attempt to explain the trends in circular cavity drag. In reviewing previous results, the investigators expanded on the observation that the cavity drag seemed to be a cyclic function of h/D, by proposing that this effect was due to the cavity alternating between unstable flow regimes and stable ones. If the vortices formed in the cavity were stable and remained contained inside the cavity the external flow would pass quite easily over the cavity opening, essentially seeing it as a free surface. This would minimize the momentum lost by the external flow thus minimizing the drag. However, for geometric configurations that

caused vortices to continually be shed downstream, a large wake would be formed and thus interaction between the external flow and the cavity would be high and hence the drag would increase.

The next contribution to this research was an experimental work (Hiwada et. al., 1983) that was the first to deal exclusively with the flow and heat transfer related to circular cavities in particular and did so with remarkable detail combining pressure, temperature, surface flow patterns and some wake flow measurements. The pressure measurements in their investigation were conducted by monitoring a series of pressure taps in a cavity model using pressure transducers. The data acquired using this method formed the first detailed set of mean pressure contours along the cavity base (Figures 2-10a and 12a) and sidewall (Figures 2-11a and 1-13a) using a dimensionless measure of pressure called the pressure coefficient. This quantity, denoted Cp, is defined as follows:

$$Cp = \frac{p - p_s}{\frac{1}{2}\rho_a U_0^{\,2}}$$

Where $\overline{p}$ is the mean of the measured surface pressure at a point on the model surface, p_s is the measured static pressure in the tunnel free stream at the time of surface pressure measurement, and $q_0 = \frac{1}{2}\rho_a U_0^{\,2}$ with ρ_a being the density of the air in the wind tunnel and U_0 the mean free-stream velocity. Figures displaying a series of such surface pressure patterns are presented below.

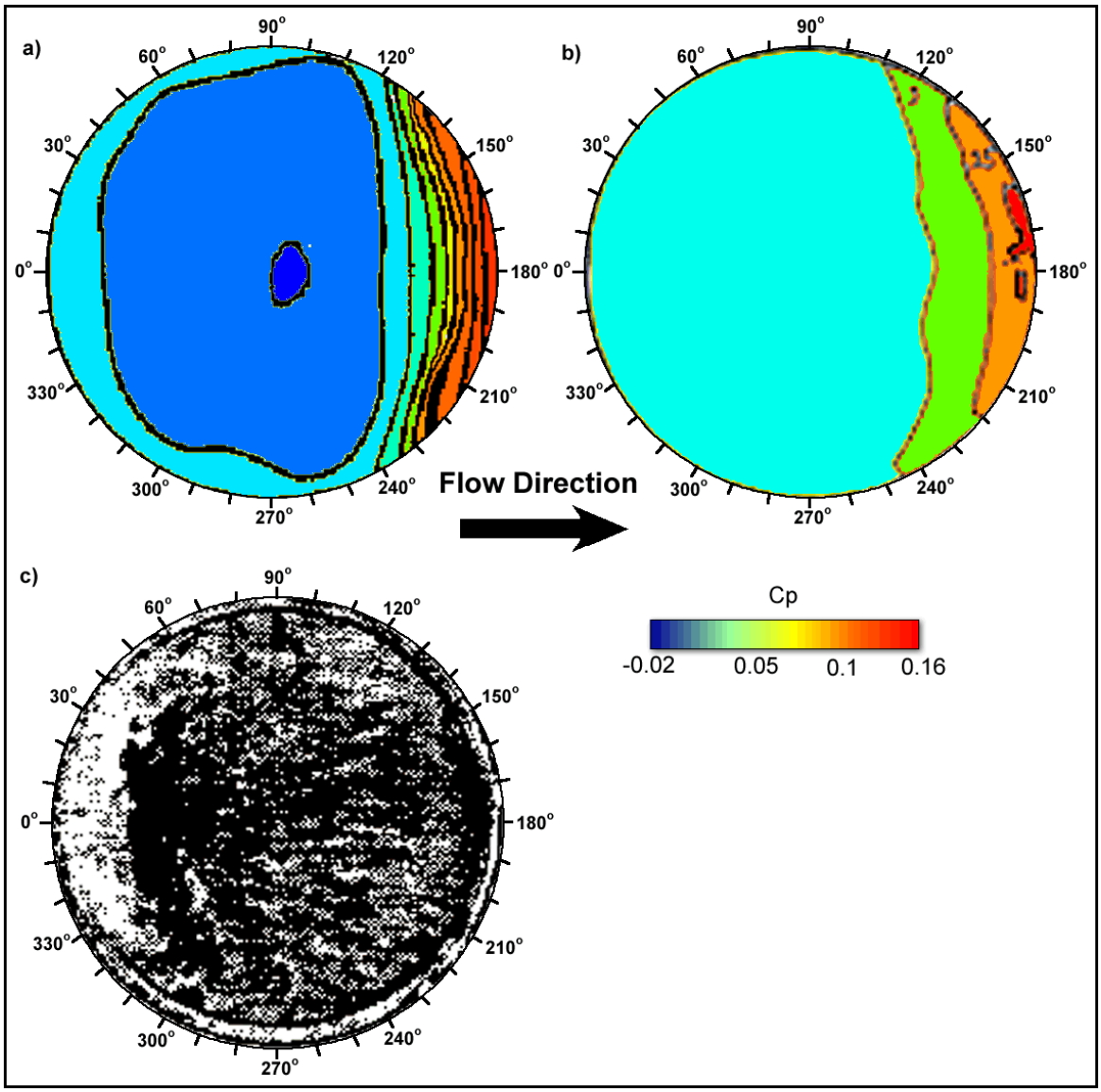

Figure 2-10 – A compilation of all previous measurements on the cavity base for h/D = 0.20. Mean pressure distributions from Hiwada et. al. (1983) and Savory et. al. (1996) (figures a and b, respectively) and a surface oil-film pattern from Hiwada et.al. (1983) are presented.

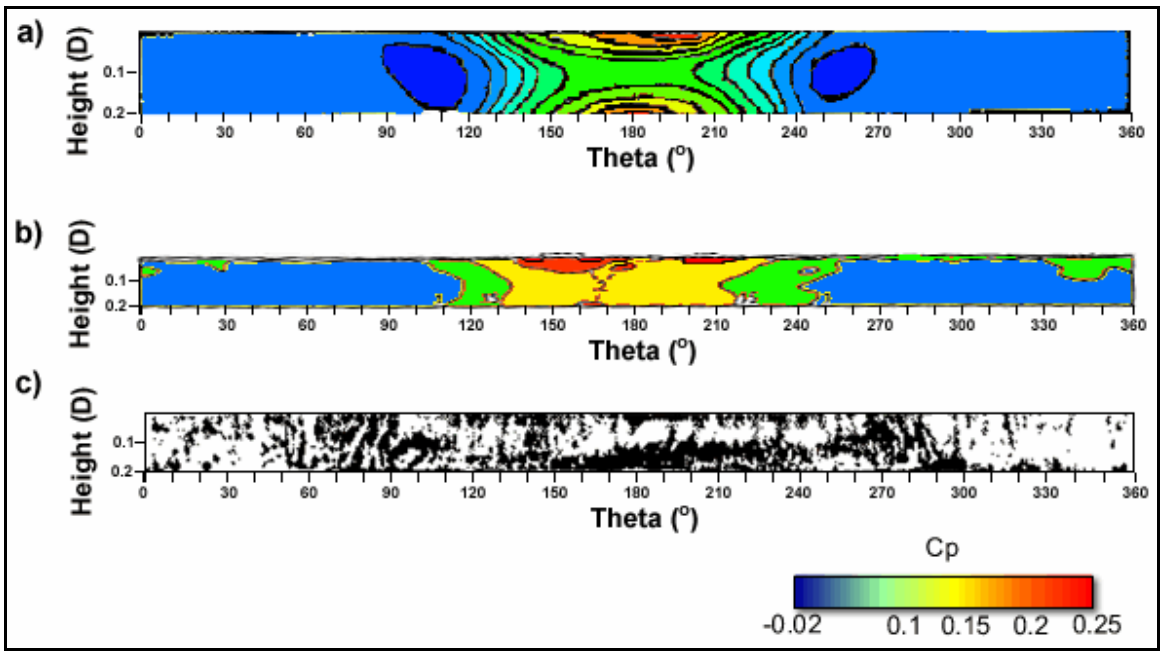

Figure 2-11 – A compilation of all previous measurements on the cavity sidewall for h/D = 0.20. Mean pressure distributions from Hiwada et. al. (1983) and Savory et. al. (1996) (figures a and b, respectively) and a surface oil-film pattern from Hiwada et. al. (1983) are presented.

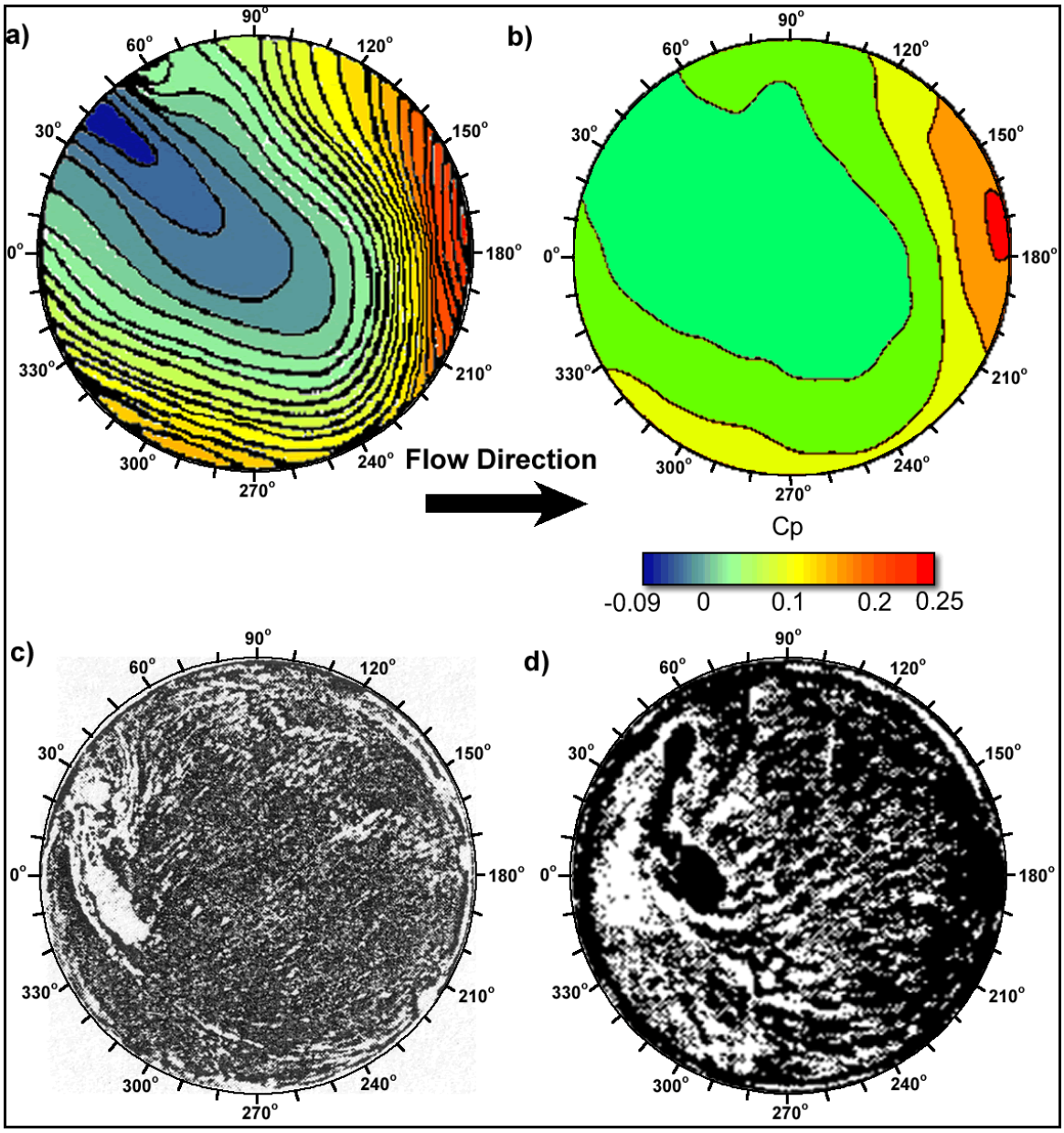

Figure 2-12 – A compilation of all previous measurements on the cavity base for h/D = 0.50. Mean pressure distributions from Hiwada et. al. (1983) and Savory et. al. (1996) (figures a and b, respectively) and surface oil-film patterns from Gaudet and Winter (1971) and Hiwada et.al. (1983) (figures c and d, respectively) are presented. Figure c) was taken for h/D = 0.47 rather than 0.50.

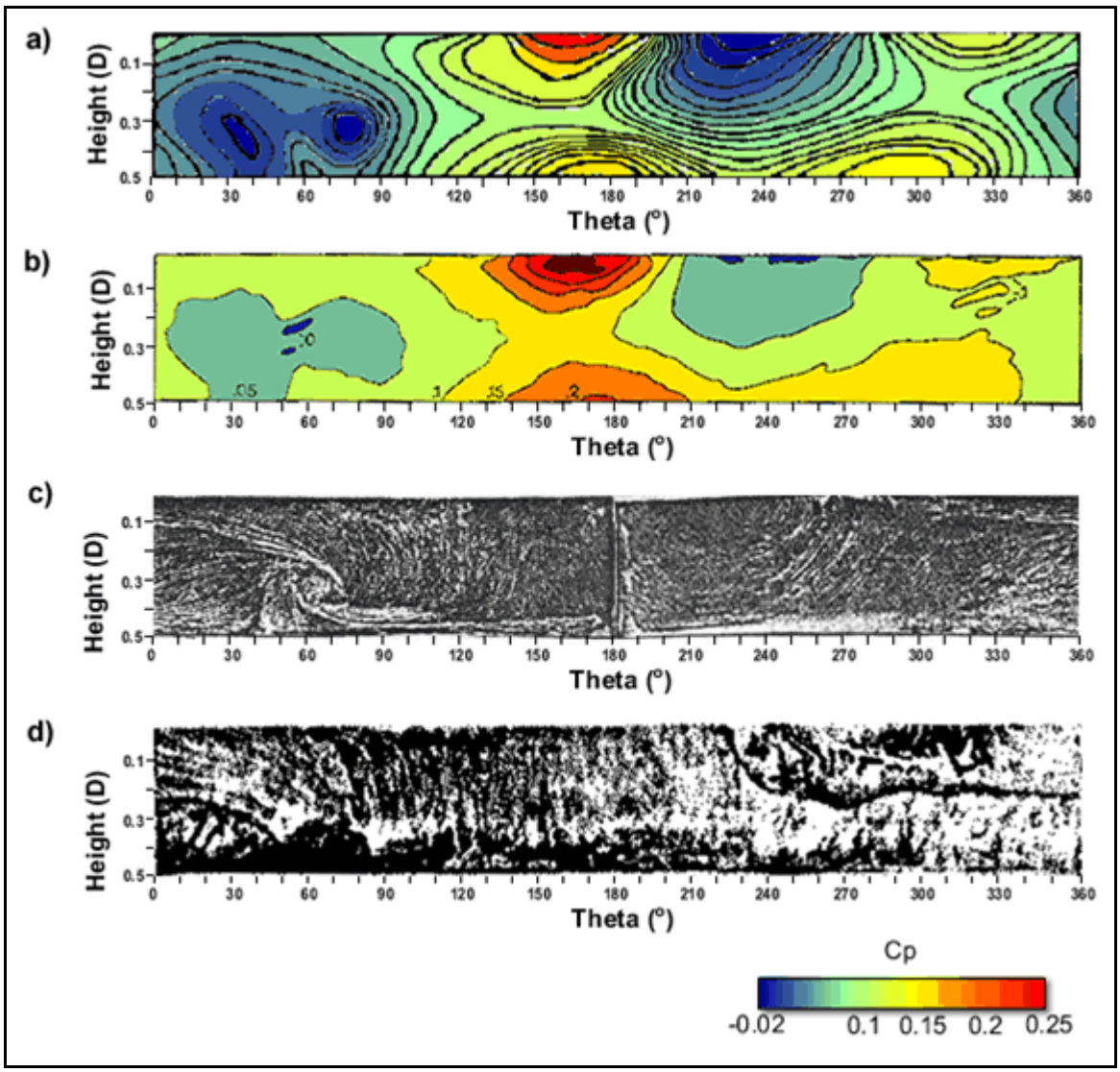

Figure 2-13 – A compilation of all previous measurements on the cavity sidewall for h/D = 0.50. Mean pressure distributions from Hiwada et. al. (1983) and Savory et. al. (1996) (figures a and b, respectively) and surface oil-film patterns from Gaudet and Winter (1971) and Hiwada et.al. (1983) (figures c and d, respectively) are presented. Figure c) was taken for h/D = 0.47 rather than 0.50.

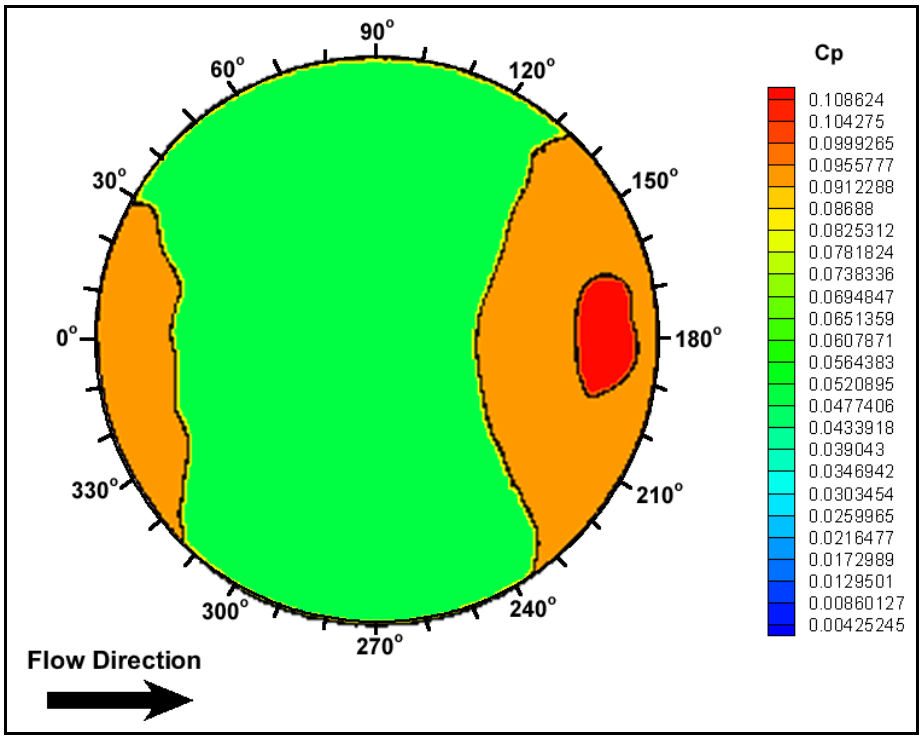

Figure 2-14 – Mean surface pressure distribution along cavity base for h/D = 0.70 (Savory et. al., 1996).

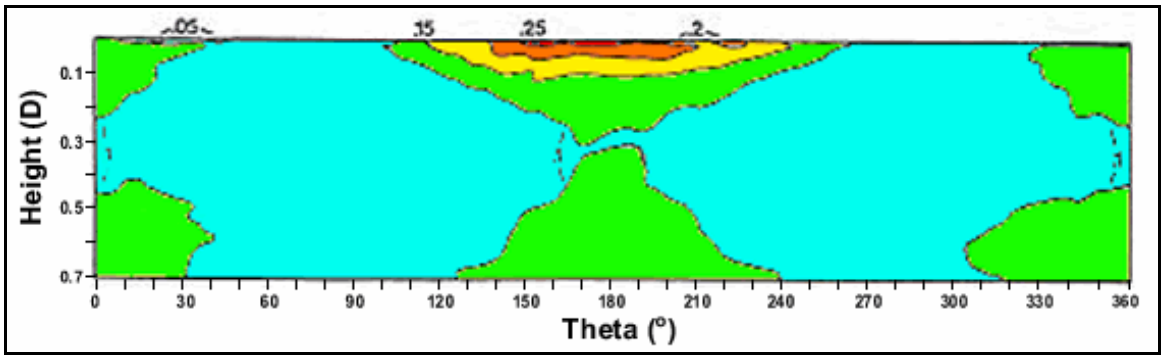

Figure 2-15 – Mean surface pressure distribution along cavity sidewall for h/D = 0.70 (Savory et. al., 1996). Cp values are written onto corresponding contour lines.

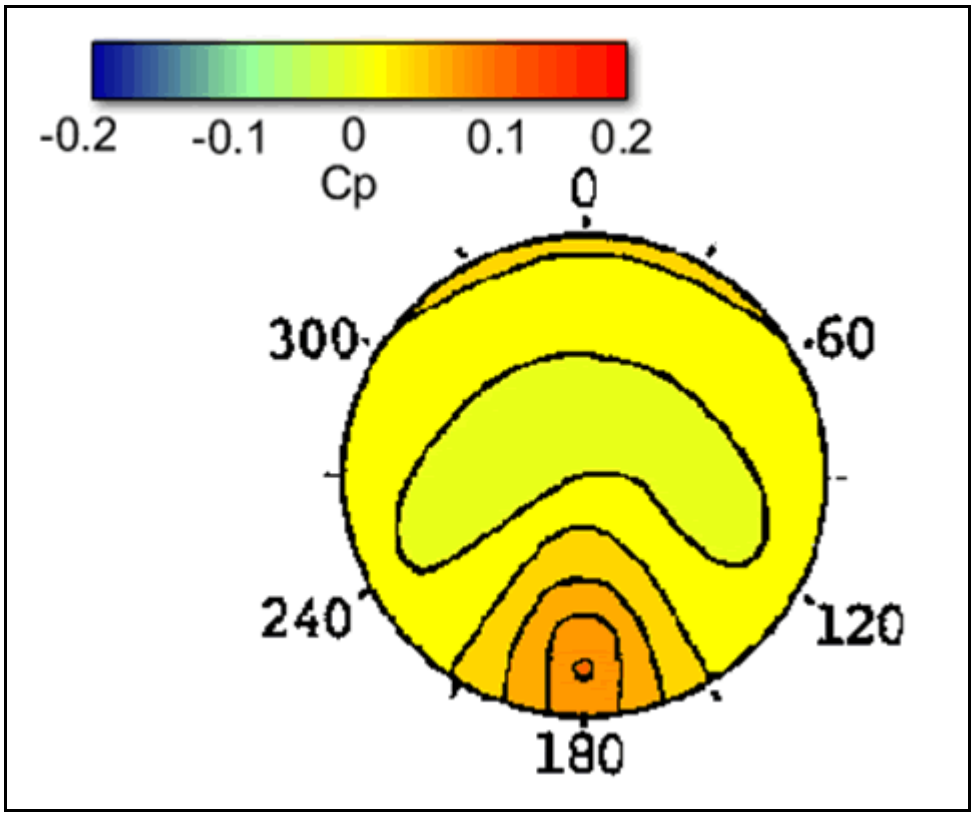

Figure 2-16 – Colourized mean surface pressure distribution on cavity base for h/D = 1.0 from Hiwada et, al, (1983) inferring 3-D flow configuration.

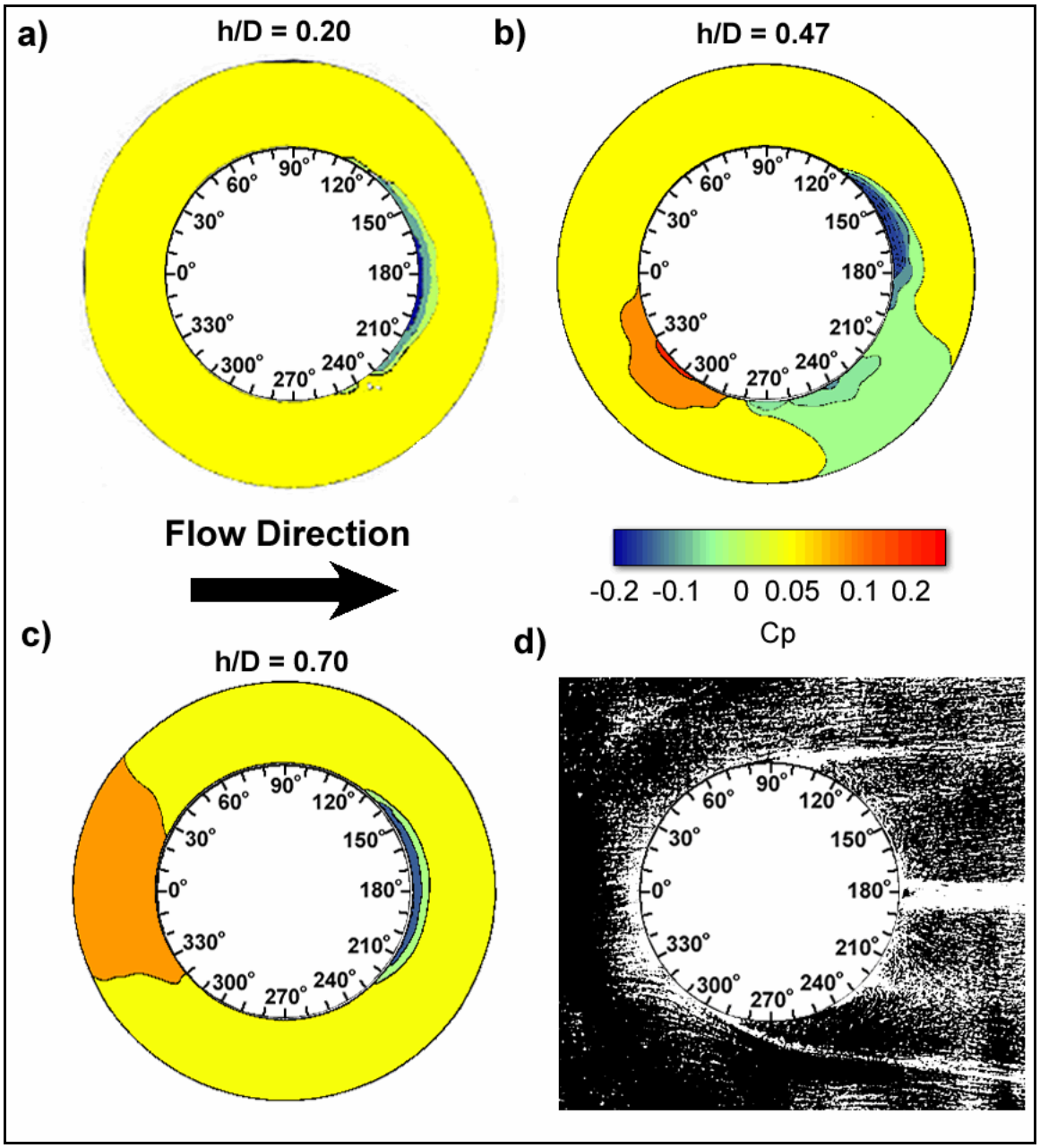

Figure 2-17 – A compilation of mean surface pressure distributions outside the cavity outer lip (figures a,b and c, Savory et. al., 1996) and an surface oil-film pattern from along the cavity outer rim for h/D = 0.47 (figure d, Gaudet and Winter, 1971)

These investigators also carried out a limited investigation of the pressure fluctuations for certain cavity geometries and discussed the flow pattern in the cavity wake.

The mean pressure contours generated using the surface pressure measurements of this experiment allowed the first quantified glimpse of circular cavity flow patterns on the cavity base and along its sidewall. Four cavity depths: h/D = 0.2, 0.37, 0.5, and 1.0 were at the focus of discussion in this investigation.

For the cases of h/D = 0.2 and h/D = 1.0 (Figs. 2-10a, 2-11a and 2-16) a remarkable symmetry was shown in both the cavity base and in the sidewall distributions. From this observation, along with the appearance of the pressure-time series at these depths, the investigators inferred that the flow at these configurations was stable. For the case of h/D = 0.2, a series of parallel iso-pressure lines normal to the free stream flow direction near the downstream edge of the cavity base graph (see Figure 2-10a) suggested a "two-dimensional reverse flow" (Hiwada et. al., 1983) along the cavity base at this point. This was in obvious contrast to the h/D = 1.0 case (Figure 2-16) where the flow was strongly three dimensional along the base.

For the h/D = 0.5 case, the investigators stated that this configuration yielded the greatest amount of drag due to the fact that the mean surface pressures on the downstream sidewall were at a maximum, suggesting that this was the configuration that drew the greatest amount of fluid into the cavity – and thus maximized the drag.

A unique contribution made in this study was the use of pressure transducers to generate pressure-time histories measured near the cavity rim for various depth configurations (summarized in Figure 2-18). For $h/D \leq 0.2$ and $h/D \geq 0.8$, a stable flow regime was proposed and at h/D = 0.2, the fluctuations became larger. Hence, this was considered to be the beginning of the "flapping" regime. These larger "flapping" fluctuations were of the order of 1 Hz and amplitude $Cp \cong 0.08$ for the h/D = 0.2 case and, with increasing h/D, slowly changed in amplitude and frequency until h/D = 0.37 (Figure 2-19) where the frequency decreased to ≈ 0.125 Hz and reached a maximum amplitude of $Cp \approx 0.14$. This flapping regime was said to extend from h/D = 0.2 – 0.4 at which point a regime named the "switch flow" regime began. In this

regime, which extends from h/D = 0.4 – 0.7, the cavity flow was said to be vulnerable to large steps in mean Cp (seen in Figure 2-18) when a disturbance was introduced upstream of the cavity model.

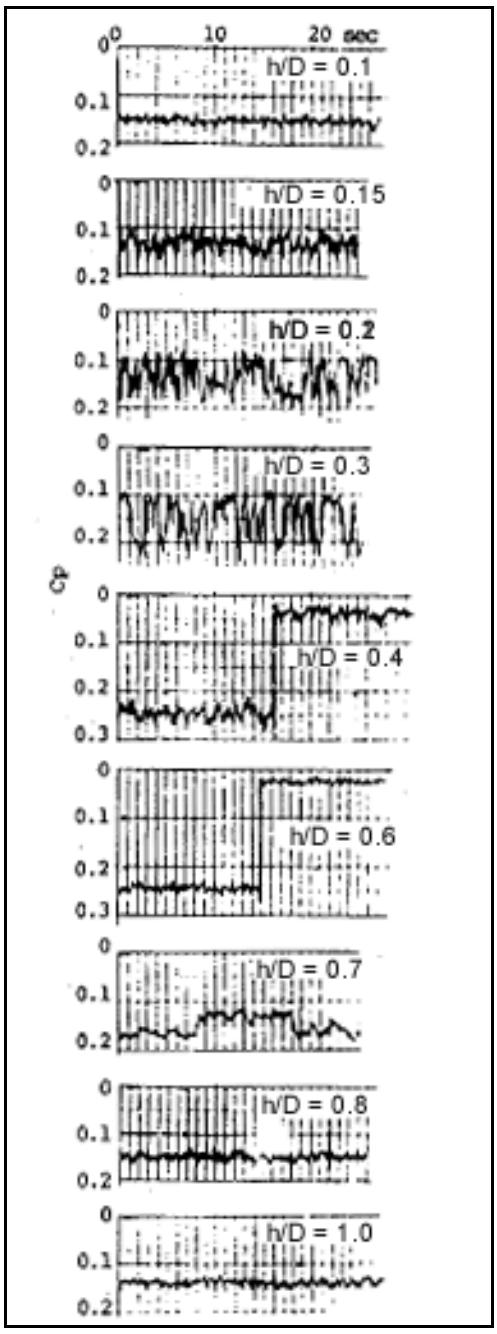

Figure 2-18 – Non-dimensional pressure-time histories from Hiwada et. al. (1983) for various cavity depths.

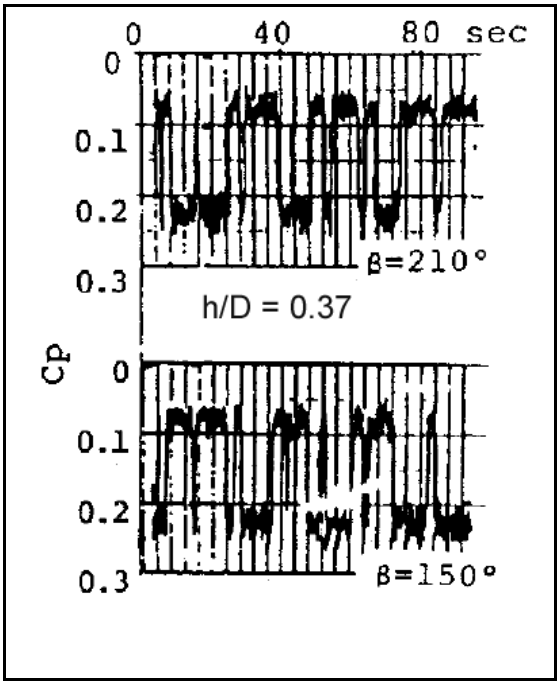

Figure 2-19 – Pressure-time history for h/D = 0.37 from Hiwada et. al. (1983) showing "flapping" behaviour.

Also included in their report was a stream-wise velocity distribution measured at many points across the span of the working section at a location downstream of the cavity (shown in Figure 2-20) for h/D = 0.5, demonstrating the asymmetry in the velocity distribution in the cavity wake.

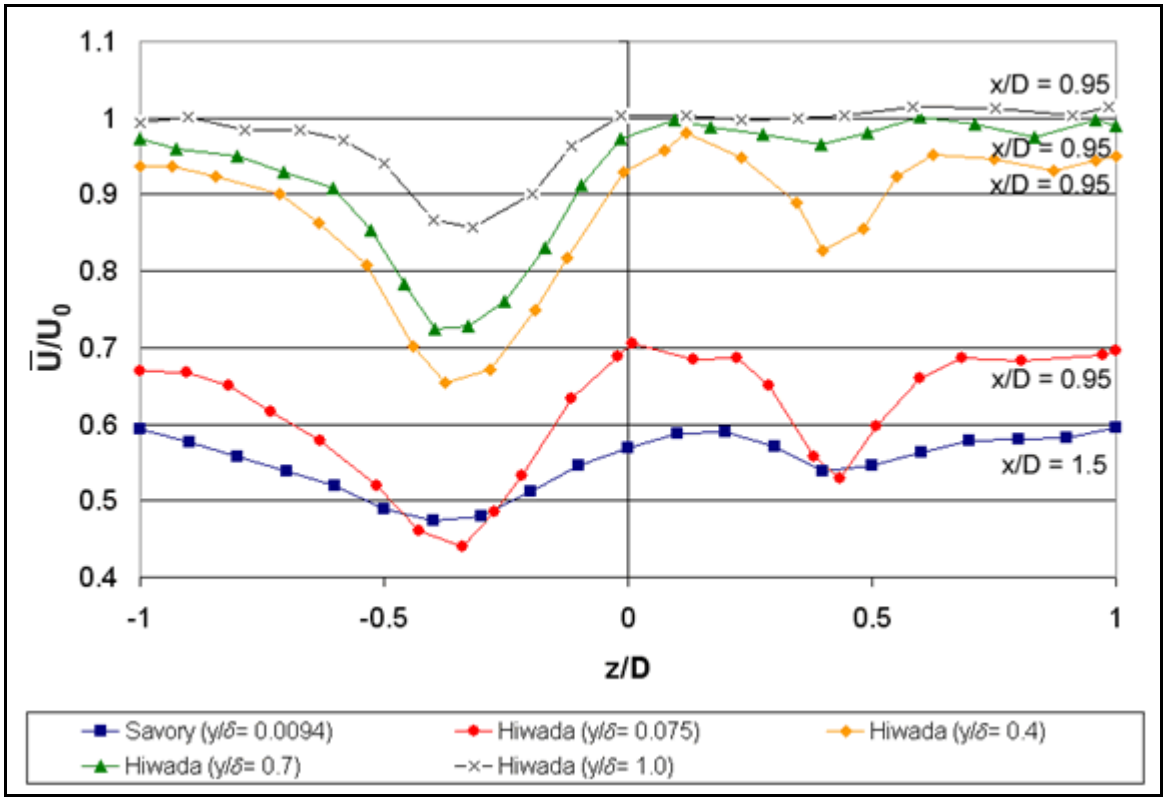

Figure 2-20 – A compilation of wake velocity profile measurements by previous investigators Savory et. al. (1996) and Hiwada et. al. (1983) for h/D = 0.5.

The most recent investigation of this topic was published in the 1990's (Savory et. al., 1996). Though the main purpose of this particular study was to investigate the effect of cavity lip rounding on the cavity drag, a large amount of data was also included for the case of a circular cavity with unrounded or sharp lip such as the case for the present investigation. The relevant measurements taken in this study included: mean cavity surface pressures, direct measurement of cavity related drag and mean velocity and turbulence intensity measurements at select points above the cavity and in its wake.

Using a free stream velocity of 12 m/s with boundary layer thickness δ = 320 mm, skin friction factor c_f = 0.00265 and cavity diameter D = 75 mm for the pressure measurements, mean pressure distribution figures were reported – seen in Figures (2-10 to 2-17).

These figures represent mean pressure distributions along the base of the cavity (Figs. 2-10b, 2-12b and 2-14) and the "unwrapped" sidewall (Figs. 2-11b, 2-13b and 2-15) with the left and right boundaries being the upstream point and the horizontal centre point being the downstream point, finally distributions along the outside of the cavity surrounding its lip were also presented (Fig. 2-17), the first of their kind.

For the case of h/D = 0.2, the investigators observed a symmetric pressure distribution and inferred shear layer reattachment to explain the pressure maximum found on the downstream face of the sidewall (Fig. 2-11b) and the suction (pressure minimum) in the cavity wake (Fig. 2-17). Using reasoning originated by Roshko, the authors also pointed to lower pressures found on the cavity sidewall at 90° and 270° as indicating the presence of a single vortex with axis in the span-wise direction.

For h/D = 0.5, an asymmetric distribution was again observed and the investigators suggested that the relatively high stagnation pressure due to the shear layer reattachment on the downstream sidewall was caused by the drawing of fluid with higher momentum from higher up in the boundary layer. The trailing vortex caused by the exposed main vortex tube at this configuration was used to account for the appearance of an asymmetric flow pattern in the cavity wake (Fig. 2-17b).

For h/D = 0.7, the symmetry in the distribution on the cavity sidewall (Fig. 2-15), especially of the pressure minima therein at θ = 90° and 270°, was used as evidence for the existence of a single large vortex, once again with its axis in the span-wise direction across the cavity.

Using a one-component hot-wire anemometer these investigators were also able to obtain velocity and turbulence intensity profiles across a portion of the cavity wake as seen in Figures 2-20, 2-21 and 2-22.

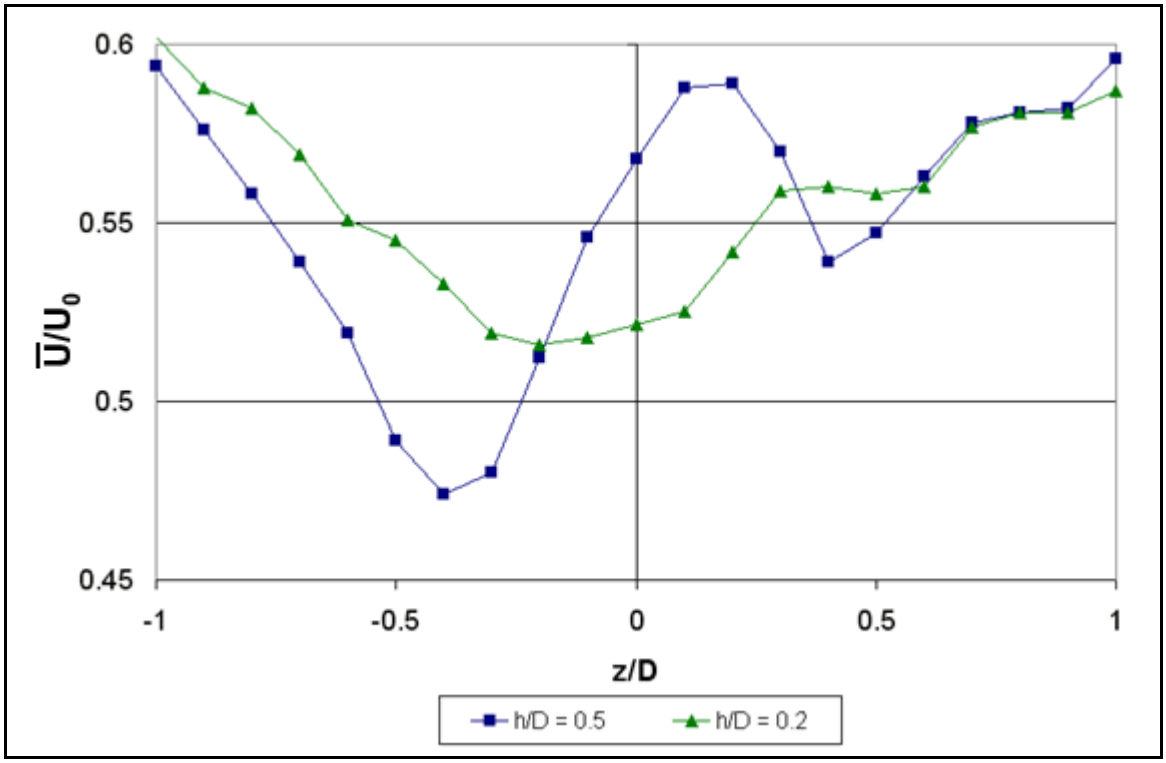

Figure 2-21 – Stream-wise velocity profiles for h/D = 0.2 and 0.5 from Savory et. al. (1996).

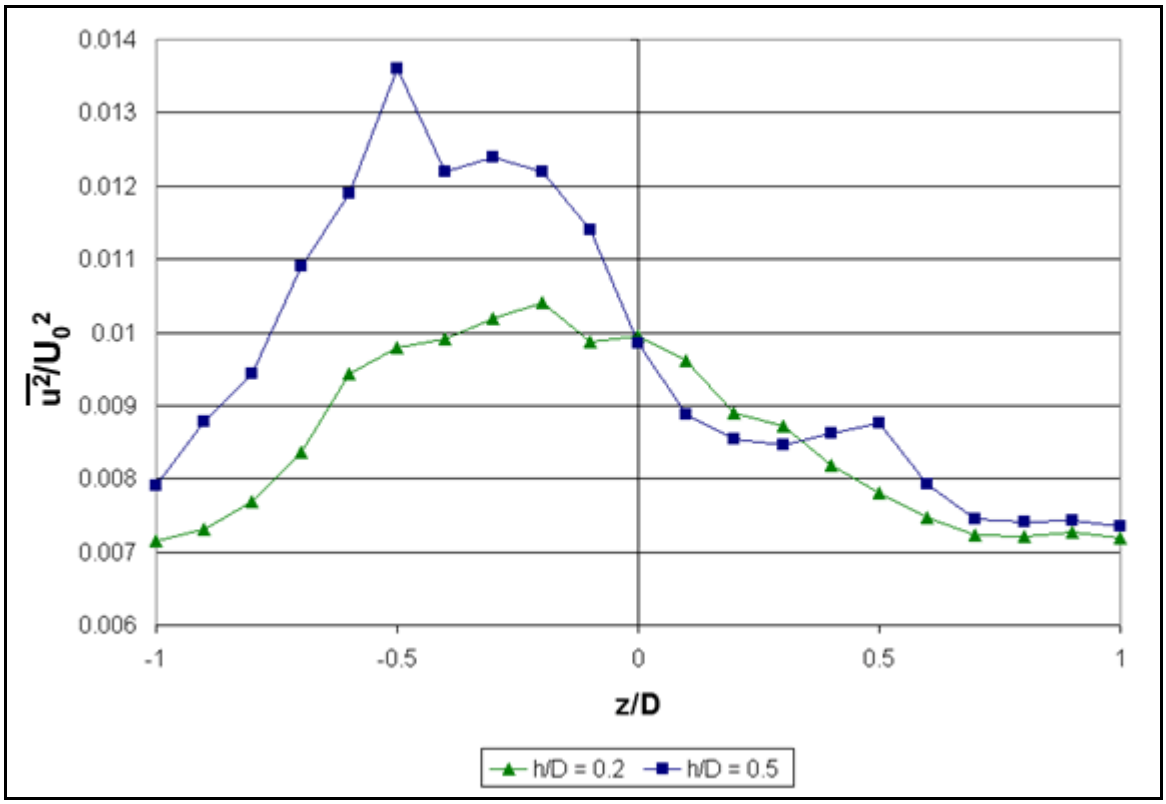

Figure 2-22 – A compilation of stream-wise turbulence profiles in the cavity wake by Savory et. al. (1996) for h/D = 0.5.

These profiles were taken 1.5D (112.5 mm) downstream of the cavity centre at a height of 0.04D (0.009375 δ) from the tunnel wall. For h/D = 0.2, it was noted that a broad, slightly asymmetric stream-wise velocity deficit was observed spanning from approx. z = -D to +D. This asymmetry was attributed to possible slight model asymmetries or non-uniformities in the approach flow. For h/D = 0.5, both the velocity profile and the turbulence intensity profile exhibited extreme asymmetry and in both cases the main feature of the profile was found on the left side (-z) of the profile. The investigators attributed these features (a velocity deficit for the velocity profile and a peak in the turbulence intensity profile) to the existence of the trailing vortex in this region. In the velocity profile, the small excess of stream-wise velocity found at z/D = 0.1 as compared to the case with no cavity model in place was explained by the investigators as the result of the trailing vortex sweeping down higher momentum fluid from higher in the boundary layer.

Having discussed the research done in the form of mean pressure distributions and wake velocity profiles, the possible cavity flow oscillation mechanisms will now be considered.

2.4 Driving Mechanisms for Oscillations

The examination of pressure fluctuations on the cavity surfaces and velocity fluctuations in the cavity wake is a major objective in this current study and thus this sub-section is intended as a summary of important known sources of oscillation for cavity flows. Where appropriate, frequency prediction methods are applied to the current experiment to estimate frequencies of interest for the present study.

2.4.1 Fluid Dynamic Mechanisms

Fluid dynamic fluctuations are fluctuations in the velocity of a fluid and can be caused by a variety of mechanisms of which a few are explained here:

1. Turbulent Boundary Layer - The flow in a turbulent boundary layer, the type of flow used in the present experiments, is by definition turbulent and thus, is a major contributor to broad-band fluctuations in velocity. Although any stream-wise or lateral velocity fluctuations are zero at the wall, vertical ones are not and thus turbulent boundary layers can still be producers of noise at points on the wall (Milbank, 2004).
2. Flow over a leading or trailing edge – broad-band fluctuations can be caused by the flow over leading and trailing edges including those found in a surface mounted cavity (Milbank, 2004).
3. Vortex Fluctuation – fluid trapped in a vortex causes narrow-band fluctuations related to the size of the vortex and the circulation velocity of the fluid therein. For the current experiment, stable vortices are often found inside the cavity, and thus, fluctuations in the wake velocity and model surface pressure

related to this phenomenon are likely to be observed (Lin and Rockwell, 2001).

2.4.2 Fluid Resonant Mechanisms

Standing wave acoustic oscillations can be generated when the wavelength of a noise source in the flow closely matches the length of an open feature in the experimental apparatus geometry (Sen, 1990). A common instance of this includes resonance due to the length or width of the wind tunnel used. For the case of a rectangular resonator closed at both ends, the frequency of sound contributed by the axial mode is predicted using the following equation:

$$\boxed{f_n = \frac{c}{2}\left(\frac{N}{l}\right)} \text{ (Bies and Hansen, 1996)}$$

Where N is a positive integer, c is the speed of sound and l is the length of the feature in question.

Air column vibration can also occur in open cylinders such as the case of the cavity model used for this experiment. The equation often used to estimate the frequency of such oscillations is shown below:

$$\boxed{f = \frac{Nc}{4(h + 0.3D)}} \text{ (Sen, 1990)}$$

Where N is an odd integer, c is the local speed of sound, h is the column depth and D is the column diameter. Such oscillations are unlikely for short columns, but using this equation, frequencies of 2329 Hz, 1512 Hz and 1164 Hz for h/D = 0.2, 0.47 and 0.7, respectively.

2.4.3 Feedback Resonance

Feedback resonance (defined in Section 2.2.2) refers to an interaction between a pressure pulse created at the downstream cavity lip by shear layer vortex stagnation and an unstable shear layer at the upstream cavity lip. Rossiter's formula is used to predict the frequency of sound due to this mechanism, and while this prediction was formulated only for rectangular cavities, if this formula were to be applied to the cavities used in this experiment using the cavity diameter in place of the cavity length L, the following equation is derived:

$$\boxed{\frac{fD}{U_0} = \frac{m - \gamma}{M + 1/\kappa}}$$

Substituting the appropriate values relating to the current experiment, D = 0.076 m, U_0 = 27 m/s, and M = 0.077, a value of 145.5 Hz is returned for the predicted 1st mode frequency.

2.5 Summary

Although quite a large amount of research has been focused on the flow over cavities of rectangular planform, only a few investigations have dealt with the flow over cavities of curved planform, and circular planform in particular. Most of the developments that aid in the understanding of the flow over cavities in general have resulted from the study of flow over rectangular cavities.

Roshko's pioneering classification of "open" and "closed" cavity flows (Roshko, 1955) by the location of the shear layer reattachment point, Rossiter's classification of cavity-related oscillations and his discovery of the feedback mechanism that drives strong oscillations (Rossiter, 1964) were all results of the study of the flow over rectangular cavities and are still used today to aid in the description and understanding of cavity flows.

Gaudet and Winter were the first to make breakthroughs in the understanding of the flow over cavities of circular planform in particular (Gaudet and Winter, 1971). Through their introduction of the drag parameters A and B, results from circular cavity measurements of widely varying approaching flow conditions were able to be compared on a single graph. Additionally, Gaudet and Winter were the first to conduct a flow visualization experiment with this type of cavity and so extracted a great deal of information regarding the internal and external flow structures present in this type of flow. In particular, for h/D = 0.47, these investigators proposed a "slant recirculating vortex" in the cavity, which due to its exposure to the external flow, accounted for the higher drag at this configuration and also accounted for the asymmetric flow observed in this case.

Hiwada et. al. were the first to develop pictures of the mean pressure fields along the cavity model surfaces (Hiwada et. al., 1983), lending quantitative support to Gaudet and Winter's flow visualization observations. Through a detailed investigation of pressure-time histories for a wide range of cavity depths, these investigators also suggested a series of cavity flow regimes dependent on cavity depth to describe observed pressure oscillations, which may prove to be a useful tool for further classification of this type of flow.

Savory et. al. were the first to show the mean pressure fields along the cavity's outside rim (Savory et. al., 1996) which, combined with span-wise lines of single component hot-wire measurements at points in the cavity wake, allowed for a greater understanding of the flow in the cavity wake, in terms of mean velocities and turbulence intensities.

A table summarizing circular cavity flow investigations is seen below:

Authors	Contributions	U_0 (m/s)	D/δ	c_f	h/D range
Friesing	- Single line mean Cp distributions - Direct drag balance measurements	40	20.3*	0.0056	0.02 – 1.2
Wieghardt	- Direct drag balance measurements	25	1.49, 2.24	0.00258	0.02 – 1.5
Tillman	- Large amount of drag data	28	0.60	0.00254	0.02 – 1.5
Gaudet and Winter	- Surface oil-film patterns, surface flow analysis - major contribution to understanding of circular cavity flow structure - Drag coefficient A introduced independent of flow conditions	69	unknown/190 mm	0.00225	0.04 – 1.34
Hiwada et. al.	- Mean surface pressure contours - Mention of reversible asymmetric flow for h/D = 0.5 given upstream disturbance - Proposal of flow regimes for various h/D using pressure-time histories	25	0.20	0.0047*	0.1-0.8
Savory et. al.	- Mean surface pressure contours on outer cavity rim - Span of turbulence measurements in cavity wake	12	0.23	0.00265	0.1-0.7

Table 2-1 – Summary of available circular cavity research details and significant contributions.

* - Boundary layer thickness was predicted using 1/7th power law over flat plate

Oscillations in cavity flows are generally driven by velocity fluctuations in the turbulent boundary layer, flow over leading or trailing edges and cavity recirculation. If one of these driving mechanisms has a frequency component near a resonance frequency of the cavity apparatus, the system can be drawn into resonant oscillation. Resonant conditions can cause cavity feedback resonance between the upstream and downstream cavity lips or depth-mode oscillation related to cavity geometry.

The experiments carried out in the present experiment to extend this previously described research are described in the following section.

3 EXPERIMENTAL DETAILS AND METHODS

3.1 Overview

This section describes the measurement apparatus, experimental methods, and the uncertainties related to the present experiments to give the reader an understanding of the experimental setups used in order to obtain the data discussed in the results and discussion section. Decisions related to the experimental design as well as the design and construction of components of the experimental apparatus are also presented in this section. This section is divided into subsections to allow the discussion of the different types of measurement systems individually.

3.2 Experimental Details

3.2.1 Wind Tunnel and Geometry

Co-ordinate Definitions

Three sets of co-ordinates are used to discuss the experiments in this thesis: co-ordinates relative to the tunnel working section inlet for external flow evaluation (Figure 3-1), a polar co-ordinate system relative to the centre of the cavity model mouth plane for surface pressure measurements (Figure 3-2) and a rectangular co-ordinate system relative to the same cavity model centre for analyzing velocities in the cavity wake (Figure 3-3).

The wind tunnel used for the present experiment was a dual-fan hydraulic pump powered closed loop tunnel (as seen in Figures 3-4 and 3-5) in the Boundary Layer Wind Tunnel Laboratory at the University of Western Ontario.

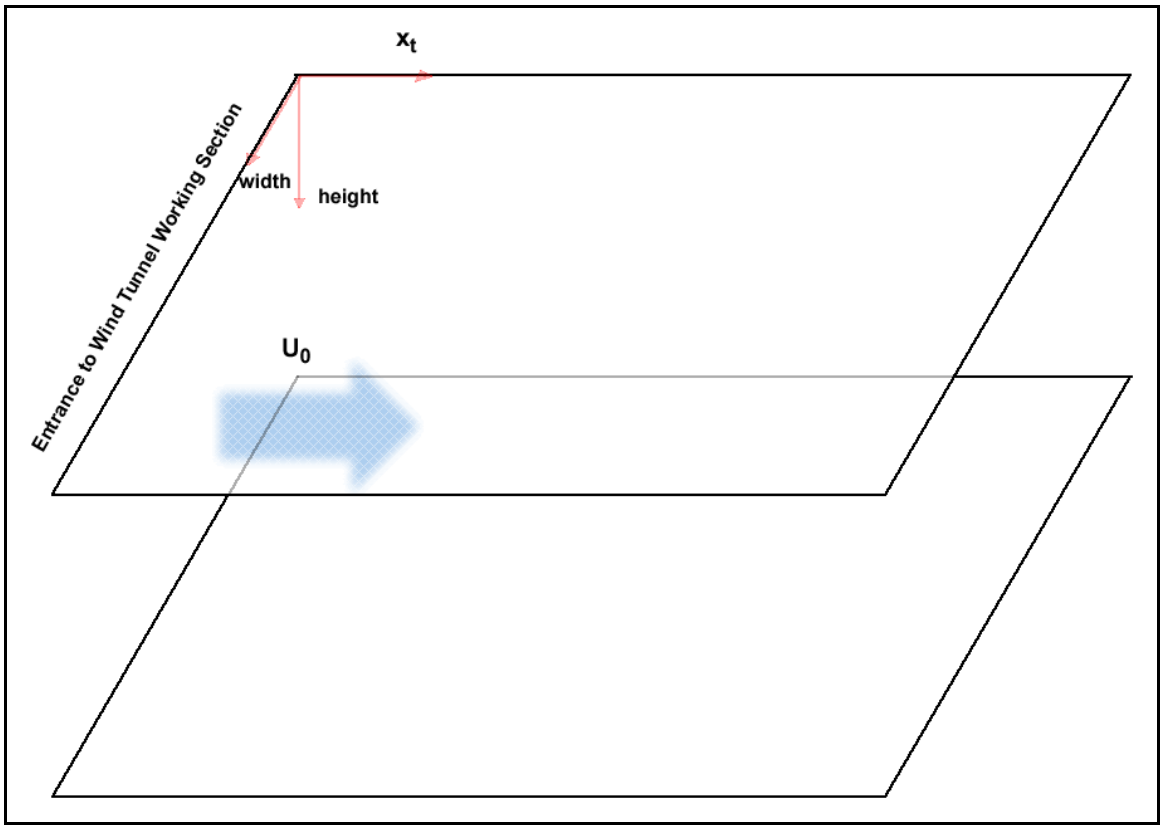

Figure 3-1 – Rectangular co-ordinate system used in wind tunnel external flow evaluation. Left side of diagram shows end of wind tunnel contraction and entrance to working section.

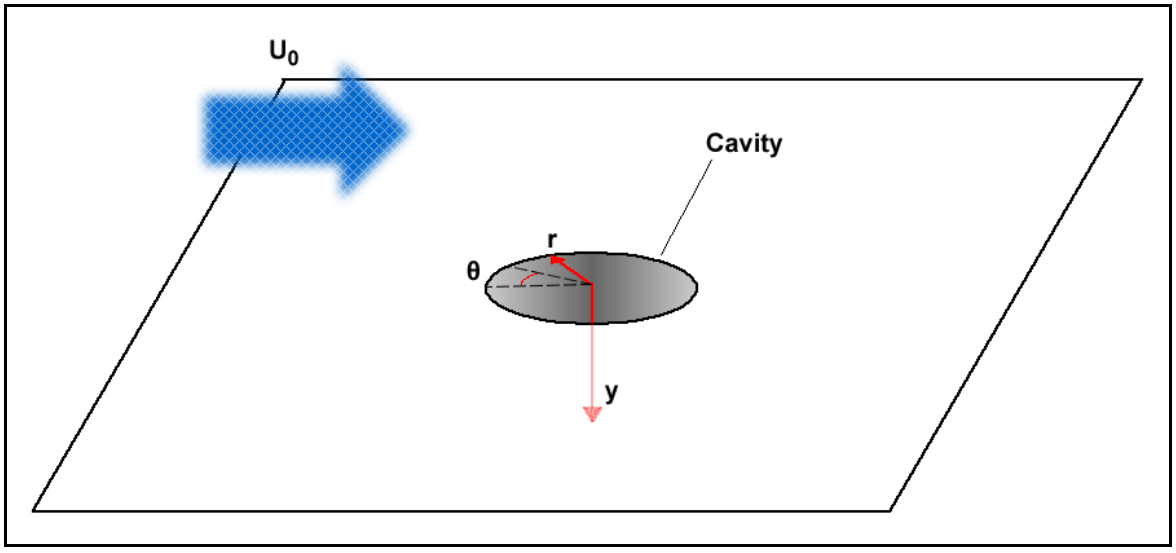

Figure 3-2 – Polar co-ordinate system used in analysis of cavity model surface pressures.

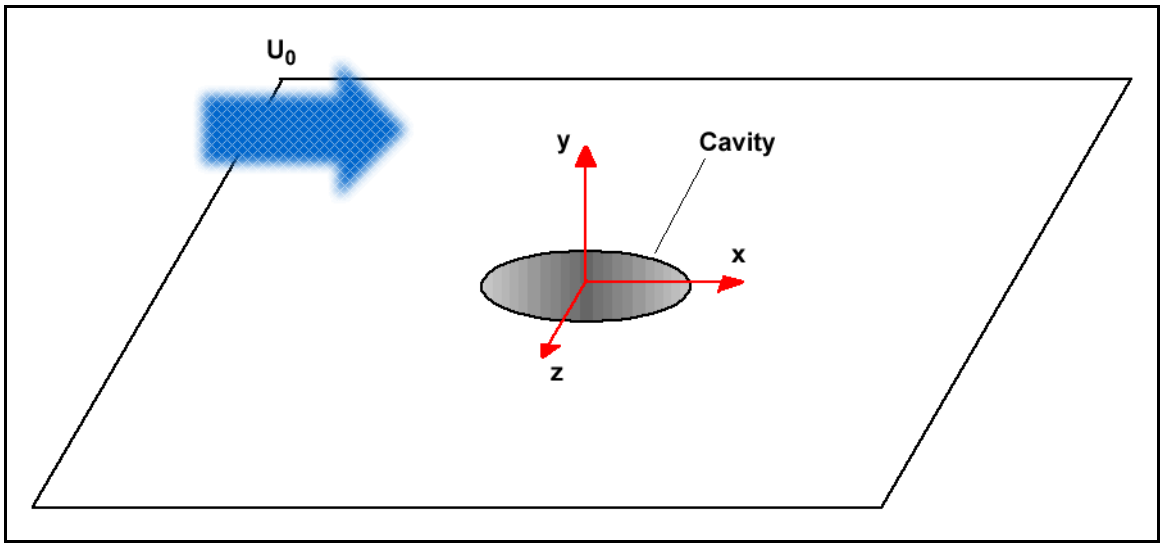

Figure 3-3 – Rectangular co-ordinate system used in analysis of velocities in cavity wake.

The wind tunnel's working section dimensions are as follows: height: 214 mm (2.82D), width: 611 mm (8.04D), length: 6500 mm (85.5D), where D is the cavity model diameter. The inlet contraction ratio for this tunnel is 4.12. The maximum sustainable free-stream speed of this tunnel was found to be 27 m/s with free-stream turbulence of ~0.5%.

Since the wind tunnel used for experiments was a closed loop tunnel, there was insufficient room to place a cavity model in the floor of the working section, hence, models were designed to be placed in the tunnel roof. Before the current experiment this tunnel had a working section with a flexible acrylic roof allowing the introduction of stream-wise pressure gradients. Due to the present experiment's requirement of pressure and acoustic signal measurements, the roof was redesigned and changed to minimize any noise generated by oscillations of the flexible roof. The change was also made so as to allow the original flexible roof to be reinstalled and used for other purposes in the future.

As can be seen in Figures 3-4 and 3-5, the new roof was constructed from sections of ¾" thick MDF with seven 390 mm diameter span-centred holes cut at the following downstream locations relative to the tunnel inlet: 958 (12.6), 1720 (22.6),

2443 (32.1), 3155 (41.5), 3713 (48.9), 4285 (56.4), 4831 mm (63.6D – all bracketed figures are in terms of cavity diameter D). The inclusion of these holes in the roof allowed the possibility for the model to be inserted at various downstream locations of the working section and hence permitted variation of the Reynolds' number based on downstream position and approaching turbulent boundary layer thickness (hereafter δ), were this to be required.

Figure 3-4 (L) and 3-5 (R) – Photos of the closed-loop wind tunnel used with new MDF roof installed. The left photo shows the view downstream with circular plug outlines visible. The right photo shows how the roof is supported using iron screw-down supports.

The roof was supported from above using the screw-down supports visible in Figure 3-5 which were already present. The supports were adjusted to maintain a working section height of 214 +/- 0.5 mm (2.82 +/- 0.007D) across the entire stream-wise length of the working section of the tunnel.

Downstream of the 6th hole in the roof (4285 mm, 56.4D downstream from working section entry) a span-wise slot was cut into the roof of the tunnel to allow the hot-wire apparatus to take measurements in the cavity model wake. This was the location at which the cavity model was placed during measurements and the slot was cut such that measurements were possible at x = 1.85D downstream of the centre of

the cavity. The reason for choosing this location in the working section for measurements is discussed in Section 3.4.1.

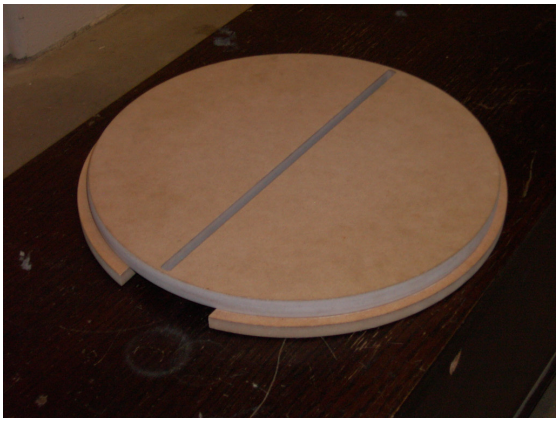

Figures 3-6 (L) and 3-7 (R) – Pictures of the slotted plug used for tunnel boundary layer evaluation shown in profile (L) and in place in the wind tunnel.

When a hole in the roof was not being used to house the cavity model for measurement it was plugged with a sized MDF plug. One of these plugs was modified with a narrow slot cut across its diameter allowing for a probe to be traversed span-wise across the working section at various locations in the tunnel – this apparatus is seen in Figures 3-6 and 3-7.

3.2.2 Model Specifications

The wind tunnel roof modifications described above were all introduced to accommodate the design of a circular cavity model and, hence, to allow measurement of the effects due to the presence of the cavity.

Two separate models were designed by the author – one with built-in pressure taps for the measurement of surface pressures and another with holes to fit miniature microphones for measuring unsteady pressures and acoustics. Both models were designed to fit into any of the 7 roof holes thus permitting the variation of external flow conditions. The general design for the two models was very similar; a four piece

assembly of a 390 mm (5.1D) diameter turntable, a tubular cavity sidewall with inner diameter of 76 mm, a cavity base and a tubular cavity plunger allowing the depth of the cavity to be changed from h/D = 0 to 1.6.

The diameter of the cavity turntable was chosen to allow measurements at the widest range of locations along the surface of the working section without experiencing interference with the wall boundary layers of the working section. Cavity diameter and variable depth dimensions were designed to allow the measurement of cavity conditions studied by previous investigators in an attempt to check the present results against previous work. These assemblies are displayed and labeled in Figures 3-8 to 3-11.

Pressure Tapped Model

The pressure tapped model (Figures 3-8 and 3-9) was machined from acrylic and contained 40 brass pressure taps each measuring 1 mm in outer diameter and 0.5 mm in inner diameter. The taps were distributed about the model surfaces as follows (visually represented in Figures 3-8 and 3-9):

- 10 in a single radial line along the cavity base, at the following radial coordinates relative to the cavity centre: 0, 3.2, 6.4, 11.5, 16.5, 21.5, 24.5, 27.5, 31.2, 34.2 mm
- 14 in three vertical lines along the inner cavity sidewall allowing measurements at the following vertical coordinates relative to the tunnel roof surface: 1, 2, 5.2, 8.4, 12.7, 14.5, 16, 18, 21, 26, 31, 36, 41, 46 mm
- 16 in three radial lines along the cavity turntable surface with radial coordinates relative to the cavity centre: 40, 43.2, 46.4, 47, 51.7, 54.2, 56.7, 59.2, 61.7, 69.2, 79.2, 82, 92.7, 149.2, 172.5, 179.5 mm.

Dimensioned schematic drawings of this model are included in Appendix A.

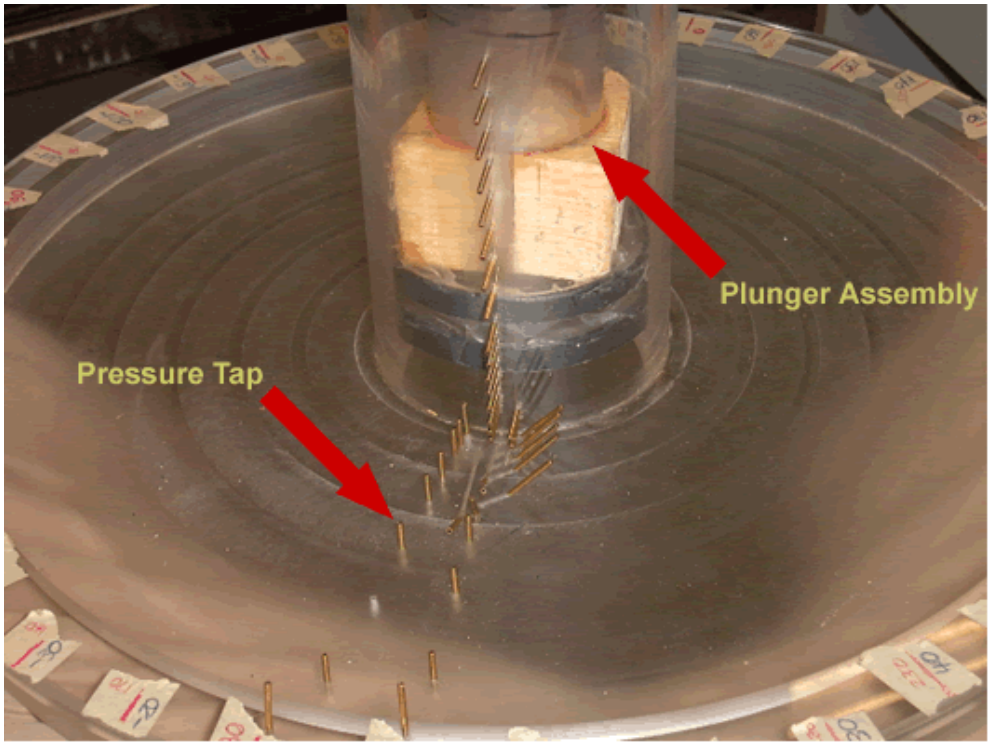

Figure 3-8 – Top view of pressure-tapped cavity model. Two lines of wake tappings are visible along with main line of sidewall taps.

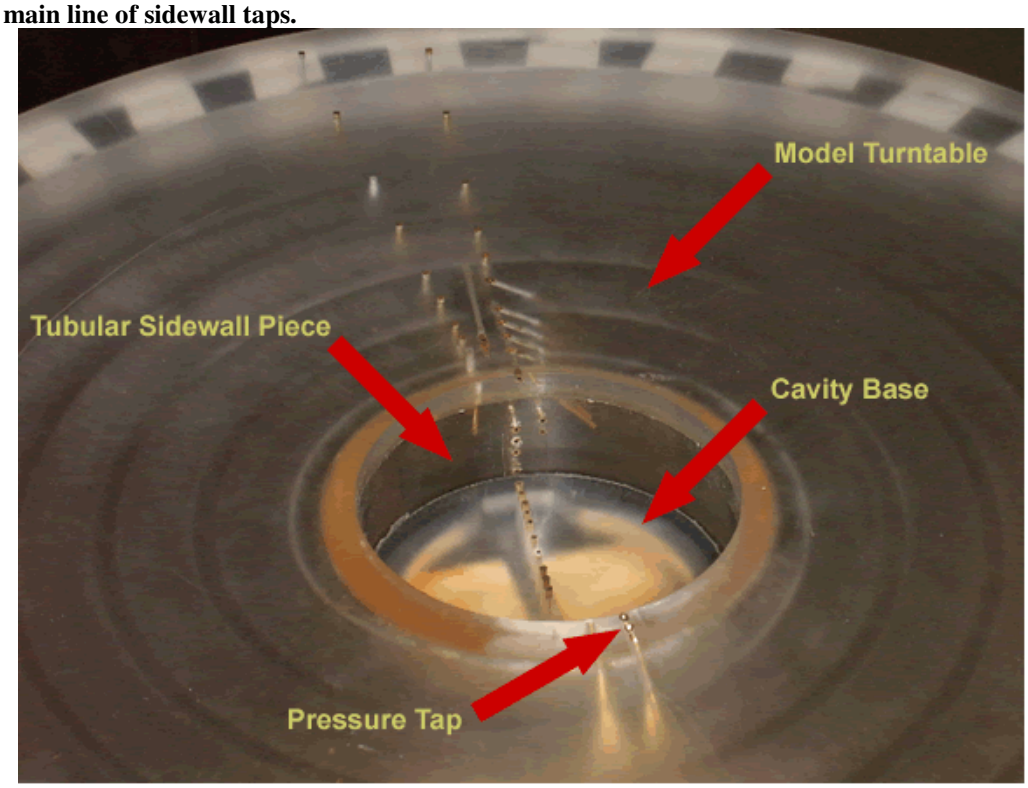

Figure 3-9 - Bottom view of flow-exposed side of pressure-tapped cavity model. Taps along cavity bottom are visible.

These pressure tappings were more densely distributed near cavity model boundaries such as the cavity lip, and the outer region of the cavity base near the sidewall since previous investigations had indicated large pressure gradients in these regions.

Each of these taps was attached to a pressure transducer via a length of tubing to measure the pressure at the surface (further described later in this section).

Microphone Model

The miniature microphone model housed 13 microphones (each of 6 mm diameter, described later in this section) distributed about the cavity base, sidewall and turntable to measure the unsteady surface pressures and acoustics related to the presence of the cavity model. These devices were distributed about the model in the following manner (visually represented in Figures 3-10 and 3-11):

- On the cavity base two perpendicular lines for a total of 9 microphones at radial coordinates of 0, 14 and 28 mm from the cavity centre.
- On the cavity sidewall one vertical line of 3 microphones spaced at 10.5, 26.5 and 41.5 mm from the cavity rim.
- On the cavity turntable 1 microphone located at 88 mm from the cavity centre.

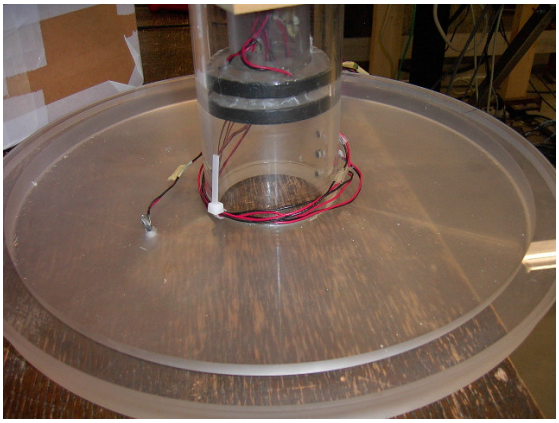

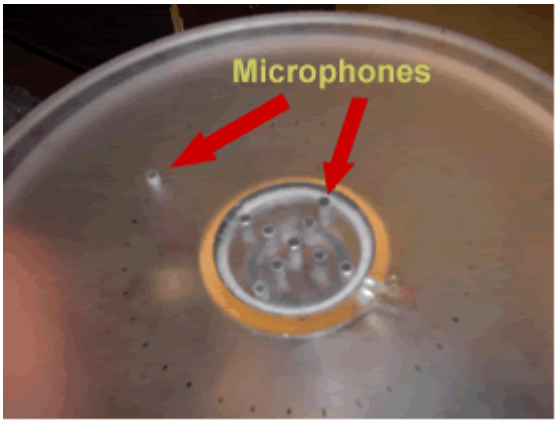

Figure 3-10 (L) and 3-11 (R) – Left picture shows top view of turntable and sidewall-mounted microphones and right picture shows bottom view of turntable and cavity base-mounted microphones.

Once again, dimensioned schematic drawings of this apparatus are included in Appendix A.

Due to the relatively large dimensions of these devices, ideal placement near cavity model boundaries as described for the pressure tapped model was not possible and thus the microphones were distributed quite evenly about the model surfaces to focus on exploring the unsteady pressures on the cavity base and sidewall.

3.3 Measurement Equipment

3.3.1 Hot-wire Anemometry Apparatus

Two-component hot-wire anemometry was used to first define the approach flow and then to measure the velocity point-by-point downstream of the cavity model with the aid of a two-axis computer-controlled traverse. No adequate system for these measurements was available at the inception of this project and, hence, the author was responsible for the ordering, setup and calibration of this equipment, including the labour-intensive work of writing a LabVIEW program to allow

consecutive traverse movements and instances of data acquisition (this program is further described in Appendix O

.

Apparatus Description

Some major elements of this hot-wire anemometry apparatus are shown and described in Table 3-1. The setup for the measurements carried out using the hot-wire anemometers is displayed below in Figure 3-12 in the form of a schematic signal path diagram:

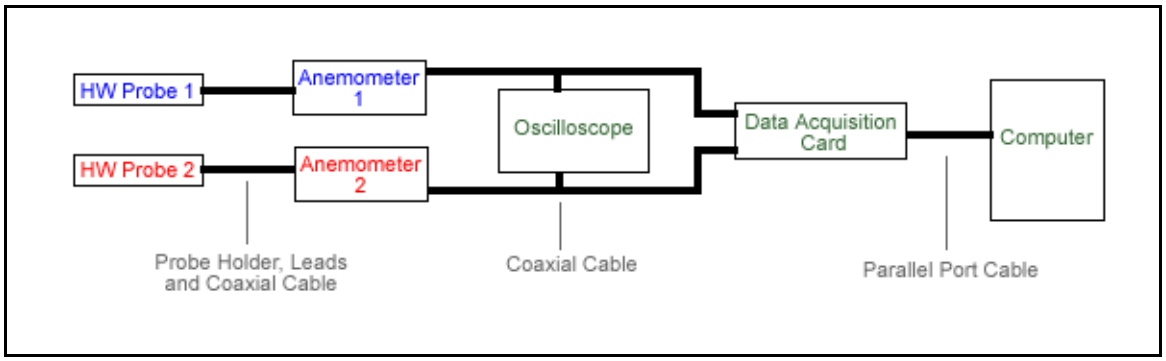

Figure 3-12 – Block signal path diagram representing signal transmission from hot-wire probes to computer. Signal direction is from left to right.

The velocities of the flow were measured in two orthogonal components by the hot-wire probe wires. An electrical signal proportional to the velocities measured by the wires was and then sent to the anemometers for signal conditioning. A coaxial T-junction was used to probe the signals from each wire using an oscilloscope to avoid the need to output the signal to the computer screen and waste valuable RAM. The signals were then acquired by the data acquisition card after which they were stored on the computer's hard drive.

The movement of the hot-wire probe about the wind tunnel working section was facilitated through the use of a new two-axis traverse shown below in the equipment table. A LabVIEW program developed by the author and Cliff Nichols of Velmex Inc. for the sake of this project was used to alternate between the movement of the probe via the traverse and the measurement of the probe's two output channels

using the data acquisition card. This program allowed the traverse to be used to quickly move the hot-wire probe around the working section so that a rectangular grid of measurement points for any particular experimental condition was possible with a positional accuracy of +/-0.003 mm in the horizontal co-ordinate and +/-0.0015 mm in the vertical.

Thumbnail Picture	Device	Purpose
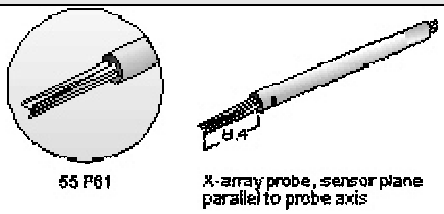 (Diagram courtesy of Dantec Dynamics)	55P61 Miniature Two-Component "X-Wire" hot-wire probe	Initial measurement of fluid velocity in tunnel flow in two orthogonal components.
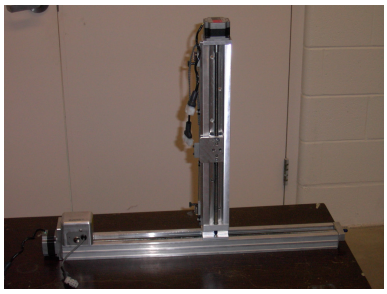	Velmex Two-Axis Stepper Motor Powered Traverse	To allow quick and accurate movement of the hot-wire probe about the tunnel working section.
	Hewlett Packard 6545C PC	To store read and store measurements from the data acquisition card.
	Tektronix Digital Oscilloscope	To display hot-wire signals to screen to ensure equipment is working correctly.

Table 3-1 – Table showing and describing some of the components used in hot-wire anemometry measurements for this experiment.

Wake velocity profiles were achieved using the hot-wire anemometry system described above. A sealable slot was cut behind the cavity measurement position, spanning nearly the entire width of the working section such that the hot-wire probe could be positioned in a plane perpendicular to the flow direction at a distance of 1.85D from the cavity centre (see Figures 2-10 and 2-11) with the use of the right-angled probe holder and two-axis traverse. The location of the slot minimized the protrusion of the measurement apparatus into the flow and was located as close to the cavity centre as possible without cutting into the cavity model turntable.

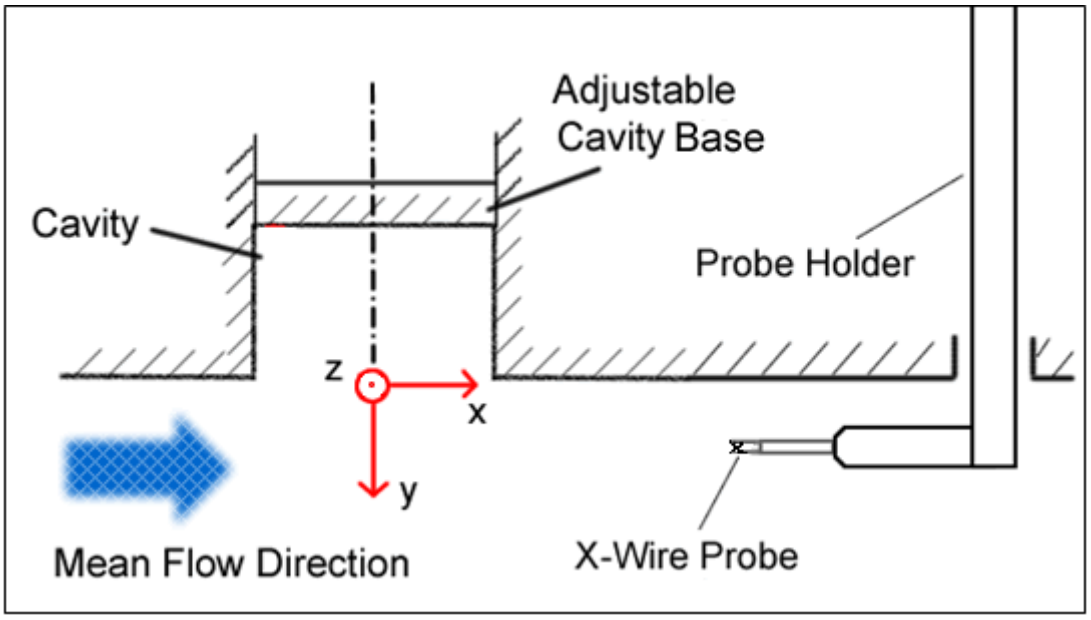

Figure 3-13 - Cross-sectional side view sketch of hot-wire setup used to take wake velocity measurements at x/D = 1.85 from cavity centre.

This setup is further illustrated in Figure 2-14 showing a cavity model in place with the measurement slot visible behind it. The model is in the downstream location that was used for all cavity measurements for this experiment.

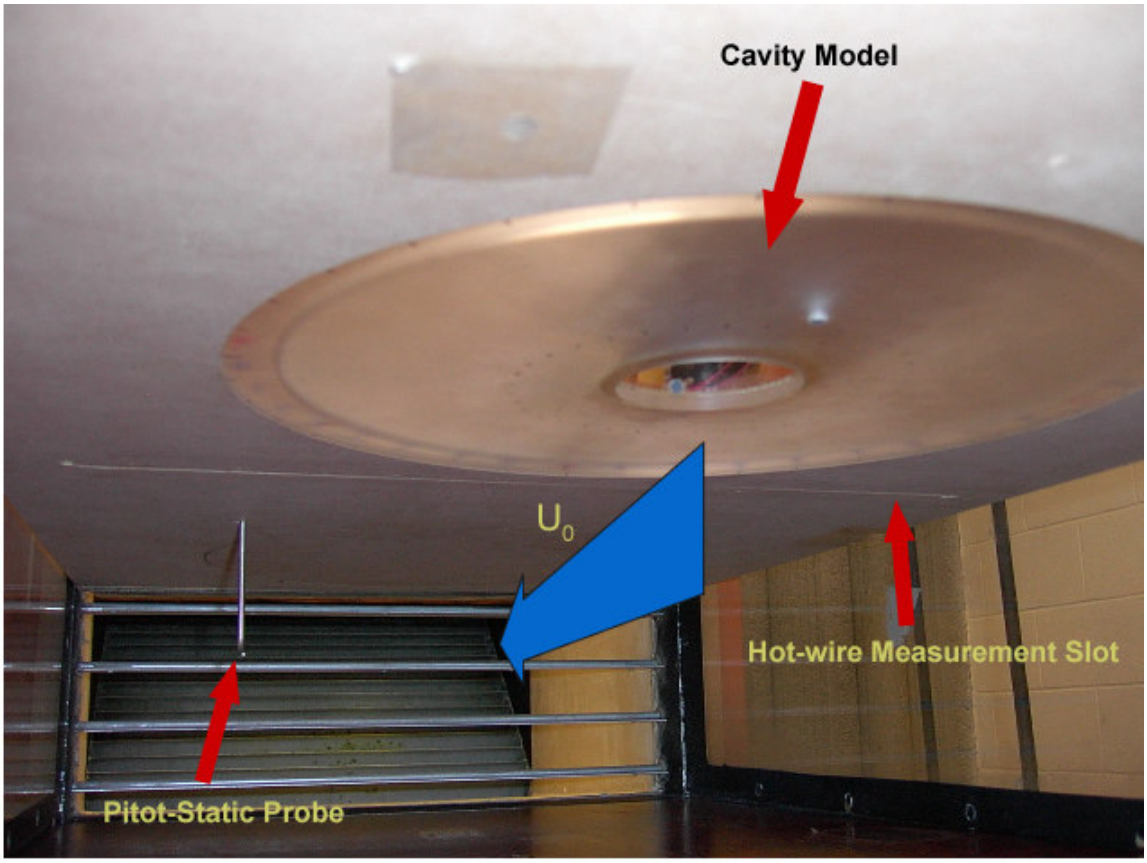

Figure 3-14 - Tunnel in cavity measurement configuration. Span-wise slot is visible behind cavity model turntable, free stream direction points to rear of tunnel in this picture. Placement of the Pitot-Static tube is discussed in the Experimental Measurements section.

3.3.2 Pressure Measurement Equipment

Both mean and unsteady pressure measurements were made in this experiment along the surfaces of the cavity model using pressure transducers and surface mounted microphones. At the time of project inception, too few pressure transducers were available to allow efficient measurements to be taken, and no microphone system was available. Hence, the author was responsible for the ordering, setup and calibration of these devices including the design and construction of signal conditioning circuits for both devices.

Pressure Transducer Setup

Pressure transducers were used to measure mean surface pressures and low frequency pressure fluctuations via the cavity pressure taps and flexible plastic tubing. These transducers were suspended from above by a wooden isolation frame (seen in Figure 3-15) to reduce unwanted noise caused by contact with the vibrating wind tunnel.

Transducer Details

Two types of pressure transducers were used: Honeywell DCAL4 SURSENSE Ultra Low Differential Pressure Sensors and Honeywell DC001NDR4 Ultra Low Differential Pressure Sensors both capable of measuring pressures of +/-250 Pa (gage). Though both of these products had the same physical size and measurement range, the DC001NDR4 had a much smaller frequency response band than the DCAL4. This is discussed further in Appendix F and in the tubing section to follow.

Fourteen transducers were used in all – 9 DCAL4's and 5 NDR4's - and were mounted on custom designed circuit boards (seen in Appendix B) and mounted in protective steel boxes each accommodating up to 4 transducers. All transducers were powered by a 9 VDC wall-powered adapter. A photograph of one such box of transducers is seen in Figure 3-15.

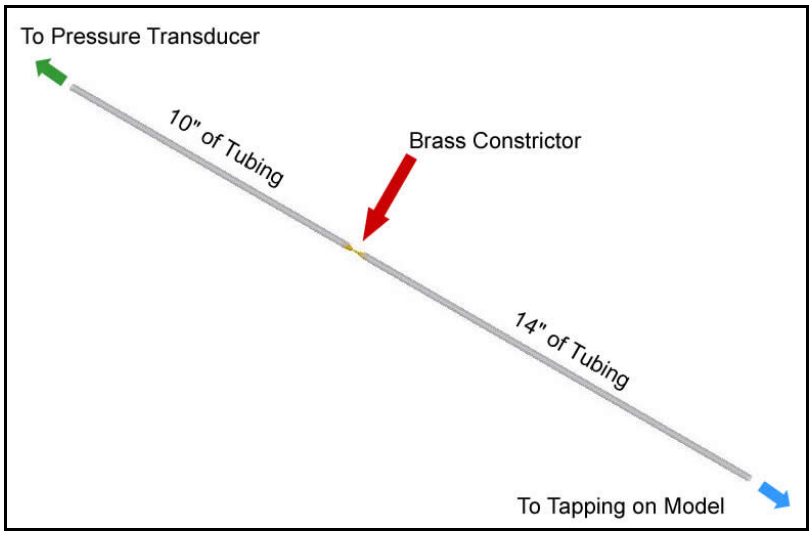

Figures 3-15 (L) and 3-16 (R) – Left shows one of the boxes of 4 transducers used for pressure measurement. Right shows the tubing configuration used for the pressure measurements.

Tubing

Tubes were used between the cavity model and the pressure transducers so as to isolate the pressure transducers from the vibrations of the tunnel roof. Though this type of tube provides vibration isolation, it also has a significant effect on the frequency response of the pressure transducer measurement system. By varying the length of the tubing used for measurement, the frequency response of the system is changed. Many tubing configurations were experimented with to find the widest and flattest frequency response over the frequency range of interest that would also meet the geometric requirements of the project.

The tubing used was #16 PVC tubing and after trying various tubing configurations, the one seen in Figure 3-16 was used for measurements. A brass constrictor was used in the point specified in the figure to force a node at this point, thus influencing the frequency response of the system. This yielded a flat frequency response within +/- 10% from 0 to 80 Hz for the DCAL4's and 0 to 20 Hz for the

NDR4's. Response curves for this and other configurations experimented with can be seen in Appendix F.

Isolation Frame

A wooden isolation frame, seen in Figures 3-17 and 3-18, was designed and built by the author and an undergraduate research assistant (Rita Patel) to support the pressure transducers, allowing them to be isolated from the vibrations of the wind tunnel by being suspended above the wind tunnel using a system of ropes.

Figures 3-17 and 3-18 - These show the isolation frame that allowed the pressure transducers to be isolated from the wind tunnel. Ropes were tied to the part of the frame above the wind tunnel and then tied to the transducers so that they could be connected to pressure taps on the cavity model.

This frame was attached to the wheeled computer cart seen in Figure 3-18 allowing the whole measurement system to be moved together.

3.3.3 Microphone System

Fluctuating pressures at the cavity model surfaces were measured by surface-mounted microphones in the microphone cavity model. Previously used to measure fluctuating surface pressures by investigators such as Czech et. al. (2001) and Johnston and Sullivan (1994), these very inexpensive (approx. $1/unit) miniature microphones were used in experiment to test their effectiveness at measuring fluctuating surface

pressures to allow the generation of flow pattern contours and Power Spectral Density plots over a large frequency band. A block diagram of the signal path for this measurement system is shown in Figure 3-19:

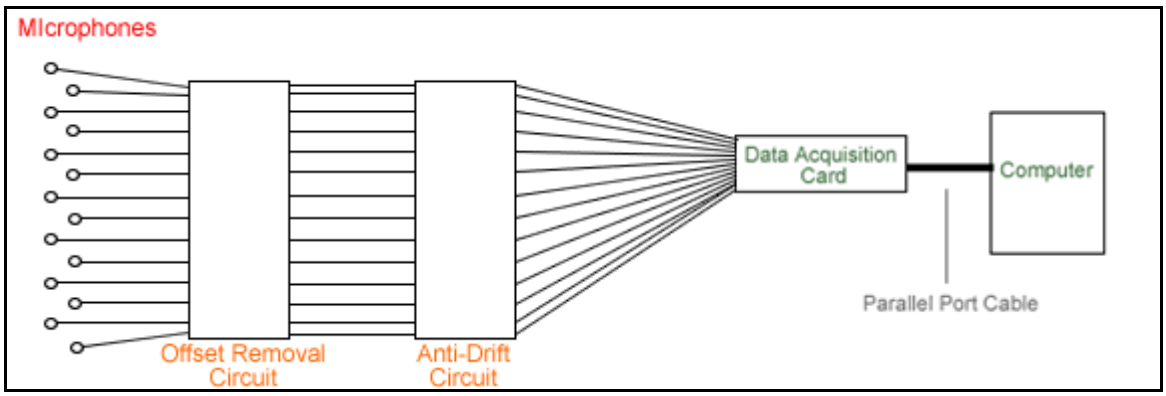

Figure 3-19 – Block signal path diagram representing signal transmission from miniature microphones to computer. Signal direction is from left to right and various stages of signal status are shown.

The microphones used for measurement were Panasonic WM-61B Miniature Omni-directional Back Electret Condenser Microphones seen in Figures 3-20 and 3-21.

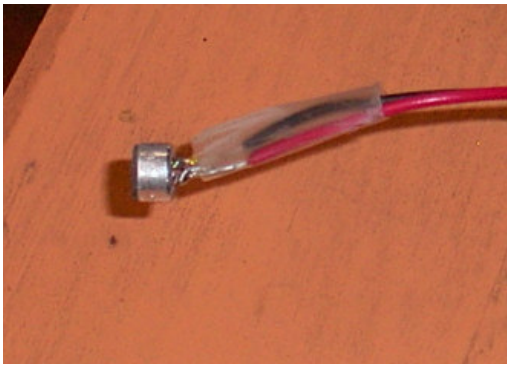

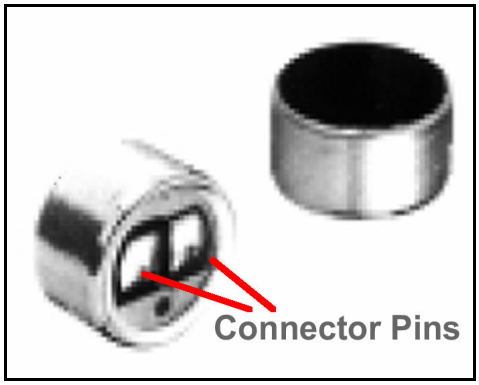

Figures 3-20 (Left) and 3-21 (Right) – L – Side view of wired miniature microphone used in measurement. R – Oblique views of microphones used in measurement showing connector pins soldered to for wiring (photo courtesy of Panasonic Corporation).

All microphones were powered by a 9.6VDC Nickel-Metal-Hydride rechargeable battery to remove the risk of having the very small (+/- 50mV)

microphone signals tainted by any fluctuation in the building's main power. Each microphone output was also run through a series of conditioning circuits built by the author. The first circuit was a manufacturer-recommended circuit to remove the DC offset of the signal caused by the power supply, since the mean of the signal was to be 0 V anyway, the manufacturer-suggested circuit diagram used for this circuit is included in Appendix B. The second circuit (Figure 3-22) was recommended by the UWO Engineering Electronics Shop to remove a large-scale transient drift that was being observed in the signals.

Output leads from the microphones were electrically shielded using aluminum foil to minimize signal interference. Photographs of the anti-drift circuit and the electrical wire shielding can be seen in Figures 3-22 and 3-23.

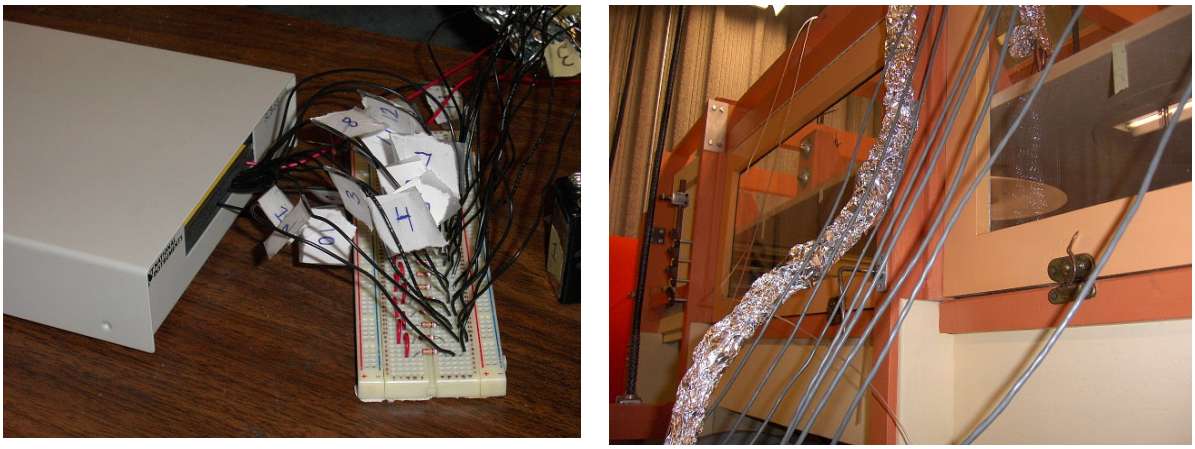

Figures 3-22 (L) and 3-23 (R) – L - Anti-drift circuit with leads being fed into the data acquisition card via a connector box. R - aluminum foil-shielded microphone leads.

3.3.4 Data Acquisition System

All measurements taken using the previously described systems were acquired and stored using a multi-channel data acquisition system acquired for the purpose of this thesis and future experiments. Wires transmitting the analog measurement signals were fed into analog input ports on a National Instruments SCB-68 Connector Box which transmitted the signals to a National Instruments PCI-6052E 16 Channel

Data Acquisition Card mounted in a Hewlett-Packard 6545C PC where the now-digital signals were stored on the computer's hard drive. Coordination of the acquisition process was accomplished using programs written in LabVIEW 7.0 – most acquisition procedures were carried out using modifications of the 'Continuous Acquisition to Spreadsheet File.vi' – an example program provided with most versions of LabVIEW.

With the system described above, the maximum achievable total sample rate was 44 kS/s – far below the acquisition card's quoted maximum sample rate of 333 kS/s. This discrepancy was likely due to the computer's low RAM (256 MB) and processor speed (500 MHz), however, the largest achievable sample rate was acceptable for the purposes of this experiment.

3.4 Experimental Measurements

The measurement and processing methods used to monitor the measurement equipment described in the previous section are briefly described in this section. The methods used for the various measurement systems differed considerably and thus the methods are divided into the different types of measurement systems used.

3.4.1 Measurement of Free-Stream Velocity

For all types of cavity-related measurement the free stream velocity in the tunnel was measured at a point located 320 mm (4.21D) downstream of the cavity centre, offset span-wise a distance of 190 mm (2.5D) from the cavity centre and located at 100 mm (1.32D) from the tunnel roof. The free-stream velocity was measured using a Pitot-Static probe with the output monitored using an electric manometer with a digital display. The Pitot-Static probe was placed a distance downstream of the model and offset span-wise to minimize the effect that the tube's

presence would have on the cavity-related flow. Comparing measurements of the free-stream velocity at this measurement point to measurements of the same taken at the location of the cavity centre with zero depth yielded agreement to within the accuracy of the digital display used (+/-0.05 m/s).

A further reason for placing the probe downstream of the model was that due to the need to rotate the cavity model turntable between measurements, measuring the free-stream velocity at the downstream location of the cavity centre would require offsetting the probe horizontally (span-wise) from the edge of the cavity turntable to in the roof of the working section to allow safe rotation of the turntable. The Pitot-Static tube could alternatively have been installed upstream of the model but when this was experimented with, wake velocity results were affected unless the tube was placed quite far upstream in a region where the free stream velocity was slightly different than the value measured at the model site. Due to the large diameter of the cavity model turntable in proportion to the width of the working section, attempts to measure the free-stream velocity using this method resulted in the probe being positioned in the outer region of the wall boundary layer of the working section. Due to this boundary layer interference, a more turbulent velocity with a lower mean value than that of the free-stream was measured, and hence, it was decided to move the probe downstream to the aforementioned location.

The flow temperature was also measured slightly downstream of the cavity model using a glass thermometer with +/-0.5°C maximum uncertainty.

3.4.2 Hot-wire Measurements

Using the two-component hot-wire anemometry system, velocity measurements were obtained in two components simultaneously at points in a plane perpendicular to the direction of the free-stream flow.

The two channels of the hot-wire signal were acquired simultaneously at 20000 Hz for a sample length of 30 seconds and the signal was filtered in real-time using a 10 kHz Low Pass filter housed in the MiniCTA boxes.

All cavity-related measurements were taken downstream of the 6th roof hole located 4285 mm (56.4D) from the tunnel inlet. The hot-wire probe was positioned 1.85D behind the cavity model centre as seen in Figure 3-13 and using the two-axis traverse, the probe was moved through a series of measurement points ranging from –D (-76 mm) to +D (+76 mm) in the span-wise direction (z-axis) and 0.02D (1.5 mm) to 0.415D (31.5 mm) in the vertical direction (y-axis). The grid of 66 points that was used for these wake measurements is shown in Figure 3-24, where line crossings in the grid image indicate a measurement point:

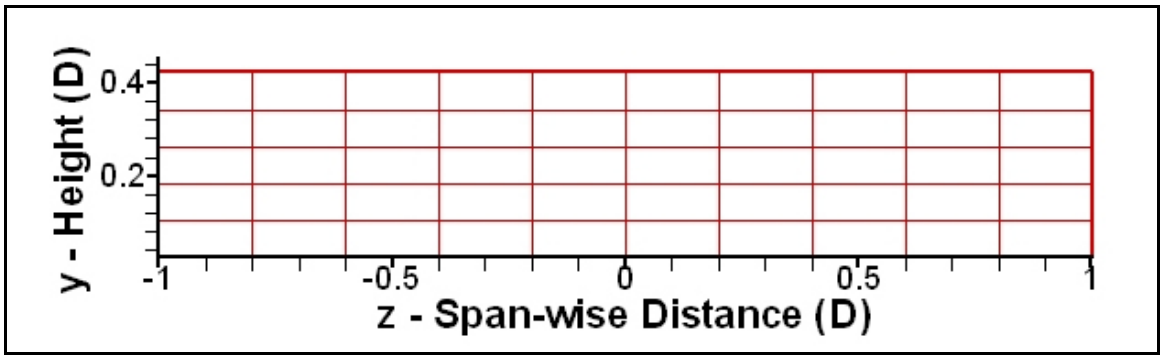

Figure 3-24 – Measurement grid used for hot-wire wake measurements. Coordinates in terms of cavity diameter D.

Cavity measurements were limited to only two cavity depth configurations: h/D = 0.20 and 0.47 due to limited time availability for the hot-wire anemometry apparatus.

Calibration

The hot-wire probe used for measurement was calibrated before every set of measurements *in situ* at the downstream location of measurements once the tunnel had reached the warm-up temperature. During calibration, both the hot-wire probe

and a Pitot-Static probe were positioned near the vertical and horizontal centre of the tunnel working section to avoid turbulence due to the wall boundary layers. The probe and tube were spaced 50 mm span-wise from one another to avoid interference. The velocity of the flow at this calibration point was measured by using a calibrated electric manometer to monitor the output of the Pitot-Static probe.

Each calibration was done with 11 points over a velocity range from 10 to 28.5 m/s, or in terms of U_0, 0.37 to 1.06 U_0. The points measured in the calibration were used to generate a 6th order polynomial fit which, on average, yielded a confidence or $R^2 = 0.99999$. An example calibration curve for this probe can be seen in Appendix G.

Processing

Hot-wire measurements were recorded using a LabVIEW program written by the author which stored each grid of measurement points as one large ".txt" file. A Java program was also written by the author that separated the large files into the two signal channels and into the 66 measurement points. The program also converted the voltage signals into velocity signals using the hot-wire calibration equations to create look-up tables for each channel. These velocities were then decomposed into the two orthogonal components desired by using the following transformations:

$$u = \frac{1}{2}\left(\sqrt{(1+k_2^{\,2})U_{cal2}^{\,2} - k_2^{\,2}U_{cal1}^{\,2}} + \sqrt{(1+k_1^{\,2})U_{cal1}^{\,2} - k_1^{\,2}U_{cal2}^{\,2}}\right)$$ (Jorgensen, 2002)

$$w = \frac{1}{2}\left(\sqrt{(1+k_2^{\,2})U_{cal2}^{\,2} - k_2^{\,2}U_{cal1}^{\,2}} - \sqrt{(1+k_1^{\,2})U_{cal1}^{\,2} - k_1^{\,2}U_{cal2}^{\,2}}\right)$$ (Jorgensen, 2002)

Where k_1 and k_2 are yaw coefficients related to the heat transfer characteristics of the wires in the hot-wire probe determined by a hot-wire yaw calibration, U_{cal1} and U_{cal2} are velocities calculated from look-up tables generated

from the hot-wire velocity calibration, u is the stream-wise component of the measured velocity and w is the span-wise component of this measured velocity. The v component (vertical) can also be measured by rotating the probe 90 degrees, but for most measurements in the present experiment, the span-wise velocity was the only secondary velocity component of concern.

Once velocity-time series were obtained for the 66 measurement points, the following quantities were calculated to analyze the flow at these points: mean velocity, RMS velocity, and, since the two velocity components were acquired simultaneously, it was possible to calculate $\overline{uw}$ to determine the mean shear stresses. Contours in the grid plane for each of these quantities were generated using TecPlot to gain a greater understanding of the flow patterns in the cavity wake.

Power Spectral Density plots were also generated from these time series using MATLAB with a 32768 point FFT with 50% window overlap to look for periodicity in the velocity fluctuations due to the cavity presence. The MATLAB calls used to calculate these power spectral density plots are listed in Appendix P.

3.4.3 Pressure Transducer Measurement

The pressure transducer system was used to investigate the mean and fluctuating pressure field along the cavity model surface as well as to investigate the existence of flapping and switching flow regimes reported in the literature (Hiwada et. al., 1983).

Investigation of the Mean and Fluctuating Pressure Field along the Cavity Model Surface

In order to capture the pressure fields along the cavity model surface, pressure measurements were taken using the 14 pressure transducers which were sampled simultaneously at a rate of 1000 Hz / channel for a sample length of 30 seconds. This

sample rate was chosen due to the observed frequency response of the pressure measurement system yielding a maximum intelligible frequency of about 500 Hz (see Appendix M for more details). Since the pressure-tapped model was axi-symmetric, a large number of measurement points were possible by rotating the model in 10 degree increments (see Figures 3-25 and 3-26). In categorizing the measurement points by their location on the model, the number of points in each case was:

- 325 points on the cavity base
- 684 points on the cavity turntable
- values on the sidewall ranged from:
    - 252 for h/D = 0.20
    - 432 for h/D = 0.47
    - 504 for h/D = 0.70

This yielded a total of 1261 points for h/D = 0.20, 1441 points for h/D = 0.47 and 1513 points for h/D = 0.70. As seen in Figure 3-26, sidewall measurement points for h/D = 0.70 did not reach completely to the cavity base due to pressure tapping placement. The effects of this are further discussed in the results section.

During all measurements, one pressure transducer was reserved to measure the static pressure in the tunnel from the static tap of the Pitot-Static tube.

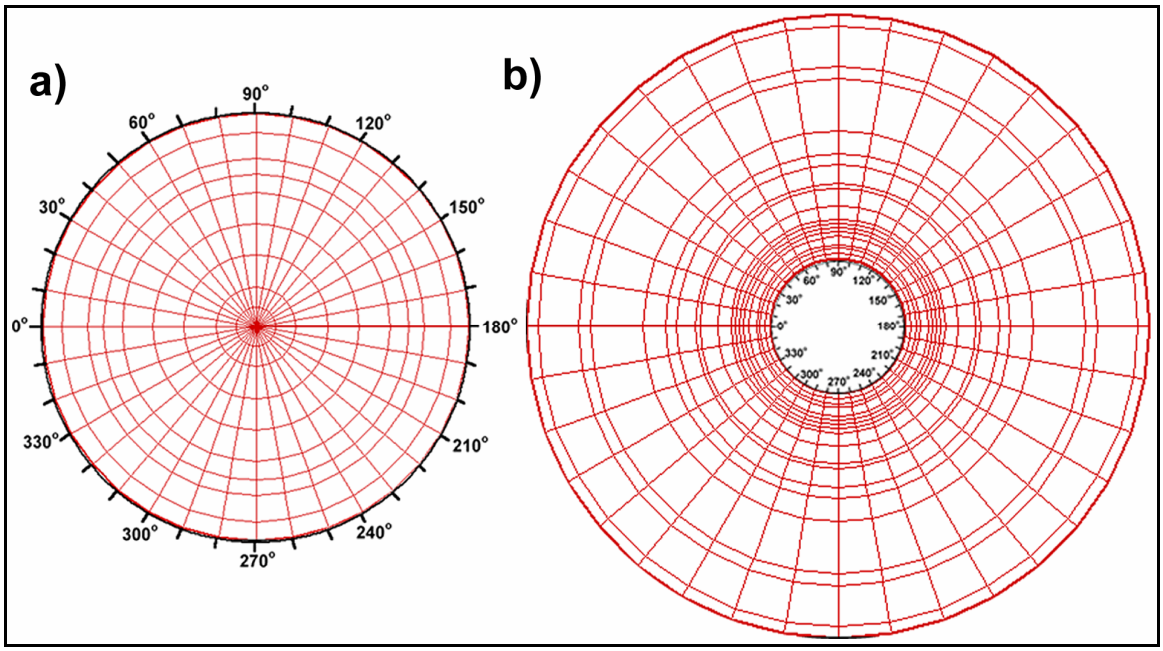

Figure 3-25 – Measurement grids used for pressure transducer measurements on cavity base (a) and on cavity model turntable (b). The cavity base was increased in scale in order to show further detail.

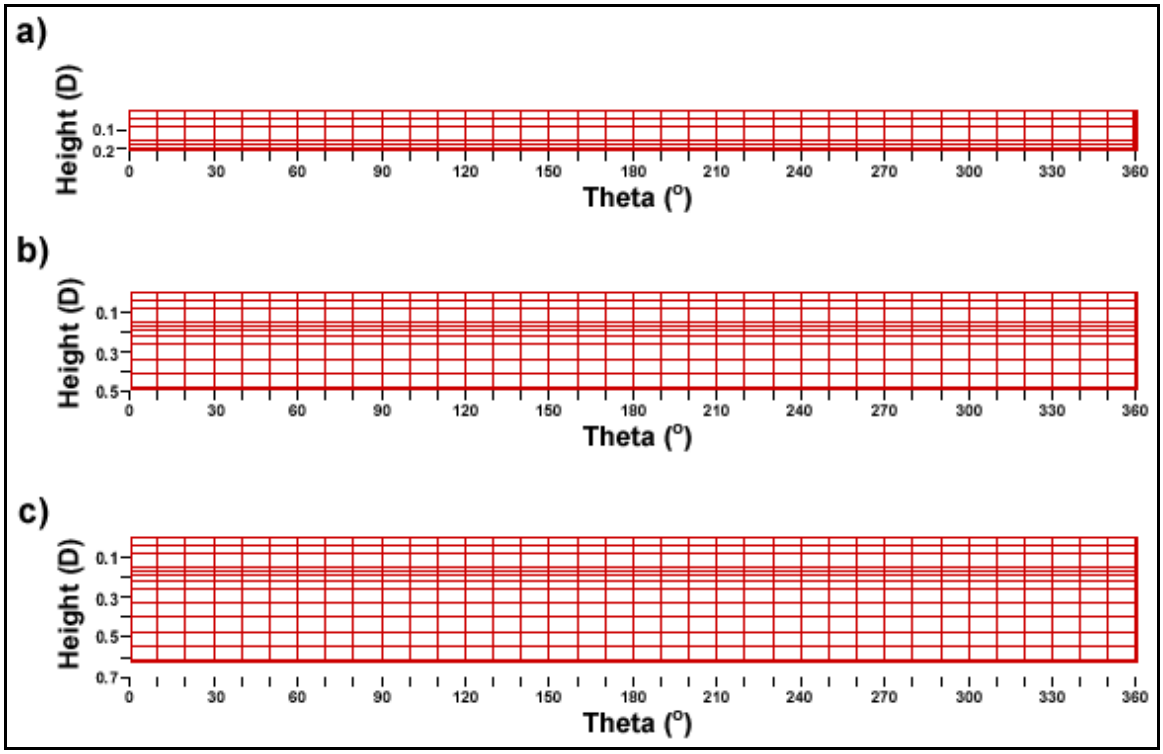

Figure 3-26 – Measurement grids used for pressure transducer measurements on cavity sidewall for h/D = 0.20 (a), h/D = 0.47 (b) and h/D = 0.70 (c). The top of each of these grids represents the cavity upper lip.

Investigation of Flapping and Switching Flow Regimes

In one previous investigation of flow over circular cavities (Hiwada et. al., 1983), the investigators inferred the existence of a series of flow regimes dependent on cavity depth ratio h/D. Although the observation of a switching phenomenon was mentioned by other investigators at h/D = 0.5 (Gaudet & Winter, 1971, Savory et. al., 1996), this report by Hiwada et. al. was the only to mention the flapping regime as well as being the only one to present evidence for the switching phenomenon.

Due to the lack of information on these flow regimes, the present investigation sought to confirm or deny the existence of the flapping regime and to expand the knowledge of the switching regime and its control.

A depth of h/D = 0.37 was selected for investigating the flapping regime, due to the very large pressure flapping observed at this configuration by previous investigators (Hiwada et. al., 1983). A pressure tap on the cavity sidewall was selected for measurement located 2 mm from the cavity lip and positioned at θ = 150 degrees to match the measurement conditions of the previous investigators (Hiwada et. al., 1983). The tap was sampled with a pressure transducer at a sample rate of 1000 Hz for 100 s over multiple trials to ensure the repeatability of this flapping phenomenon.

For the more detailed experiment to investigate the switching phenomenon, a measurement configuration of h/D = 0.47 was chosen due to the observed asymmetric flow and high drag associated with this configuration by many previous investigators. As mentioned in previous work (Hiwada et. al., 1983, Gaudet and Winter, 1971), the switching phenomenon does not occur automatically and takes place when a forced disturbance has been applied to the flow. Having no information from previous work on how to correctly disturb the upstream flow in this situation, the slotted plug was inserted into the wind tunnel roof upstream of the cavity model turntable installation as seen in Figure 3-28. With the slot open, a narrow sheet of plywood 30 cm in width was labeled with distance markings and inserted a certain distance into the wind

tunnel flow through the slot in the roof. This allowed a variable amount of blockage to be applied asymmetrically to the flow upstream of the cavity.

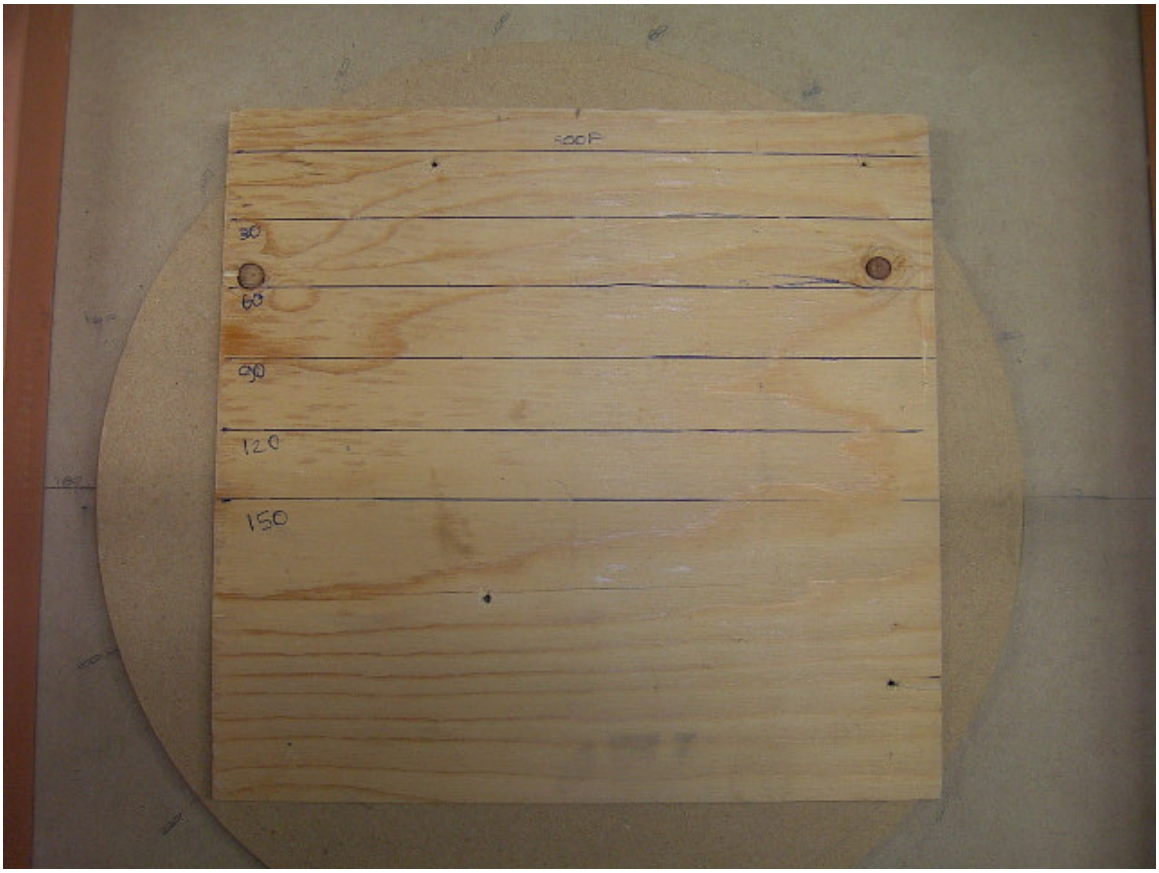

Figure 3-27 – Plywood board used for wake asymmetry switch experiment for h/D = 0.47.

Figure 3-28 – Disturbance method used for wake asymmetry switch with board causing blockage on left hand side forcing wake asymmetry to right hand side.

Figure 3-29 – Blockage shown relative to location of cavity model with blockage on left hand side.

Calibration

The pressure transducers were calibrated daily and simultaneously using a liquid manometer as a reference.

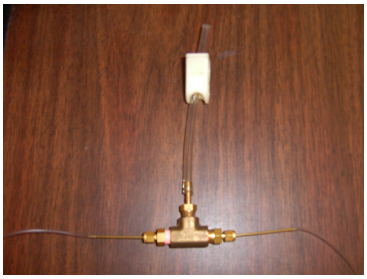

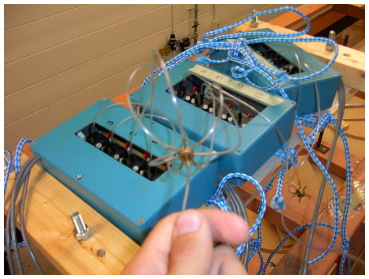

Figures 3-30 (L), 3-31 (C) and 3-32 (R) – Left – the mouthpiece and tubing "T". Centre – Mouthpiece attached to liquid manometer. Right – 7-way splitter held in the foreground with attached transducers in background.

In referring to Figures 3-30, 3-31 and 3-32 above, a calibration pressure was applied to the calibration system by sucking or blowing into the mouthpiece seen in Figure 3-31. This pressure was equally applied throughout the whole system through the brass "T" in Figure 3-30 which had one side attached to the liquid manometer in Figure 3-31 and the other side attached to two 7-way splitters as seen in Figure 3-32 which in turn were attached to the 14 transducers so as to apply equal pressure to the transducers and to the liquid manometer.

A series of 10 different pressures were used to set a line of best fit to for the calculation of a calibration equation for each transducer. The outputs of the transducers were acquired simultaneously at these different pressures using a LabVIEW program written by a UWO M.E.Sc. candidate (Tom Hering). This calibration method routinely yielded a value of $R^2 = 0.9998$ between the data and a linear line of best fit. A typical example of a calibration graph obtained using this method can be seen in Appendix G.

Processing

Using a LabVIEW program co-written by the author and UWO M.E.Sc. candidate Tom Hering, mean and RMS values for the pressure signals were calculated in real time which, once calibrated, allowed TecPlot to generate contours of these quantities for the different cavity model surfaces. These mean and RMS pressures were non-dimensionalized by converting them to Cp quantities (see Equation below).

For RMS pressures, the following equation was used for Cp conversion:

$$Cp_{rms} = \frac{(p - p_s)_{rms}}{q_0}$$

Where p is the pressure measured at a point on the cavity model surface and p_s is the static pressure measured in the free stream.

The drag due to the presence of the cavity model was measured indirectly through the integration of mean Cp values projected in the direction of the free-stream on the cavity model sidewall, with the aid of an application of Simpson's rule (Stewart, 1999). By integrating these mean Cp values over the sidewall area, a drag force coefficient was obtained, which was converted to an incremental drag coefficient using the following transformation:

$$\boxed{\Delta C_D = C_D - c_f}$$

Where C_D is the drag coefficient calculated from the Cp integration on the cavity sidewall, and c_f is the local skin friction coefficient on the ground plane as calculated from hot-wire measurements discussed in Appendix G. This skin friction coefficient is subtracted from the drag coefficient to account for the absence of ground plane at the position of the cavity.

The LabVIEW program used for data acquisition also acquired pressure-time histories for each measurement which were processed using MATLAB to generate Power Spectral Density plots. These plots were created using a 2048 point FFT with 50% overlap between windows.

3.4.4 *Miniature Microphone Measurements*

The 13 miniature microphones were used to measure pressure fluctuations at the surface of the cavity model and these were measured simultaneously at a sample rate of 10000 Hz / channel for a sample length of 30 seconds. This sample rate allowed frequency components to be resolved from 0 to 5000 Hz. Since no previous investigations of the frequencies associated with these flows had been done, the maximum attainable sample rate for the data acquisition system was used to resolve frequencies over the largest possible range.

Once again, due to the axi-symmetric nature of the model used for these measurements, it was possible to rotate the model to measure various points on the cavity model's surface. Incremental rotations of 20 degrees were compiled in an attempt to visualize the fluctuating pressure pattern across the cavity model surfaces, and for the cavity base especially. The effective grid of measurement points for the miniature microphones on the cavity base is seen in Figure 3-33.

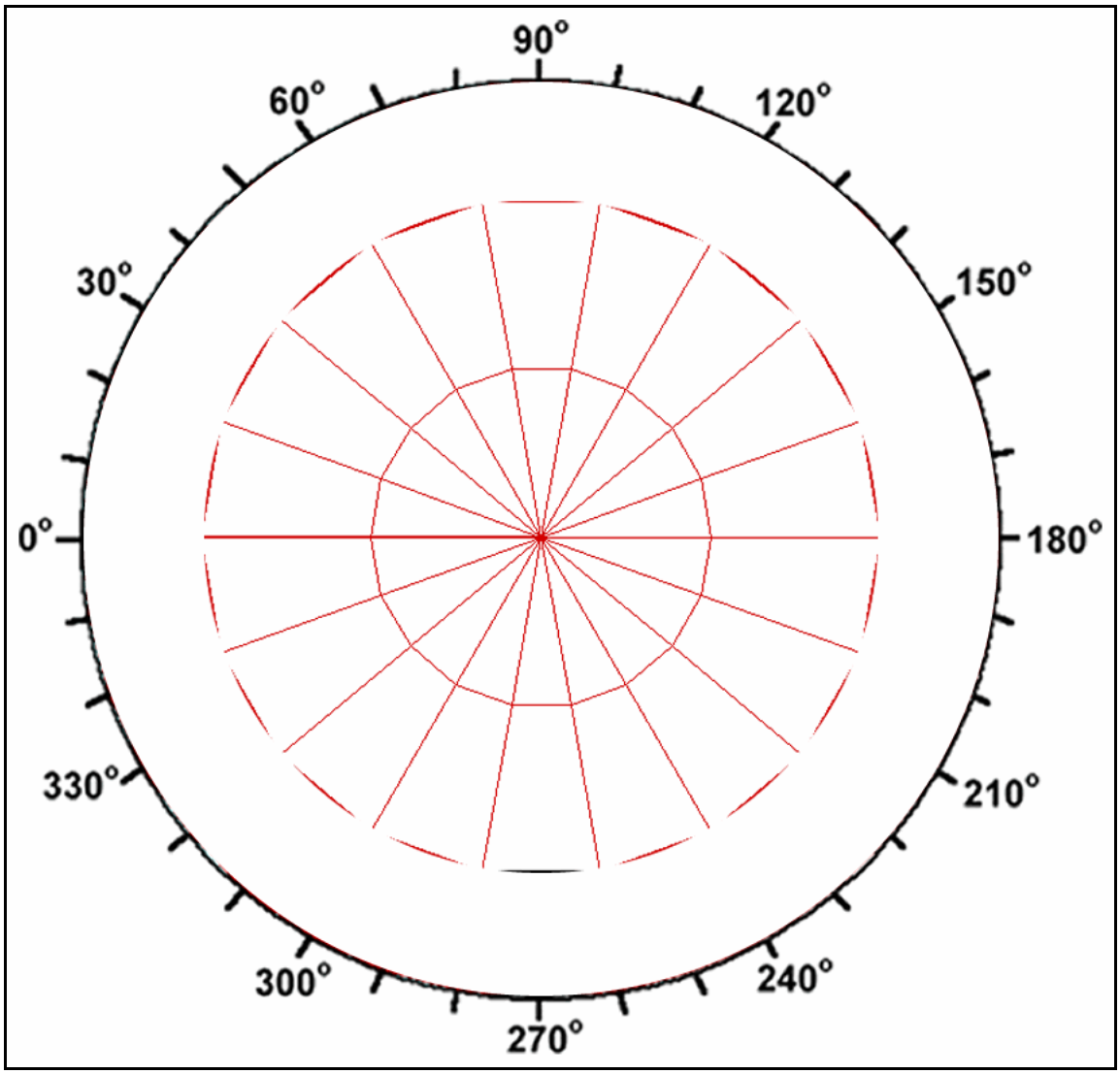

Figure 3-33 – Measurement grid used for miniature microphone measurements on cavity base.

Calibration

Due to the fact that these microphones were used to measure fluctuating pressures and not mean pressures, and that the microphones were permanently fixed to the microphone cavity model, calibration was a difficult task. For this reason, the microphones were only absolutely calibrated once, using a sound pressure level meter (SPL meter). Each microphone was calibrated separately by mounting it next to the SPL meter sensor in anechoic material such that each sensor was separated an equal distance from a computer controlled speaker. Using a discrete frequency sound generator computer program, a range of discrete frequencies was produced at constant amplitude to analyze the response of the microphones to various frequencies.

In addition, the sensitivity of the microphones was further examined by subjecting the devices to three different amplitudes of sound at constant frequency.

Although this absolute calibration was done, other methods were carried out with the microphones *in situ* to attempt to isolate the flow-related signals from noise.

Processing

The RMS of the microphone time series was calculated during measurement using a LabVIEW program and these values were plotted as a function of model angle θ for the turntable and sidewall microphones, and the measurements on the cavity base were plotted using TecPlot to generate contour plots along this surface.

MATLAB was also used to generate Power Spectral Density plots of the acquired time series. These plots were created using a 16384 point FFT with 50% overlap between windows. In all cases, plots were created by subtracting no-cavity PSD from PSD calculated from cavity measurements in an attempt to isolate the effects of the cavity from the residual ambient noise.

3.5 Error Analysis

Errors incurred during the measurements described previously are summarized in this section. A more detailed analysis of the error for each measurement system is included in Appendix C. Major contributing sources of error are listed in table format and are combined into a total uncertainty using the RSS (root square sum) method described by Wheeler and Ganji (1996).

3.5.1 Summary of Total Uncertainties

Measurement System	Total Uncertainty as % of Nominal Measurement	Single largest source of uncorrected error	
		Systematic	Random
Pressure Transducers – DCAL4	±2.14%	None	Drift over duration of trial
Pressure Transducers – NDR4	±2.28%	None	Drift over duration of trial
Microphones	±12.6%	Drain of Power Supply Voltage	Repeatability between Microphones
Hot-wires	±1.46%	Temperature Effect	Probe Yaw Angle Uncertainty

Table 3-2 – Summary of error analysis for all measurement systems.

3.6 Summary

The individual measurement systems and intended experiments have been clearly described in this section outlining the setup of the measurement systems, the general procedure for the proposed experiments and processing and uncertainties involved in these measurements. The results gathered using these apparatus and methods are presented and discussed in the following section.

4 RESULTS AND DISCUSSION

4.1 Overview

In this section, results are presented from the experiments described in the previous section. Results are presented and discussed in subsections according to the various types of experimental methods used for measurement.

4.2 External Flow Analysis and Selection

4.2.1 Tunnel Measurement Speed Selection

The measurements considered in the present study were carried out at one tunnel free stream velocity U_0. This tunnel velocity was selected according to its stability, warm-up time (time required at this velocity to reach a steady state flow temperature) and its free stream dynamic pressure.

From previous investigations of circular cavity flow it was discovered that measured mean surface pressures are of the range from Cp = $-0.25 \rightarrow +0.4$ (Savory et. al., 1996, Hiwada et. al., 1983) with most measurements falling into the range of Cp = -0.1 to 0.15. Since the maximum sustainable U_0 of the tunnel used was 27 m/s, this would result in a free stream dynamic pressure of 175 Pascals (hereafter Pa) and, hence, using previous results the estimated maximum measured pressure would be 70 Pa and the minimum would be -43.75 Pa (both estimates relative to the tunnel static pressure).

Considering the fact that the lowest pressure range that was available in a differential transducer was +/- 250 Pa, it was decided to attempt to run all experiments at as close to the maximum U_0 as possible in order to make most use of the pressure range available.

The wind tunnel used for measurements was observed to have essentially three main flow regimes:

Tunnel Free Stream Velocity	Approx. Warm Up Time	Fan Stability
9.3 – 18.1 m/s	< 30 mins.	+/- 0.1 m/s periodic instability
18.1 – 27 m/s	45-55 mins.	+/- 0.05 m/s long period instability
>27 m/s	Warm up not achieveable	Large uncontrollable intermittent fan speed adjustments on order of +/- 1.5 m/s

Table 4-1– Observed flow regimes of closed loop wind tunnel used in experiment.

Since 27 m/s was the highest attainable speed in the stable tunnel flow regime, it was chosen as the free-stream speed for measurements.

4.2.2 Experimental Location Selection

The tunnel roof designed and built for this experiment featured 7 holes allowing for model installation and measurement. Originally, the experimental plan for this project included cavity measurements at many of these downstream locations to investigate the effect that varying the Reynolds' number and boundary layer thickness had on the cavity flow. However, due to timing restrictions, measurements were limited to one downstream location and therefore the criteria used to select this single location were as follows:

1. Two-dimensionality of the model ground plane turbulent boundary layer (hereafter BL) at the location.
2. State of development of the turbulent BL – How close is the BL at this point to being fully developed?
3. Thickness of the turbulent BL – Does it still allow a free-stream to exist beyond the ground plane BL?

Taking these criteria into consideration, stream-wise velocity profiles were taken across the working section at all 7 locations, the results of which are seen below in Figure 4-1 below.

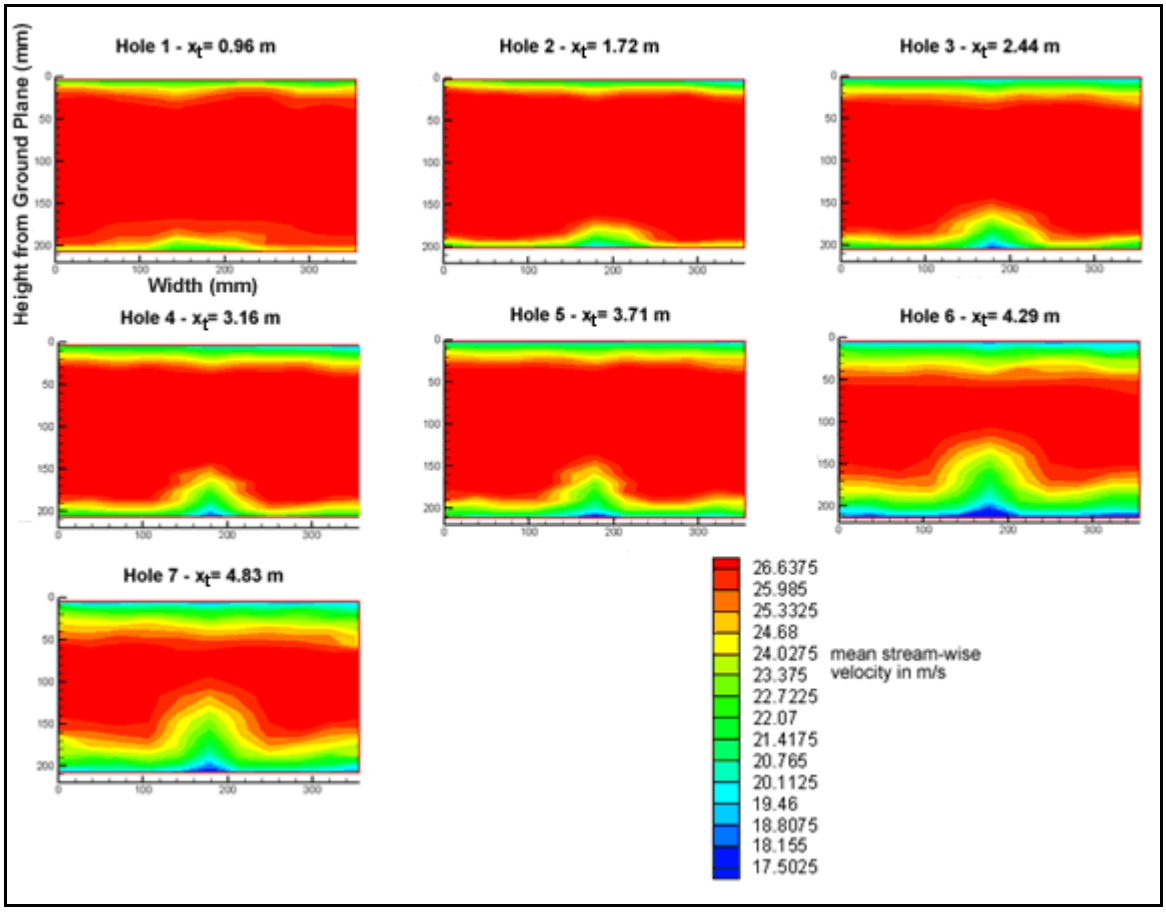

Figure 4-1 - Stream-wise mean velocity profiles across the tunnel's working section at the available downstream locations for measurement (Ground Plane is located at top of plots). Axes for individual plots are identical to that for Hole 1.

The model was to be inserted in the roof for measurements and thus the roof boundary layer was of prime importance in this investigation. As expected, both the roof and floor boundary layers were observed to increase in depth as downstream distance increased and a large central stream-wise velocity defect of unknown origin was seen on the tunnel floor. The existence of this defect, however, did not seem to affect the boundary layer on the roof in any noticeable way.

After analyzing these downstream measurements, Hole 6 was chosen as the site for cavity measurements due to the two-dimensionality of its roof BL across the span and, being one of the farthest locations downstream the location also exhibited a well-developed BL without sacrificing the existence of a free-stream (a region situated neither in the roof BL nor the floor BL).

Once Hole 6 was chosen as the site for the cavity experiments, a more detailed investigation of the boundary layer was done using the traversed two-component hot-wire anemometer. A grid of measurements was taken across a good portion of the tunnel working section at this downstream location to gain a general idea of the span-wise variability of the flow. Graphs of relevant quantities related to these experiments are presented in Appendix J. A table presenting flow quantities of interest calculated from the data of these aforementioned experiments is shown below in Table 4-2.

	Height from tunnel wall (mm)										
Quantity	2.0	10.6	19.1	27.7	36.3	44.9	53.4	62.0	70.6	79.2	87.7
$\overline{U}$	±2.5	±1.5	±2.0	±2.2	±2.6	±2.1	±2.0	±0.8	±0.4	±0.4	±0.3
$\sqrt{\overline{u^2}}$	±0.5	±0.6	±0.2	±0.4	±0.5	±0.8	±0.9	±0.9	±0.7	±0.3	±0.2
$\sqrt{\overline{w^2}}$	±0.4	±0.1	±0.2	±0.4	±0.5	±0.6	±0.7	±0.6	±0.5	±0.3	±0.1

Table 4-2 - Span-wise variability of boundary layer flow quantities at various heights from model ground plane. Units of table values are percent values in relation to the tunnel free-stream velocity of 27 m/s.

In Table 4-2, the span-wise variability of flow quantities at various heights from the model ground plane are presented in % values such that values presented are of the maximum range of the quantity across the span, divided by U_0. In the free-stream region, span-wise variability is less than 0.5% of U_0 for all quantities. Despite this apparently impressive degree of two-dimensionality in these quantities, the boundary layer thickness varied ± 20% across the span of the working section at the location of measurements.

In an attempt to improve the two-dimensionality of the boundary layer thickness, a 12.7 mm high fence was installed on the tunnel wall near the inlet of the working section to promote lateral mixing. Although the fence did marginally improve the span-wise uniformity of the boundary thickness, it caused a large increase in the boundary layer thickness across the span such that a free-stream was no longer observed at the downstream location of measurements. Thus, the fence was not used and the presented boundary layer characteristics pertain to the external flow used for all subsequent measurements.

Quantity	Value at z = -D	Value at z = 0	Value at z = +D	Average	Range
δ	52.9 mm	63.2 mm	56.5 mm	54.7 mm	+/- 8.9%
δ_*	6.3 mm	8.0 mm	7.6 mm	7.0 mm	+/- 12.0%
δ_θ	4.6 mm	5.91 mm	5.5 mm	5.1 mm	+/- 12.7%
Shear Stress (τ_w)	1.30 Pa	1.23 Pa	1.26 Pa	1.28 Pa	+/- 2.7%
c_f	0.0031	0.0029	0.0029	0.0030	+/- 3.0%
u_*	1.140 m/s	1.109 m/s	1.122 m/s	1.131 m/s	+/- 1.4%

Table 4-3 - Flow quantities related to the roof boundary layer at the location of cavity measurements.

Another, more detailed investigation of the tunnel boundary layer flow was conducted to closely observe the flow directly in the vicinity of the cavity model. Three vertical traverses of very densely placed grid points (2.8 mm vertical spacing) were done at three separate span-wise locations z = -D, z = 0 and z = +D relative to the eventual position of the cavity centre. The data collected show a boundary layer thickness with maximum variability of +/- 9% across the span as well as a skin friction coefficient within +/- 3.0% across the span.

Using the data from the three densely spaced vertical traverses mentioned above, a Law of the Wall investigation was also carried out to compare the observed flow to this empirical approximation for classical wall turbulent boundary layer flow (Cebeci and Smith, 1974). Discussed in further detail in Appendices H and I,

comparing the boundary layer data to the Law of the Wall approximation, one can derive a value for the friction velocity u_* from the Law of the Wall formula, which, when compared to the measured friction velocity calculated from the measured boundary layer data using the equation below, gives a rough evaluation of how the measured data compares to classical flat-plate turbulent boundary layer flow.

$$u_* = \sqrt{\frac{\tau_0}{\rho}}$$ (Monin and Yaglom, 1965)

Where τ_0 is the wall shear stress measured in the region of its maximum near the tunnel wall, and ρ is the density of the air in the tunnel at the time of measurement.

Quantity	Value at z = -D	Value at z = 0	Value at z = +D	Average	Range
u_* from Law of the Wall	1.032 m/s	1.005 m/s	1.010 m/s	1.016 m/s	+/- 1.6%
Measured u_*	1.140 m/s	1.109 m/s	1.122 m/s	1.124 m/s	+/- 1.4%
(Measured – Law)/Law	+10.5%	+10.3%	+11.1%	+10.6%	

Table 4-4 - Comparing measured friction velocity to Law of the Wall predicted friction velocity at the location of cavity measurements.

4.3 Mean and Fluctuating Pressure Contour Analysis

Due to the great number of measurement points used in the analysis of the flow over the pressure-tapped cavity model and the microphone model, the main method used to display this data such that all measurement points could be viewed simultaneously was through the use of contours. For any given configuration, two contour plots were generated: one displaying the mean pressure values and the other displaying the RMS pressure values. The plots generated in this manner are discussed in this section.

4.3.1 Mean Pressure Contours

These contours were generated by taking the mean of the pressure-time series at each point and using TecPLOT to form contours from these data. Analyzing these contour patterns aids the understanding of flow behaviour at the model surfaces.

The pressure coefficient contour patterns over the cavity base, sidewall and model turntable for the various depth configurations are shown in Figures 4-2, 4-3 and 4-4. Higher resolution images of these contour patterns are also found in Appendix Q.

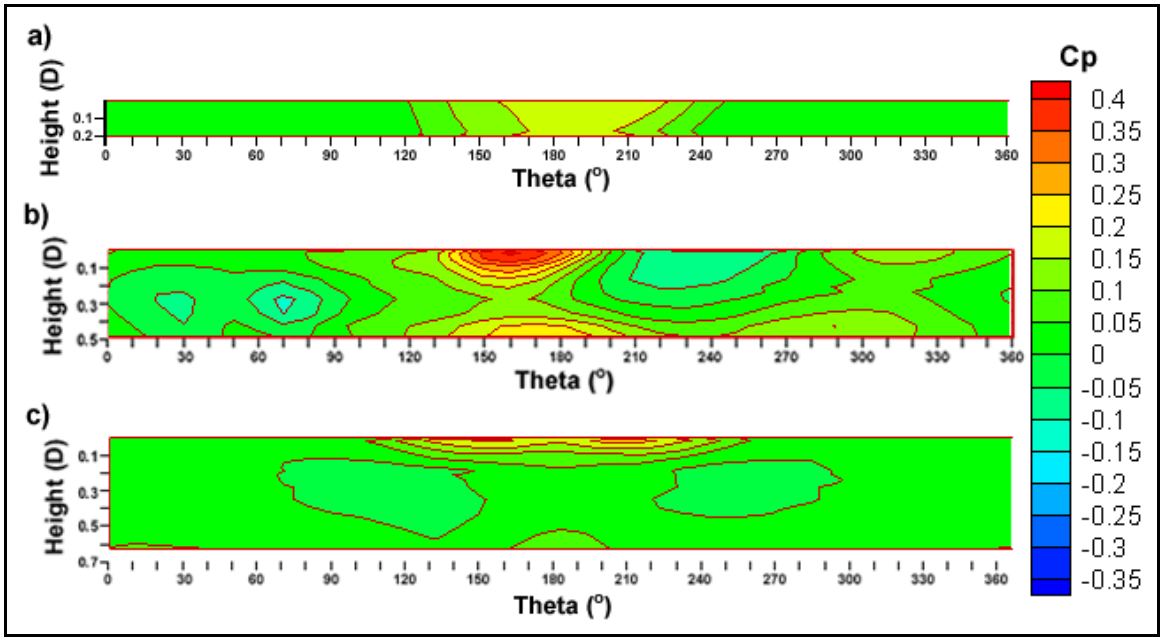

Figure 4-2 - Mean surface pressure contour patterns along the unwrapped cavity sidewall for h/D = 0.20 (a), h/D = 0.47 (b) and h/D = 0.70 (c).

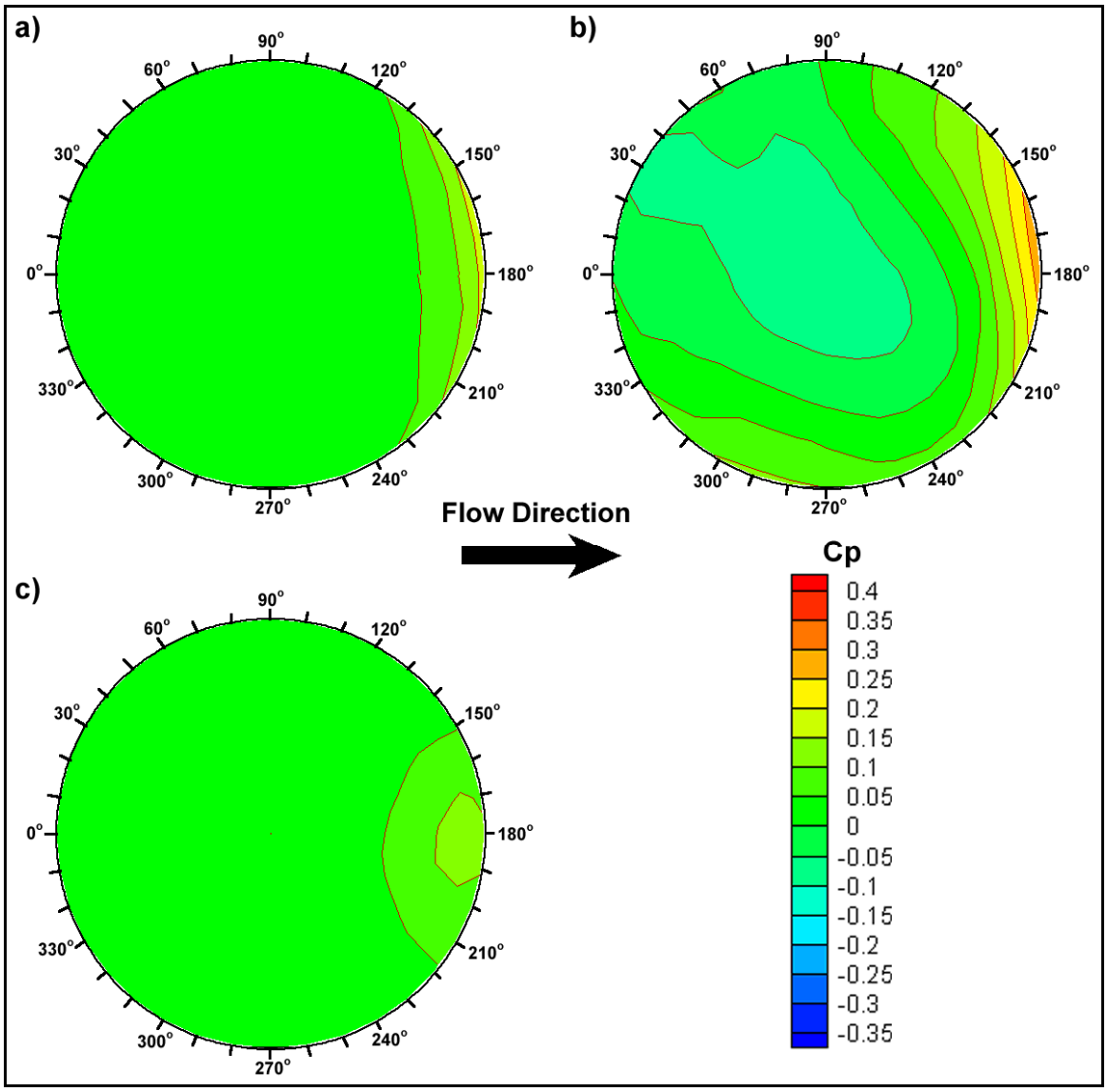

Figure 4-3 - Mean surface pressure contour patterns along the cavity base for h/D = 0.20 (a), h/D = 0.47 (b) and h/D = 0.70 (c).

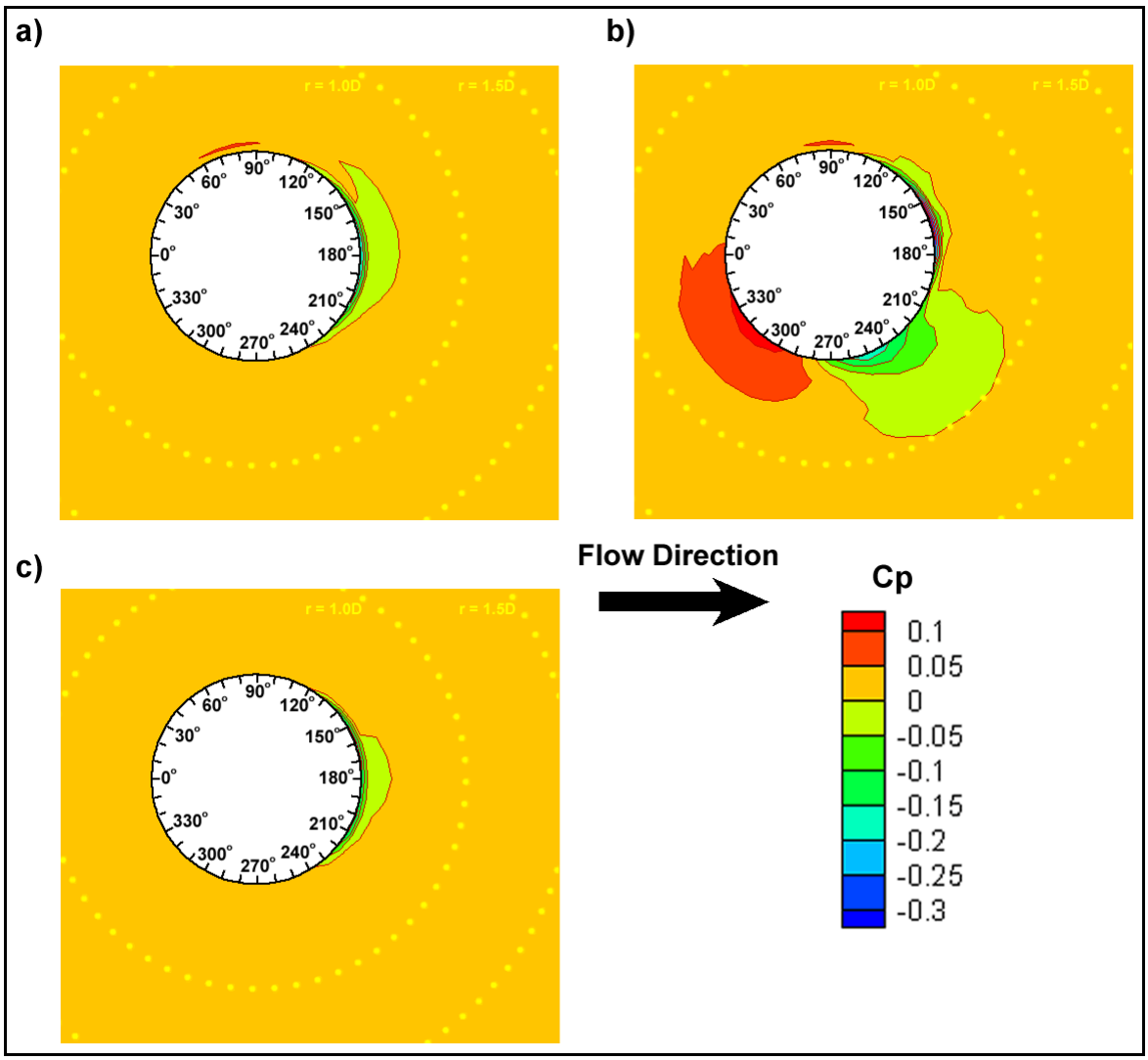

Figure 4-4 - Mean surface pressure contour patterns along the cavity outer rim (model turntable) for h/D = 0.20 (a), h/D = 0.47 (b) and h/D = 0.70 (c).

For the case of h/D = 0.2, the sidewall contours show a relatively high pressure region maximized near the cavity rim but extending across the full depth of the downstream side from 125° to 245° greater than Cp = 0.1 in magnitude. This is evidence of the fluid in the turbulent boundary layer above the cavity being drawn down into the cavity and impinging on this sidewall.

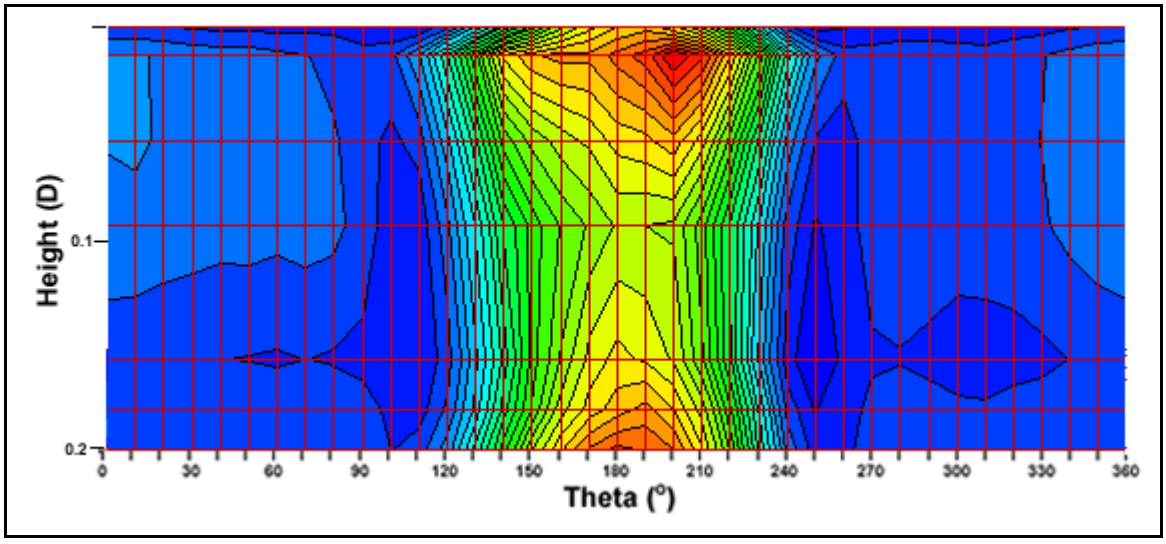

Figure 4-5 – Mean pressure contours representing patterns along the cavity sidewall "unwrapped" for h/D = 0.20, zoomed in to reveal the two ends of the stable vortex (circular regions on either side of the figure).

As observed by many previous investigators, a vortex structure is often identifiable in a mean pressure contour plot by identifying a reasonably circular low-pressure region which is the vortex centre of rotation, followed by a region around this low pressure region that increases in the radial direction moving away from this vortex centre.

Following this method, evidence for the existence of a stable vortex can be found in the sidewall contour plot. A plot with greater contour resolution and expanded vertical scale for h/D = 0.20 is seen in Figure 4-5 to point out this evidence for the captive vortex seen in the somewhat circular, closed contour lines in the low pressure regions on either side of the figure at θ = 105° and 250°.

On the cavity base in this instance, the pressure contour lines are perpendicular to the free-stream direction and are nearly all parallel to one another on the downstream side of the figure. This pressure gradient suggests a reverse flow (a flow in the direction opposite to the direction of the free-stream) moving from the region of high pressure to the lower pressure region along the cavity base.

In observing the pressure contours on the cavity model turntable for this configuration there is a notable zone downstream of the cavity beginning at the cavity downstream lip which is one of negative pressure relative to the ambient free-stream static pressure (yellow-green zone at θ = 180°). This is evidence for suction occurring in this region resulting in external flow being sucked into the cavity at its downstream edge. The location of this "suction zone" is consistent with the patterns on the sidewall which show the impingement of external fluid in this same angular range. All contours related to this configuration are reasonably symmetric about a cavity centreline in the direction of the free-stream.

For the case where h/D = 0.7, the contours on the sidewall show a high pressure region on the downstream lip over an angular range from 105° to 255° and over a vertical range from y = 0 to about 0.1D. A clear separation between two flow structures is visible at this depth of 0.1D: the impingement of the external turbulent boundary layer on the downstream lip and then below this, beginning at about 0.15D, there is evidence of a large captive vortex beginning at this point reaching to the cavity base.

Following the vortex identification method mentioned earlier, this large captive vortex is seen with its axis of rotation intersecting the cavity sidewall near θ = 105° and 205° at a depth of about 0.2D. These vortex axis roots are highlighted in Figure 4-6, an image that has been created by focusing the pressure contour range in the range of pressures noted in these low pressure zones while expanding both the vertical and horizontal ranges to focus on this area. A curved higher pressure contour

near the bottom of Figure 4-6 starting at a depth of about 0.5D at θ = 180° is an indicator of stagnation occurring as the flow downwards into the cavity down this sidewall is resisted by the presence of the cavity base. This stagnation feature is notable on the cavity sidewall for each cavity depth tested and is clear for the h/D = 0.20 case in expanded Figure 4-6.

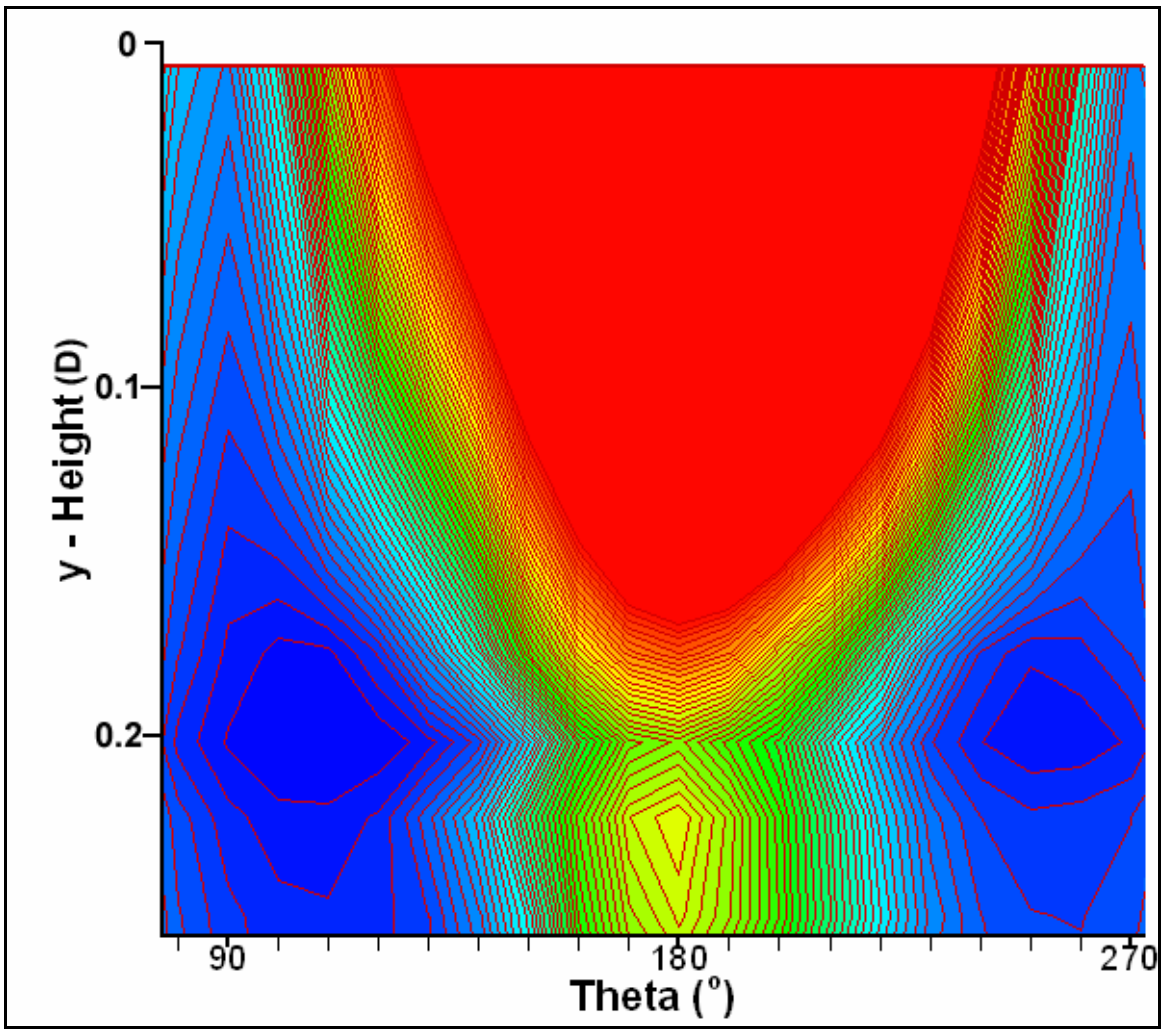

Figure 4-6 – Mean pressure contours representing patterns along the cavity sidewall "unwrapped" for h/D = 0.70, zoomed in with a tight range to reveal the two ends of the stable vortex (circular regions on either side of the figure).

The negative pressure contour patterns discussed as evidence for the stable recirculating vortex rooted to the cavity sidewall for h/D = 0.2 and 0.7 are not exactly circular. These patterns are compressed from above at the cavity rear by the high

pressure shear layer reattachment region near the downstream lip on the cavity sidewall.

Although the shear layer impingement at the downstream lip compresses the captive vortex, it also serves as the driving source for the vortex by introducing relatively high speed fluid into the cavity with a downward component sending fluid along the downstream cavity wall towards the base thus feeding the large scale vortex motion.

The mean pressure distribution on the cavity turntable for this configuration, like the h/D = 0.2 case, shows a "suction zone" along the downstream rim of the cavity where fluid is entrained into the cavity. The maximum value of suction in the "suction zone" for the h/D = 0.7 case of Cp = -0.17 was weaker (in terms of suction) than the h/D = 0.2 case of Cp = -0.19 and the area of this zone for the h/D = 0.7 case was notably less than the h/D = 0.2 case. Both of these facts would lead to a lesser amount of fluid entrainment for the h/D = 0.7 case. It is also notable that all of the distributions for this configuration displayed strong symmetry about the cavity centreline in the direction of the free-stream.

For the h/D = 0.47 case, the symmetry noted in the other mean pressure distributions is no longer observed. In the sidewall distribution for this configuration (Figure 4-2 b), a very strong shear layer impingement (represented by the red zone) is seen offset from the cavity centerline by about 20° near the cavity downstream lip and is located at the θ = 160° mark. This impingement zone exhibits a maximum pressure of about Cp = 0.35 compared to maxima of Cp = 0.19 and 0.21 for the h/D = 0.2 and 0.7 cases, respectively. As noted by Savory et. al. (1996), this much larger maximum impingement pressure suggests that fluid is being entrained into the cavity from a point higher in the external flow boundary layer, and thus having a higher velocity than the fluid drawn into the cavity at the other configurations. This ability to entrain higher momentum fluid from higher up in the boundary layer is due to the

much stronger suction in the cavity wake near the downstream lip visible in yellow-green zone in the distribution on the cavity turntable (Figure 4-4 b, more clearly seen in higher resolution Figure 4-7).

Once again using the method of identifying vortices by finding circular low pressure regions in the mean pressure distribution, it would seem that three major zones fitting this description can be found in the pressure distributions on the cavity base and the cavity sidewall. In the sidewall distribution the largest and most prominent low pressure zone is seen near the downstream lip at θ = 235°. This feature indicates the presence of a large vortex and the region reaches right to the cavity lip and is not fully contained by the cavity sidewall. This vortex then seems to reach outside the cavity and is hence a stable trailing vortex. This conclusion is further supported by looking at the pressure distribution on the turntable around the cavity downstream lip at θ = 235° where a lower pressure region can be seen trailing behind the cavity at this point. This vortex seems to be angled upwards, away from the cavity, such that its pressure-lowering effect on the cavity wake is visible for a certain distance until about r = 1.0D. This trailing vortex is further discussed in the hot-wire wake velocity analysis in Section 4.4. Another blue circular zone is noted on the upstream sidewall at about θ = 70° and is most likely the origin of the trailing vortex discussed earlier.

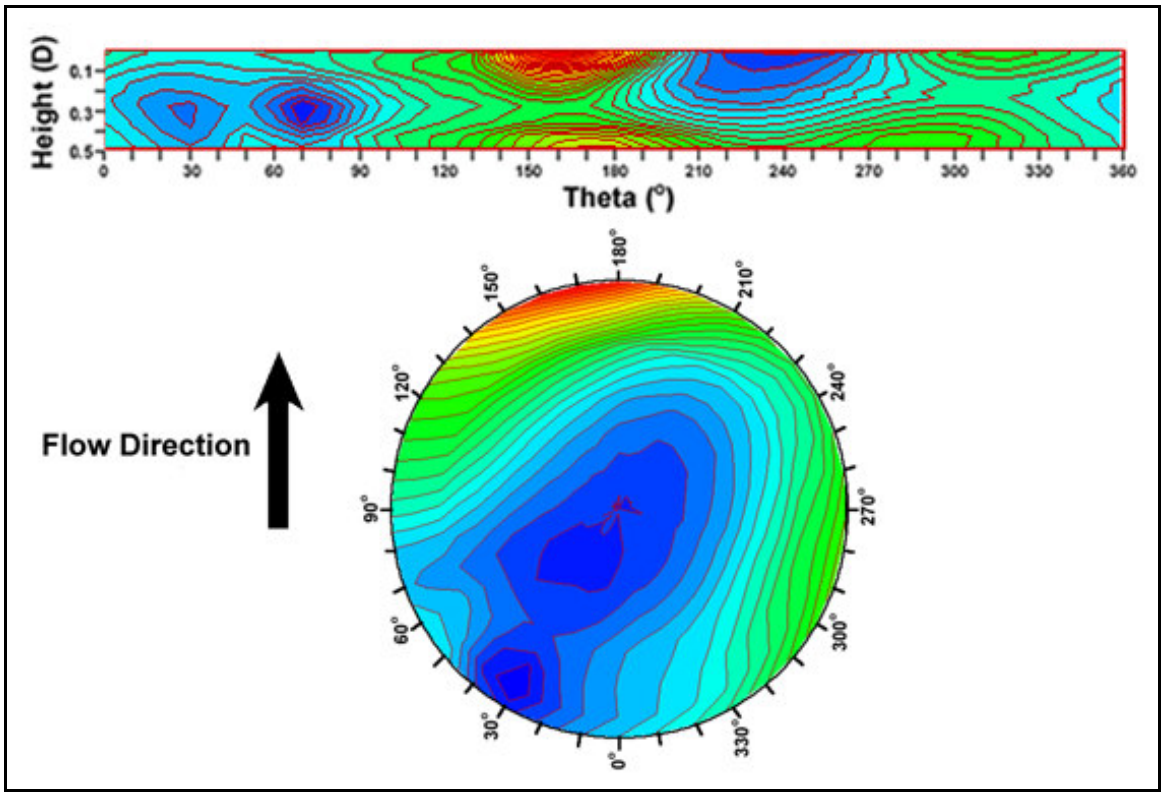

Figure 4-7 – High-resolution, locally ranged mean pressure contours representing patterns along the unwrapped cavity sidewall and cavity base for h/D = 0.47.

Paying further attention to the higher resolution images of the sidewall and the cavity base seen in Figure 4-7, a small, yet intensely low pressure feature on the cavity base can be seen near the upstream cavity wall at θ = 30° and is intersected by the large low pressure zone spanning a large portion of the cavity base. This small feature is likely a vortex tube rooted to the cavity base and rising to join the large vortex tube connecting from θ = 70° to θ = 235°. Due to the circular shape of these cavities, the strong, stable vortices, or vortex tubes, can be bent according to their surrounding boundary geometry. It seems that often when these vortex tubes bend, "off-shoot" vortex tubes are formed (such as the one on the cavity base at θ = 30° in this case) which remain connected to the major recirculating vortex tube in the cavity. Another strong example of this vortex tube bending to match the shape of its boundaries is seen on the cavity base contour pattern for h/D = 0.70 (Figure Q-1c - Appendix Q), where the low-pressure (blue) zone, corresponding to the location of

the main vortex tube axis, is clearly bent into an arc joining the circular pressure minima on the cavity sidewalls.

Flow topology is further discussed and elucidated in the surface flow diagram discussion in Section 4.3.5 following the discussion of fluctuating pressure patterns on these same cavity surfaces in the next section.

4.3.2 Fluctuating Pressure Contours

Fluctuating contour patterns were generated by taking the root-mean-squared value of the pressure-time series at each point (shown in grids in Figures 3-25 and 3-26) to gain a measure of the average level of fluctuation in the pressure series at any particular point. TecPLOT was then used to form contours from these data using the quantity of $C_{p_{RMS}}$ – a normalized measure of the RMS pressure relative to the free-stream dynamic pressure.

The RMS pressure contours corresponding to pressures along the cavity base, sidewall and model turntable for the various depth configurations are shown in Figures 4-18, 4-9 and 4-10. Although there is no existing literature regarding such pressure fluctuation patterns, such an analysis is useful to find the regions on the cavity boundary where fluctuation is most intense and to compare these to regions of interest in the mean surface pressure patterns discussed in the previous section.

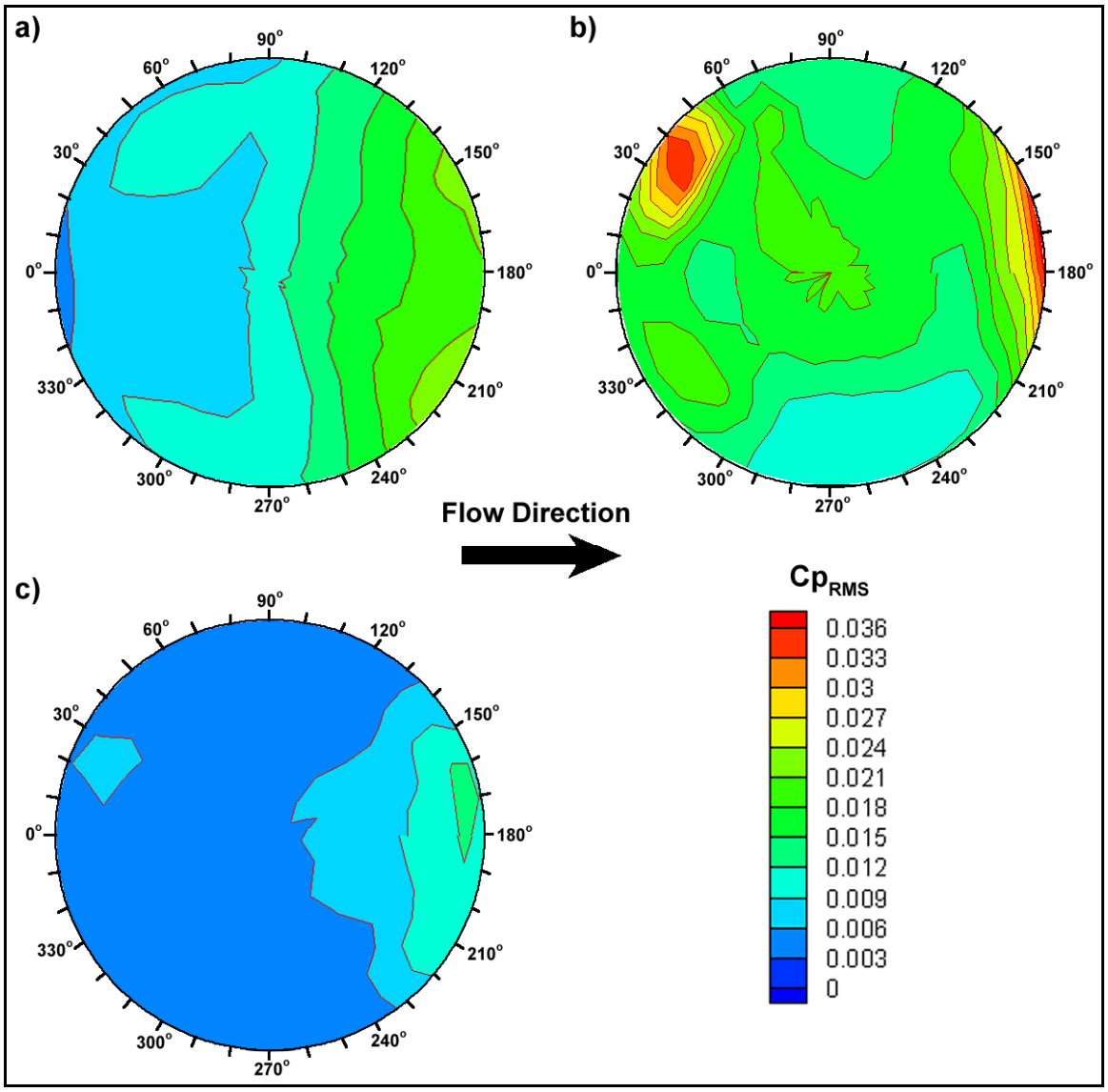

Figure 4-8 – Contour patterns of fluctuating pressures on the cavity base for h/D = 0.20 (a), 0.47 (b) and 0.70 (c).

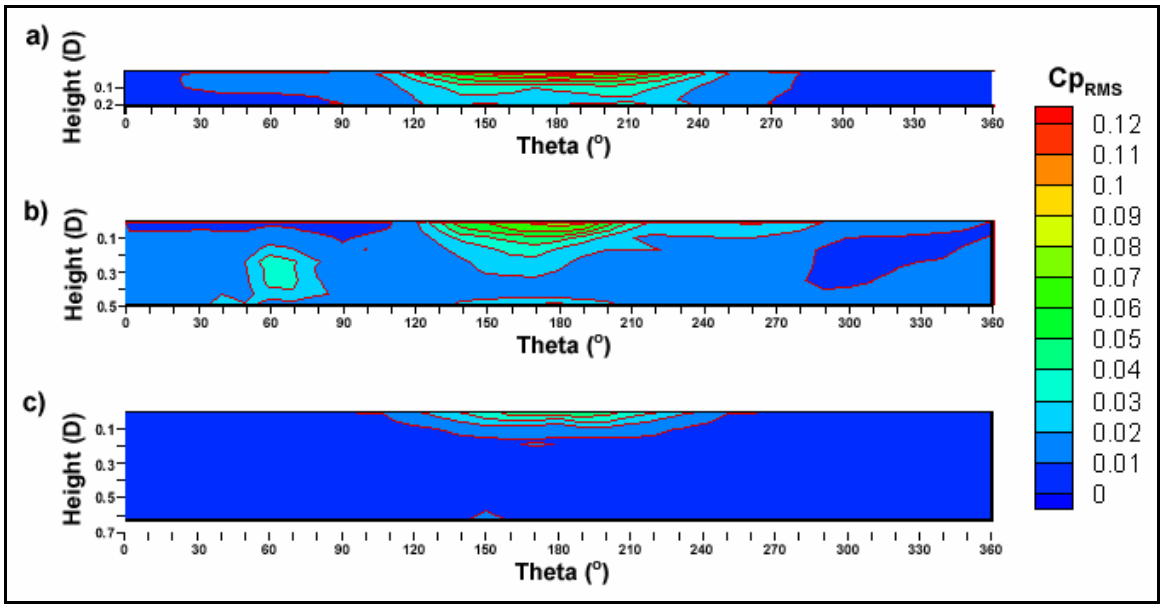

Figure 4-9 – Contour patterns of fluctuating pressures on the cavity sidewall for h/D = 0.20 (a), 0.47 (b) and 0.70 (c).

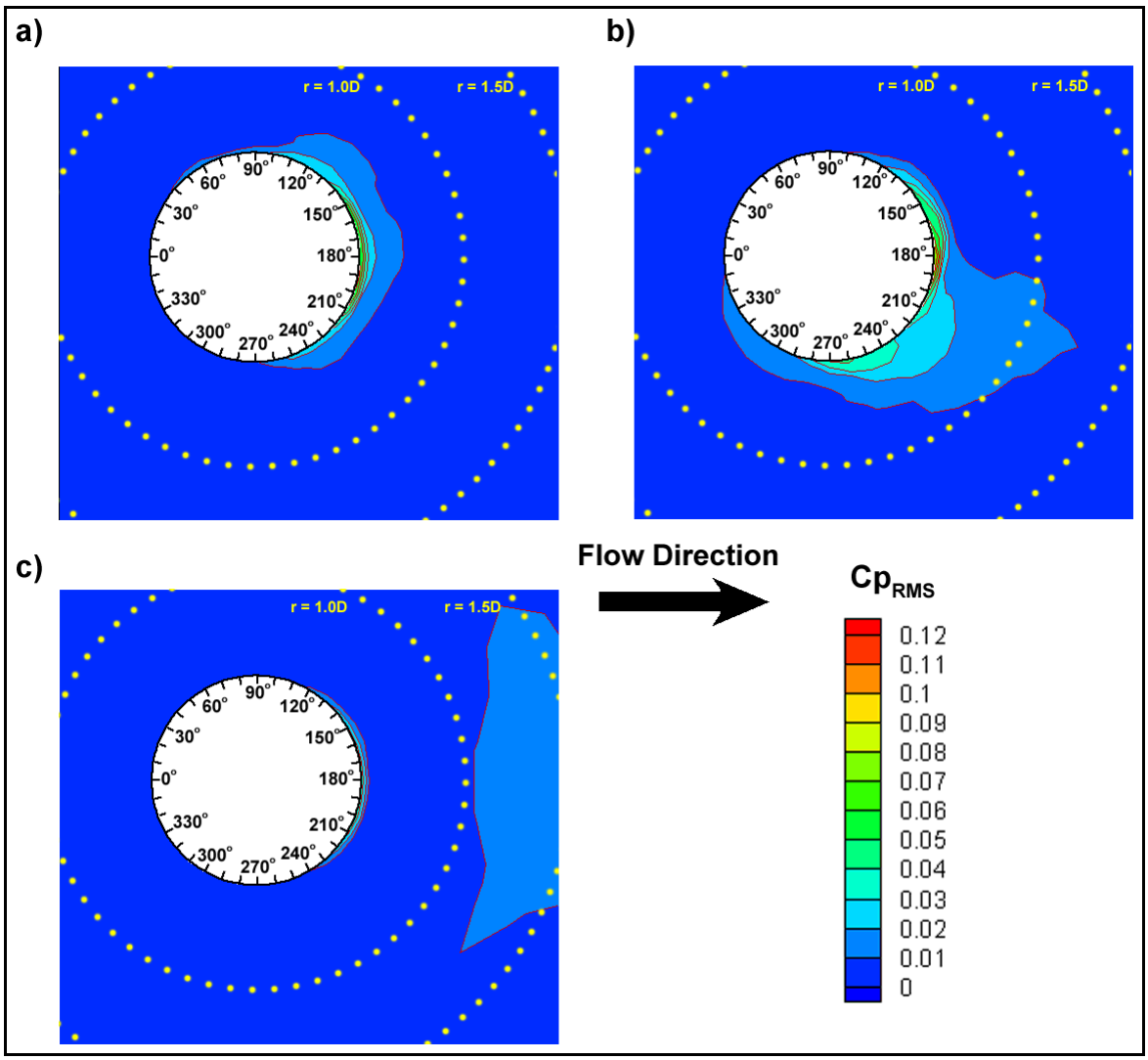

Figure 4-10 – Contour patterns of fluctuating pressures in the cavity wake for h/D = 0.20 (a), 0.47 (b) and 0.70 (c).

By observing the figures representing the case for h/D = 0.20, a notable symmetry about the cavity centreline in the direction of the free-stream is once again seen in all cases. The sidewall RMS pressure plot is qualitatively similar to the sidewall mean pressure plot and the RMS plot further supports the evidence from the mean plot that the shear layer attaches to the downstream wall, by showing a maximum value for the fluctuating pressure near the downstream cavity lip. This fluctuation is due to the fluctuating velocity of the turbulent boundary layer drawn down into contact with the cavity sidewall. The turbulent fluid from the turbulent

boundary layer is deflected down the downstream cavity sidewall and also interacts with the downstream edge of the cavity base and this is evidenced by the higher fluctuating pressures in these regions.

In the RMS pressure distribution along the turntable, higher fluctuation is seen near the rim of the downstream side of the cavity from about θ = 90° to 265°, most likely due to the fluctuating nature of the turbulent fluid drawn into the cavity near this region.

For the case of h/D = 0.70, symmetry is once again noted in all related distributions. There is a small region of higher turbulence in the sidewall near the downstream cavity lip showing the point of impingement of the turbulent boundary layer. Comparing this sidewall plot to the plots for the other configurations, it is obvious that the in the h/D = 0.70 case, the shear layer above the cavity is drawn down the cavity sidewall the least amount, likely attributable to the resistance provided by the large depth of the cavity.

The cavity base RMS contour plot shows only a small amount of fluctuation in the surface pressure at the downstream edge of the base, suggesting that the fluid entrained into the cavity is from the turbulent lower boundary layer which is also likely to lose energy while flowing along the deep cavity sidewall before impacting the base. The RMS contour plot for the model turntable at this configuration also shows the effect of the large cavity depth of resisting any significant fluid entrainment into the cavity.

The symmetry observed in the RMS plots for h/D = 0.20 and 0.70 cases is not seen in the h/D = 0.47 case in which strongly asymmetric features are seen on the cavity base, sidewall and turntable. On the cavity sidewall, a large region of high fluctuation pressure is seen at the shear layer reattachment point centred at θ = 160°, showing similarities to the mean pressure profile in this same region. Other regions of high RMS pressure are seen on the sidewall around θ = 65° and on the cavity base

at θ = 35°, both nearly coincident with vortex roots discussed at this configuration for the mean pressure patterns. The point of exit of the cavity main vortex into the external flow can also be discerned at θ = 260°. The main flow features implied from this analysis of the pressure contour patterns are described more clearly in a future section through the use of surface flow diagrams.

4.3.3 Comparing Present Pressure Distributions with all Previous Data

In this section, mean and fluctuating pressure patterns from the present experiment are presented alongside results from previous experiments at similar depth configurations.

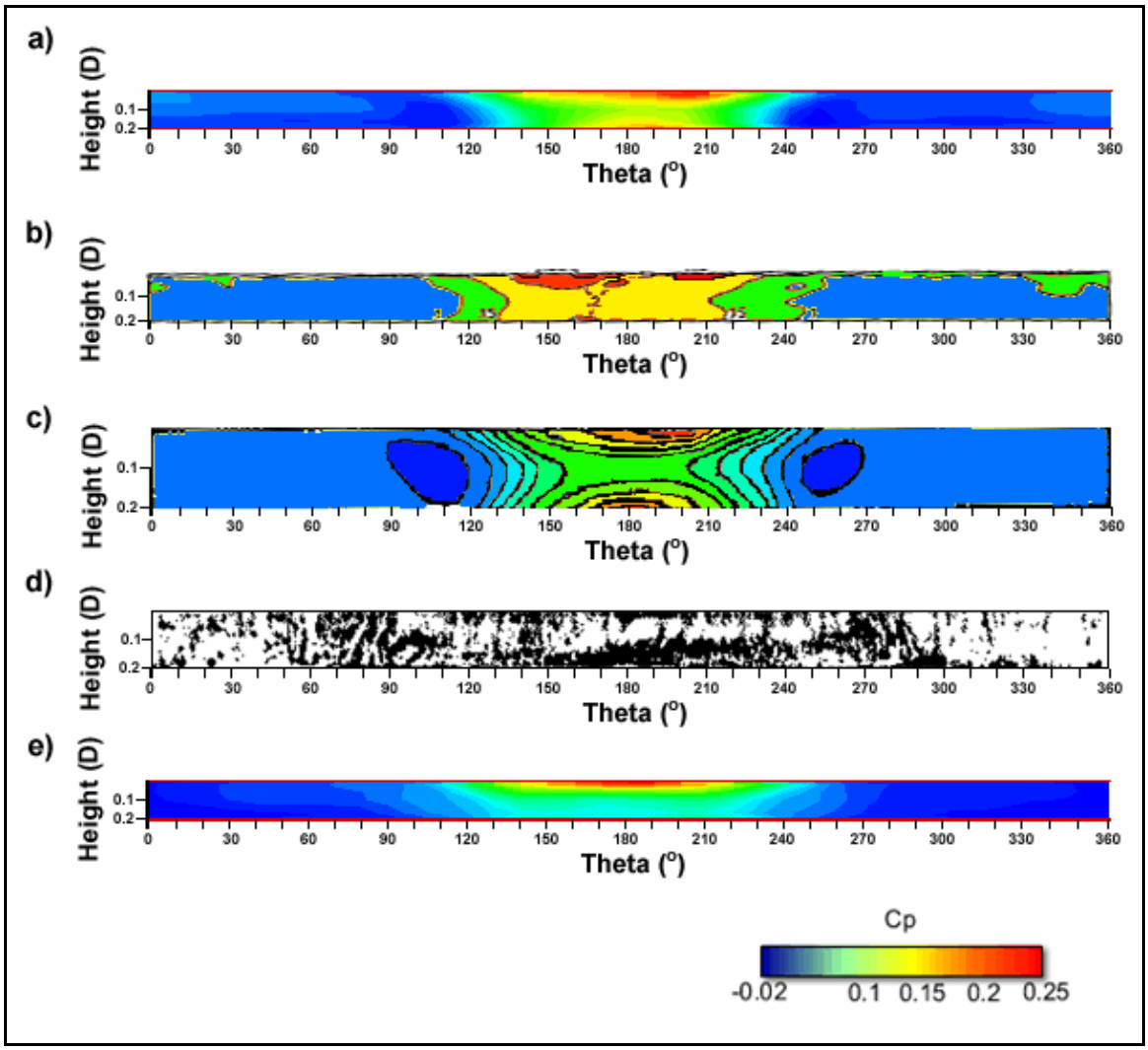

Figure 4-11 – All previous results on unwrapped cavity sidewall for h/D = 0.20. a) Present mean pressure contour pattern, b) Savory mean pressure (Savory et.al., 1996), c) Hiwada mean pressure (Hiwada et. al., 1983), d) Surface Oil-film pattern (Hiwada et. al., 1983) and e) Present RMS pressure contour pattern.

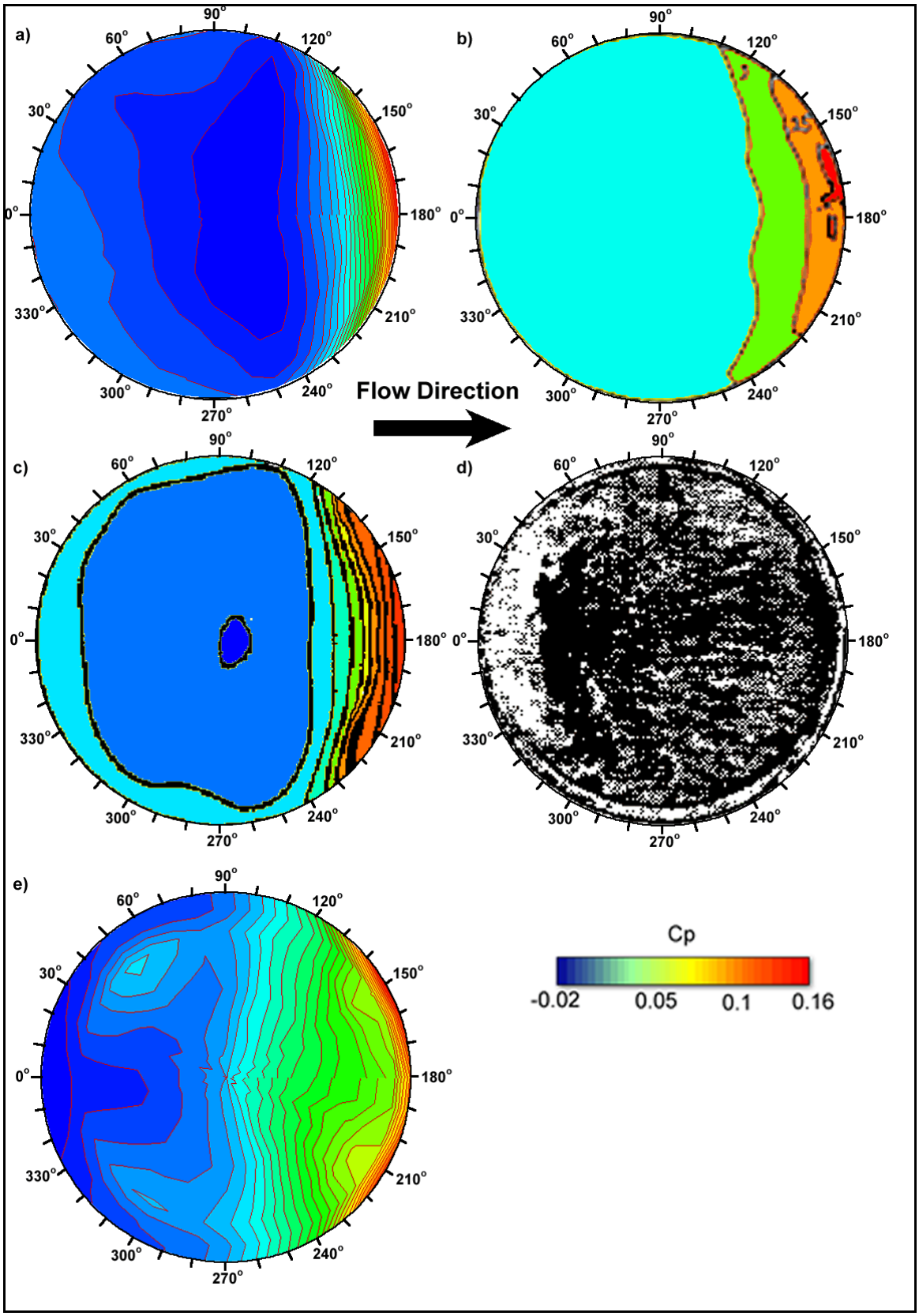

Figure 4-12 – All previous results on cavity base for h/D = 0.20. a) Present mean pressure contour pattern, b) Savory mean pressure (Savory et. al., 1996), c) Hiwada mean pressure (Hiwada et. al., 1983), d) Surface Oil-film pattern (Hiwada et. al., 1983) and e) Present RMS pressure contour pattern

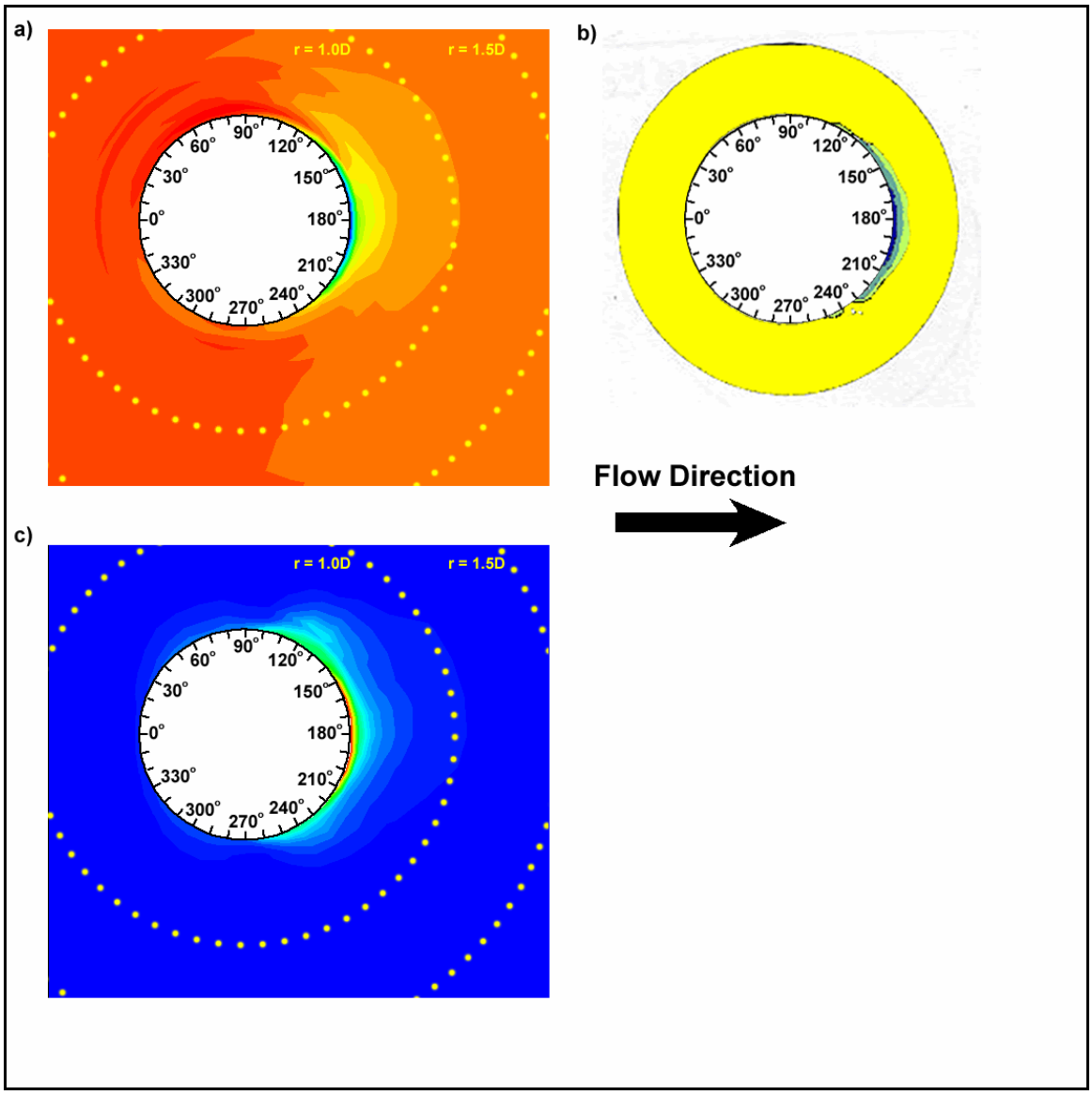

Figure 4-13 – All previous results in cavity wake for h/D = 0.20. a) Present mean pressure contour pattern, b) Savory mean pressure (Savory et. al., 1996), and c) Present RMS pressure contour pattern

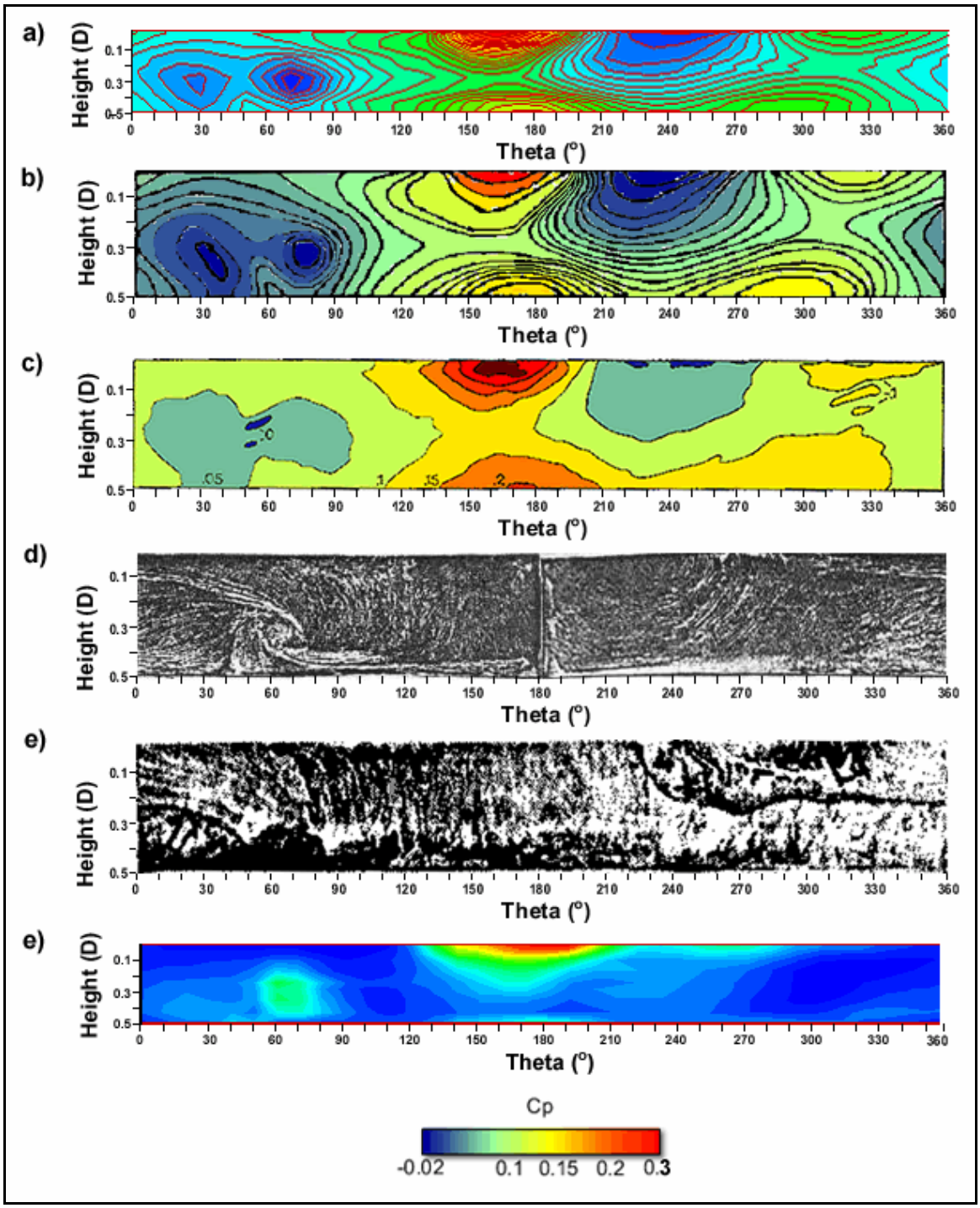

Figure 4-14 – All previous results on cavity sidewall for h/D = 0.5 and 0.47. a) Present mean pressure contour pattern (0.47), b) Hiwada mean pressure (Hiwada et. al., 1983) (0.5), c) Savory mean pressure (Savory et. al., 1996) (0.5), d) Surface Oil-film pattern (Gaudet and Winter et. al., 1971) (0.47), e) Surface Oil-film pattern (Hiwada et. al., 1983) (0.5), and f) Present RMS pressure contour pattern (0.47).

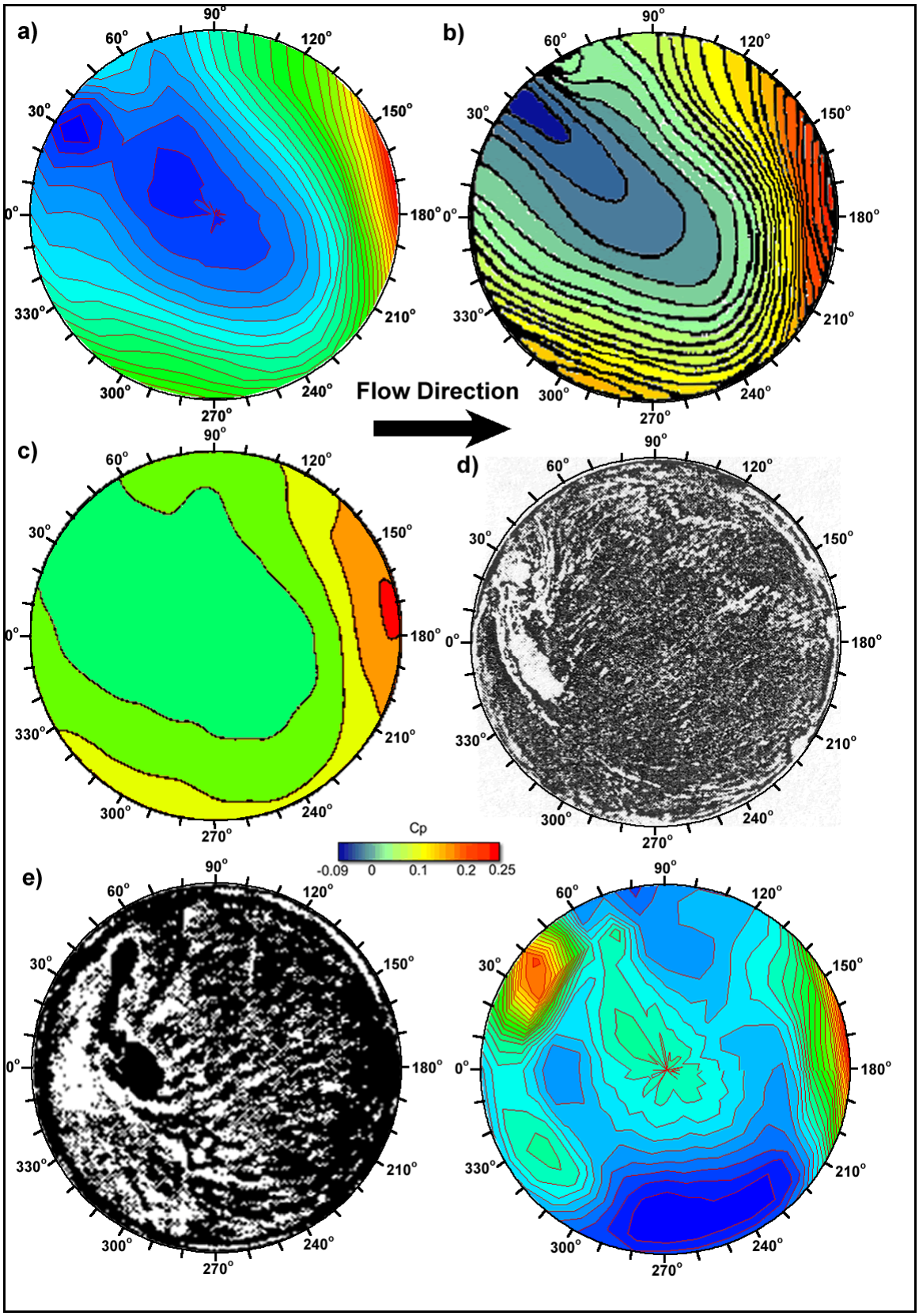

Figure 4-15 – All previous results on cavity base for h/D = 0.5 and 0.47. a) Present mean pressure contour pattern (0.47), b) Hiwada mean pressure (Hiwada et. al., 1983) (0.5), c) Savory mean pressure (Savory et. al., 1996) (0.5), d) Surface Oil-film pattern (Gaudet and Winter et. al., 1971) (0.47), e) Surface Oil-film pattern (Hiwada et. al., 1983) (0.5), and f) Present RMS pressure contour pattern (0.47).

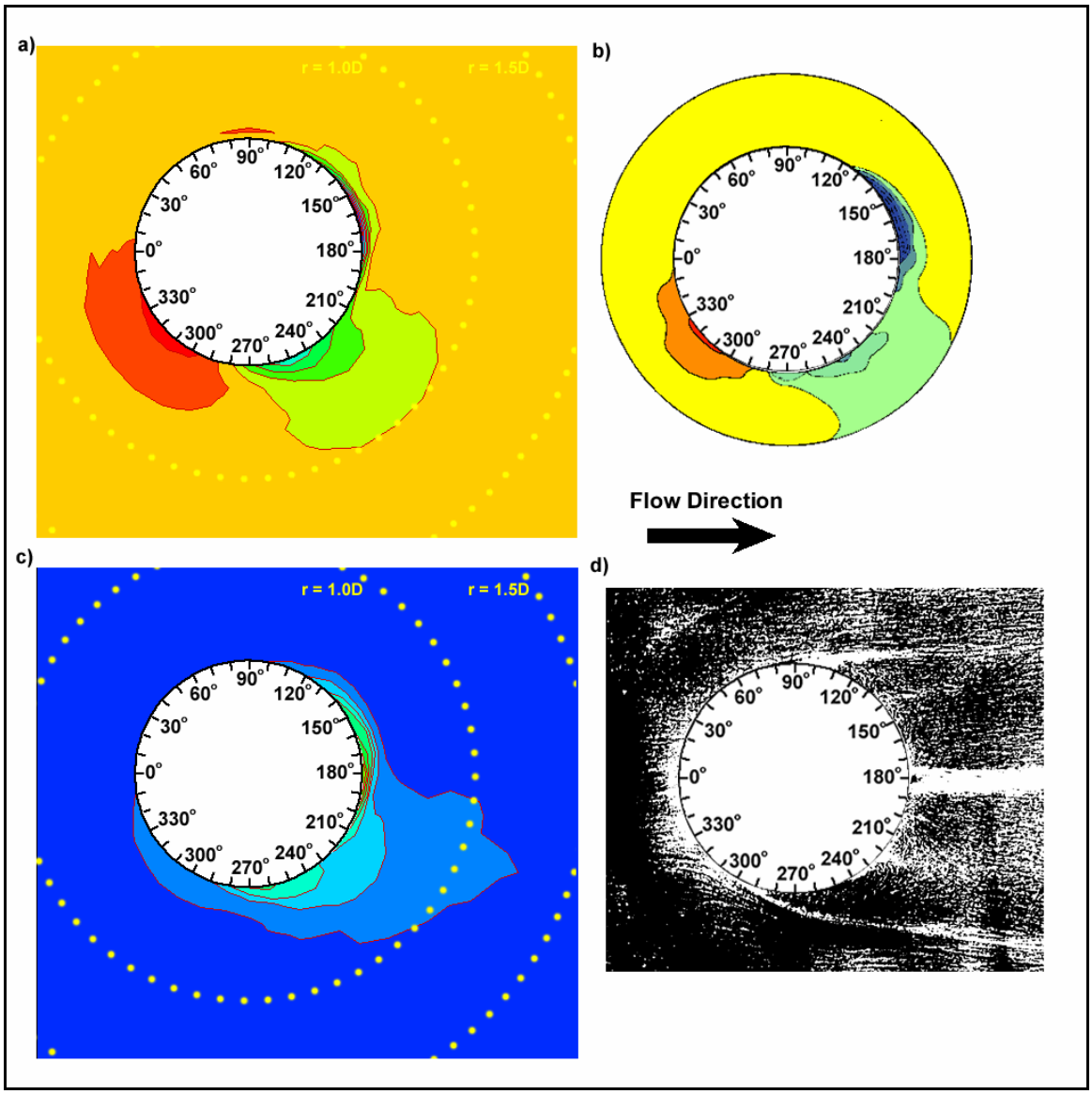

Figure 4-16 – All previous results in cavity wake for h/D = 0.5 and 0.47. a) Present mean pressure contour pattern (0.47), b) Savory mean pressure (Savory et. al., 1996) (0.5), and c) Present RMS pressure contour pattern (0.47).

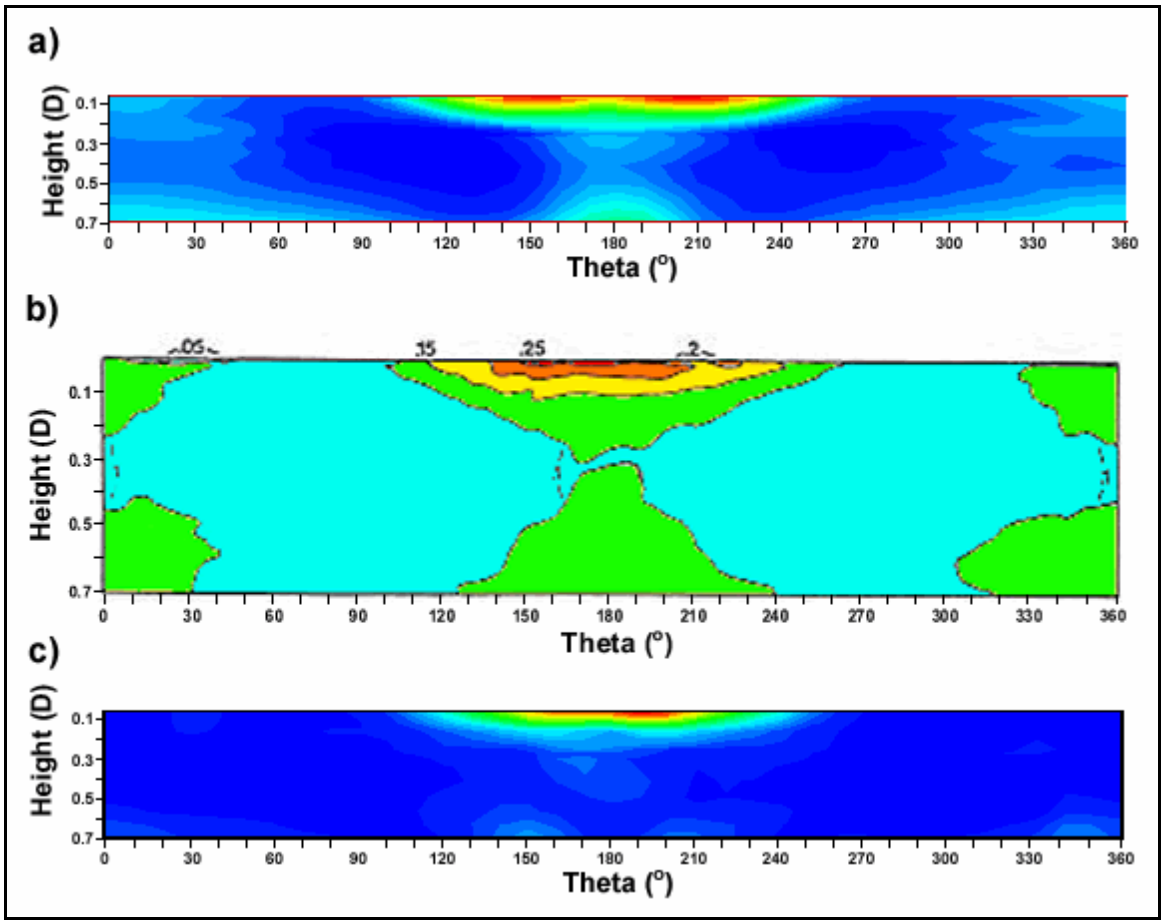

Figure 4-17 – All previous results on cavity sidewall for h/D = 0.7. a) Present mean pressure contour pattern, b) Savory mean pressure (Savory et. al., 1996), and c) Present RMS pressure contour pattern.

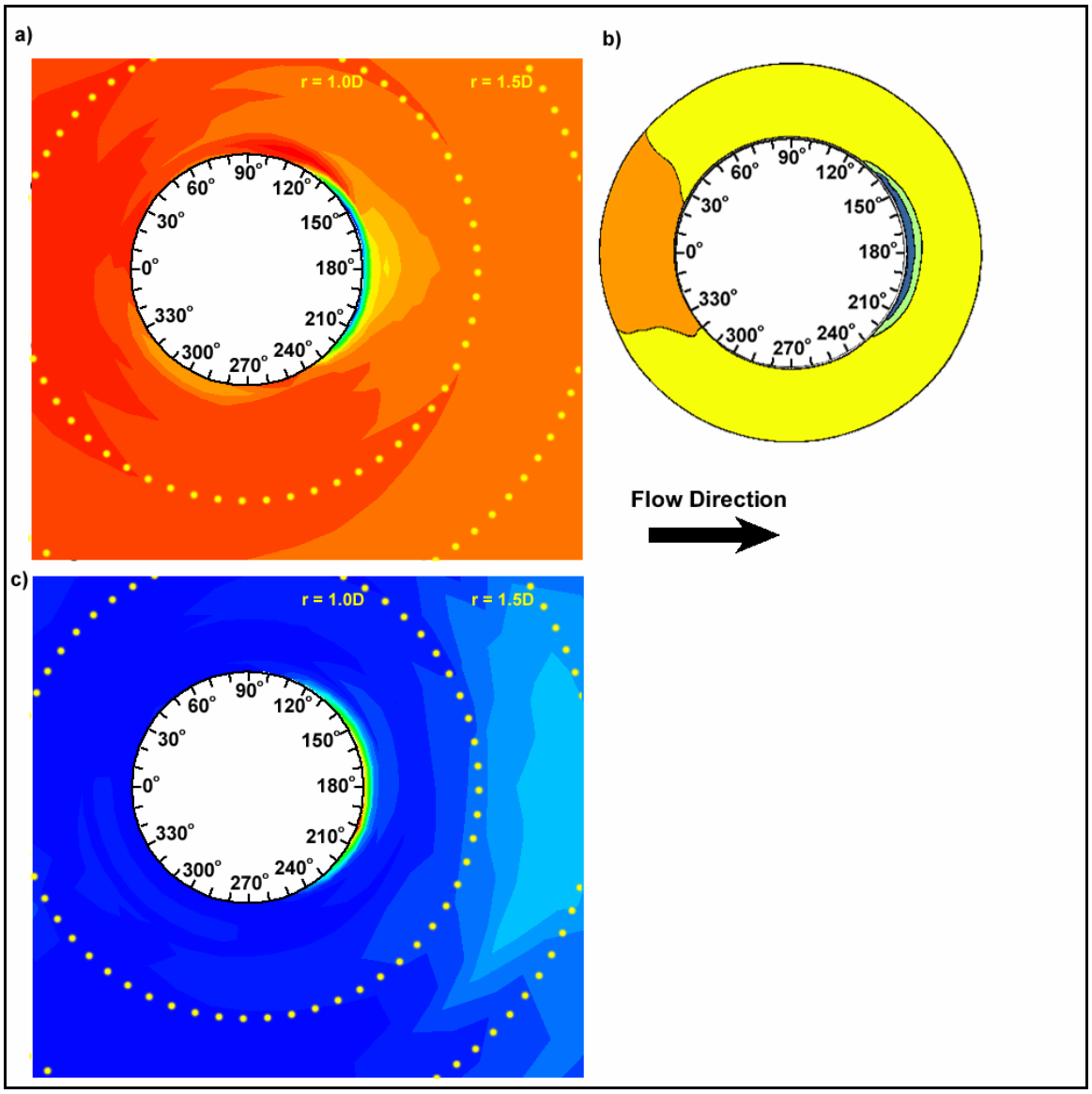

Figure 4-18 – All previous results in cavity wake for h/D = 0.7. a) Present mean pressure contour pattern, b) Savory mean pressure (Savory et. al., 1996), and c) Present RMS pressure contour pattern.

As can be seen in the above comparisons, the mean pressure measurements obtained in the present experiment agree well with those from previous experiments. Minor differences between results are visible such as in the h/D = 0.20 sidewall figures, the present experimental results agree more closely with the Hiwada et. al. (1983) results than those from Savory et. al. (1996) in terms of the sense of the slight asymmetry in the shear layer reattachment point near the cavity downstream lip.

This agreement between previous mean pressure measurements and those from the present experiment adds confidence to the fluctuating pressure measurements from the present experiment. Since no previous fluctuating pressure contour patterns exist for circular cavity flow, this validation of agreement between other results is important towards establishing the accuracy of the fluctuating pressure measurements presented in this thesis.

4.3.4 Three-Dimensional Vortex Skeleton Drawings

The vortex flow in the cavities has been interpreted through the creation of three-dimensional drawings of the proposed locations of vortex skeletons for each cavity configuration tested. These drawings are presented in Figures 4-19 to 4-21 below. Each diagram contains a side view (top left), a top view (bottom left) and an isometric view (right) to add clarity. These drawings were created by examining the location of pressure minima on the cavity surfaces and inferring the curvature of the tubes from pressure patterns on these surfaces as well.

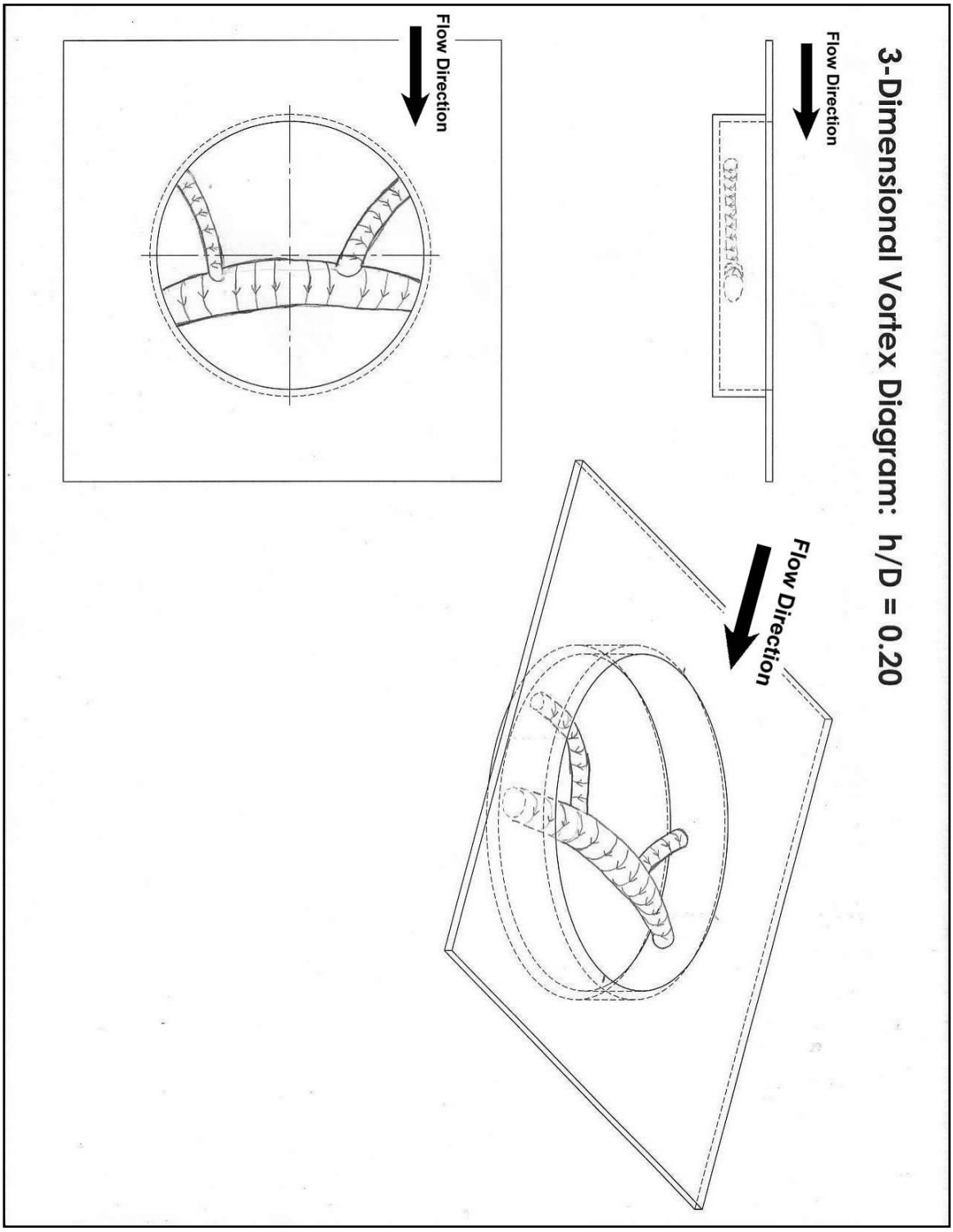

Figure 4-19 – Three-dimensional interpretation of vortex tubes for h/D = 0.20.

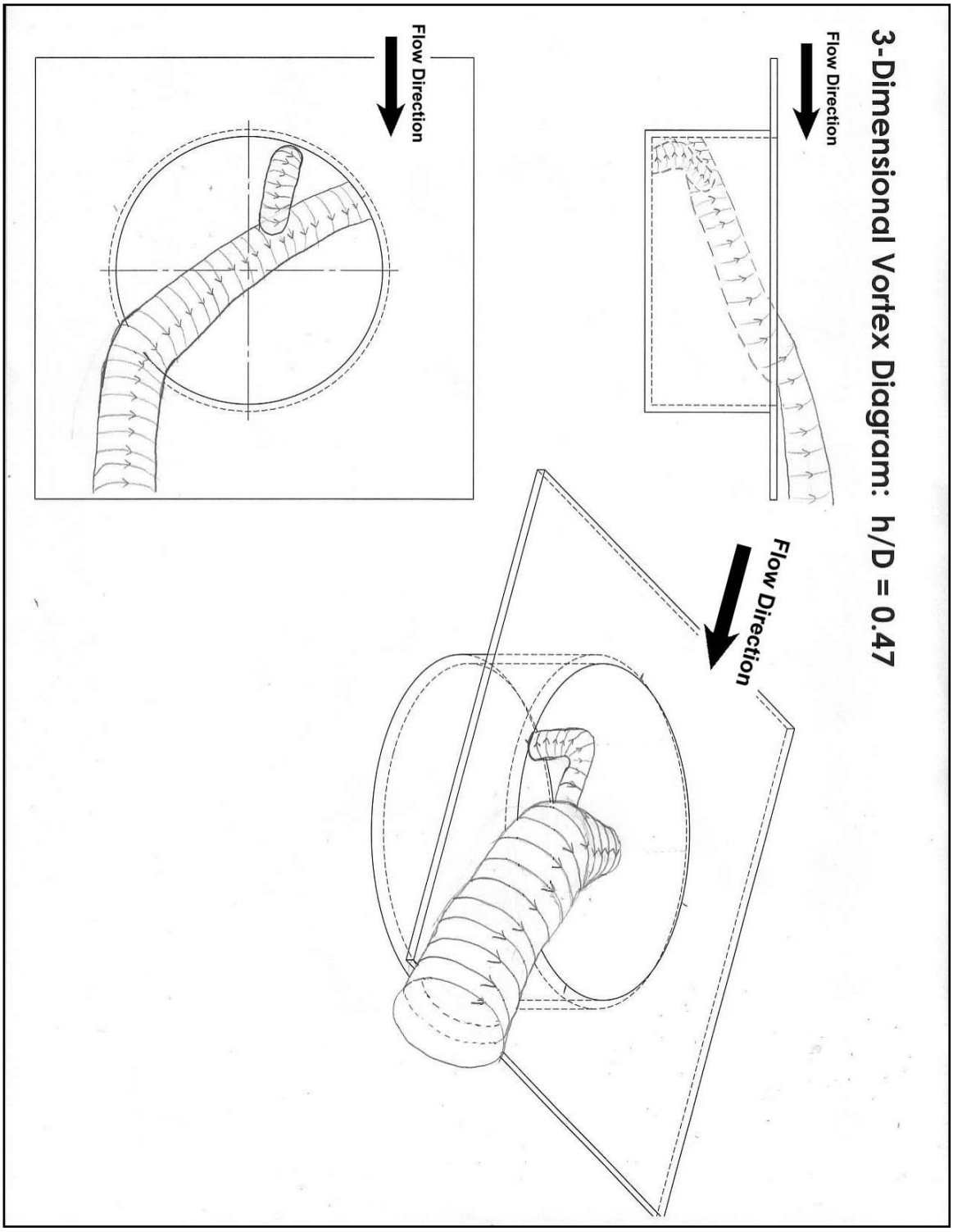

Figure 4-20 – Three-dimensional interpretation of vortex tubes for h/D = 0.47L.

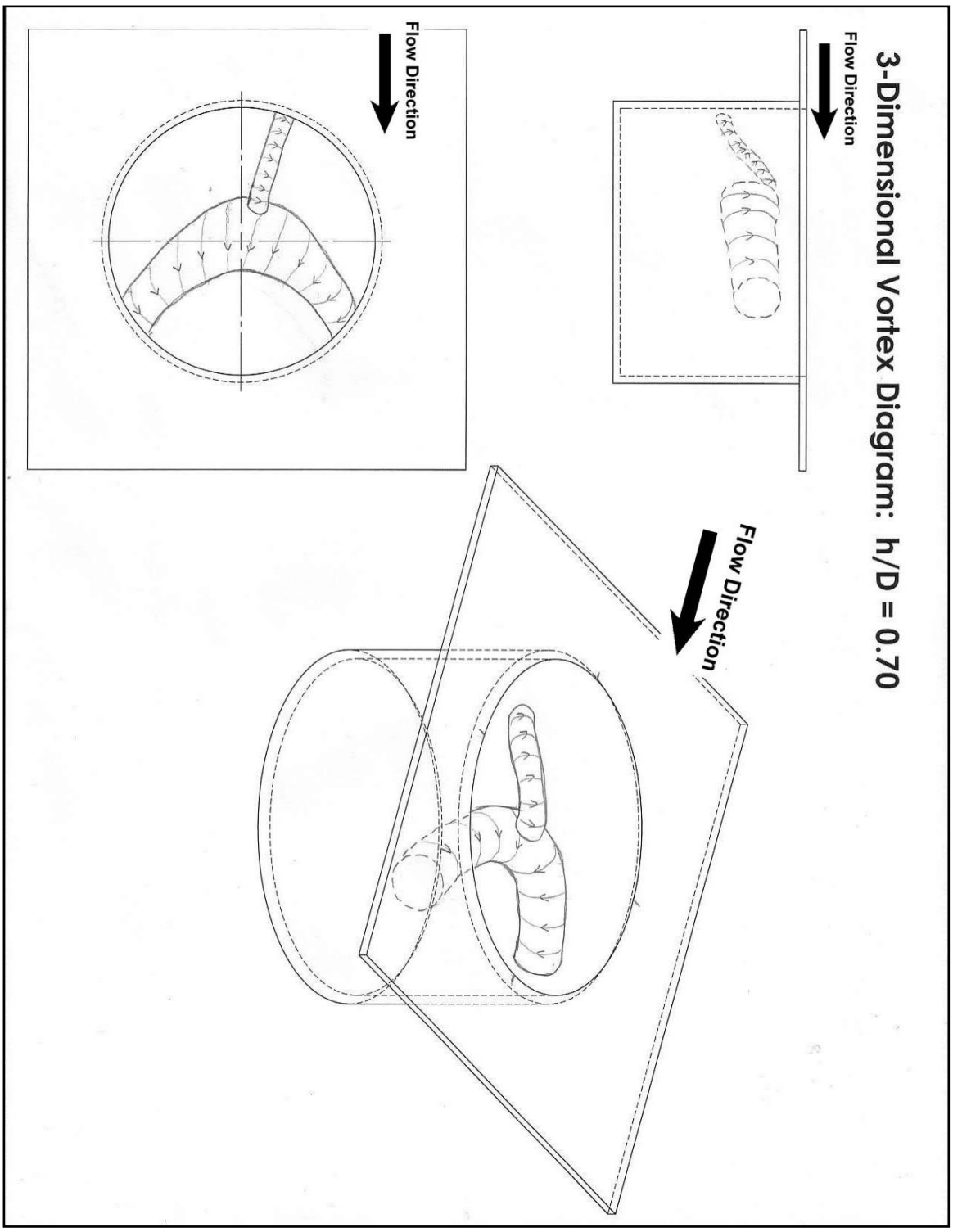

Figure 4-21 – Three-dimensional interpretation of vortex tubes for h/D = 0.70.

The proposed flow structure shown in these diagrams is discussed in the following section which presents and discusses Surface Flow Diagrams, also proposed from the analysis of the mean pressure contours.

4.3.5 Surface Flow Diagrams

The complex, three-dimensional flows that occur in cavities such as those used in the current investigation can be very difficult to visualize and thus, previous investigators have used diagrams showing the trends of the mean flow occurring along the cavity surfaces to aid in this visualization. Gaudet and Winter (1971) pioneered this practice for cavity flows by creating surface flow diagrams from a surface oil-flow investigation for circular cavities. Using this method, diagrams were created of flow separation and attachment points, separation and attachment lines, and focal features such as vortices. This method for surface flow diagrams was very well documented by Hunt et. al. (1978).

Mean surface pressure diagrams, such as those generated from the present measurements, do not reveal as much feature detail as streaklines from surface oil-flow diagrams do, but certain features such as vortex centres and strong flow attachment points are still discernable from mean pressure patterns at the surface. Organized circular low mean-pressure zones can be vortex centre indicators and high mean pressure zones are often evidence of flow stagnation at the model surface.

Surface flow diagrams have been generated from the mean surface pressure data obtained in the present experiment.

Presentation of Diagrams

Surface flow diagrams created using mean surface pressure data are presented in Figures 4-23 to 4-25. A legend for the features shown in these figures is shown below in Figure 4-22.

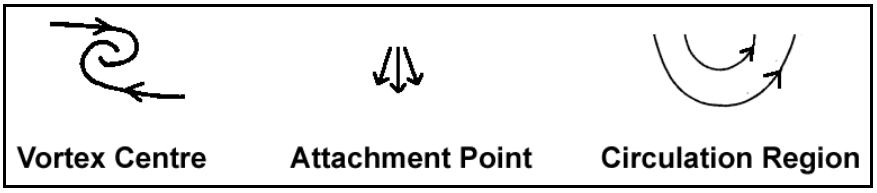

Figure 4-22 – Legend for symbols used in surface flow diagrams.

Each feature is labeled with an A, V or C, representing non-focal Attachment nodal points (flow attachment points – depicting flow away from these points), focal Vortex nodal points (vortex centres), and focal Circulation regions, respectively. Strong features are labeled in a black font while weaker, more secondary features are labeled in red, and accordingly, these features were not as immediately visible in the mean pressure patterns as the strong features.

Cylindrical co-ordinates for all features shown in these diagrams are listed in Table K-1 in Appendix K.

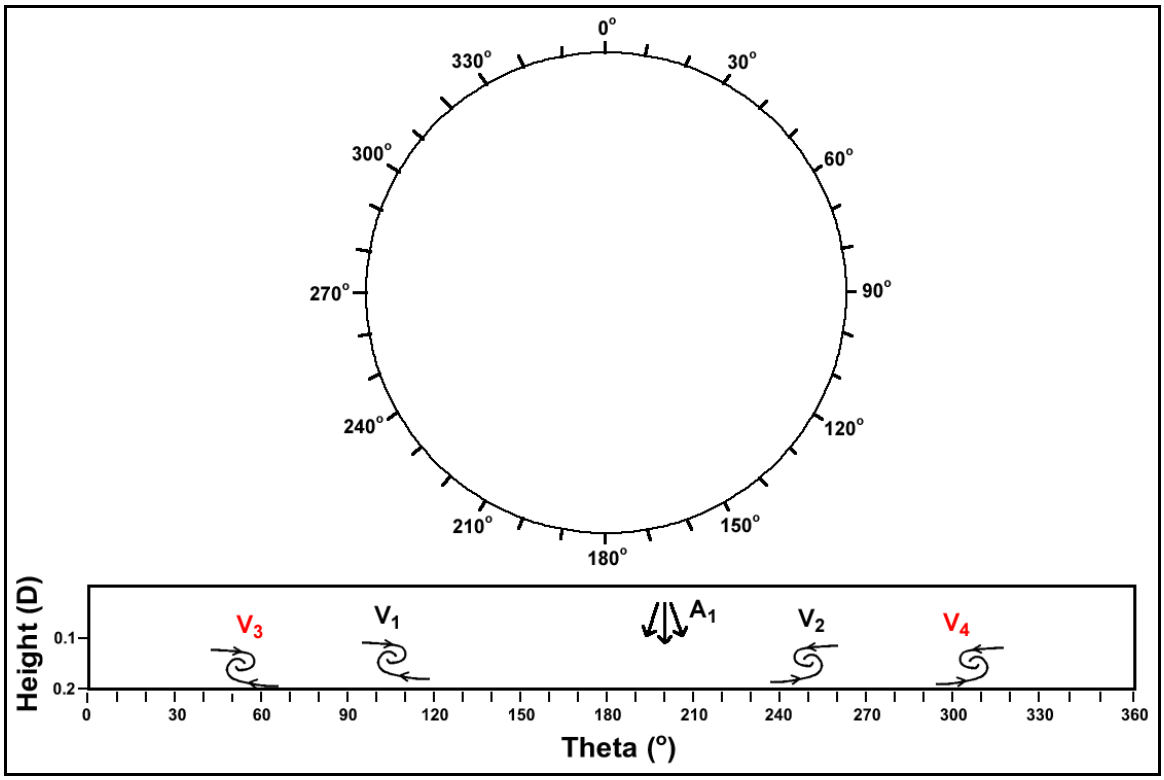

Figure 4-23 – Surface flow diagram along cavity base and "unwrapped" cavity sidewall for h/D = 0.20.

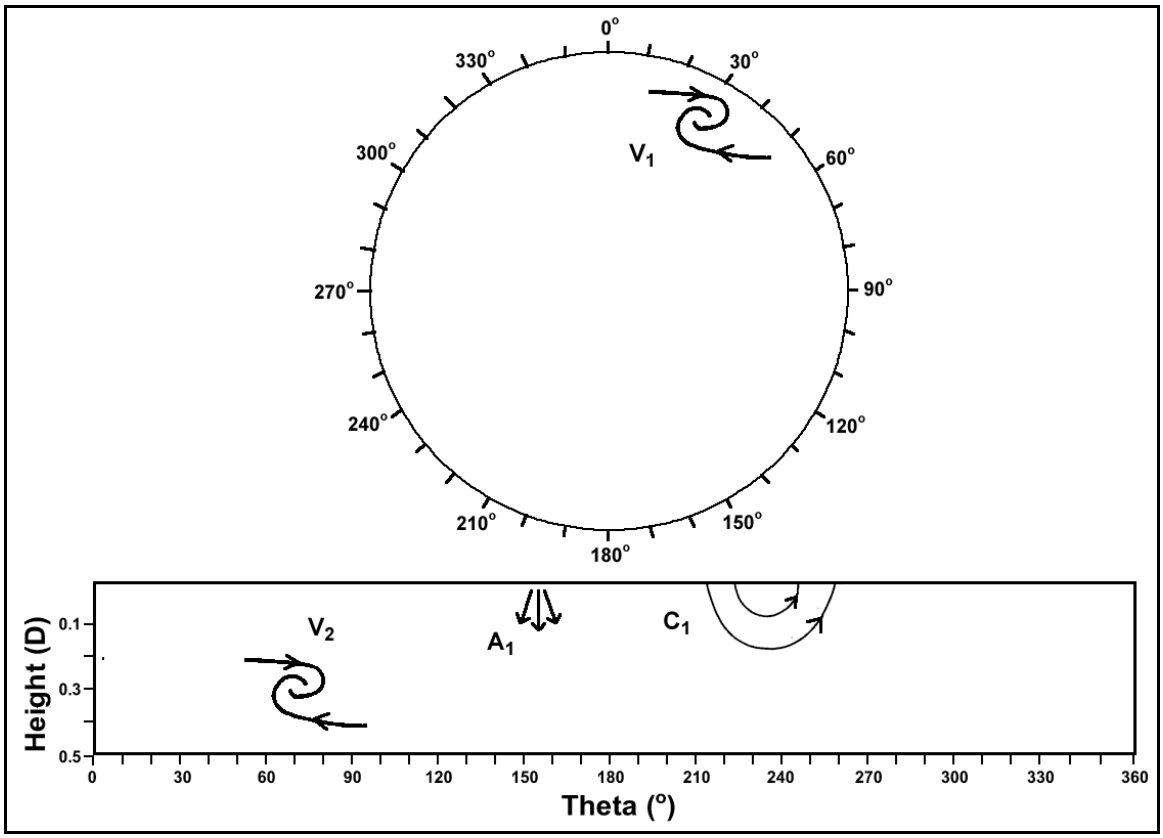

Figure 4-24 – Surface flow diagram along cavity base and "unwrapped" cavity sidewall for h/D = 0.47.

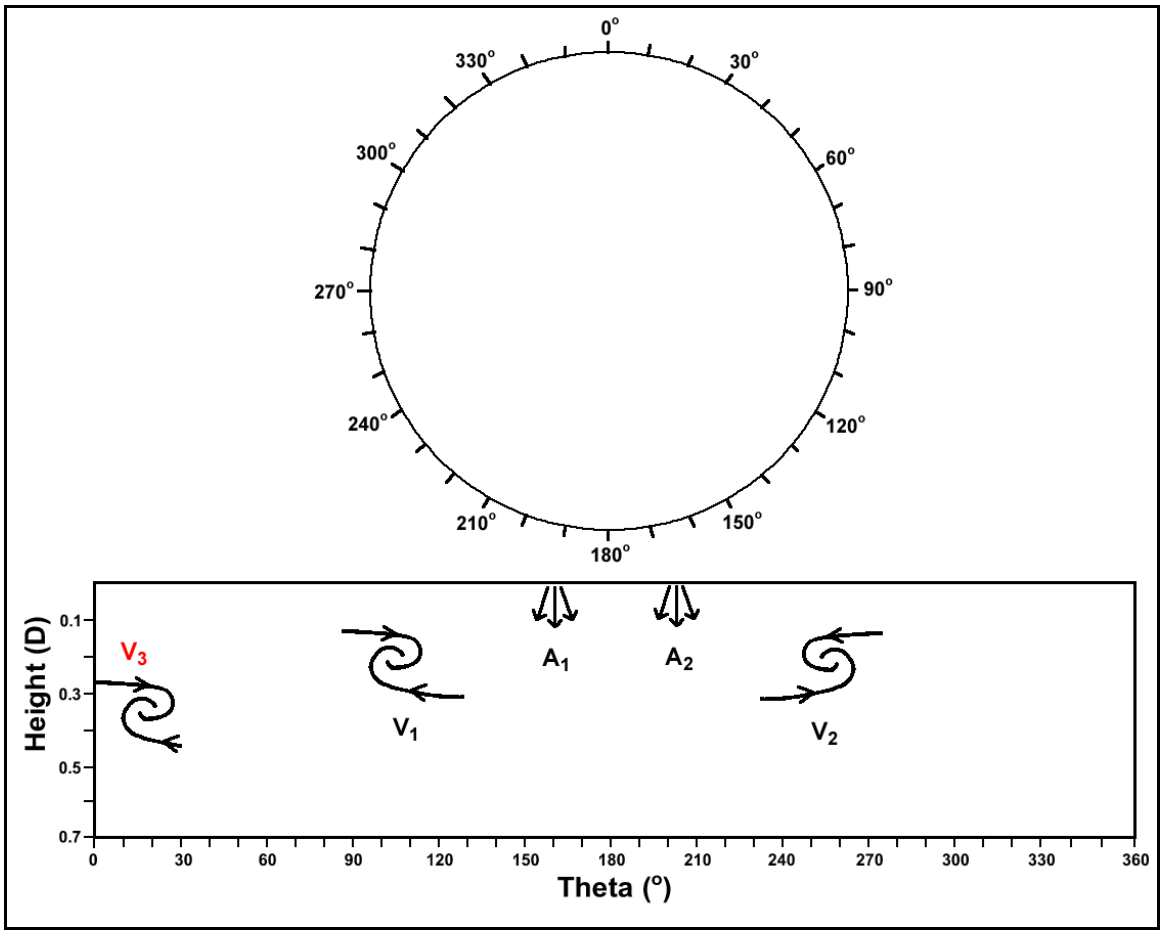

Figure 4-25 – Surface flow diagram along cavity base and "unwrapped" cavity sidewall for h/D = 0.70.

A more clear discussion of the flow for different cavity depth configurations is made possible with the use of these diagrams and making reference to the three-dimensional flow interpretations in Section 4.3.4. For the h/D = 0.20 case (2D: Figure 4-23, 3D: Figure 4-19), the main cavity recirculation is caused by a large vortex tube rooted on either side of the cavity sidewall as shown by features V_1 and V_2. This recirculation is driven by the reattachment of the shear layer at A_1 at a relatively deep point on the sidewall, y/h = 0.13, which causes flow down the rear of the wall and along the cavity base before separation near the upstream wall and recirculation back to the attachment point. Shear layer reattachment occurs at a relatively deep point on the wall due to the low resistance posed to the flow by this cavity configuration of low depth and thus fluid is drawn quite far down the sidewall. Secondary "offshoot"

vortex branches are also implied on the cavity sidewall at V_3 and V_4 as evidenced by weaker circular low-pressure zones in the mean pressure pattern. Once again, these are caused by the bending and rolling up of the major vortex tube in the cavity due to its curved, three-dimensional geometry. The curved nature of the cavity boundaries does not allow the stable existence of a single, straight recirculating vortex of the type observed for rectangular cavities at certain configurations (Roshko, 1955).

For h/D = 0.47 (2D: Figure 4-24, 3D: Figure 4-20), the surface flow diagram is asymmetric about the cavity stream-wise centreline with the main trailing vortex originating on the upstream sidewall at V_2 and spanning the cavity diameter to exit the cavity at the circulation zone C_1. An offshoot vortex branch discussed earlier is also seen rooted to the cavity base at V_1. Shear layer reattachment for this configuration takes place off-centre of the sidewall horizontal centre at about θ = 160°, thus driving the asymmetric flow condition.

For h/D = 0.70 (2D: Figure 4-25, 3D: Figure 4-21), a symmetric flow pattern is surmised for the primary flow features with the major recirculating vortex being rooted to fairly shallow locations on the cavity sidewall at θ = 105° and 255°. The axis of this main vortex is bent to match the cavity boundaries as seen by the arced low pressure zone on the cavity base in Appendix Q, FigureQ-1c. This bent main vortex tube seems to give rise to a secondary offshoot vortex rooted to the cavity sidewall near θ = 15°.

The differing surface flows observed between tested depth configurations lead to large differences in induced drag. This drag is discussed in the following section.

4.3.6 Cavity Drag Analysis

Measurements of the drag due to the presence of the cavity, whether measured directly or indirectly, have been made by nearly all previous investigators of the flow over this type of cavity and thus an indirect measurement of the cavity model

incremental drag coefficient was made using the method described in Section 3.4.3. The incremental drag coefficients calculated using this method were plotted together with results from previous experiments in Figure 4-26. Another non-dimensional measure of cavity drag, explained in Section 3.4.3, has been calculated for the current measurements and is plotted together with the same from previous experiments in Figure 4-27.

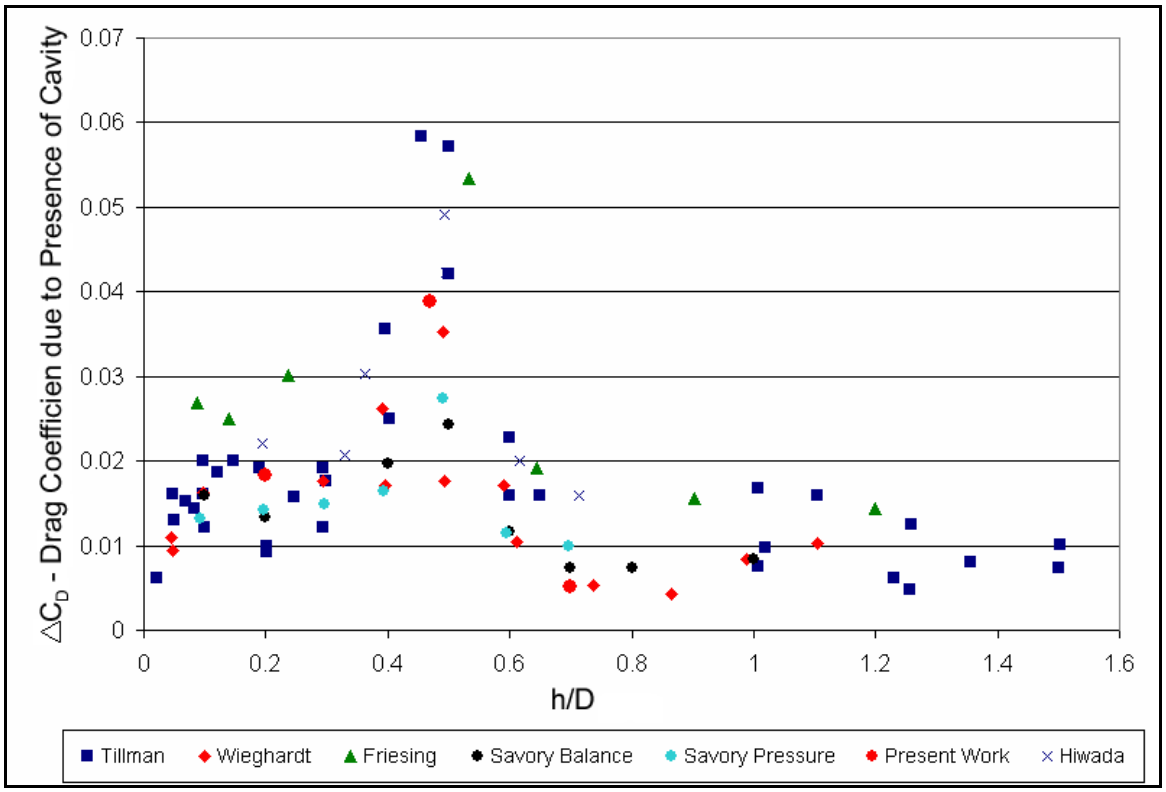

Figure 4-26 – Comparing drag measured due to presence of circular cavity for present experiment to previous investigations using incremental drag coefficient ΔC_D.

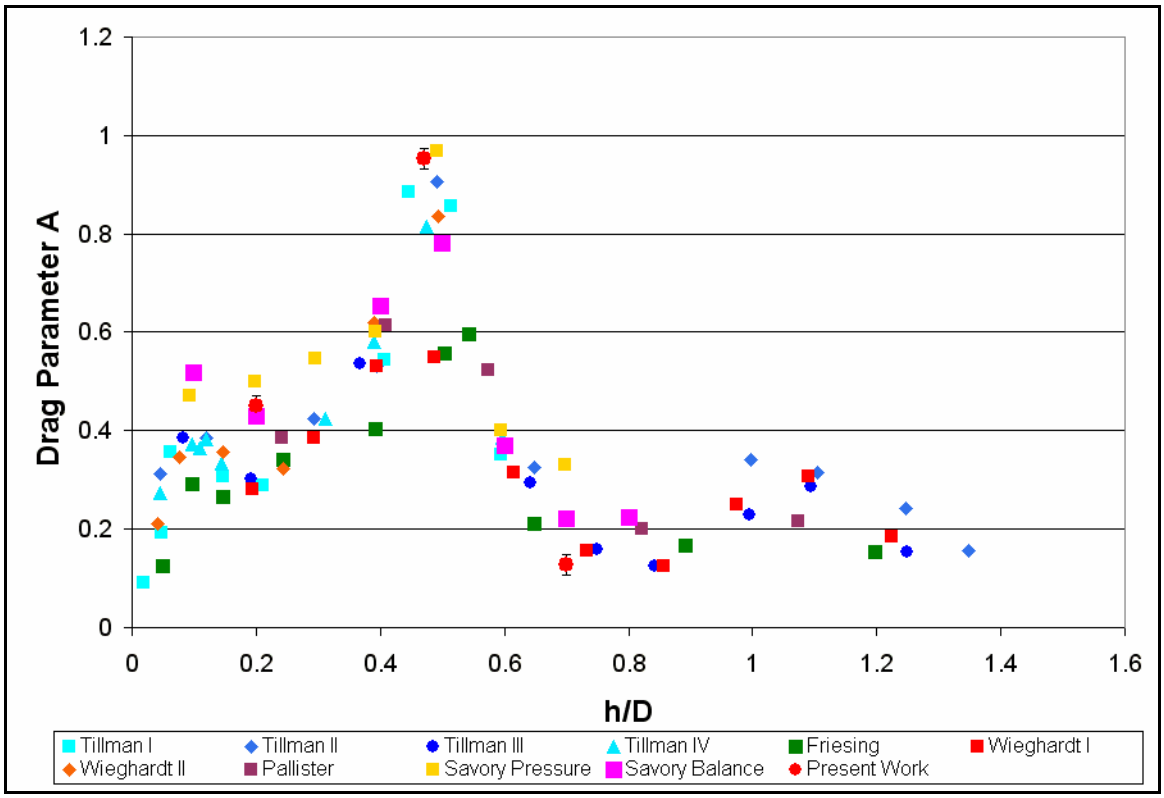

Figure 4-27 – Comparing drag measured due to presence of circular cavity for present experiment to previous investigations using incremental drag parameter A.

As shown by these figures, the agreement between the present measurements and previous experiments is quite good. In both comparisons, the data from the present experiment fit into the scatter from previous investigations.

4.4 Cavity Wake Velocity Profiles

A traversed two-component hot-wire anemometry system was used to acquire a grid of velocity-time series in the cavity model wake as described in Section 3.4.2. The two cavity depth configurations of h/D = 0.20 and 0.47 were used in this experiment and two separate measurements were taken for the 0.47 to investigate the effect of switching the wake flow on the wake velocity measurements. Hence, one set of measurements was taken for the left-handed case (b in the Figures) and one set was taken for the right-handed case (c in the Figures).

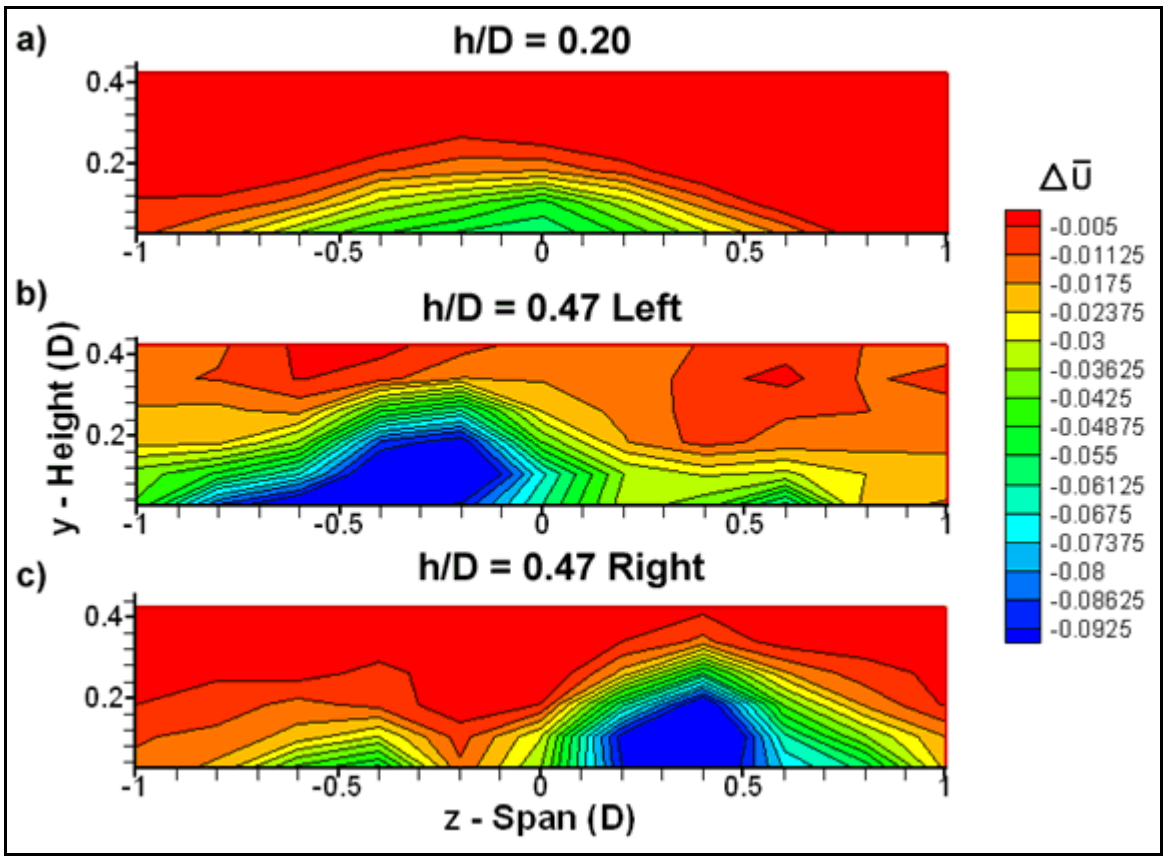

Figure 4-28 - A composite image of the cavity effect on mean stream-wise flow in the cavity wake at x/D = 1.85. Image a) shows the effect for h/D = 0.20, b) shows the left-handed h/D = 0.47 case and c) shows the right-handed h/D = 0.47 case.

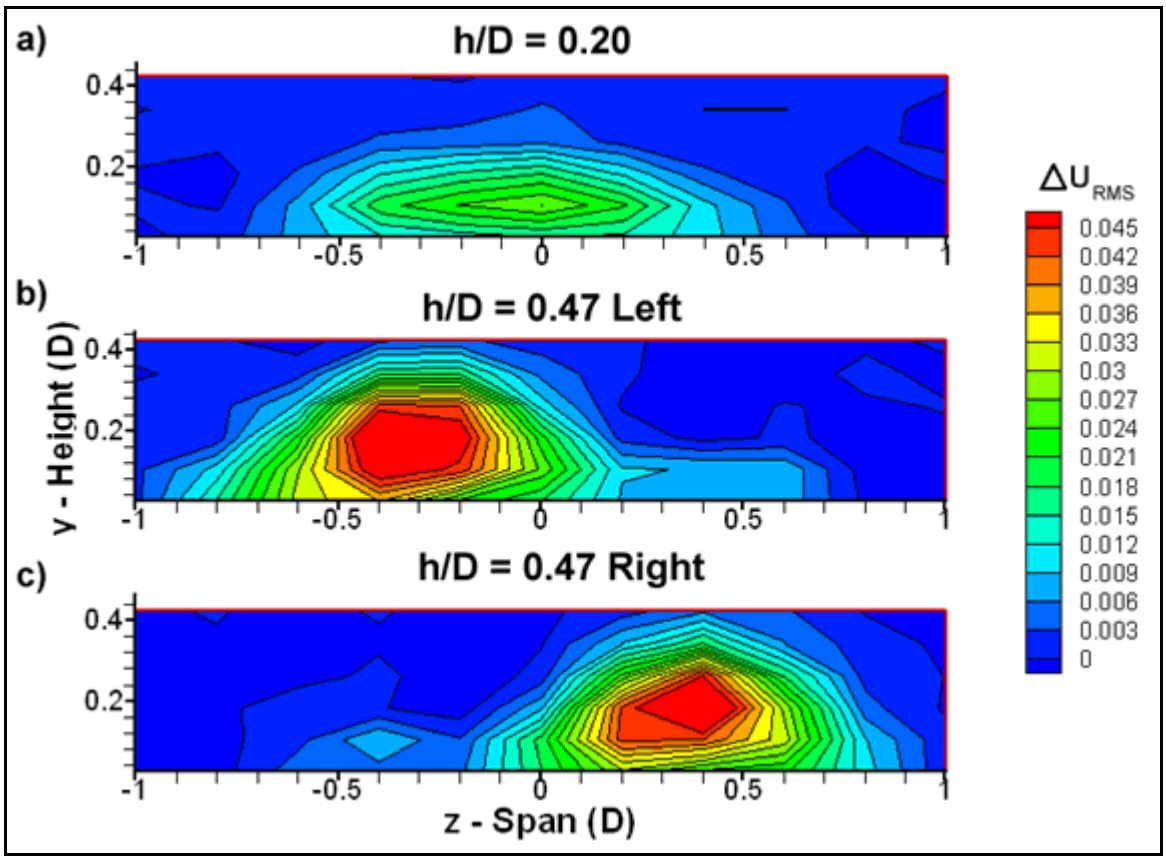

Figure 4-29 - A composite image of the cavity effect on mean stream-wise velocity fluctuations in the cavity wake at x/D = 1.85. Image a) shows the effect for h/D = 0.20, b) shows the left-handed h/D = 0.47 case and c) shows the right-handed h/D = 0.47 case.

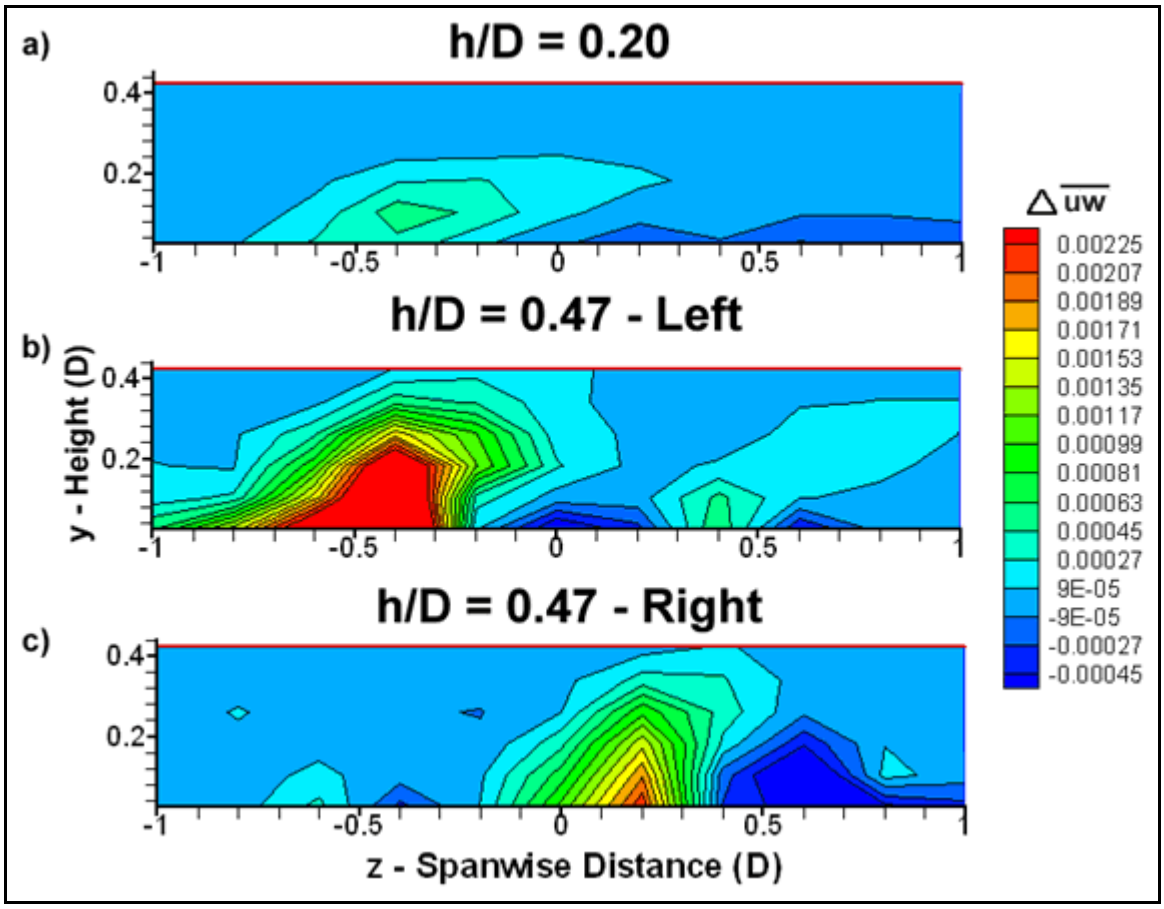

Figure 4-30 - A composite image of the cavity effect on uw mean shear stress in the cavity wake at x/D = 1.85. Image a) shows the effect for h/D = 0.20, b) shows the left-handed h/D = 0.47 case and c) shows the right-handed h/D = 0.47 case.

4.4.1 Flow Quantities Used

In Figures 4-28 to 4-30 the cavity's effect on various mean and RMS velocities in the wake are displayed by showing contours of the following quantity:

$$\Delta V = \frac{V_{cav} - V_{ud}}{U_0}$$

Where V_{cav} is the measured generalized mean or RMS velocity at a wake grid point with the cavity model in place, V_{ud} is the undisturbed measured generalized mean or RMS velocity at this same point with cavity model not in place and U_0 is the mean velocity of the free-stream. By processing the results in this way, the external

flow is essentially subtracted and only the effects related to the cavity presence can be seen.

The effects of the cavity on the mean shear stresses in the wake were also examined using a slightly modified equation to account for the different unit of this quantity:

$$\Delta\overline{uw} = \frac{\overline{uw}_{cav} - \overline{uw}_{ud}}{U_0^{\,2}}$$

Where $\overline{uw}_{cav}$ is the measured mean uw shear stress at a wake grid point with the cavity model in place, $\overline{uw}_{ud}$ is the undisturbed measured mean uw shear stress at this same point with no cavity in place, and U_0 is the mean velocity of the free-stream.

Discussion

Velocity profiles carried out by Hiwada et. al. (1983) and Savory et. al. (1996) consisted of single span-wise lines of stream-wise velocity profiles and Savory et. al. also measured a single span-wise line of stream-wise turbulence. Single span-wise lines of such profiles from the present experiment are compared to the results from these previous investigations in Figures 4-31 to 4-33.

Although these results are difficult to compare quantitatively due to differing boundary layer thicknesses, cavity diameters and downstream locations of measurement between experiments, a qualitative comparison can be done in this way.

The present results, being taken at a greater distance from the downstream edge of the cavity than the previous profiles, have less pronounced velocity deficits in the stream-wise profiles (Figure 4-31) than those previous. In both Figures 4-31 and 4-32, when comparing the present velocity deficits to those obtained previously, the present deficits seem to be shifted slight to the right (+z) by approximately 0.15D. Since this z-shift is not observed between the previous measurements at x/D = 0.92

and 1.5, it is proposed that this shift may be due to a slight w-component (span-wise) velocity in the tunnel for the present experiment, thus causing these features to be convected slightly to the right.

The agreement between the present results is much greater for Savory's measurements than Hiwada's. This is undoubtedly due to the closer proximity between the downstream location of the present experiments (1.85D) to Savory's (1.5D) than to Hiwada's (0.92D). It is assumed that the wake flow features are dispersed as the downstream distance from the rear of the cavity (x) increases. The trailing vortex is seen in the profiles in the z/D =-0.3 to -0.5 range in the larger velocity deficit.

Qualitative agreement between the present results and those from Savory et. al. is also noted in Figure 4-32 for the h/D = 0.2 case in terms of the sense of the slight asymmetry in the profile and the shape of the velocity deficit.

Agreement between the stream-wise turbulence measurements and those by Savory et. al. is quite good (Figure 4-33), similar profile shapes are noted for both the h/D = 0.2 and 0.5 cases with the present results once again shifted slightly to the right of the figure relative to previous results as mentioned earlier.

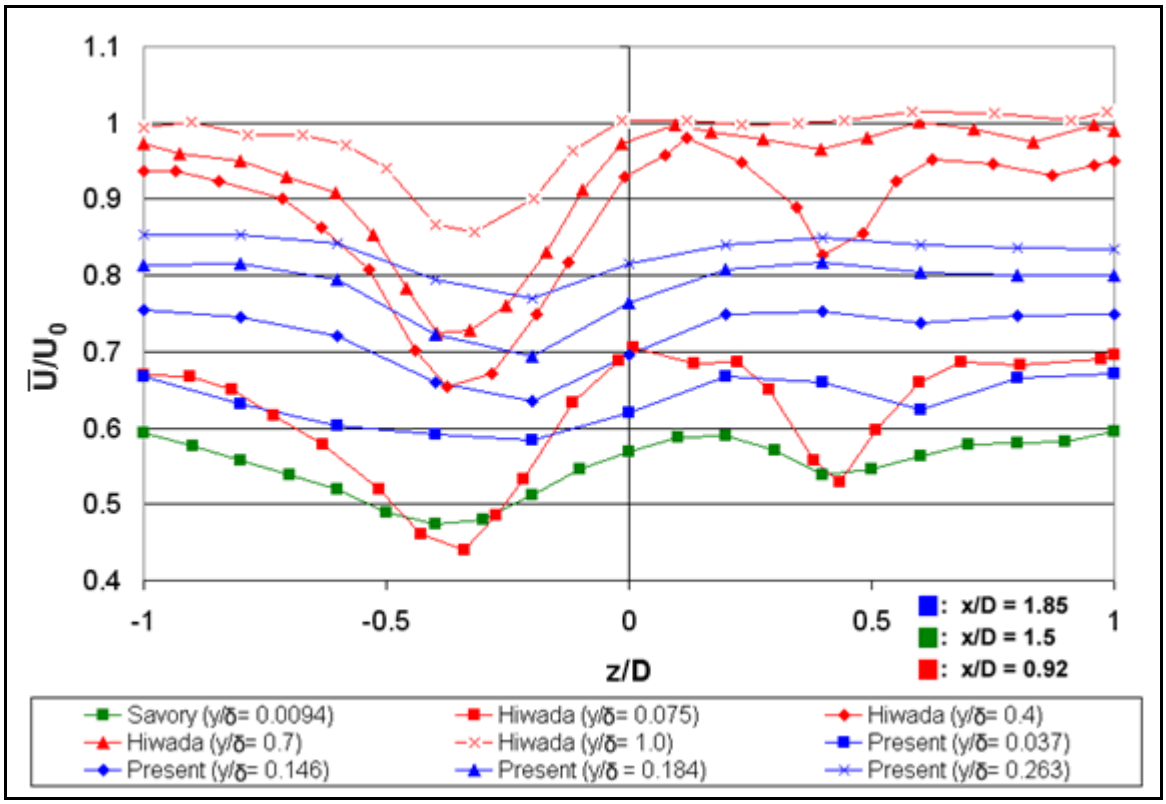

Figure 4-31 - Span-wise lines of present and previous stream-wise velocity profiles for h/D = 0.5 and 0.47. Past profiles (red and green points in Figure) were captured for h/D = 0.5 and the present profiles (blue points in Figure) were acquired for h/D = 0.47.

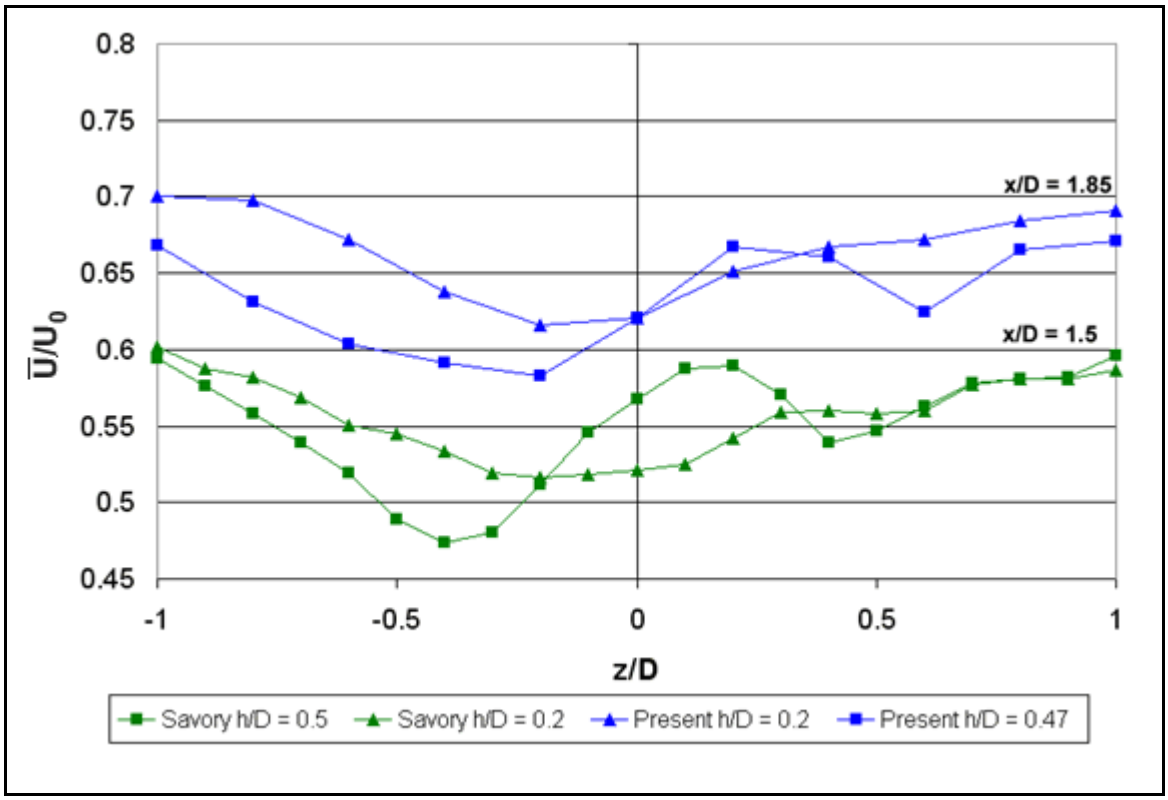

Figure 4-32 - Span-wise lines of present and previous stream-wise velocity profiles for h/D = 0.2, 0.47 and 0.5.

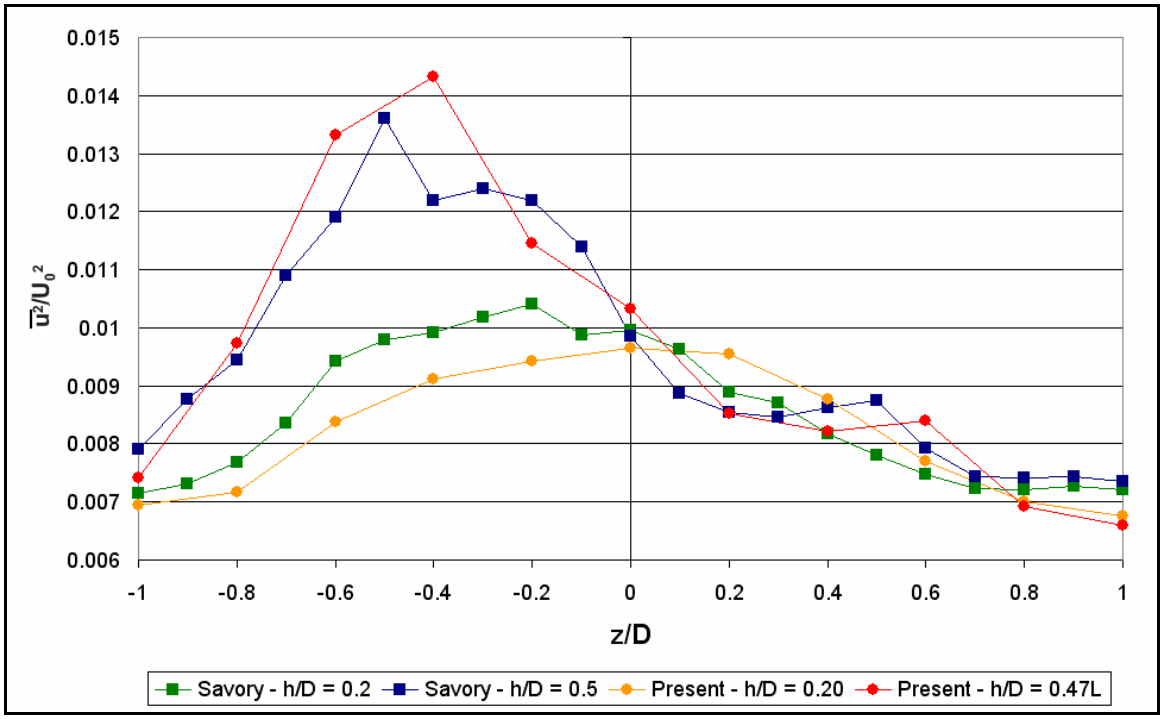

Figure 4-33 - Span-wise lines of present and previous stream-wise turbulence profiles for h/D = 0.2, 0.47 and 0.5.

The h/D = 0.47 configuration caused the greatest free-stream mean velocity loss, reaching an 11.6% velocity loss at the centre of the velocity defect centred at 0.35D for the right-handed profile. The h/D = 0.20 configuration caused a maximum stream-wise mean velocity loss of 6.0% in the span-wise centred velocity defect nearest the tunnel wall. Accordingly, the h/D = 0.47 case yielded a greater integrated velocity loss across the measurement grid than the h/D = 0.20 case, accounted for by the observed greater cavity-fluid entrainment in the mean surface pressure profiles for the h/D = 0.47 case.

Qualitatively, the profiles yielded the expected results in that the h/D = 0.20 case yielded a span-wise centred symmetric profile and for the h/D = 0.47 case an asymmetric profile was found with velocity defect feature matching the side of the cavity which exhibited the exposed and shed vortex seen in the pressure measurements. Also, in all cases, regions with large mean U-velocity deficits coincide with nearly identically shaped regions of high turbulence intensity and mean $\overline{uw}$ shear stress, demonstrating conversion from energy in the stream-wise flow to turbulent kinetic energy (Delannoy et. al., 1994) via the mean shear created by the interaction between the external flow and the trailing vortex feature from the cavity in this instance.

The somewhat circular features seen in the mean stream-wise velocity profile (Figure 4-28) as a velocity deficit and in the RMS velocity profile (Figure 4-29) as a turbulence peak for the h/D = 0.47 cases (located at z = -0.3D for the left-handed case and z = +0.35D for the right-handed case) are consistent with the trailing vortex surmised from the low mean pressure pattern near the cavity lip on the sidewall for this depth configuration (see Figure 4-4). Drawing a straight line in the stream-wise direction from the centre of this feature on the cavity lip to the location of hot-wire measurements would line these two features up almost exactly. This shows that the

trailing vortex is convected downstream from the cavity lip by the external flow to the location of hot-wire measurements.

The effect of switching the cavity wake flow handedness between experiments represented in parts b and c of Figures 4-28 to 4-30 was to reflect the mean velocity, RMS velocity and shear stress profiles about the span-wise centre of the working section (z = 0).

This switching phenomenon observed for h/D = 0.47 is investigated further in the following section through focused pressure measurements along the cavity model lip.

4.5 Investigating Switching and Flapping Phenomena

4.5.1 Flapping Regime Experiment

By monitoring a pressure tap on the cavity sidewall for h/D = 0.37 through the use of a pressure transducer, as explained in Section 3.4.3, the existence of a "flapping" pressure regime at this configuration as suggested by previous investigators (Hiwada et. al., 1983), was confirmed. The pressure-time histories acquired in this experiment are presented in Figure 4-34. For comparison, the time history presented by Hiwada et. al. (1983) is also shown in this Figure (4-34 f).

As seen in this figure, five separate 100 second histories were recorded to ensure the repeatability of this phenomenon.

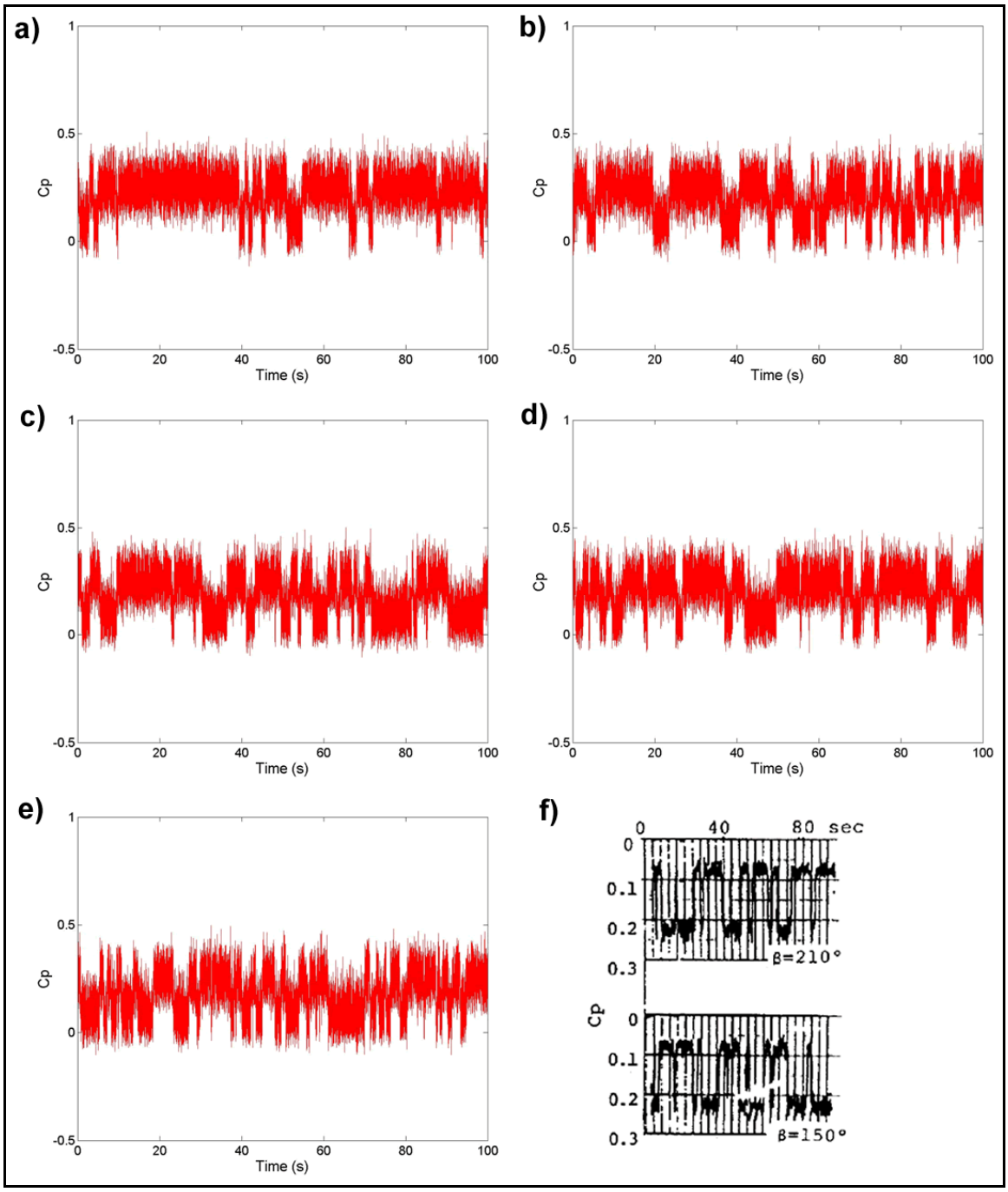

Figure 4-34 – Pressure time series confirming flapping phenomenon proposed by Hiwada et. al. (1983).

Trial	Number of Flaps over 100 s
1	21
2	29
3	30
4	28
5	50
Hiwada et. al. (1983)	20

Table 4-5 – Analysis of flapping frequency observed in trials conducted in the present work and compared to previous results.

Flapping events are defined as the movement from a high mean pressure to a lower one, or vice versa. The number of flapping events observed for various pressure-time histories are shown in Table 4-5. This table shows that the number of observed flaps varies greatly between trials but seems to range somewhere between 20 and 50. Although this phenomenon was termed periodic by previous investigators (Hiwada et. al., 1983), the presented figures definitely do not exhibit periodicity. Rather, although the observed flapping is somewhat regular over a long period of time, it seems to be intermittent.

Though the equipment used for this present experiment did not allow simultaneous measurement of pressure taps on opposite sides of the cavity sidewall, Figure 4-34 f) shows such simultaneous measurements conducted by previous investigators (Hiwada et. al., 1983), showing an anti-symmetry between mean pressure measurements between the two transducers showing that when one transducer is measuring the peak pressure ($Cp = 0.23$), the transducer on the opposite side measures the minimum pressure ($Cp = 0.08$). This could mean that the shear layer stagnation point is not stable at a single point on the cavity sidewall at this configuration and that the observed flapping is due to the flapping of the shear layer reattachment point between two particular points on the sidewall. In this way, when the reattachment point is closer to one measured pressure tap, a higher pressure is

seen, while simultaneously the tap on the other side is farther away from the reattached shear layer and thus, a lower pressure is measured there.

4.5.2 Switching Regime Experiment

An experiment was carried out according to Section 3.4.3 to investigate the possibility of switching the handedness of the wake flow asymmetry through the introduction of a disturbance to the flow as claimed by previous investigators (Gaudet & Winter, 1971, Hiwada et. al., 1983). It was observed that by inserting a small sheet of plywood into the flow upstream of the cavity on the side which the asymmetric wake feature (trailing vortex) was observed, the side of the wake asymmetry (or handedness) could be switched to the opposite side of the cavity. For example, for a right-handed asymmetry such as the one measured in Figure 4-28c, a disturbance introduced on the right-handed side of the tunnel would force the flow to switch to a left-handed asymmetry (4-28b) (reflecting the pressure distribution about the stream-wise axis). This type of disturbance is termed a "same-handed" disturbance while a disturbance applied on the opposite side of the working section as the trailing vortex side is termed an "off-handed" disturbance.

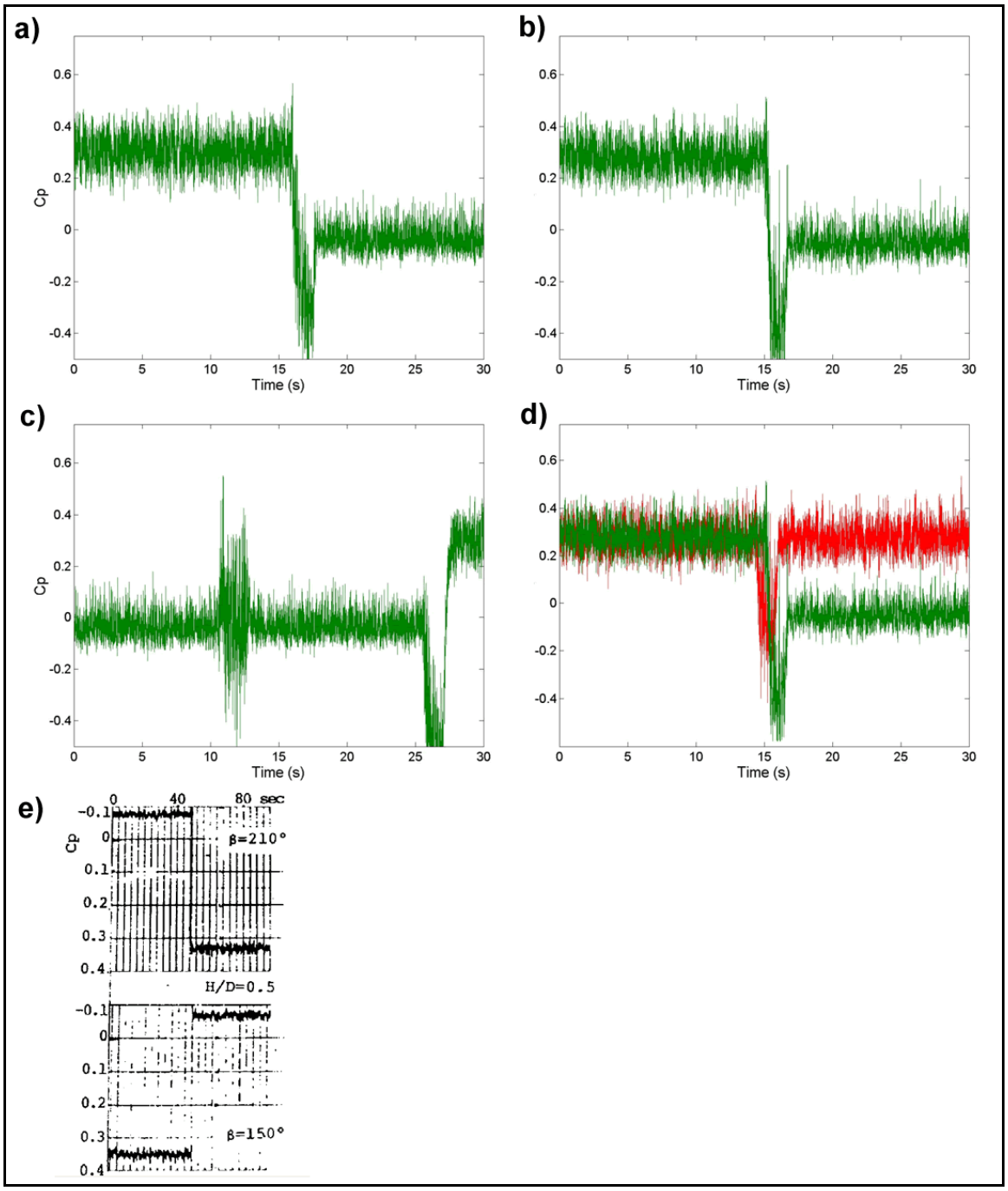

Figure 4-35 – Pressure time series of switching experiments for h/D = 0.47 under various disturbance conditions: a) Left to right wake-side switch attempt, b) Right to left wake-side switch attempt, c) off-side switch attempt (at 12 s) followed by wake-side switch attempt (at 25 s), d) superposed small-magnitude wake-side switch attempt (red) and large-magnitude wake-side switch attempt (green), e) simultaneous measurements at opposite sides of cavity rim showing wake switch for h/D = 0.5. (Hiwada, et. al., 1983)

Evidence of this switching is seen in the pressure-time histories presented in Figure 4-35, and, for comparison, previous work (Hiwada et. al., 1983) is shown in Figure 4-35e). A pressure tap was monitored 2 mm from the cavity rim on the sidewall for two separate orientations: $\theta = 150°$ and 210°. From close analysis of a high resolution mean pressure contour plot on the cavity sidewall for h/D = 0.47 (Figure 4-7), mean pressures of approximately Cp = 0.3 and -0.03 were measured at these points for $\theta = 150°$ and 210°, respectively, for the case of a right-handed asymmetry. Thus, if a switch in the handedness of the wake feature were to occur, one would expect that the mean values measured at these points to switch, since they are equally offset from the cavity centre on opposite sides.

Figures 4-35a) and 4-35b) show exactly such a switch in the mean pressure measured at these locations, thus indicating that a switch in the flow had taken place. Figure 4-35a) shows a pressure-time history for $\theta = 210°$ indicating a switch from left-handedness (high pressure) to right handedness (low pressure) and Figure 4-35b) shows the opposite switch in a pressure-time history for $\theta = 150°$. It was also apparent that a minimum strength of disturbance was required to cause a switch. The strength of disturbance was controlled by the amount of plywood sheet introduced to the flow and by the duration over which the disturbance was allowed to occur. The two superposed time histories seen in Figure 4-35d) represent two switch attempts: the red trace represents a failed attempt and the green, a successful one. Looking at this figure, it seems that a certain pressure drop is required at the measurement point during the disturbance in order to cause the switch – the pressure drop caused by the disturbance in the failed attempt in the figure is noticeably lower than that for the successful attempt.

Although disturbing the flow on the same side as that of the trailing vortex (same-handed disturbance) was sometimes successful at causing a wake flow switch, it was not possible to cause such a switch by disturbing the flow on the opposite side as

that of the trailing vortex (off-handed disturbance) regardless of the disturbance strength or duration. Evidence for this is seen in the unsuccessful flow switch attempt using the "off-handed" disturbance method seen in Figure 4-35c) at approximately 12 seconds followed by a successful switch caused by a "same-handed" disturbance at about 27 seconds. Though these two disturbances were of the same strength and duration, only one the "same-handed" attempt was able to cause the wake flow to switch.

Both the amount of blockage caused by the plywood board and the duration of this disturbance are variables which influence the pressure drop caused by the disturbance: a larger blockage increases the pressure drop as does a longer disturbance duration. An experiment was devised to examine the required blockage and disturbance duration to cause switching: by varying the amount of board introduced into the external flow and the duration of this disturbance, a rough idea of the conditions required for switching was obtained.

The results of this experiment are presented in tabular form below:

Blockage Ratio	Exposed board area (m^2) \ Duration (s)	1 s	3 s
7.2%	0.009	N	N
14.4%	0.018	N	Y
21.6%	0.027	N	Y
28.8%	0.036	N	Y
36.0%	0.045	Y	Y

Table 4-6 – Results of experiment varying the amount of a same-handed upstream disturbance as related to wake flow switching for h/D = 0.47. Cells filled with "N" indicate a failed switch attempt, "Y" indicates a successful attempt.

As shown in the table, successful flow switches were made for 1 second disturbances with 0.045 m^2 blockage area, and 3 second disturbances for a blockage area of 0.018 m^2 and greater. It is believed that this is due to the greater pressure drop induced for longer disturbances. The blockage ratio is also included in the table

showing the blockage area as a percentage of the total working section cross-sectional area.

By blocking the flow on the side of the tunnel with the asymmetric feature it is possible that the reduced external flow on this side is no longer able to supply the cavity with the energy required to allow the trailing vortex to be located on that side of the cavity. When the disturbance is applied, the mean flow structure in the cavity likely switches and once the disturbance is removed, the vortex shedding continues to occur on this side of the cavity and is stabilized until another large disturbance of this sort is applied to this side.

This final state of this vortex tube seems marginally stable to disturbance due to the fact that a large directional disturbance would be required to shift the vortex tube to the other side of the cavity so as to change the handedness of the asymmetry. The handedness of the asymmetry was never observed to change in the presence of naturally-present perturbations in stable turbulent boundary layer flow, as was the case for the present experiment, this flow switch requires a directionally placed disturbance with a minimum pressure drop of Cp = 0.4 (for present experiment) on the side of the cavity with the trailing vortex.

The frequency of oscillations in surface pressures at the cavity surfaces and velocities in the cavity wake for this cavity configuration and others are considered in part to further understand the differences between the flow at this configuration of h/D = 0.47 and the flow at other depths.

4.6 Frequency Analysis

4.6.1 Oscillation Frequencies Predicted by Theory

As discussed in the introduction chapter, mechanisms that are likely to cause cavity oscillation for the present experiment are fluid-dynamic and fluid-resonant sources.

The oscillations due to the fluid-resonant mechanism are dependent on cavity depth and can be predicted with the equation listed below.

$$\boxed{f = \frac{Nc}{4(h + 0.3D)}}$$

The appropriate values pertinent to this equation for the present experiment are: c = 348 m/s, h = 0.0152, 0.0357 or 0.0532 m (depending on cavity depth settings of h/D = 0.2, 0.47 and 0.70, respectively), D = 0.076 m, yielding predicted frequencies of 2329 Hz, 1512 Hz and 1164 Hz for first mode oscillation for h/D = 0.2, 0.47 and 0.7, respectively.

The oscillations due to the fluid dynamic mechanism, specifically feedback resonance, are independent of cavity depth and are predicted by Rossiter's formula, listed below.

$$\boxed{\frac{fD}{U_0} = \frac{m - \gamma}{M + 1/\kappa}}$$

The appropriate values to be substituted for this equation are γ = 0.25, $1/\kappa$ = 1.754 and M = 0.077, and predict a frequency of 145.5 Hz for first mode oscillation for all cavity depths.

4.6.2 Surface Pressure Fluctuation Frequency Analysis

Time histories were also captured for pressure and microphone measurements thus allowing Power Spectral Density plots to be created for these data as well. The microphones had very weak response below about 50 Hz and thus did not capture

low-frequency frequency features well. The pressure transducers used in experiment have a strong response from 0 -100 Hz which begins to fall off around 100 Hz.

Microphone Frequency Analysis

Although the microphone measurements did not prove to be useful for quantitative RMS pressure comparisons, these devices were an excellent tool for examining the Power Spectral Density plots at high frequency at various points on the model. The power spectral density plots displayed in the figures below were calculated by subtracting the "no-cavity" case from the cavity cases in order to clarify the effect of the cavity presence on pressure fluctuations.

Major peaks observed in the Power Spectral Density plots, not explainable by ambient tunnel noise, presented in Figures 4-36 to 4-40 are shown in Tables 4-7 to 4-9 below.

Peak Number	h/D = 0.20	h/D = 0.47	h/D = 0.70
1	105 Hz	82 Hz	155 Hz
2	128 Hz	147.5 Hz	825 – 1000 Hz
3		1320 Hz	985 Hz
4		1370 Hz	1115 Hz
5		1545 Hz	1250 Hz

Table 4-7 – Noted peaks in the power spectral density plots calculated from microphone time series data recorded at the centre of the cavity base.

Peak Number	h/D = 0.20	h/D = 0.47	h/D = 0.70
1	50 – 750 Hz	50 – 750 Hz	50 – 500 Hz
2		40 Hz	36 Hz
3		89 Hz	70 Hz
4		143.5 Hz	104 Hz
5		159 Hz	140.5 Hz
6		1000 Hz	154.5 Hz
7		1140 – 1405 Hz	760 – 1370 Hz
8		1285 Hz	1480 Hz
9		1320 Hz	2960 Hz
10		1375 Hz	

Table 4-8 – Noted peaks in the power spectral density plots calculated from microphone time series data recorded on the cavity base, r = 0.37D from its centre at θ = 170 degrees.

Peak Number	h/D = 0.20	h/D = 0.47	h/D = 0.70
1	50-700 Hz	50-1500 Hz	50-400 Hz
2	1020 Hz	150 Hz	185 Hz
3		210 Hz	750 – 1350 Hz
4		900 – 1450 Hz	960 Hz
5		1000 Hz	1115 Hz
6		1370 Hz	1250 Hz
7		1545 Hz	

Table 4-9 – Noted peaks in the power spectral density plots calculated from microphone time series data recorded on the cavity sidewall, y = 0.17D from the cavity lip at θ = 180 degrees.

From the plots related to the microphone located at the centre of the cavity bottom, the wide-band PSD shows a relatively small amount of energy in the lower part of the spectrum, with most of the displayed energy captured in a band from about 750 – 1750 Hz. The similarity between the plots for h/D = 0.47 and 0.70 in this high range may indicate that they are part of a flow regime that is different from that for the h/D = 0.20 case, as suggested by previous investigators (Hiwada et. al., 1983). The section in the 0.47 plot from roughly 900 – 1450 Hz is very similar in trend to the section in the 0.70 plot from roughly 750 – 1350 Hz suggesting that these peaks are related to cavity geometry, such that 0.70, being deeper than 0.47, shifts this resonant band of frequencies to a slightly lower frequency band.

Since these peaks in the high frequency band are seen only in the deeper cavities, and since at the deeper cavities the peaks vary with depth, these peaks are likely generated by fluid-resonant mechanisms. This would also explain why peaks were not seen in this range in the fluctuating velocity spectra, as those spectra would only display fluid-dynamic fluctuations. Large broad peaks are centred at 1550 Hz for h/D = 0.47 and 1140 Hz for h/D = 0.70, corresponding quite well to the predictions from Section 4.6.1, relating to air-column vibration. Other large peaks in this range are likely driven by tunnel noise sources and amplified in the cavity. An exhaustive list of measured tunnel noise sources is listed in Appendices D and N.

Due to the relative shallowness of the tested cavities, the lower frequency peaks (< 750 Hz) are likely due to purely fluid-dynamic mechanisms or the tunnel noise sources as listed in Appendix D. For the microphone centred on the cavity base, with related plots presented in Figures 4-36 and 4-37, strong broad peaks are seen in the low-frequency range for h/D = 0.20 and 0.47 with peaks at 105 and 128 Hz for h/D = 0.20, and 82 Hz and possibly approx. 105 Hz for h/D = 0.47, most likely due to the circulation of fluid in the cavity's strong recirculating vortex. A similar peak is

not noted at a lower frequency in the h/D = 0.70 case due to the much smaller amount of fluid pulled into the cavity at this depth, thus decreasing the strength of the circulation therein.

A strong peak is seen at 147.5 Hz for the h/D = 0.47 case, and a much weaker one is seen at 155 Hz for h/D = 0.70. For the h/D = 0.47 case, this peak is attributable to cavity feedback resonance as discussed previously, and it is possible that this is also the case for the 0.70 case, but possibly the geometry does not allow for sufficient instability in the covering shear layer to set up a truly strong feedback mechanism as observed for the h/D = 0.47 case. This common peak between the 0.47 and 0.70 cases may relate to the observation by Hiwada et. al. (1983) that these two configurations are both part of the same flow regime: the "switch" regime as termed by these investigators.

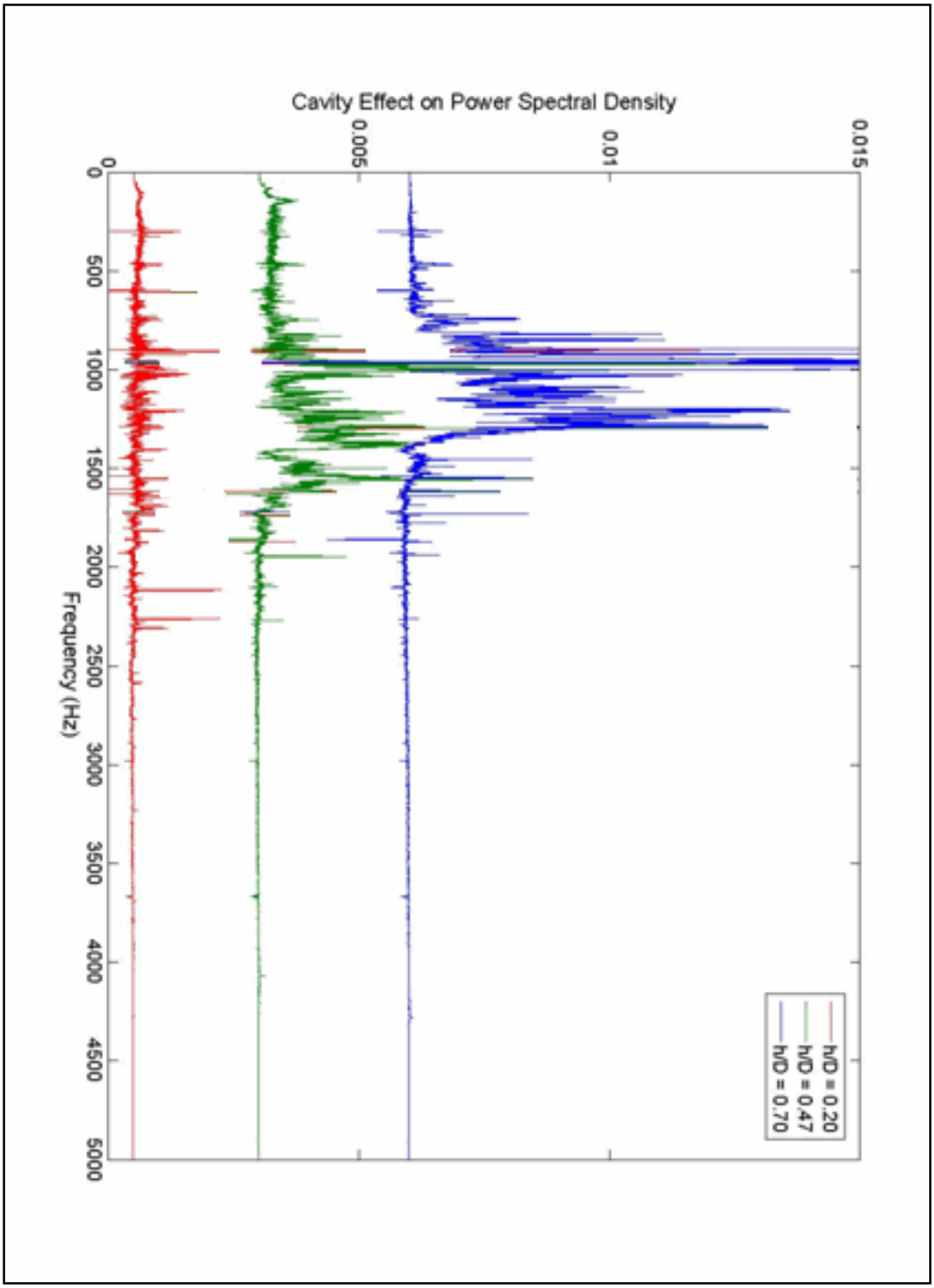

Figure 4-36 – Wide-band normalized power spectral density plot for microphone at centre of cavity base for various cavity configurations (traces offset by 0.003 for clarity).

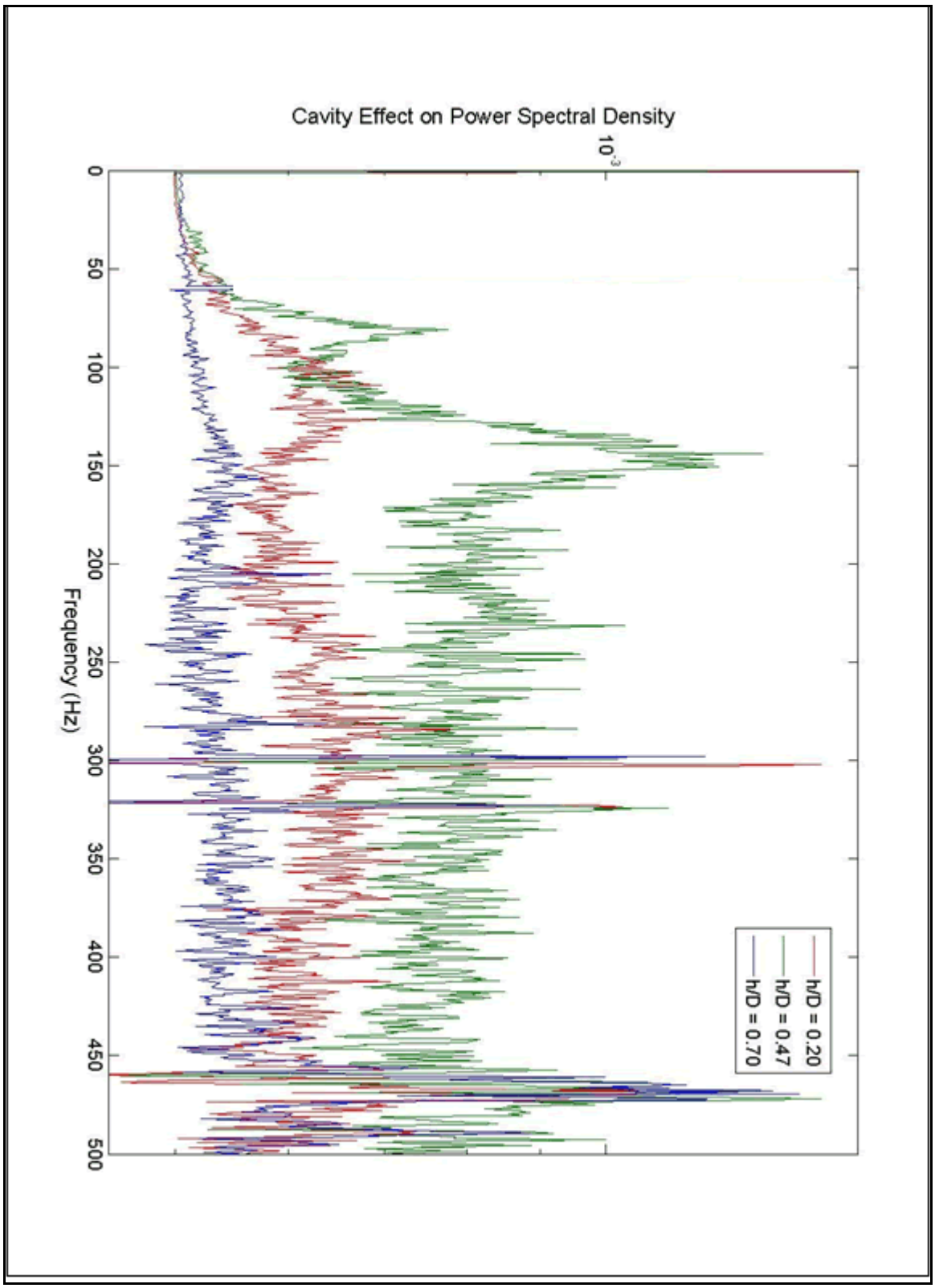

Figure 4-37 – Normalized narrow-band power spectral density plot for microphone at centre of cavity base for various depth configurations. Plots are superposed to show relative energy levels between depth configurations

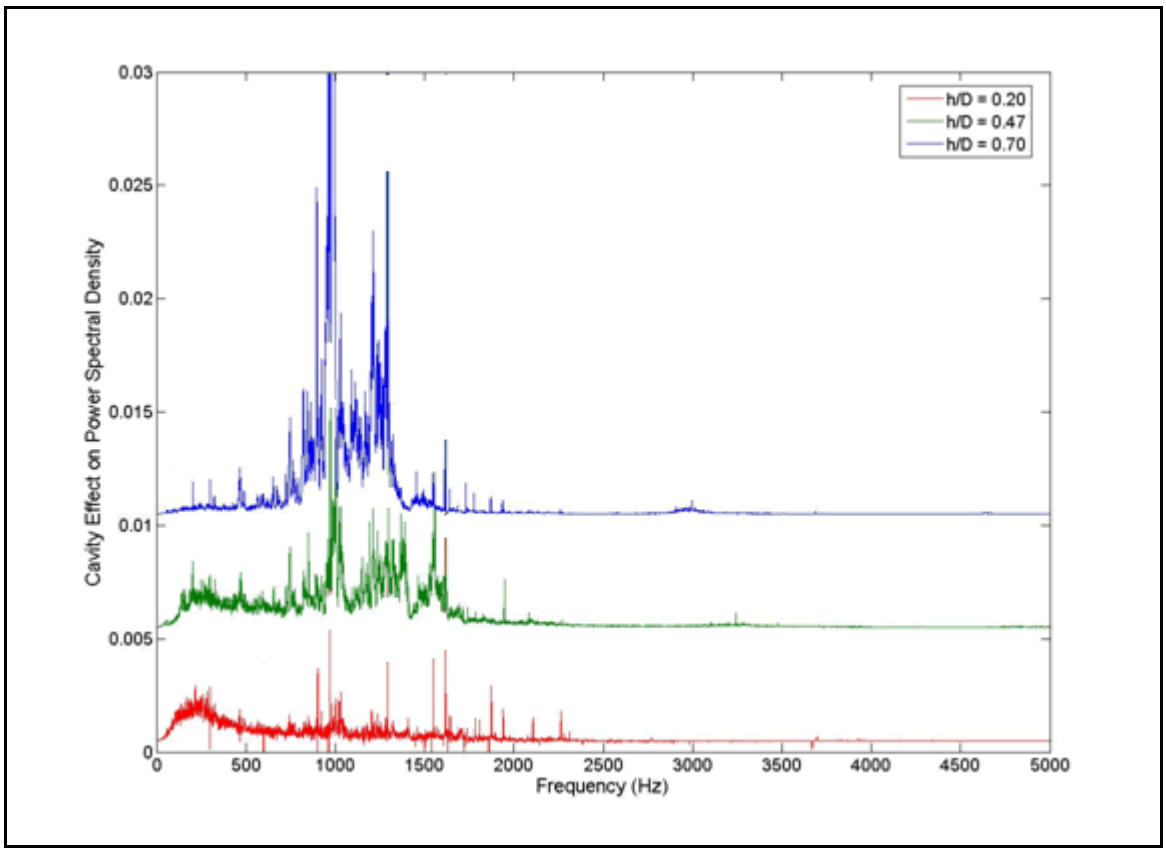

Figure 4-38 – Normalized narrow-band power spectral density plot for microphone on cavity base at r = 0.37D and θ = 170° for various depth configurations. (traces offset by 0.003 for clarity)

For the plot related to the microphone near the edge of the cavity base at $\theta = 170°$ (Figure 4-38) , h/D = 0.20 and 0.47 show a much larger amount of low frequency noise over a wide band due to the large turbulent fluid brought into the cavity in these cases and stagnating on the cavity bottom. For the 0.20 case, evidence of fluctuation due to cavity vortex circulation is drowned out by this stagnating turbulent external fluid, while it is still possible to make out this circulation frequency for the 0.47 due to the slightly lower amount of turbulent fluid stagnation on the cavity bottom as a result of the cavity's greater depth in this case, the peak due to cavity feedback resonance is once again detected by this microphone. Due to the depth of the cavity for h/D = 0.70, far less fluid is pulled into the cavity and far less makes it to this point on the cavity base to contribute to the low-band frequencies.

Similar phenomena are noted for the case of the microphone on the cavity sidewall, with related plot displayed in Figure 4-40, in this case, a very large amount of turbulent kinetic energy is displayed, concealing higher frequency features up to about 1500 Hz for h/D = 0.47, asserting more evidence for the greatest amount of turbulent fluid brought into the cavity at this configuration. The h/D = 0.20 case also shows a great deal of fluid dynamic fluctuation up to about 700 Hz and h/D = 0.70 also shows some fluid dynamic fluctuation at this point since it is near the downstream lip of the cavity.

A plot related to microphone measurements taken on the cavity base near the upstream wall at $\theta = 10°$ is shown in Figures 4-39 to show yet another difference between the h/D = 0.47 case and other configurations. Virtually no low-frequency peaks in the fluctuation are seen for h/D = 0.20 and 0.70, but two significant features are seen in this low-frequency range for h/D = 0.47 due to the microphone's proximity to the part of the cavity's large and strong vortex tube rooted to the cavity base near this point. These peaks are centred at 87 Hz, about 170 Hz, and 245 Hz, and it is presumed that these frequencies are related to circulation frequencies pertaining to different parts of this large vortex tube in the cavity at this configuration.

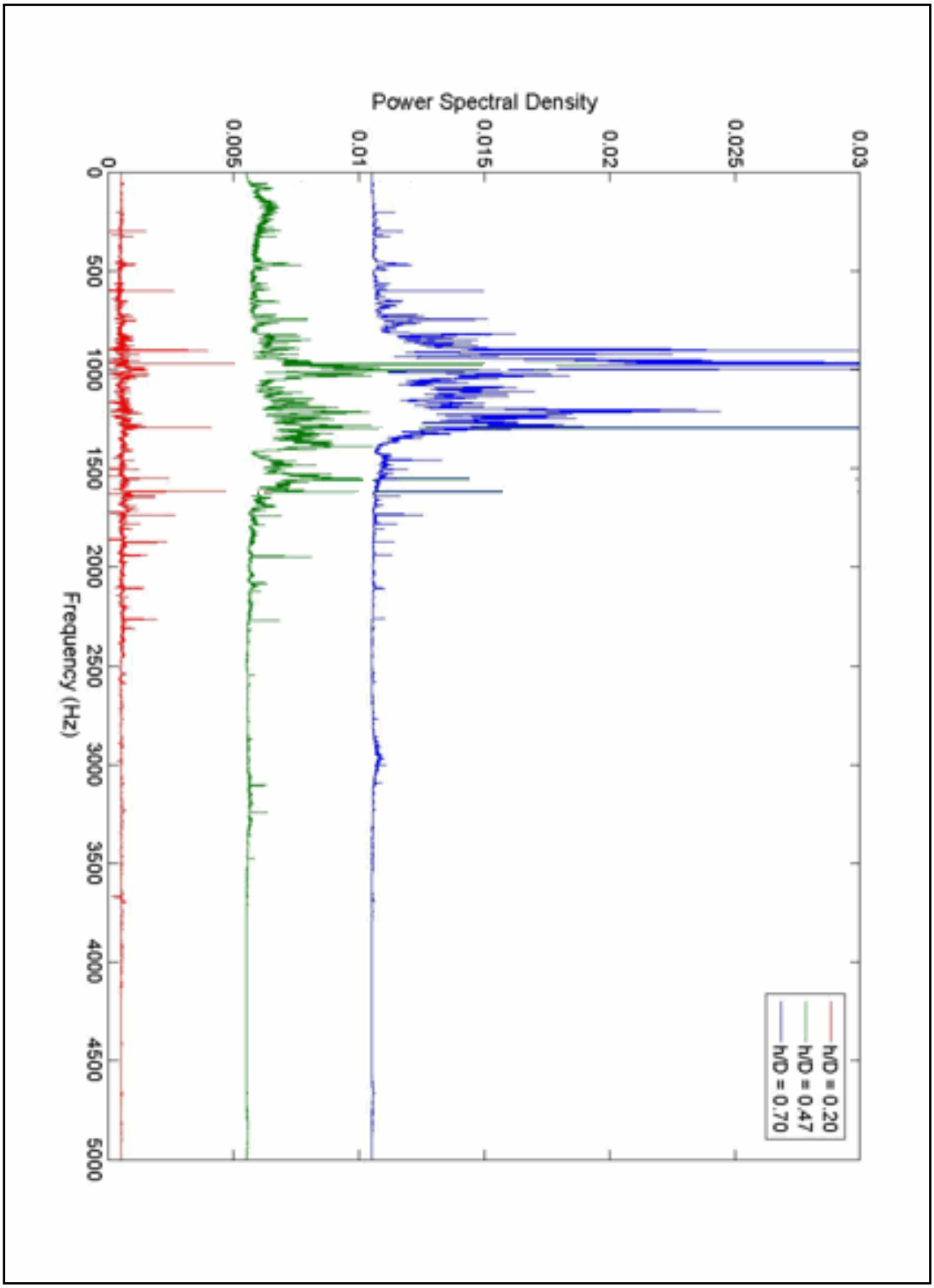

Figure 4-39 – Normalized narrow-band power spectral density plot for microphone on cavity base at r = 0.37D and θ = 10° for various depth configurations (traces offset by 0.003 for clarity).

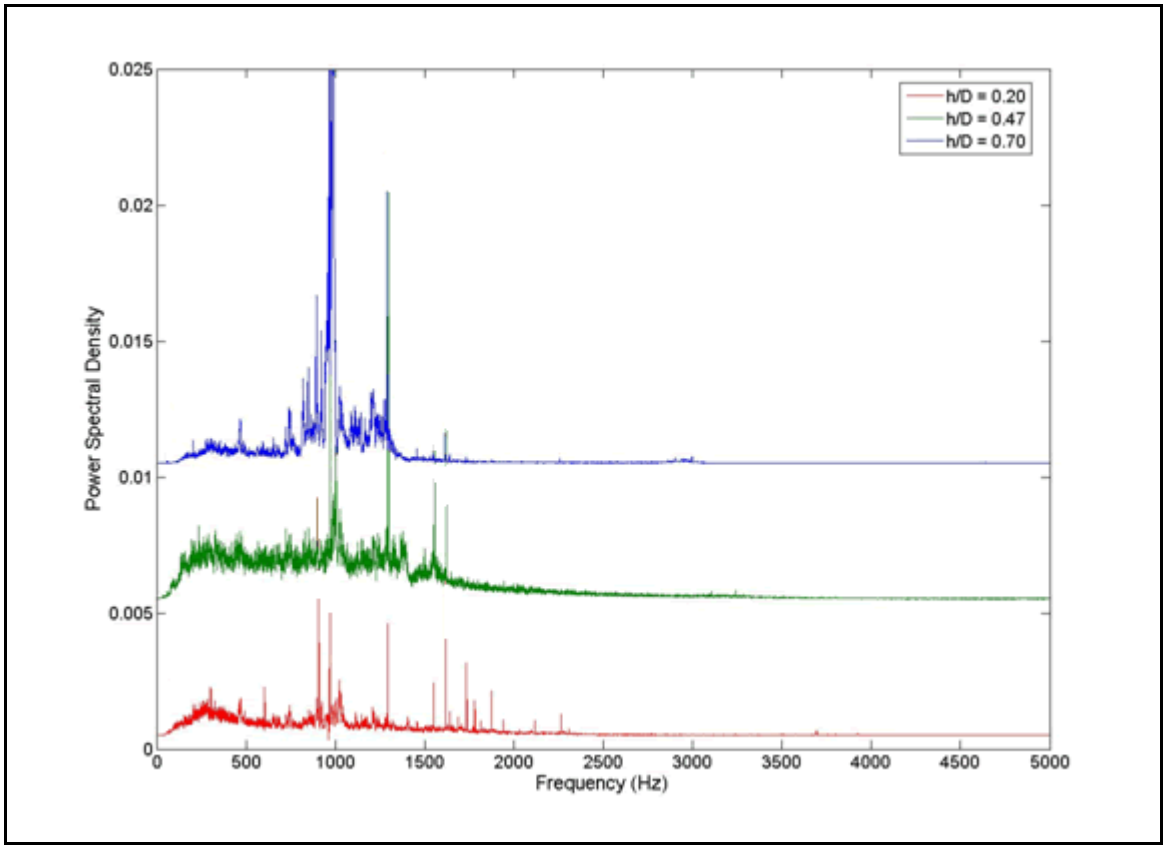

Figure 4-40 – Normalized narrow-band power spectral density plot for microphone on cavity sidewall at θ = 180° and y = 0.167D from cavity lip for various depth configurations (traces offset by 0.003 for clarity).

Pressure Transducer Frequency Analysis

Frequency analysis of the pressure transducer has yielded more information regarding the contribution of the cavity model presence to low-frequency oscillation at various depth configurations. Power spectral density plots are presented in Figures 4-41 to 4-43, relating to surface pressure data acquired on the cavity sidewall at pts. 0.013D (1 mm) and 0.167D (12.7 mm) from the cavity rim for $\theta = 180°$ and on the cavity turntable 0.013D (1 mm) from the downstream cavity lip for $\theta = 180°$.

Tables reporting notable peaks in these PSD's are presented below in Tables 4-10 to 4-12.

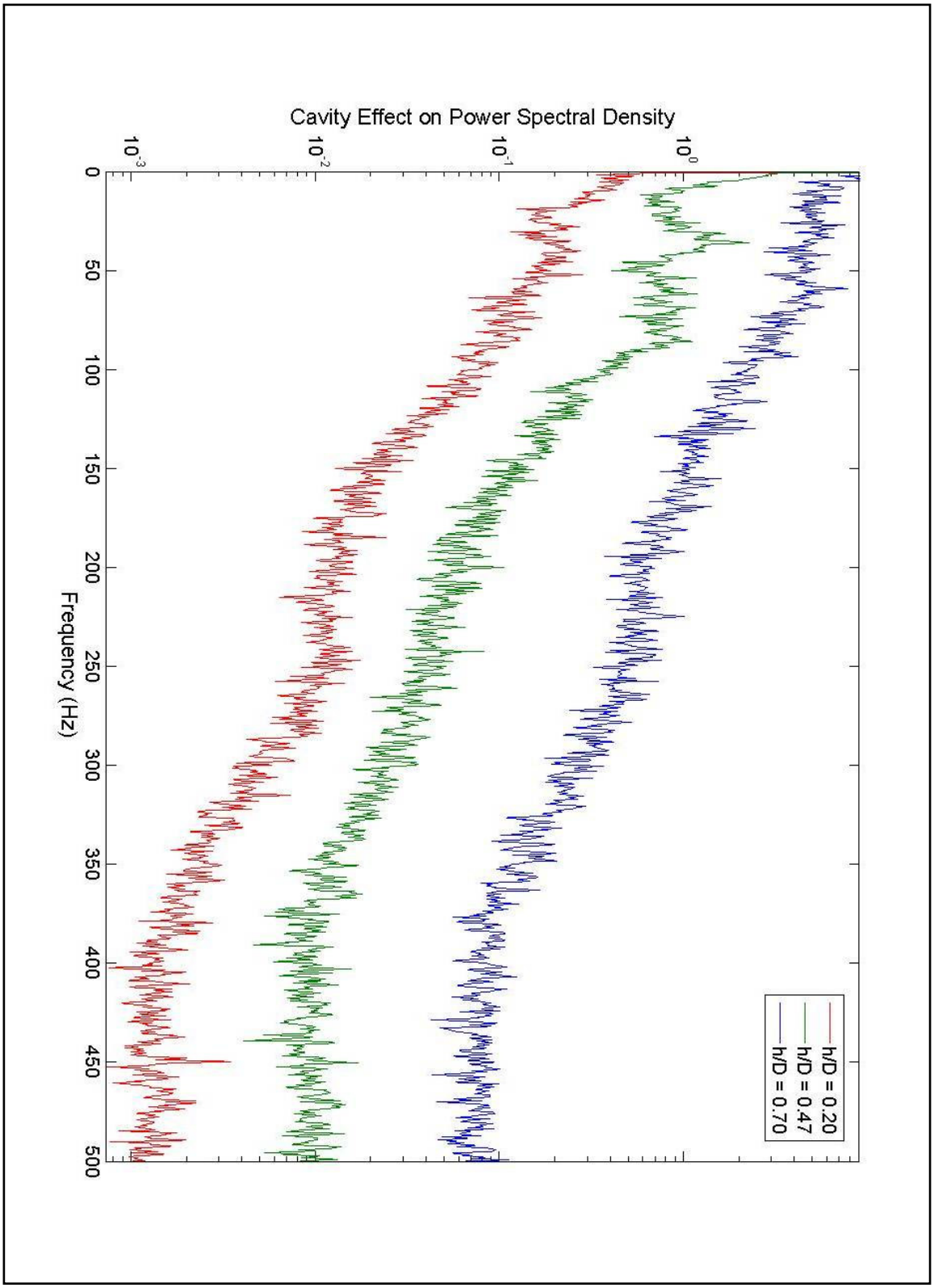

Figure 4-41 – Wide-band power spectral density plot of data from sidewall pressure tap at $\theta = 180^\circ$ and y = 0.013D from cavity lip for various depth configurations (traces offset by one order of magnitude for clarity).

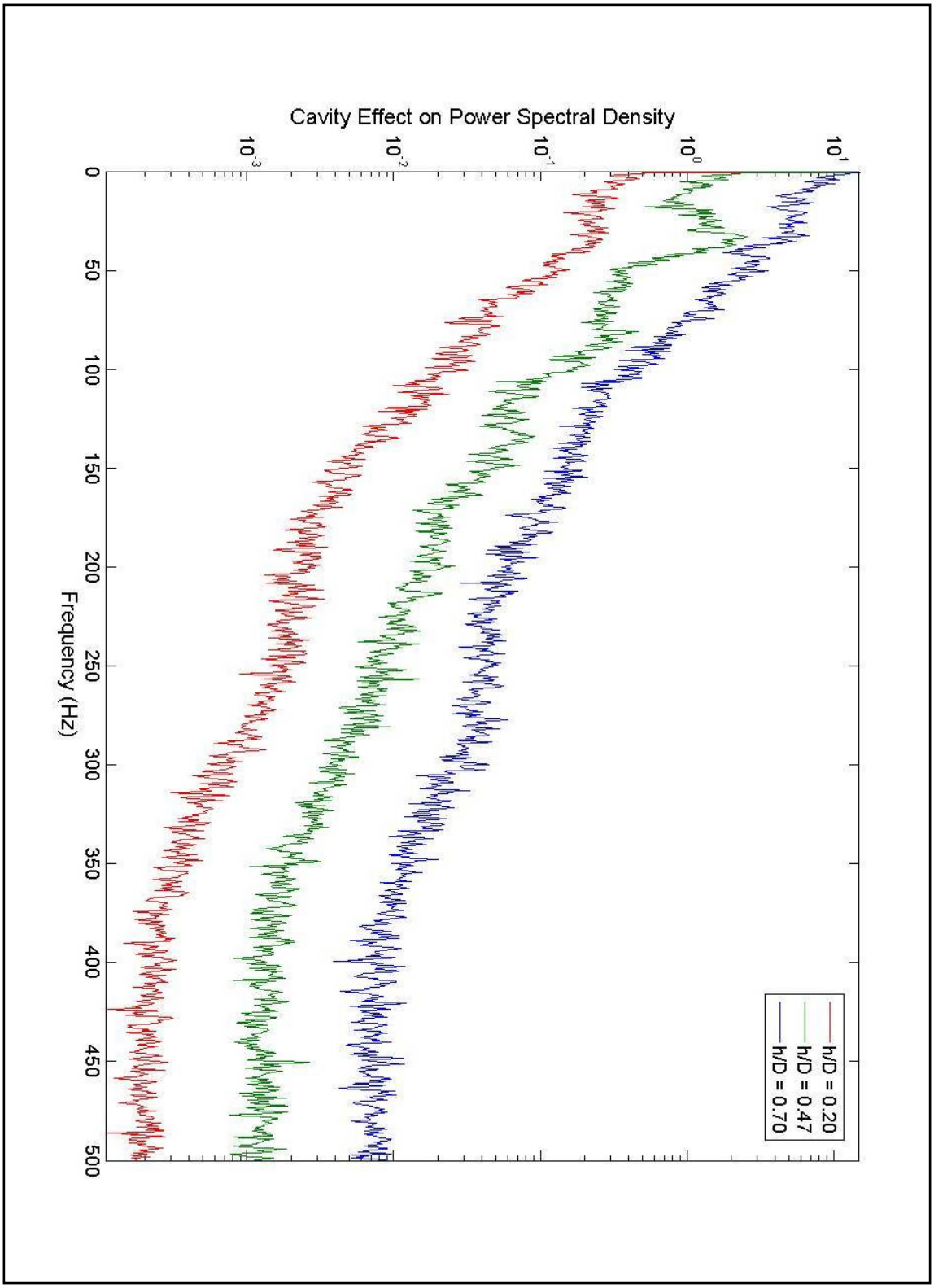

Figure 4-42 – Wide-band power spectral density plot of data from turntable pressure tap at θ = 180° and 0.013D from cavity downstream edge for various depth configurations (traces offset by one order of magnitude for clarity).

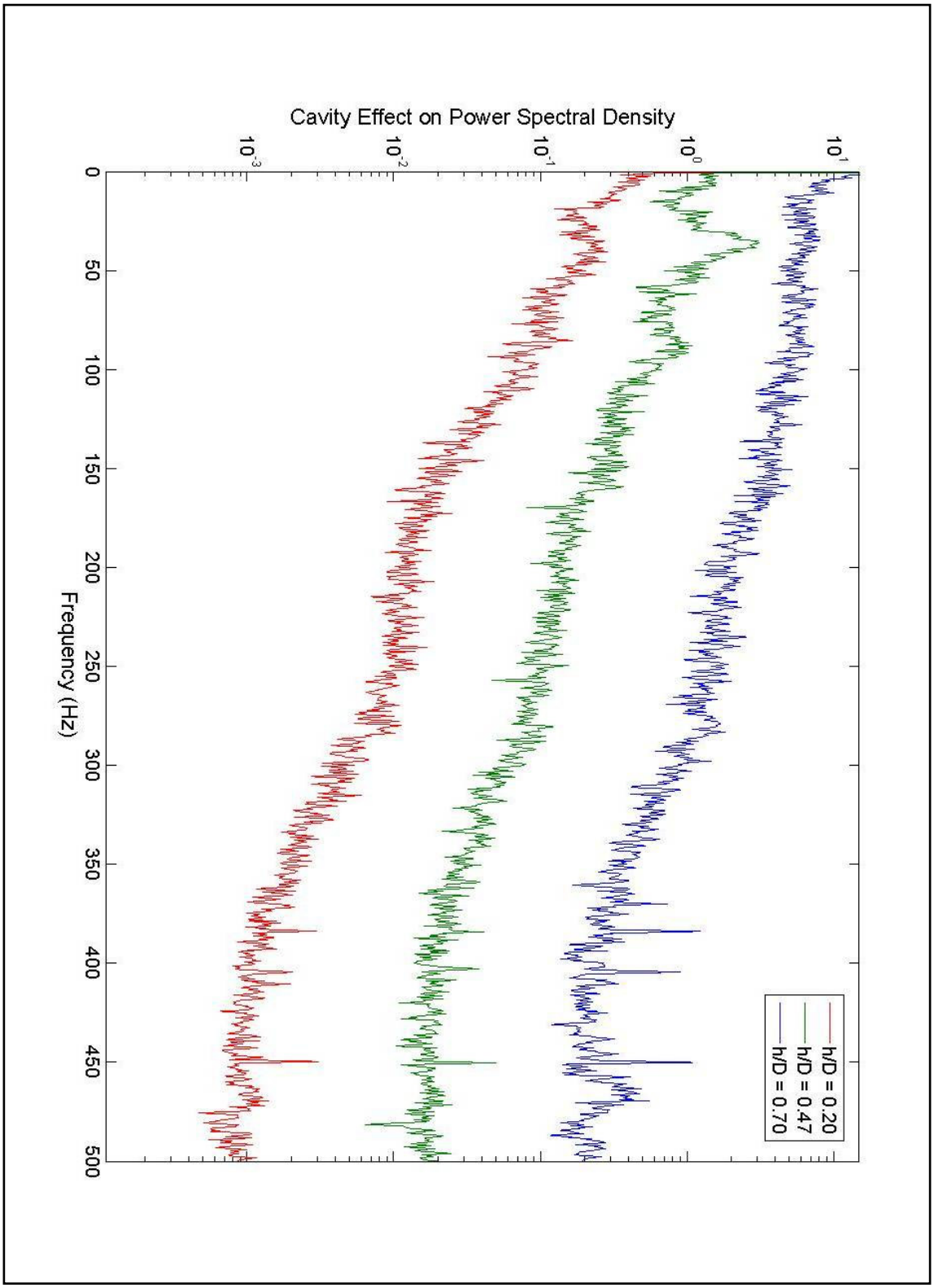

Figure 4-43 – Wide-band power spectral density plot of data from sidewall pressure tap at $\theta = 180^{\circ}$ and y = 0.191D from cavity lip for various depth configurations (traces offset by one order of magnitude for clarity).

Peak Number	h/D = 0.20	h/D = 0.47	h/D = 0.70
1	42 Hz	37 Hz	31 Hz
2		86 Hz	59 Hz
3		120 Hz	
4		140 Hz	
5		150 Hz	

Table 4-10 – Noted peaks in the power spectral density plots calculated from pressure transducer time series data recorded on the cavity sidewall 0.013D from cavity rim at θ = 180 degrees.

Peak Number	h/D = 0.20	h/D = 0.47	h/D = 0.70
1	37 Hz	27 Hz	36 Hz
2		36 Hz	50 Hz
3		86 Hz	
4		148 Hz	

Table 4-11 – Noted peaks in the power spectral density plots calculated from pressure transducer time series data recorded on the cavity turntable in the wake 0.013D from the cavity rim at θ = 180 degrees.

Peak Number	h/D = 0.20	h/D = 0.47	h/D = 0.70
1	45 Hz	7 Hz	37 Hz
2	86 Hz	37 Hz	
3		88 Hz	
4		130 Hz	
5		150 Hz	

Table 4-12 – Notable peaks from PSD's representing fluctuations in pressure-time series captured by pressure transducer 0.191D from cavity downstream edge for θ = 180°

From these plots it seems that the pressure transducers were most effective at capturing lower frequencies (< 100 Hz) and, hence, the overlap between the frequency data from the transducer data and the microphone data is limited. Repeated peaks noted in the spectra as listed in Tables 4-10 to 4-12. Peaks near 150 Hz were noted (though weakly) in the spectra for h/D = 0.47, showing agreement

with the spectra generated from microphone data at the same configuration. Strong peaks near 40 Hz and 90 Hz for h/D = 0.47 are thought to be linked to the much higher fluid entrainment (as evidenced by the high cavity drag for this configuration) by the cavity and hence higher energy fluid is circulated in the cavity at this depth as compared to others. For this reason it is thought that these two peaks are related to the circulation frequency of fluid in the cavity at this depth.

Strong peaks were not noted for the other two cavity depths of h/D = 0.20 and 0.70 in the range of frequencies measured by the transducers, however a much greater amount of turbulent kinetic energy is observed in the lower frequency band from 0-50 Hz for the h/D = 0.20 case than for the 0.70 case, as noted in the microphone spectra.

4.6.3 Frequency Analysis of Velocity Fluctuations in the Cavity Wake

Power Spectral Density plots were generated using U-component and W-component velocity data taken at Points 3, 7 and 25, marked in the grid in Figure 4-44, for h/D = 0.00 (no cavity), 0.20, 0.47 left-handed (0.47L) and 0.47 right-handed (0.47R), to examine the distribution of fluctuating velocity at these points. These points were chosen according to maximum values for the RMS velocity at these locations for various configurations. The base 10 logarithm of the power spectral density was taken for the velocity-time series at these points. Once again, the effect of the cavity presence was of interest and, hence, the base 10 logarithm of the power spectral density of the "no-cavity" case at these same points was subtracted from the cavity cases such that the effect of the cavity could be seen more clearly. These plots are presented in Figures 4-45 to 4-50 and, although they are generally useful for demonstrating the difference between the turbulent kinetic energy generated at different cavity configurations, very few distinct peaks are notable in these distributions and, hence, the plots for the various test configurations have been

superposed in the figures. In all cases, distinct peaks were only discernable in plots for h/D = 0.47.

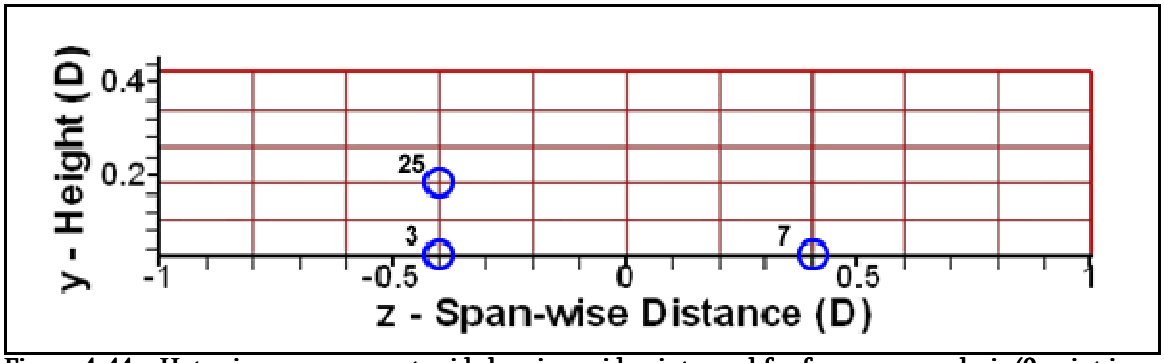

Figure 4-44 – Hot-wire measurement grid showing grid points used for frequency analysis (0 point in y-Height axis = ground plane).

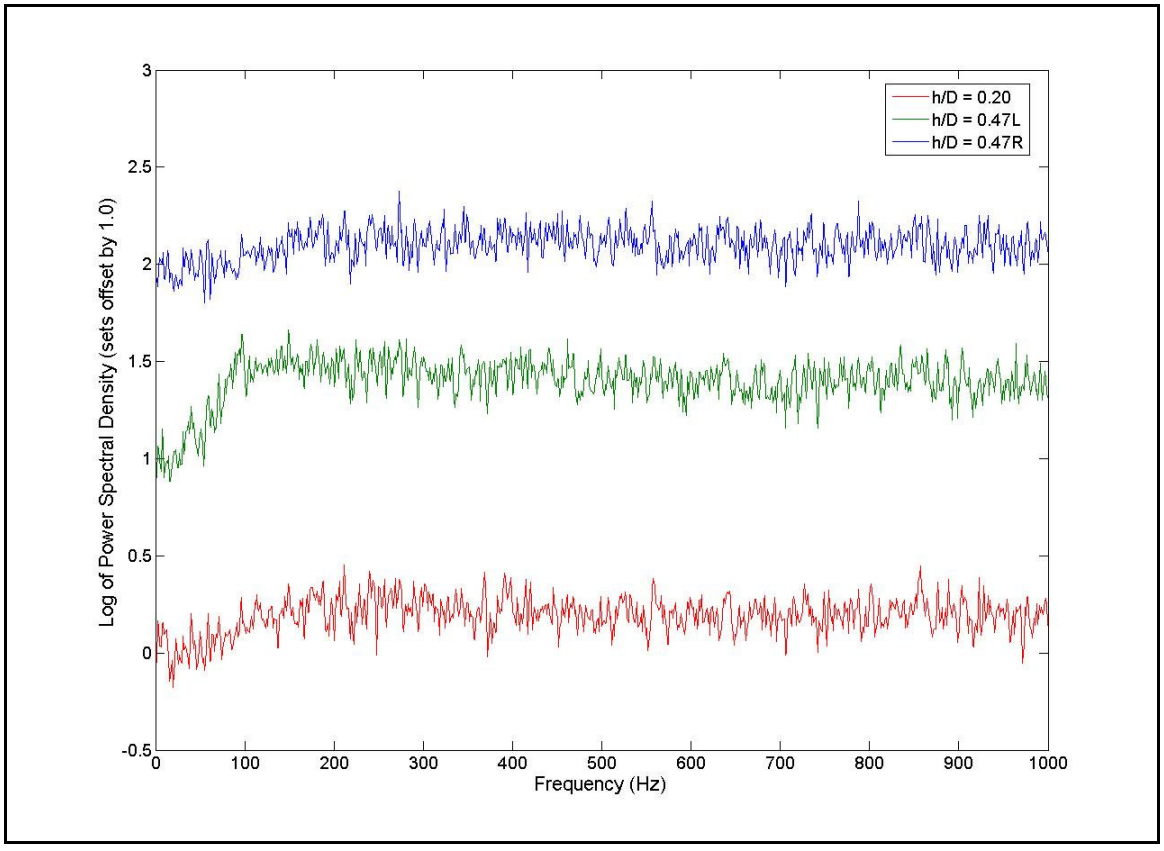

Figure 4-45 – Power Spectral Density of Stream-wise velocity-time series at Point 3 in the measurement grid for various cavity configurations.

Fan and wind tunnel-related noise sources were noted in most of the frequency spectra and though these are discussed at length in Appendices D and N, the most dominant of these sources occurred at 205, 407 and 570 Hz (all related to wind tunnel geometry) and peaks were also noted at 300 and 320 Hz (due to the wind tunnel fans blade passing frequencies). Due to the fact that peaks in the power spectral density at these frequencies are noise and not of interest to the present investigation, these will not be discussed further in the analysis.

Point 3 is located near the middle of the grid's left side close to the ground plane and is in the region of the trailing vortex for the h/D = 0.47 left-handed case (denoted by h/D = 0.47L), plots related to this point are presented in Figures 4-45 and 4-46. The h/D = 0.47L case (green trace) shows an increase in energy relative to the other traces across the measured frequency spectrum for the span-wise direction (Figure 4-46) and from 50 Hz to the highest resolved frequency for the stream-wise direction (Figure 4-45). In addition to the general increase in turbulent kinetic energy in the frequency bands discussed above, the 0.47L case displayed a few small peaks in the spectrum at approximately 40, 100 and 150 Hz. The peaks at 40 and 100 Hz are likely due to the recirculation of the trailing vortex driven by the flow into the cavity while it is possible that the peaks noted at approximately 150 Hz are attributable to the cavity feedback resonance mechanism, being very close to the predicted frequency of 145.5 Hz for this mechanism. A list of discernible peaks in this spectrum and the others analyzed here is included in Table 4-13. From this table, the only repeated peaks in the spectra are in a range from 85-97 Hz and 145-152 Hz. It should be restated that although these peaks are visible in the spectra of consideration, they are by no means strong peaks.

The h/D = 0.20 case shows a lesser broadband energy increase beginning near 100 Hz for both directions due to the point's location inside the left hand side of the main feature in the turbulent wake for h/D = 0.20. Point 3 in the h/D = 0.47R profile,

meanwhile, is in a region of the turbulent wake less affected by the cavity trailing vortex and hence displays little turbulent kinetic energy in either direction.

Point 7, being offset an equal horizontal distance from z = 0 as Point 3 on the opposite side, would be expected to have h/D = 0.47R distributions similar to the h/D = 0.47L distributions observed at Point 3, due to Point 7's location inside the wake for the right-handed case, assuming a perfectly symmetrical wake switch. Although the h/D = 0.47R case (blue trace) exhibits the highest overall fluctuating energy level across the spectrum as compared to the other cavity configurations, the general energy increase for the U-component velocity is not as high as the same for the Point 3 case. The difference between Figures 4-28b and 4-28c hints at the reason for this observed difference between the 0.47R and 0.47L cases in this situation. Figures 4-28b and 4-28c represent the same data as are traced in the power spectral density distributions for h/D = 0.47L and h/D = 0.47R, respectively, and thus by examining the U_{rms} value at Point 3 (z = -0.4D, y = 0.03D) in Figure 4-28b as compared to that at Point 7 (z = +0.4D, y = 0.03D) in Figure 4-28c, it is clear that Point 3 for h/D = 0.47L was located in a more turbulent region of the wake than was Point 7 for h/D = 0.47R. Since Figures 4-28b and 4-28c show cross-sections of the trailing vortex in the cavity wake, it appears that for the 0.47R case, the tube had migrated slightly higher into the external flow away from the ground plane than had the 0.47L case.

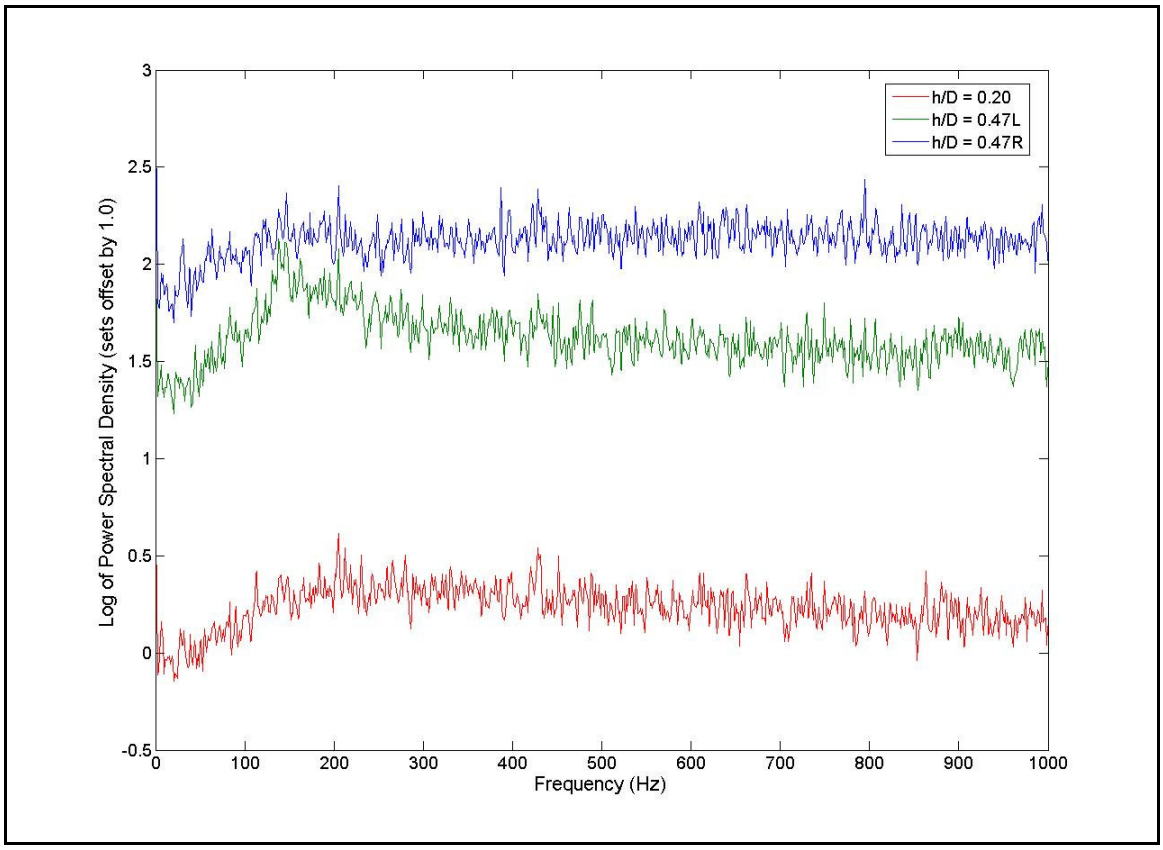

Figure 4-46 – Power Spectral Density of Span-wise velocity-time series at Point 3 in the measurement grid for various cavity configurations.

Plots related to Point 25 in Figures 4-49 and 4-50 once again show large broad increases in the power spectral density for h/D = 0.47 beginning at about 50 Hz for the stream-wise velocity plot and across the whole spectrum for the span-wise case. These broad boosts are due to the location of the measurement point at the most turbulent point of the cavity wake for h/D = 0.47L. Other than showing the extent of the broad band increases mentioned previously, wider frequency range plots, such as the one seen in Appendix L, add very little new information to this analysis and were thus omitted from this discussion.

Discernable peaks found in the distributions are listed in the table below:

Index	Point 3 – U - 0.47L	Point 3 – W – 0.47 L	Point 7 – U – 0.47R	Point 7 – W – 0.47R	Point 25 – U – 0.47L	Point 25 – W – 0.47L
A	40 Hz	145 Hz	85 Hz	149 Hz	90 Hz	152 Hz
B	97 Hz		148 Hz		146 Hz	
C	149 Hz					

Table 4-13 – Peaks discerned from power spectral density plots for points 3, 7 and 25 in the hot-wire measurement grid.

As discussed earlier, although there are peaks in the spectra at about 150 Hz for the h/D = 0.47 cases, no such peaks are observed at h/D = 0.20, and, although no configurations other than h/D = 0.20 and 0.47 were tested in these hot-wire measurements, it is possible that h/D = 0.47 is the only case for which this feedback resonance occurs for circular cavities, and may thus be a reason for why this strongly asymmetry cavity flow is observed at this configuration and no other.

Since a necessary condition for feedback resonance is an unstable shear layer over the cavity mouth, it is possible that the geometric configuration related to h/D = 0.47 causes an unstable shear layer state, thus allowing this type of resonance.

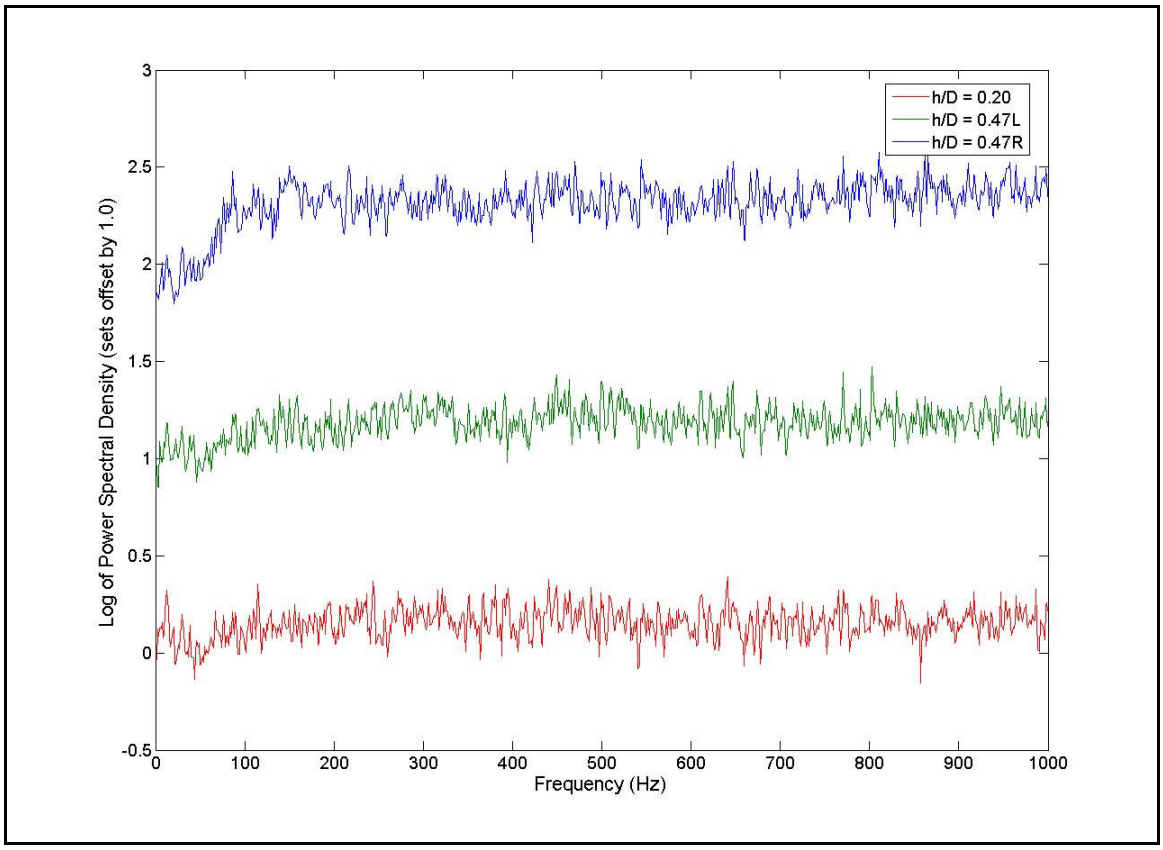

Figure 4-47 – Power Spectral Density of Stream-wise velocity-time series at Point 7 in the measurement grid for various cavity configurations.

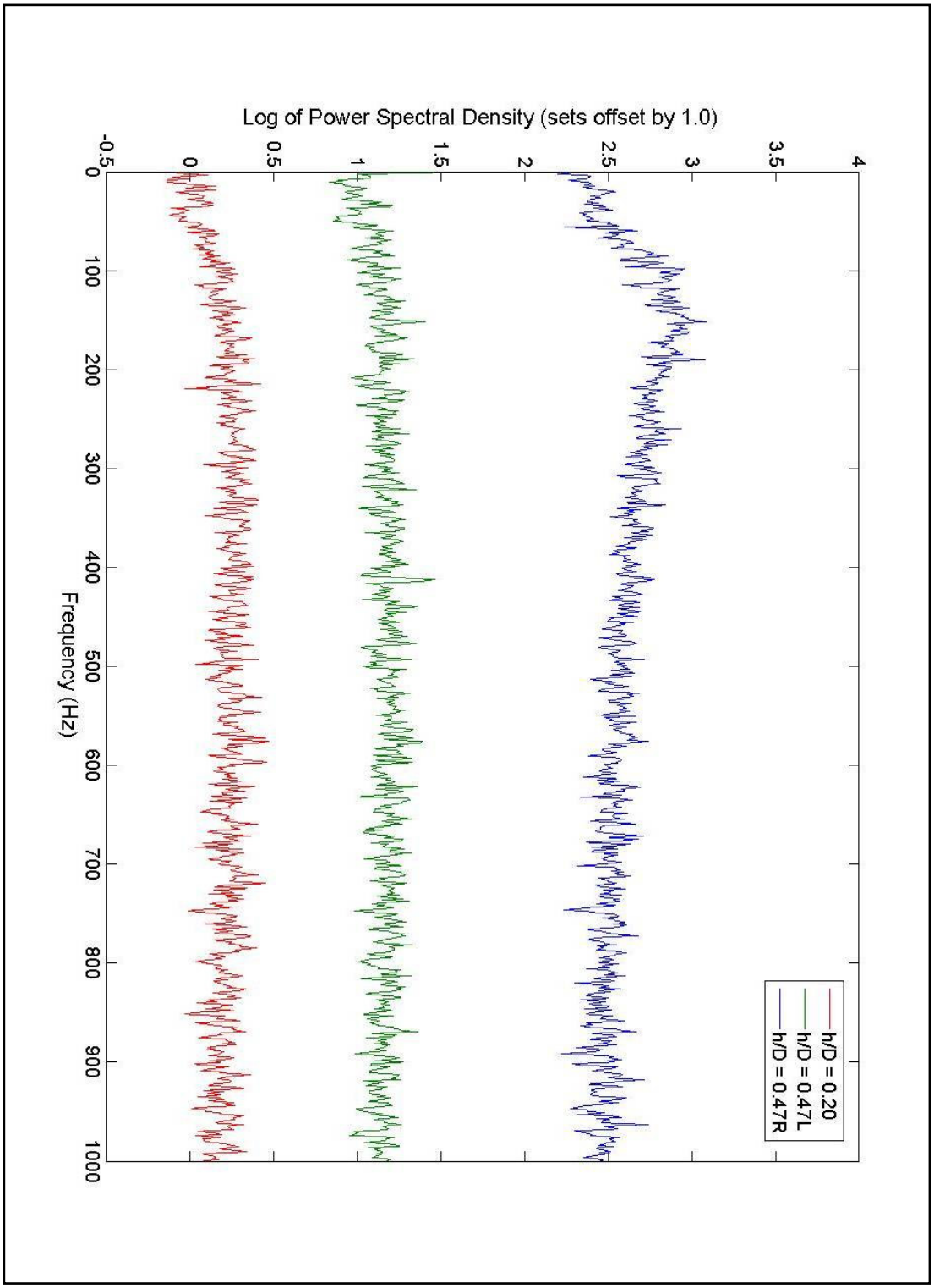

Figure 4-48 – Power Spectral Density of Span-wise velocity-time series at Point 7 in the measurement grid for various cavity configurations.

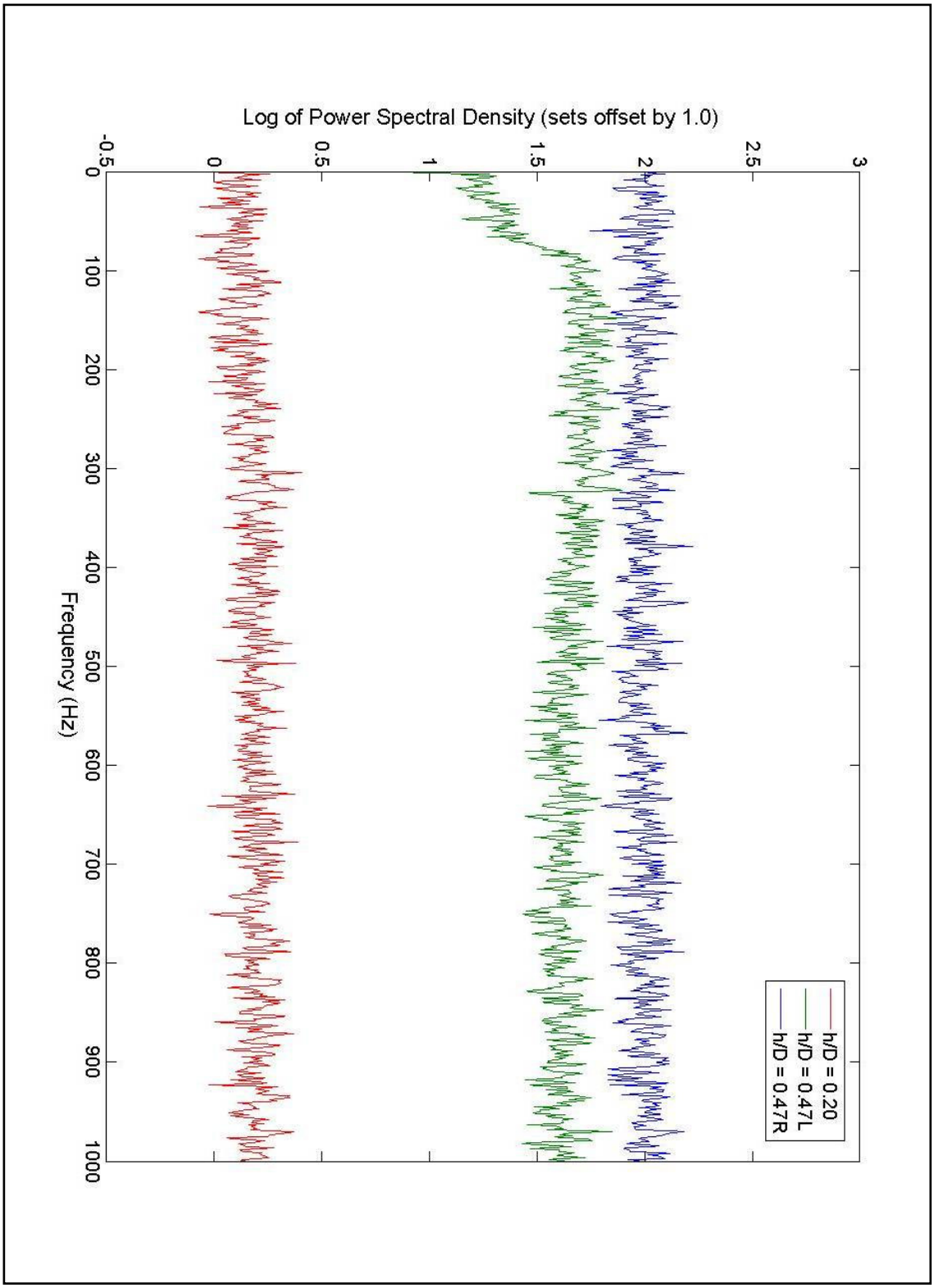

Figure 4-49 – Power Spectral Density of Stream-wise velocity-time series at Point 25 in the measurement grid for various cavity configurations.

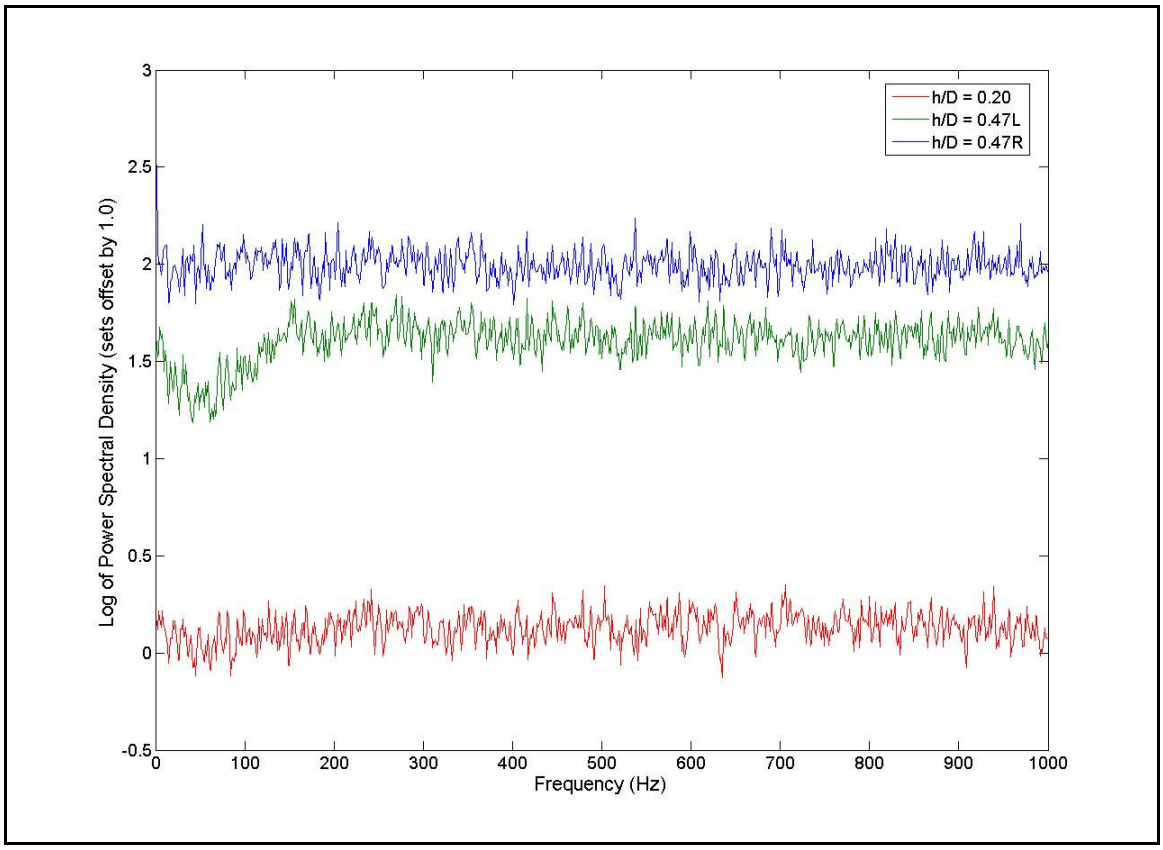

Figure 4-50 – Power Spectral Density of Span-wise velocity-time series at Point 25 in the measurement grid for various cavity configurations.

4.7 Summary

A frequency analysis of pressure fluctuations on the cavity surfaces and velocity fluctuations in the cavity wake has uncovered a very different frequency signature for each of the three cavity depth configurations tested. Microphone measurements showed that when the cavity was set to h/D = 0.47 and 0.70, high energy levels were noted in the higher frequency band of about 750 – 1450 Hz suggesting that these may be due to the fact that the cavity is deep enough at these configurations to undergo depth mode resonance. Spectra generated from the pressure transducer data showed a greater amount of general low frequency fluctuation for the h/D = 0.20 case than for the others, likely due to the large shear

layer impingement zone on the downstream cavity sidewall which, in turn, is due to the cavity's small depth at this configuration.

A peak at 150 Hz noted for h/D = 0.47 was observed in spectra generated from all three different measurement systems, though it was more weak in some than others, suggesting that this is the only configuration for which fluid-resonant oscillation occurs. Further evidence for this fluid-resonant oscillation mechanism for h/D = 0.47 is that Rossiter's equation predicts a first mode cavity resonance frequency at 145.5 Hz. A strong peak near 150 Hz was noted for h/D = 0.47 in some of the microphone spectra, demonstrating a strong acoustic source at this frequency.

5 CONCLUSIONS AND RECOMMENDATIONS

5.1 Overview

Due to the varied nature of the results from the four types of measurements performed in this thesis project, conclusions are divided into sections according to these four measurement types: mean and fluctuating pressure patterns, switching and flapping pressure analysis, cavity wake flow velocity profiles, and frequency analyses.

5.1.1 Mean and Fluctuating Pressure Patterns

As discussed in Section 4.3.3, excellent agreement was noted between previous mean surface pressure patterns and those resulting from the present experiment for cavity depths of 0.20, 0.47 and 0.70D. Integration of surface pressures to calculate a drag coefficient due to the cavity presence also yielded excellent agreement between the present results and those done previously. Symmetric mean pressure distributions about the stream-wise axis of the cavity were noted for h/D = 0.20 and 0.70 while an asymmetric distribution was measured for h/D = 0.47, as found previously. The existence of symmetry or asymmetry in the mean pressure patterns carried over into the fluctuating pressure patterns. The addition of these figures to the body of existing pressure pattern results allowed the creation of three-dimensional vortex skeletons (Section 4.3.4) and surface flow diagrams (Section 4.3.5), similar to those drawn by Gaudet and Winter (1971), for all cavity configurations tested, allowing a much more straightforward visualization of the general mean flow in the cavity for each of these configurations. Some evidence for the existence of secondary "off-shoot" vortex branches on the cavity surfaces was also made possible by the high resolution of the pressure measurement system used.

5.1.2 Switching and Flapping Pressure Analysis

A brief investigation of the flapping regime proposed by Hiwada et. al. (1983) at h/D = 0.37 confirmed the existence of this pressure flap phenomenon, though periodic oscillations (as reported by Hiwada et. al.) were not observed. Rather an intermittent flapping mechanism was noted at this configuration.

A detailed study was carried out of the cavity wake flow switch at h/D = 0.47 mentioned by previous investigators and this resulted in the discovery of a method to reliably control the handedness of the trailing vortex observed at this configuration. By disturbing the flow upstream of the cavity model on the side which the trailing vortex is noted originally (termed a "same-handed" disturbance), using a flat plate introduced normal to the free-stream, a repeatable mechanism for switching the wake flow was found. A set of disturbance requirements were also developed, possibly defining the pressure drop required for a successful wake flow switch to take place.

5.1.3 Cavity Wake Flow Velocity Profiles

Planar profiles of the stream-wise velocities downstream of the cavity revealed the presence of the trailing vortex for h/D = 0.47 in the form of a nearly circular velocity deficit region in the mean velocity case and a circular peak in the stream-wise turbulence for the RMS velocity case. Reasonably symmetric distributions were noted for the h/D = 0.20 case while, once again, the h/D = 0.47 case was strongly asymmetric. The effect of switching the wake flow for the h/D = 0.47 case was to reflect the flow distributions about the span-wise centre of the working section (z = 0). Stream-wise velocity deficits and turbulence intensities were greatest for h/D = 0.47 due to the higher induced drag imposed by this configuration compared to h/D = 0.2. Single span-wise lines of these distributions were compared to profiles carried out by previous investigators to reveal a similar nature between the measurements,

yet shifted slightly in the positive z (lateral) direction, possibly indicating the existence of a small lateral mean velocity in the tunnel flow.

5.1.4 Frequency Analyses

A frequency analysis of the velocity fluctuations in the cavity wake showed a great deal more turbulent kinetic energy in the spectra for h/D = 0.47 as compared to the 0.2 case. Peaks in the spectra, though quite weak, showed repeated contributions near 150 Hz for the h/D = 0.47 case, possibly attributable to the cavity resonance feedback mechanism. Peaks near 90 Hz were also noted for this configuration, most likely related to the rate of recirculation in the cavity trailing vortex. No significant peaks were observed at higher frequencies, demonstrating that the fluid-dynamic oscillations for this type of flow are quite low in the frequency range.

Frequency spectra generated from the surface-mounted microphone and pressure transducer measurements revealed significant contributions in the higher frequency bands (from 800-1500 Hz) for h/D = 0.47 and 0.70 related to the acoustic air column vibrations possible at these deeper cavity depths. Strong peaks were also noted at lower frequencies for the h/D = 0.2 and 0.47 cases related to the greater amount of fluid entrainment for these cavities allowing strong recirculating vortices to be set up. A very strong peak of 150 Hz was measured at the cavity base for h/D = 0.47, lending more evidence for the possibility of a cavity feedback resonance mechanism at this configuration. A much smaller peak near this same frequency was noted for the h/D = 0.70 case, indicating that these two cavity depths are likely of the same flow regime, as proposed by Hiwada et. al. (1983).

5.1.5 Summary

Good agreement between the present results and similar results from previous experiments adds confidence to the new conclusions introduced in this report. As a result of these experiments, a greater understanding of the flow structure in the cavity, through the contribution of surface flow topology, and in its wake, through stream-wise planar velocity profiles, has been obtained for some depth configurations. In addition, a simple method for the control of the trailing vortex for h/D = 0.47 has been discovered. Evidence from these experiments has likely increased the understanding of the reasons for atypical flow behaviour at h/D = 0.47 with the proposal that there is a link between this behaviour and the cavity feedback resonance mechanism. It is also possible that acoustic frequency analysis provided from the microphone measurements in this experiment could be used by vehicle manufacturers in determining causes of noise sources due to circular cavity arrangements in vehicle frames.

5.2 Recommendations

Suggestions resulting from the analysis and experiences of conducting these experiments are separated into the two major categories of recommended future research and aerodynamic design considerations.

5.2.1 Future Research

- A frequency analysis of surface-mounted microphone measurements taken for a greater range of cavity depths should be conducted, as this would be required to determine whether h/D = 0.47 is the only depth at which feedback resonance is a significant contributor to the frequency spectrum.

- Attempting to measure fluctuating pressure patterns using these microphones should be avoided due to their large size and due to the difficulty of calibrating these devices on a regular basis once the units are surface mounted.
- A wake flow analysis using Particle Image Velocimetry equipment would be very useful to further determine the mean flow structure in the cavity wake for various cavity configurations.
- A hot-wire investigation in the cavity wake, similar to the one done in the present experiment, but for many more depth configurations, should be done to elucidate the relationship between flow inside the cavity and that in the wake. This investigation would also allow further confirmation of the existence of flow regimes for varying circular cavity depth configurations, originally proposed by Hiwada et. al. (1983).
- Another interesting experiment involving hot-wire measurements in the cavity wake would be to take planar profiles of measurements (such as those taken in the present experiment) at a range of downstream distances in the cavity wake to investigate the spatial evolution of mean wake flow features for these flows. This would allow three dimensional wake flow profiles to be created.
- A wake flow investigation involving Particle Image Velocimetry would also be interesting for a cavity configuration of h/D = 0.37 to learn more about the flow at this configuration. Due to the very low-frequency flapping observed in the pressure-time histories captured at this configuration, it is assumed that the velocity distribution at this case would be symmetric as a time average over a long sample time, but if it were possible to capture the entire velocity distribution in a plane perpendicular to the free-stream simultaneously over a period of approx. 2 seconds (or any time less than the flapping period), it is

assumed that an asymmetric velocity distribution would be observed in the wake. It is possible that there would be a relationship between this asymmetric flow and the flow for h/D = 0.47.

5.2.2 Aerodynamic Design Considerations

- If possible, circular cavities built into bodies immersed in turbulent boundary layer flow should be limited to depths $\leq$ 0.2D due to the low drag and lack of high frequency acoustic noise associated with such cavities. Alternatively, if only drag is of importance, depth ranges of $h < 0.05D$ and $0.7 < h < 0.9$ are optimal.
- Applications of the wake flow control method for h/D = 0.47 are likely limited. Although the asymmetric pressure distribution on the cavity sidewall would yield a controllable, directional force, it is likely that a great number of such cavities would be required to induce forces required for vehicle direction control. Also, the high drag resulting from the inclusion of such excrescences would be prohibitive.

6 REFERENCES

Bies, D. A., Hansen, C. H., (1996). *Engineering Noise Control: Theory & Practice*, 2nd edition, E & FN SPON, London.

Cebeci, T., Smith, A. M. O., (1974). *Analysis of turbulent boundary layers*, Academic Press, New York.

Czech, M., Savory, E., et. al. (2001). *Flow regimes associated with yawed rectangular cavities*, The Aeronautical Journal, pp. 125-134, March.

Dantec Dynamics, *Technical Note: Improved Temperature Correction in Streamware*, Dantec Dynamics publication no. TN049909.

Delannoy, Y., Merie, M., (1954). *Flow above natural and ventilated cavities*, Proceedings of the 1994 ASME Fluids Engineering Division Summer Meeting Part 16, vol. 194, pp. 47-51.

Disimile, P., Toy, N., Savory, E., (2000). *Effect of Planform Aspect Ratio on Flow Oscillations in Rectangular Cavities*, Journal of Fluids Engineering, vol. 122, pp. 32-38, March.

Elder, S. A., Farabee, T. M., DeMetz, F. C., (1982). *Mechanisms of flow-excited cavity tones at low Mach number*, Journal of the Acoustical Society of America, vol. 72, no. 2, pp. 532-549, August.

Gaudet, L., Johnson, P. (1971). *Measurements of the drag of excrescences immersed in turbulent boundary layers at Mach numbers between 0.2 and 2.8*, RAE Tech Report 71181.

Gharib, M., Roshko, A., (1987). *The effect of flow oscillations on cavity drag*, Journal of Fluid Mechanics, vol. 177, pp. 501-530.

Hardin, J. C., Mason, J. P., (1977). *Broadband Noise Generation by a Vortex Model of Cavity Flow*, AIAA Journal, vol. 15, pp. 632-637.

Hardin, J. C., Pope, D. S., (1995). *Sound Generation by Flow over a Two-Dimensional Cavity*, AIAA Journal, vol. 33, no. 3, pp. 407-412, March.

Heller, H. H., Holmes, D. G., Covert, E. E., (1971). *Flow-Induced Pressure Oscillations in Shallow Cavities*, Journal of Sound and Vibration, vol. 18, no. 4, pp. 545-553.

Hiwada, M., Kawamura, T., Mabuchi, I., Kumada, M., (1983). *Some Characteristics of Flow Pattern and Heat Transfer past a Circular Cylindrical Cavity*, Bulletin of the JSME, vol. 26, no. 220, pp. 1744-1752.

Howe, M. S., (1997). *Low Strouhal number instabilities of flow over apertures and wall cavities*, Journal of the Acoustical Society of America, vol. 102, no. 2, pt. 1, pp. 772-780, August.

Hunt, J., Abell, C., Peterka, J., Woo, H., (1978). *Kinematical studies of the flows around free or surface-mounted obstacles; applying topology to flow visualization*, Journal of Fluid Mechanics, vol. 86, pp. 179-200.

Johnston, R. T., Sullivan, J. P., (1994). *An inexpensive pressure transducer for the measurement of low amplitude unsteady pressure signals*, Experiments in Fluids, vol. 16, pp. 342-344.

Jorgensen, F., (2002). *How to measure turbulence with hot-wire anemometers – a practical guide*, Dantec Dynamics publication no. 9040U6151.

Kawall, J. G., Shokr, M., Keffer, J. F., (1983). *Digital Technique for the Simultaneous Measurement of Streamwise and Lateral Velocities in Turbulent Flows*, Journal of Fluid Mechanics, vol. 133, pp. 83-112, August.

Knisely, C., Rockwell, D., (1982). *Self-sustained low-frequency components in an impinging shear layer*, Journal of Fluid Mechanics, vol. 116, pp. 157-186.

Kuo, C., Huang, S., (2003). *Effect of surface mounting of upper plate on oscillating flow structure within cavity*, Experimental Thermal and Fluid Science, vol. 27, pp. 755-768.

Lin, J.-C., Rockwell, D., (2001). *Organized Oscillations of Initially Turbulent Flow past a Cavity*, AIAA Journal, vol. 39, no. 6, pp. 1139-1151, June.

Maull, D. J., East, L. F., (1963). *Three-dimensional flow in cavities*, Journal of Fluid Mechanics, vol. 16, pp. 620-632.

McGregor, O. W., White, R. A., (1970). *Drag of Rectangular Cavities in Supersonic and Transonic Flow Including the Effects of Cavity Resonance*, AIAA Journal, vol. 8, pp. 1959-1964.

Milbank, J., (2004). Investigation *of fluid-dynamic cavity oscillations and the effects of flow angle using an open-jet wind tunnel*, Ph.D. Thesis, RMIT University.

Monin, A. S., Yaglom, A. M., (1975). *Statistical fluid mechanics: mechanics of turbulence*, MIT Press, Cambridge, Mass.

Rockwell, D., Naudascher, E., (1978). *Review – Self-Sustaining Oscillations of Flow Past Cavities*, Journal of Fluids Engineering, vol. 100, pp. 152-165, June.

Roshko, A. (1955). *Some measurement of flow in a rectangular cutout*, NACA TN 3488, August.

Rossiter, J. E., (1964). *Wind-Tunnel Experiment on the Flow over Rectangular Cavities at Subsonic and Transonic Speeds*, British ARC R&M no. 3428.

Savory, E., Toy, N., Gaudet, L., (1996). *Effect of lip configuration on the drag of a circular cavity*, Emerging Techniques in Drag Reduction, pp. 317-335.

Sen, S. N., (1990). *Acoustics – Waves and Oscillations*, Wiley Eastern Ltd., New Delhi, India.

Stewart, J., (1999). *Calculus - Early Transcendentals*. 4th ed., Brooks/Cole Publishing Company.

Tillman, W., (1951). *Additional measurements of the drag of surface irregularities in turbulent boundary layers,* NACA TM 1299 (also in "New resistance measurements with surface irregularities in the turbulent boundary layer:, Forschungshefte fur Schiffstechnik, vol. 2, pp. 81-88, (BSRA Trans No. 322), 1953).

Wheeler, A., Ganji, A., (1996). *Introduction to Engineering Experimentation*, Prentice Hall Inc.

Young, A. D., Paterson, J. H., (1981). *Aircraft Excrescence Drag*. NATO AGARD-AG-264. J. L. Jones, Editor.

7 APPENDICES

7.1 Appendix A - Cavity Model Schematic Drawings

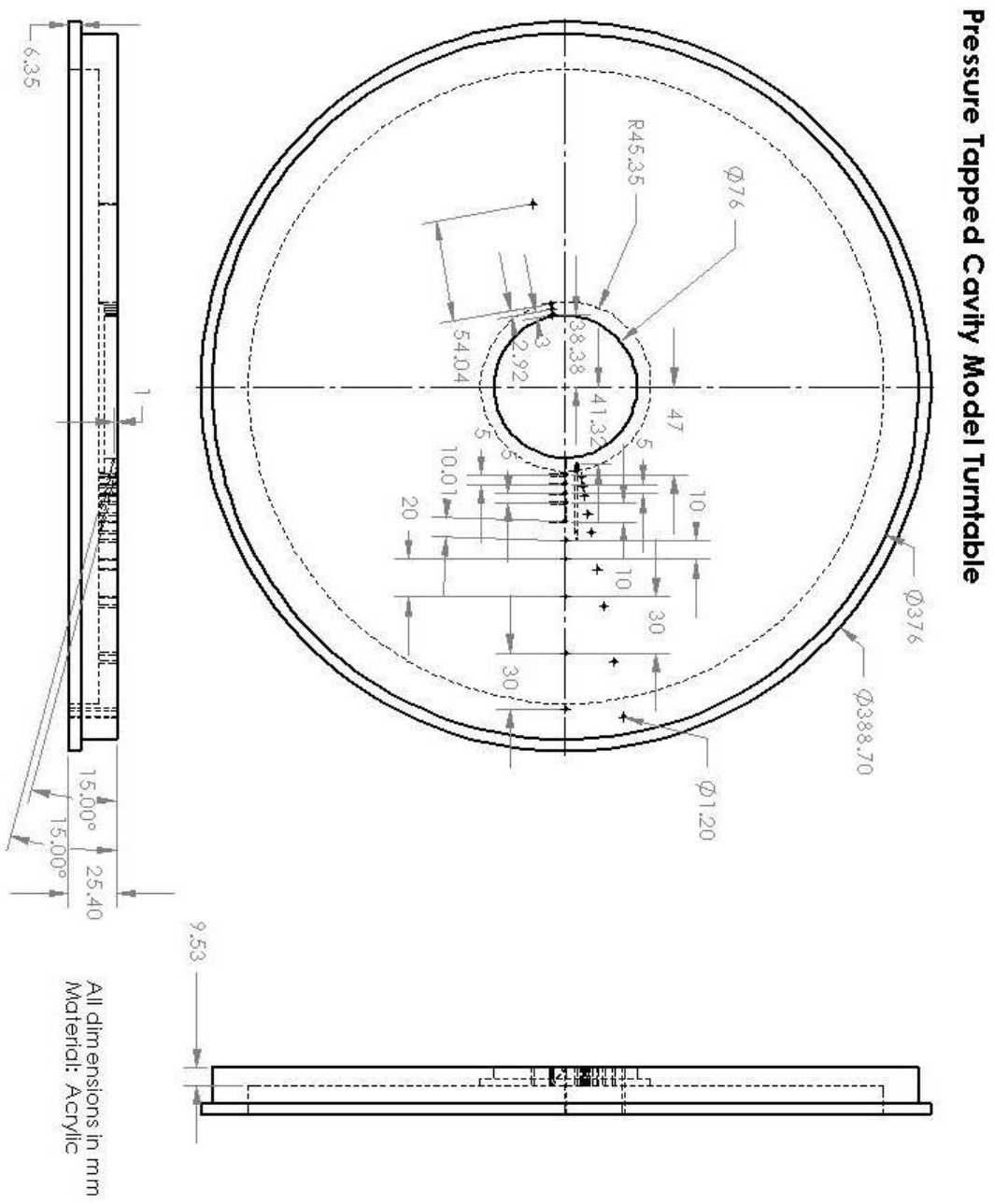

Figure A-1 – Schematic drawing of pressure tapped cavity model turntable.

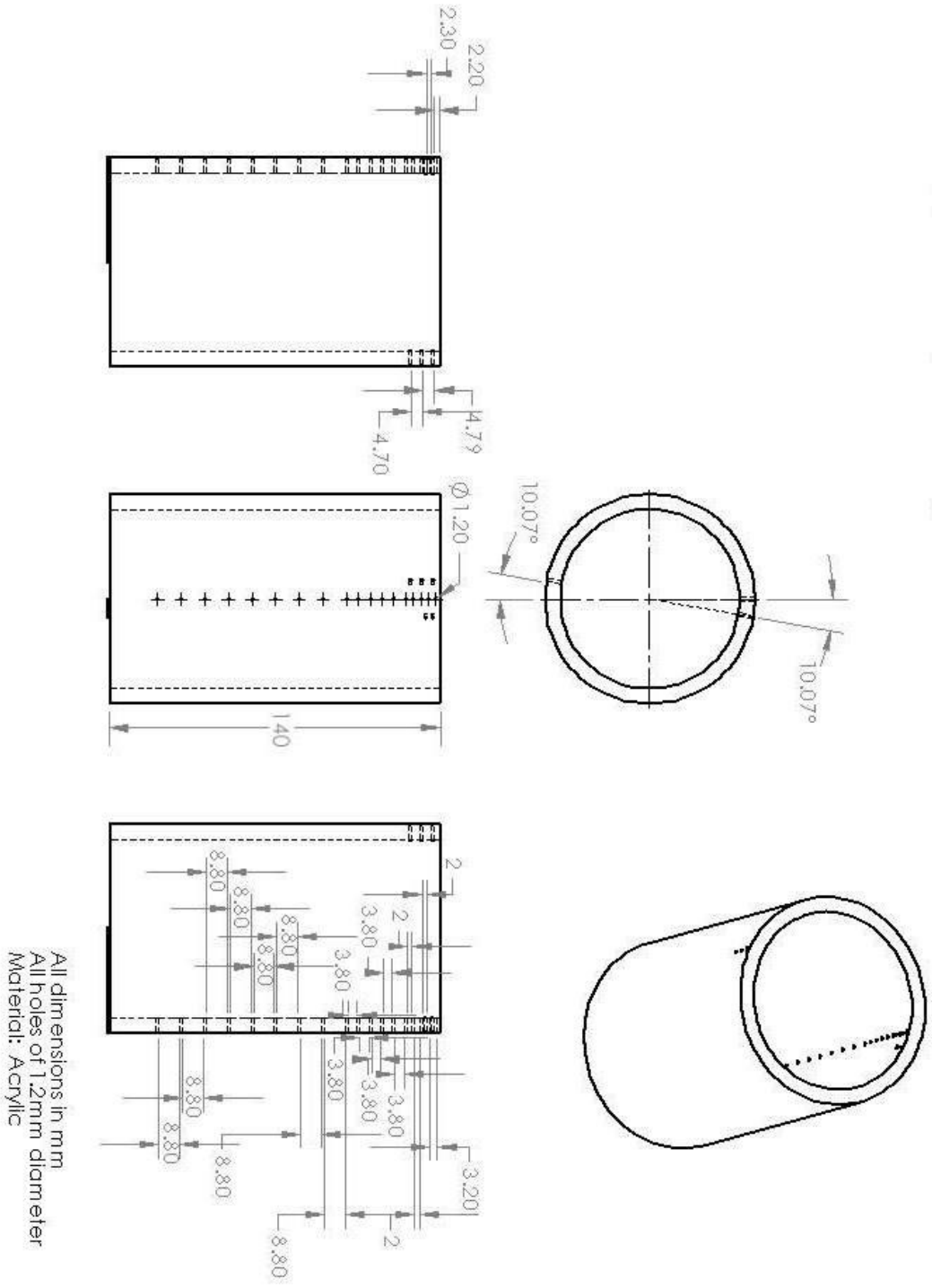

Figure A-2 – Schematic drawing of pressure tapped cavity model sidewall cylinder.

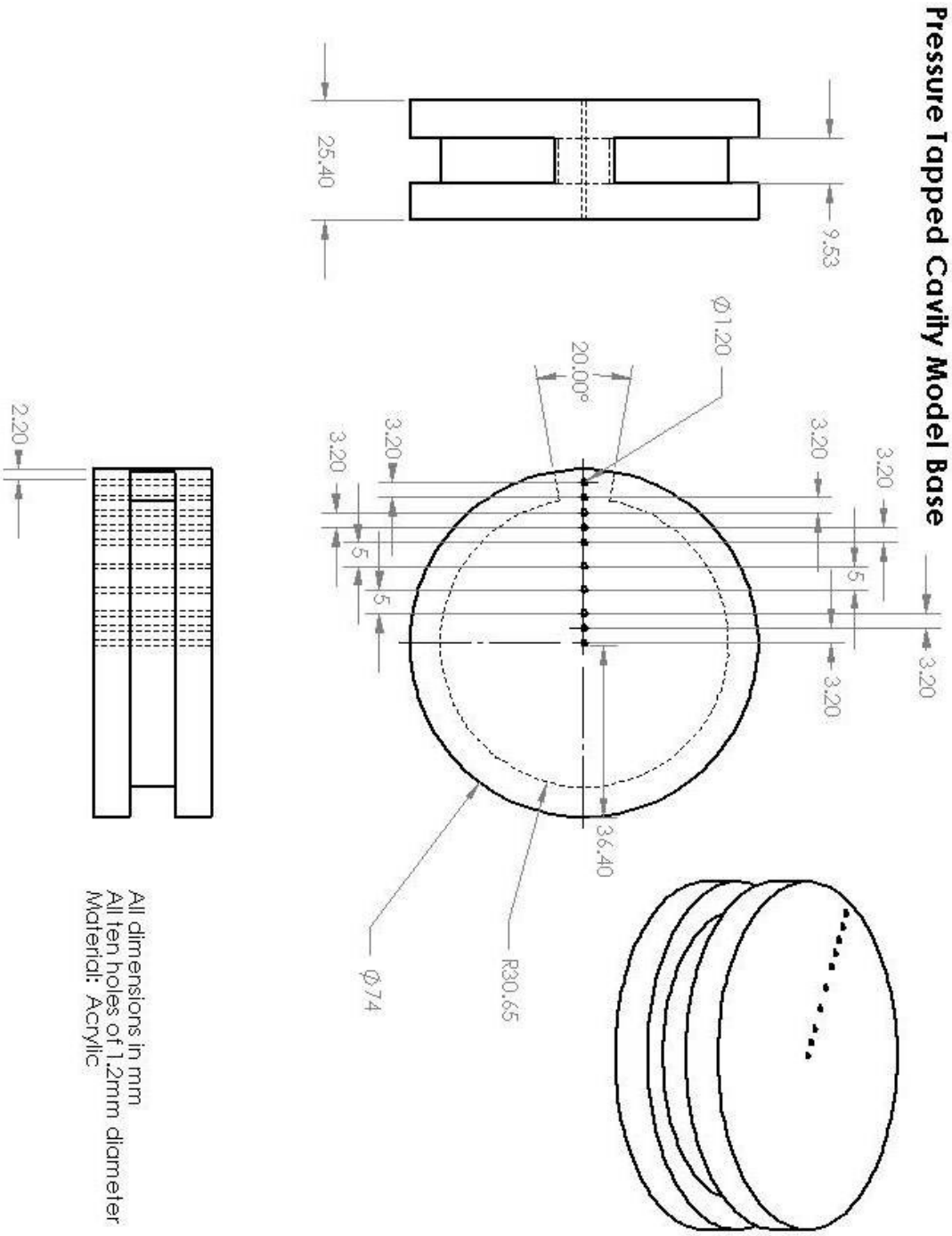

Figure A-3 – Schematic drawing of pressure tapped cavity model base.

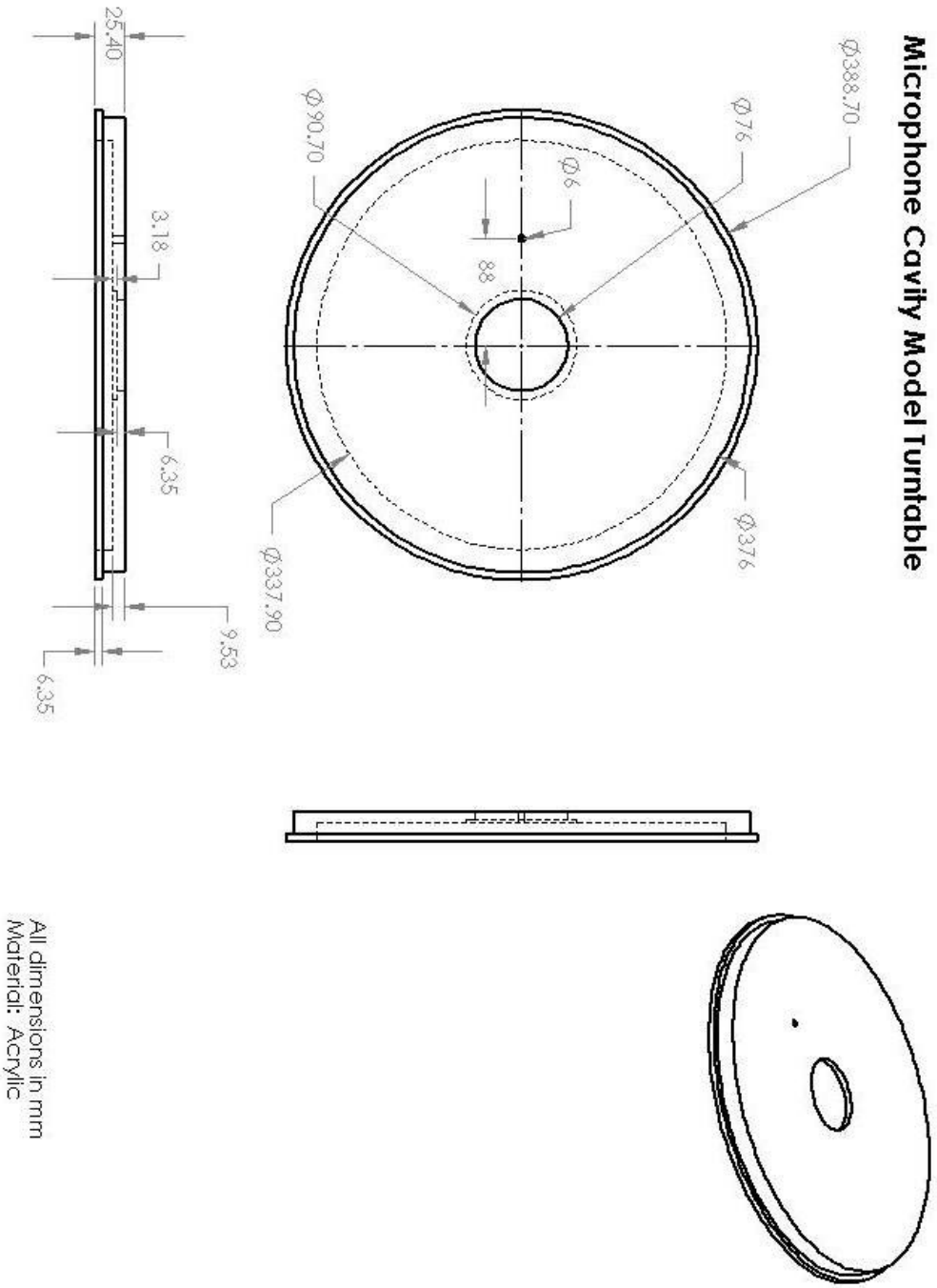

Figure A-4 – Schematic drawing of microphone cavity model turntable.

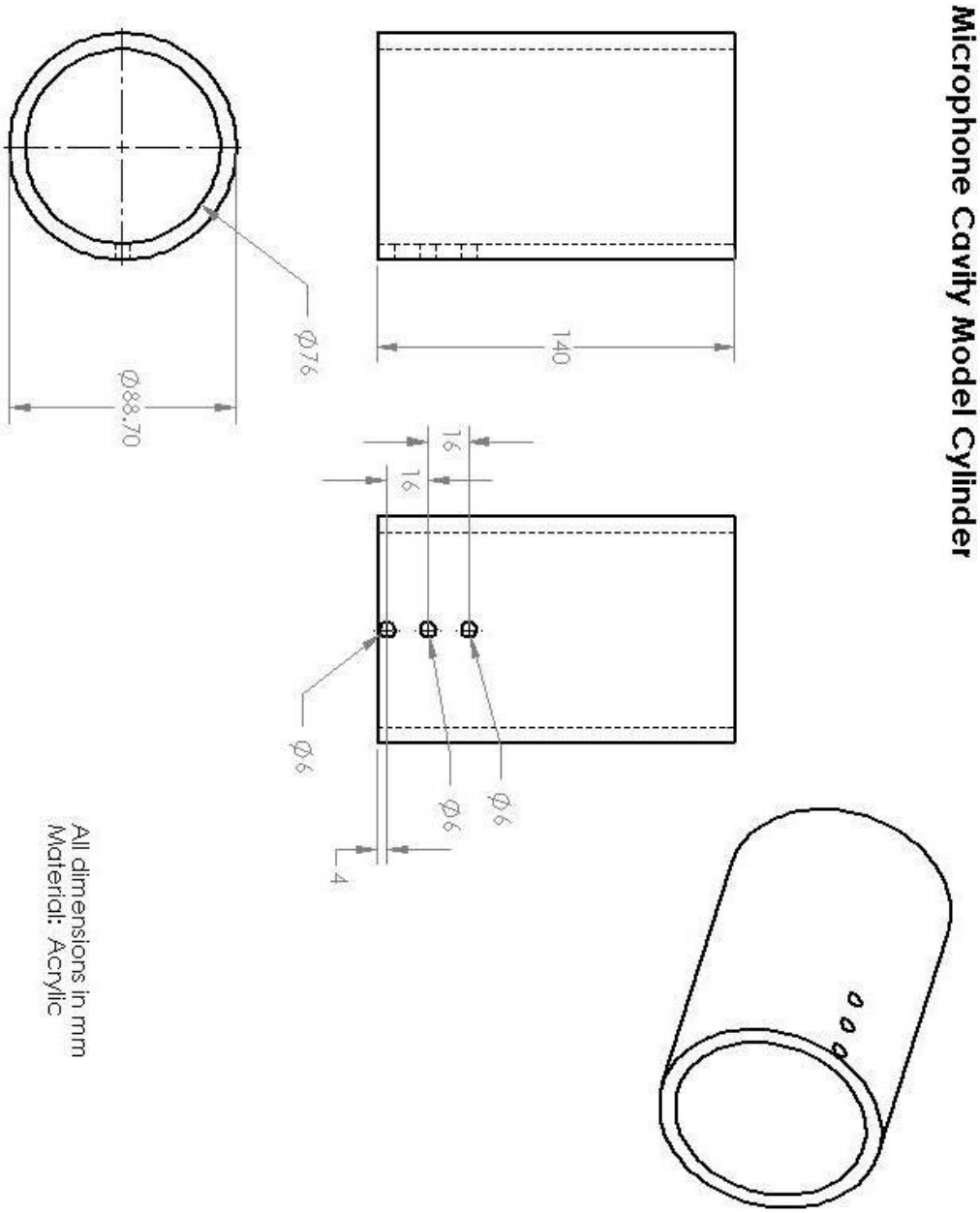

Figure A-5 – Schematic drawing of microphone cavity model sidewall cylinder.

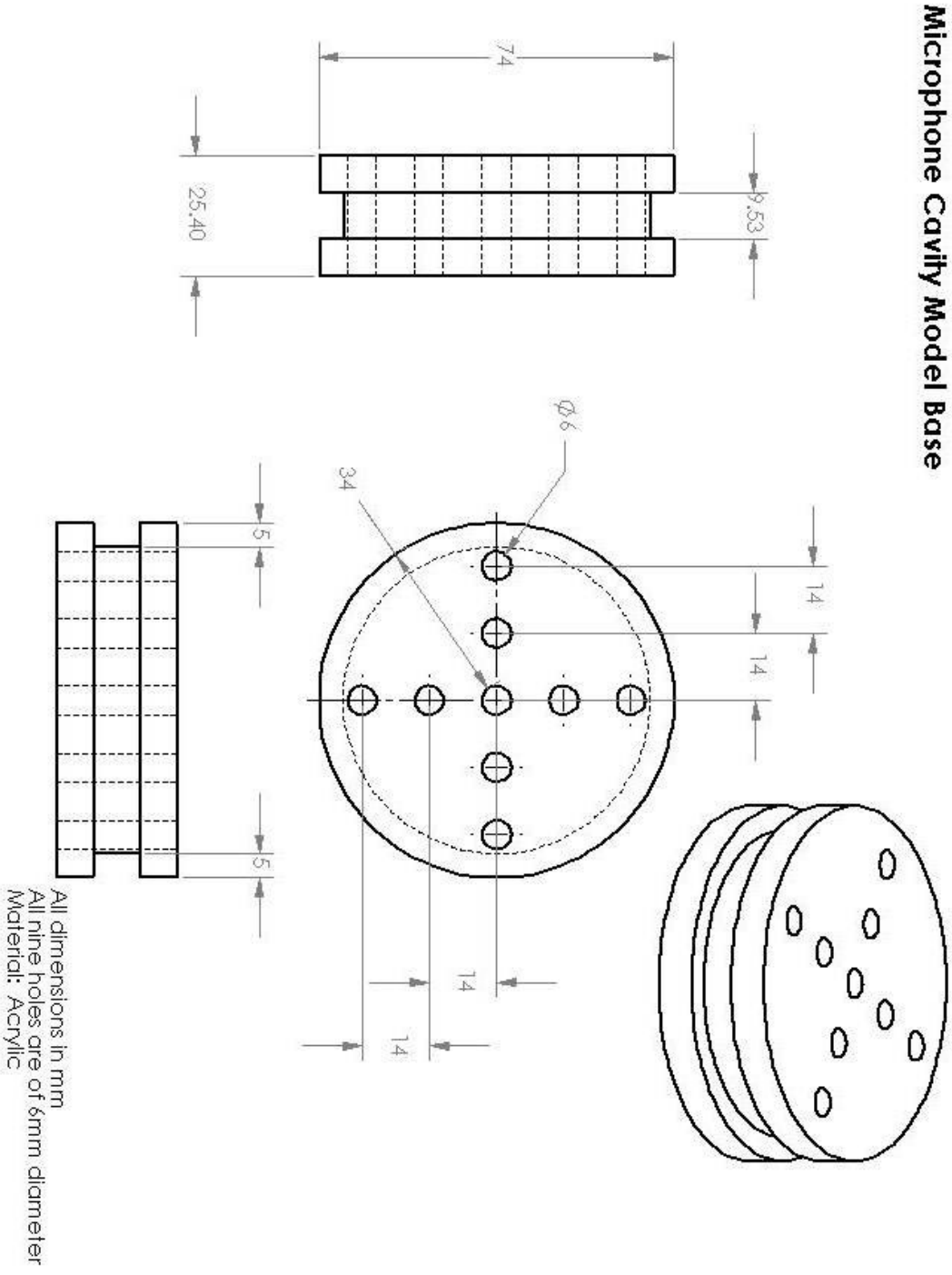

Figure A-6 – Schematic drawing of microphone cavity base.

7.2 Appendix B - Microphone and Pressure Transducer Circuit Schematic Diagrams

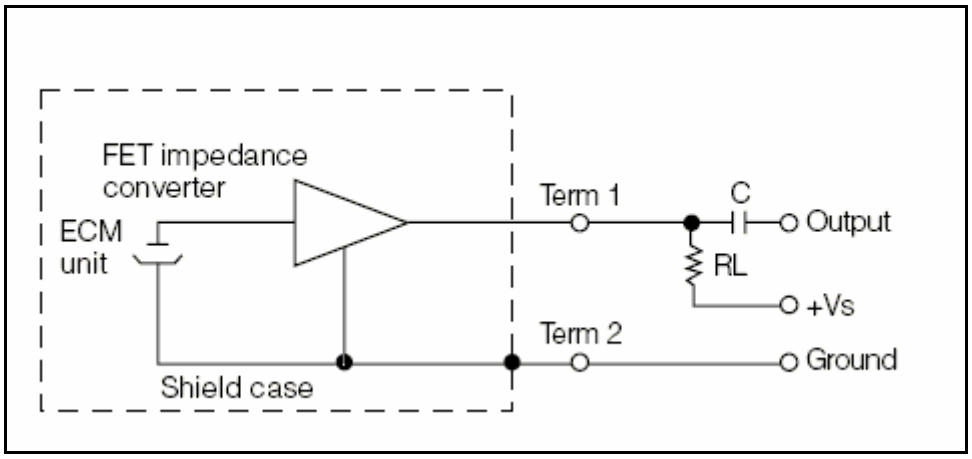

Figure B-1 – Schematic drawing of microphone offset removal circuit. RL = 2.2 kOhms and C = 33 pF.

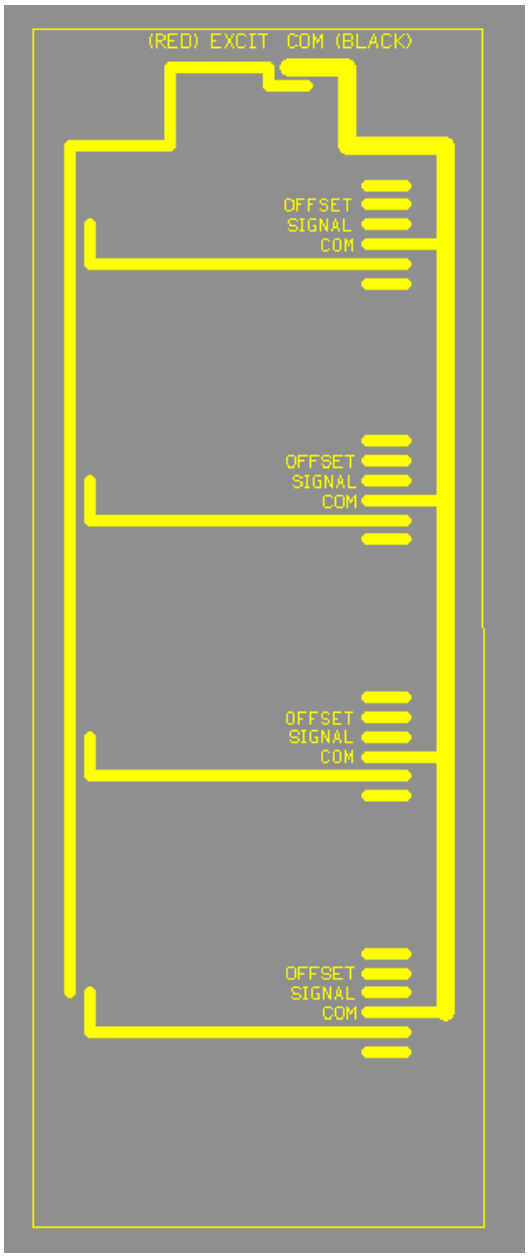

Figure B-2 – Copper trace drawing of pressure transducer box circuit.

7.3 Appendix C - Detailed Error Analysis for all Measurement Systems

Calculating Total Uncertainty

Summing errors from different sources for a given measurement system was done using the RSS method outlined by Wheeler and Ganji (1996). For adding multiple random error sources, the uncertainty to 95% confidence was calculated using the following equation:

$$w_{95} = \left(\sum_{i=1}^{n} (\Delta E_i)^2 \right)^{1/2}$$

Where i is the index for individual random error sources, n is the total number of random error sources to be summed, and ΔE is a source of uncertainty as a fraction of the nominal value of the quantity measured.

For adding random and systematic error sources, the random and systematic error sources were summed individual and then the total from each category was summed as follows:

$$w_{95} = \left(R_{TE}{}^2 + S_{TE}{}^2 \right)^{1/2}$$

Where R_{TE} is the total uncertainty due to random sources and S_{TE} is the total uncertainty due to systematic sources.

Pressure Transducer System

Error Source	Absolute Error (Cp) for Nominal Measurement of Cp = 0.15		Error Magnitude relative to Nominal Measurement of Cp = 0.15		Systematic of Random Error (S or R)
	NDR4	DCAL4	NDR4	DCAL4	
Temperature Effect and Drift over Length of Trial	±0.00047	±0.00058	±0.3%	±0.4%	R
Linearity and Hysteresis	±0.00075	±0.00015	±0.5%	±0.1%	R
Error in Calibration	±0.0033	±0.0032	±2.2%	±2.1%	R
Total Uncertainty	±0.0034	±0.0032	±2.28%	±2.14%	

Table C-1 – Summary of error analysis for pressure transducer measurement systems.

Microphone system

Error Source	Error Magnitude Relative to Nominal Measurement	Systematic of Random Error (S or R)	Corrected in Final Result (Y or N)
Dependence on Supply Voltage**	-0.8%	S	N
DAQ Noise	+0.01%	S	N
Wind Tunnel Noise and Other Errors†	+60%	S	Y
Repeatability between Microphones*	±12.5%	R	N
Total Uncorrected Uncertainty	±12.6%		

Table C-2 – Summary of error analysis for microphone measurement systems.

† - Other errors consist of: radio interference noise and signal conditioning circuit noise

* - Repeatability here refers to the average difference between measurements of identical sound sources with separate microphones.

** - Average drop in mean signal magnitude over complete round of microphone surface pressure measurements relative to original signal magnitude.

Hot-wire Anemometry System

Error Source	Uncertainty Relative to Nominal Measurement	Uncertainty Relative to Extreme Measurement	Systematic of Random Error (S or R)	Corrected in Final Result (Y or N)
Temperature Effect	$\overline{U} \rightarrow$ -2.0%*	$\overline{U} \rightarrow$ -2.9%**	S	N
Rectification and Other Errors†	$\overline{U} \rightarrow$ +0.85%* $u' \rightarrow$ +6.5%*	$\overline{U} \rightarrow$ +3.75%** $u' \rightarrow$ +2.1%**	S	N
Probe Yaw Angle	±0.9%‡	±0.9%‡	R	N
Use of Look-Up Table for Response Conversion	±0.005%	±0.005%	R	N
Calibration Velocity Measurement Error	±0.12%	±0.11%	R	N
Total Uncertainty	$\overline{U} \rightarrow$ ±1.47%	$\overline{U} \rightarrow$ ±1.24%		

Table C-3 – Summary of error analysis for hot-wire anemometry measurement system.

* - Based on 5% r.m.s. $u'/\overline{U}$ measurement

** - Based on 13% r.m.s. $u'/\overline{U}$ measurement

† - Effects of error-producing factors on listed flow statistics related to non-linear X-wire response relationships consisting of: fluctuations in out-of-plane velocity component, axial cooling of hot-wire probes, calibration errors and probe wire separation (Kawall, Shokr, Keffer, 1983 (JFM))

‡ - Based on Probe Yaw Angle uncertainty of ±0.5°

7.4 Appendix D - Residual Noise Measured by Microphones with Tunnel at Experiment Speed

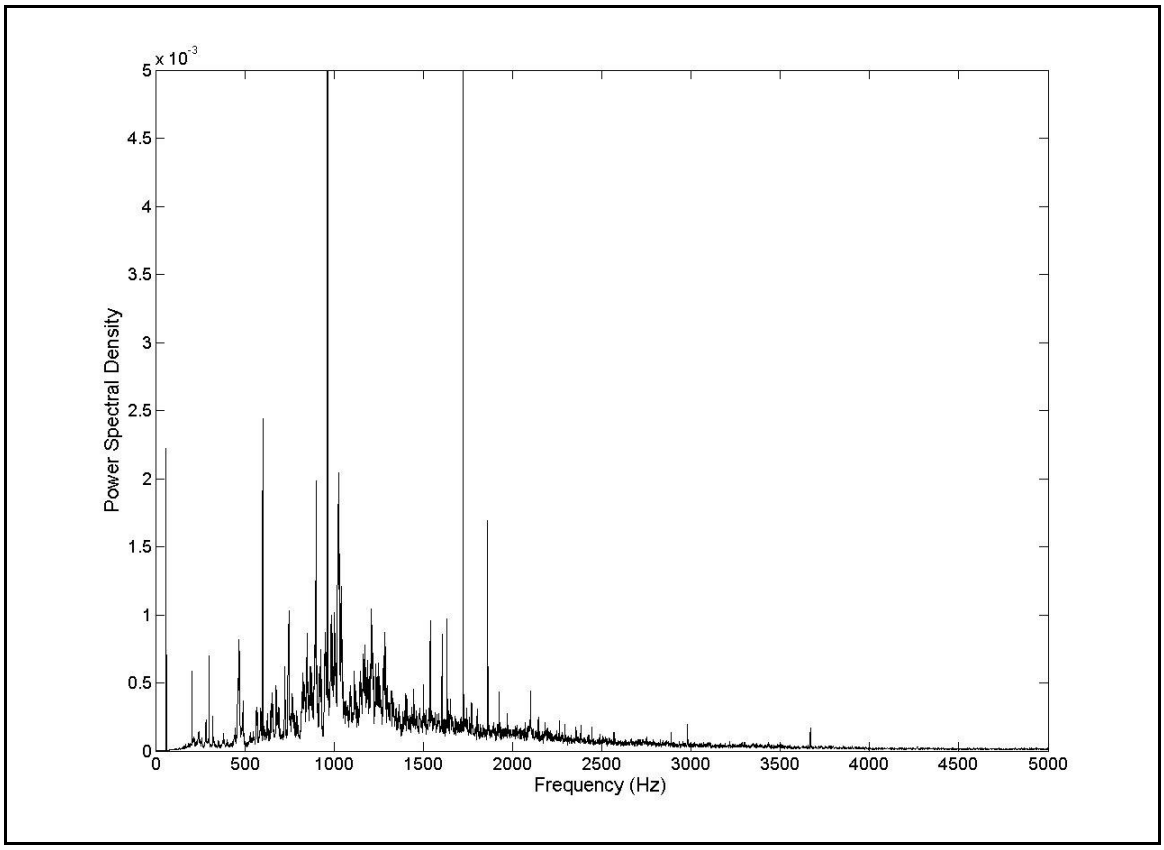

Figure D-1 – Broad-band Power Spectral Density plot of ambient tunnel noise as measured by a surface-mounted microphone in the model ground plane.

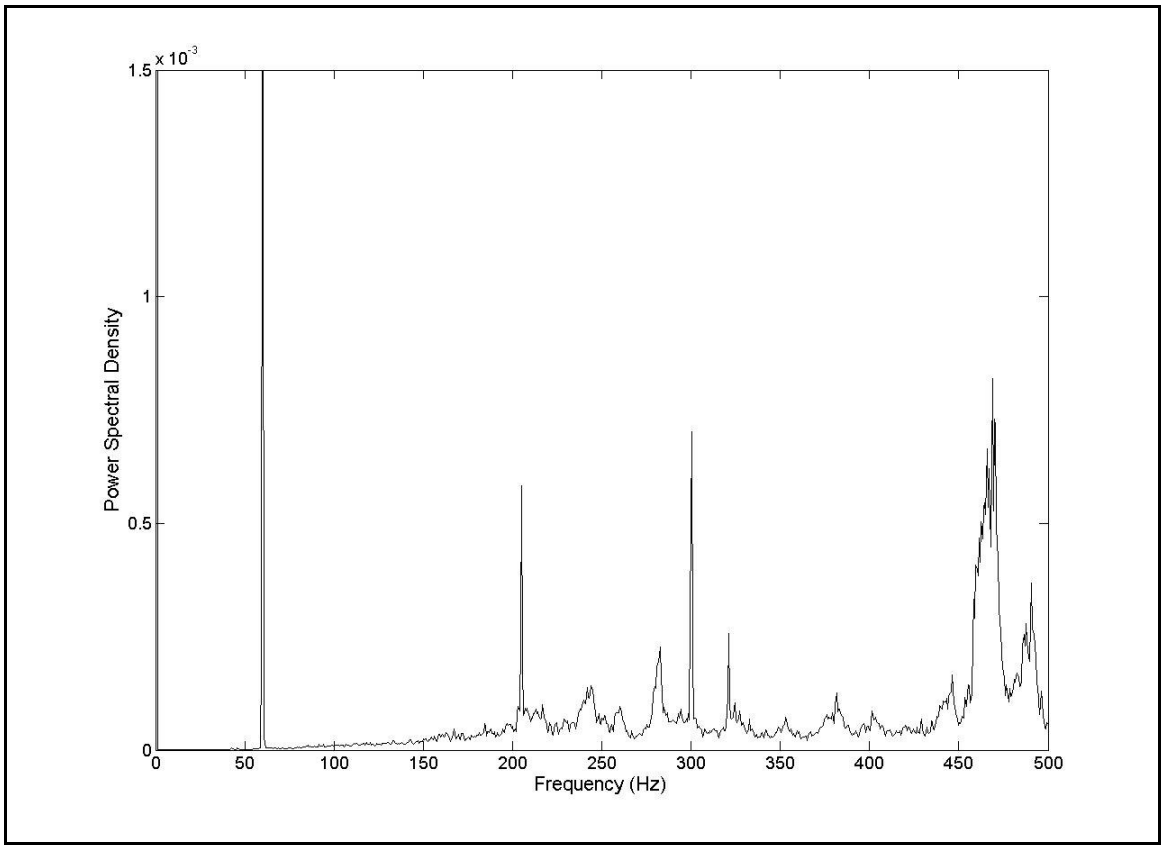

Figure D-2 – Narrow-band Power Spectral Density plot of ambient tunnel noise as measured by a surface-mounted microphone in the model ground plane.

Major peaks in these PSD's are listed in Table D-1 below, with a proposed explanation associated with some peaks.

Peak Number	Frequency (Hz)	Possible Source	Peak Number	Frequency (Hz)	Possible Source
1	60	Electrical Altenating Current in Building	17	605	2nd mode of fan-blade passing frequency
2	205	Wind Tunnel Geometry	18	765	Diameter of Fan Housing Zones
3	244		19	825	
4	259		20	850	3rd mode of Lateral Distance across Working Section
5	281	Lateral Distance Across Working Section	21	900	
6	299	Fan – Blade Passing Frequency	22	965	
7	319	Fan – Blade Passing Frequency	23	1020	Vertical Height of Tunnel Cross-Section before Contraction
8	349		24	1165	
9	379		25	1205	
10	407	2nd Mode of Peak 2	26	1280	
11	440		27	1400	
12	465	Width of Tunnel at Recirculation Section	28	1440	
13	487		29	1535	2nd mode of Diameter of Fan Housing Zones
14	530		30	1715	
15	550		31	1850	
16	570	2nd mode of Lateral Distance across Working Section	32	2275	3rd mode of Diameter of Fan Housing Zones

Table D-2 – Peaks in the ambient tunnel noise frequency spectrum.

7.5 Appendix E - List of Hot-wire Measurement Apparatus and Anemometer Dip-Switch Setting Procedure

Hotwire Setup

List of apparatus:

- Dantec 55P61 – Miniature Two-Component Crossed Hotwire Probe
- Dantec 55H240 – L-Shaped Miniature Probe Holder
- Dantec Probe Holder Mounting Tube
- 2 Dantec 54T30 MiniCTA Hotwire Anemometers
- 4 * 3 m lengths of Coaxial cable with BNC connectors
- National Instruments SCB-68 – Data Acquisition Connection Box
- National Instruments PCI-6052E – Data Acquisition Card
- Hewlett Packard Pavilion 6545C PC
- Velmex VXM Stepping Motor Controller
- Velmex Two Axis Stepping Motor Powered Traverse
- Pitot Static Tube
- Datametrics Barocell Pressure Sensor
- Datametrics Digital Transducer Monitor?
- Datametrics Electronic Manometer
- Glass Thermometer

Setting MiniCTA dipswitches

To correctly set the dipswitches of the MiniCTA anemometer boxes, the following procedure should be followed:

1. Acquire a plug-in multimeter with a low test current, preferably one with pin-style probes.

2. Detach extra coaxial cables that may be attached to the probe holder so that the metal BNC connectors of the probe holder are bare and accessible.
3. Very carefully insert the hotwire probe into the probe holder that will be used and ensure that the probe can be safely supported without the use of hands.
4. Support the probe and set the multimeter to the resistance (ohmmeter) function in a range of the order of 0-10 ohms.
5. With the greatest amount of precision possible on the multimeter, measure the resistance of each wire individually by applying an end of the multimeter probe to the outside of the BNC connector for one wire and the other end of the probe to the inside of this same connector while trying to interfere as little as possible with your fingers. Note the measured resistance and repeat for the other wire.
6. The measured resistance is actually $R_{\text{probe wire}} + R_{\text{probe leads}} + R_{\text{probe support leads}}$. The corresponding given values for 2 of these quantities can be found on the probe bottle: $R_{\text{probe wire}} \rightarrow R_{20}$ and $R_{\text{probe support lead}} \rightarrow R_L$. By assuming that R_L is correct, R_{20} can be backed out of your measured value.
7. Download dipswitch setting Excel file from Dantec's website at http://www.dantecdynamics.com
8. Open the Excel file and enter values in given cells.
9. Remove screws from tops of MiniCTA anemometer boxes. Carefully remove box tops.
10. Using a pencil or a small screwdriver depress dipswitches (small white switches) as directed by Dantec Excel file. Mark each box with a different marking (Wire 1 or Wire 2) on a piece of tape to ensure that the boxes do not get confused.
11. Refasten the box tops using the screws.

Equipment Specifications

Dantec 55P61 Two-Component Crossed Hotwire Probe

Sensor Resistance at 20˚C		Probe Lead Resistance		Temperature Effect on Sensor Output		Max. Wire Temp.
Wire 1	Wire 2	Wire 1	Wire 2	Wire 1	Wire 2	All Wires
3.50 Ω	3.59 Ω	0.5 Ω	0.5 Ω	0.36 %/˚C	0.36 %/˚C	300˚C

Table E-1 – Hot-wire probe specifications.

National Instruments PCI-6052E Data Acquisition Card

Max. Sample Rate	Resolution	Number of Analog Input Channels	Number of Differential A.I. Channels	Measurement Ranges
333 kS/s	16 bit	16	8	+/- 0.05 V +/- 0.10 V +/- 0.25 V +/- 0.5 V +/- 1.0 V +/- 2.5 V +/- 5 V?

Table E-2 – Data Acquisition Card Specifications.

Hewlett Packard Pavilion 6545C PC

Processor Speed	RAM	Hard Drive Capacity	Operating System
500 MHz Celeron	256 MB	12 GB	Windows Pro. 2000

Table E-3 – Data Acquisition Computer Specifications.

7.6 Appendix F - Tubing Frequency Transfer Function Calibration Results

DCAL4

All Broadband

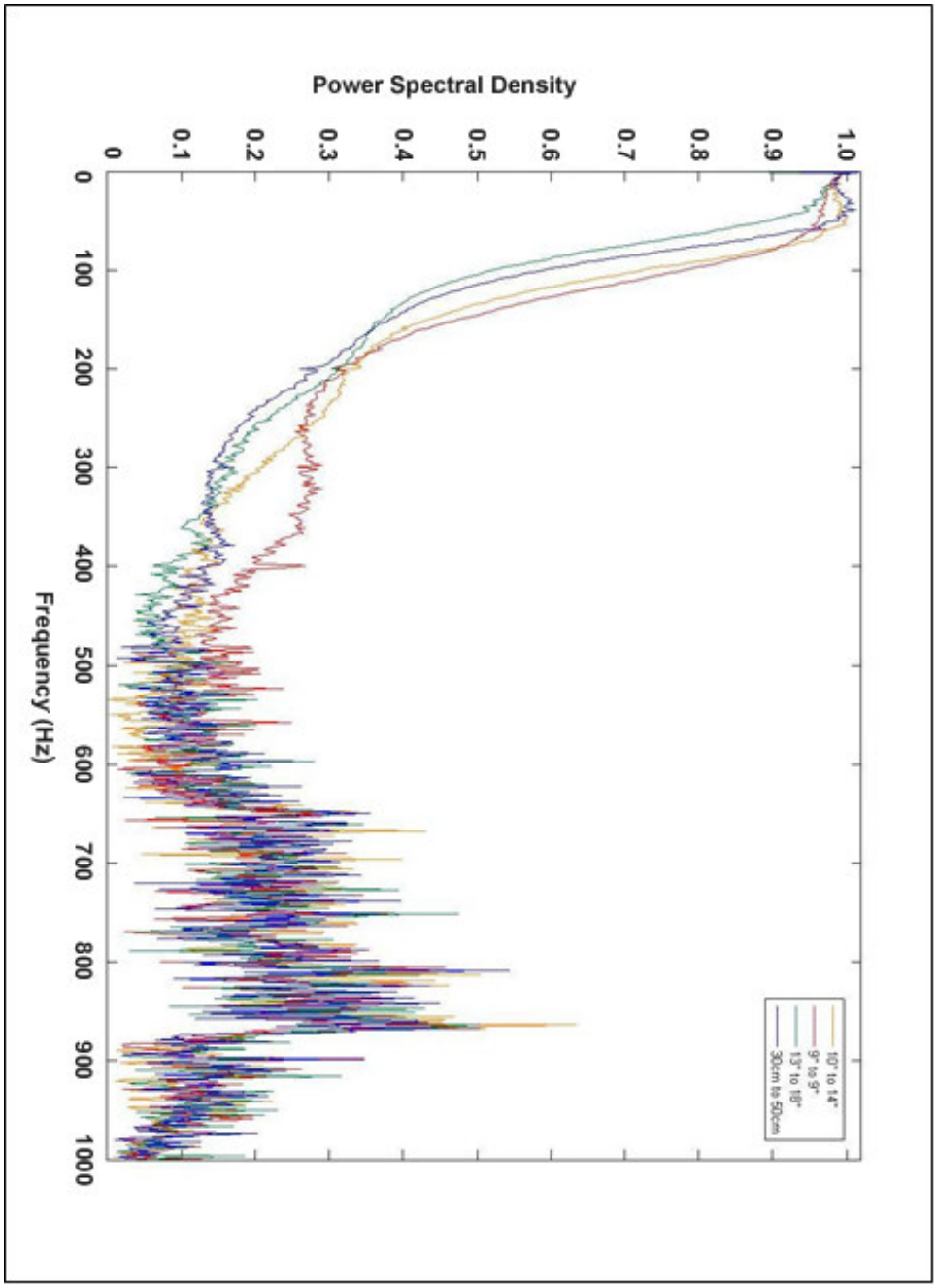

Figure F-1– Broad-band power spectral density plot for DCAL 4 pressure measurement systems with various tubing configurations.

All Narrowband

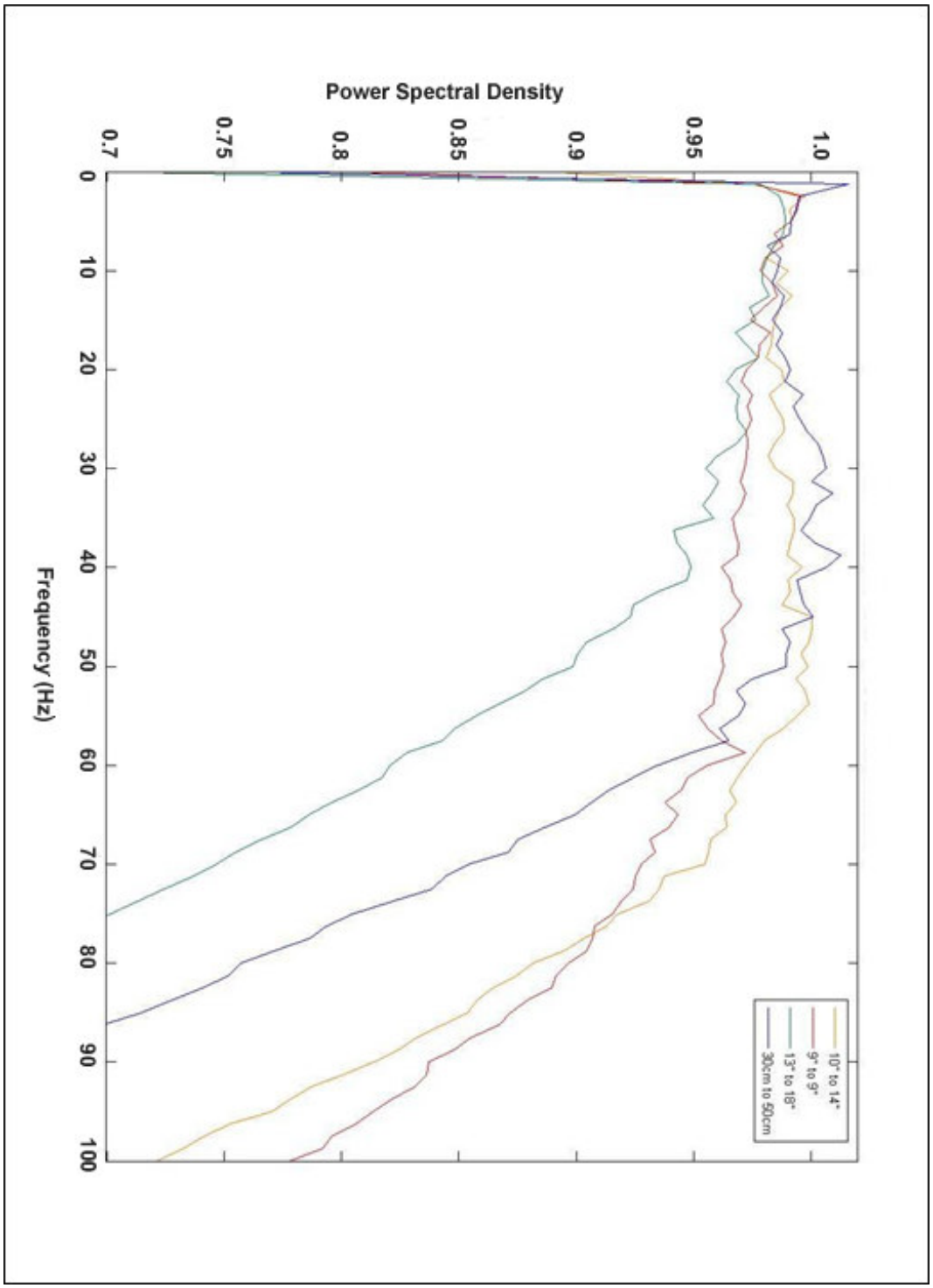

Figure F-2– Narrow-band power spectral density plot for DCAL 4 pressure measurement systems with various tubing configurations.

NDR4

All Broadband

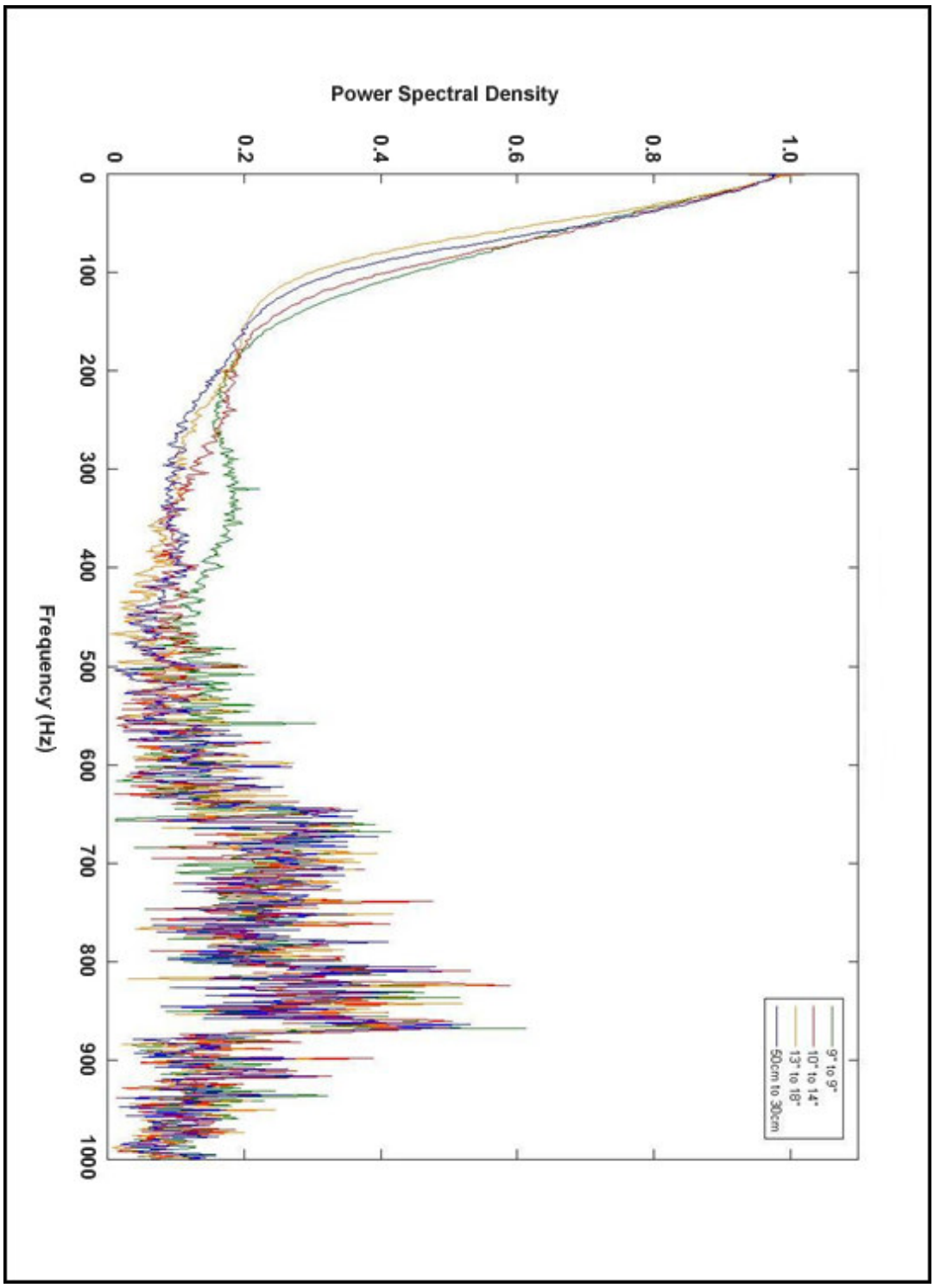

Figure F-3– Wide-band power spectral density plot for NDR4 pressure measurement systems with various tubing configurations.

All Narrowband

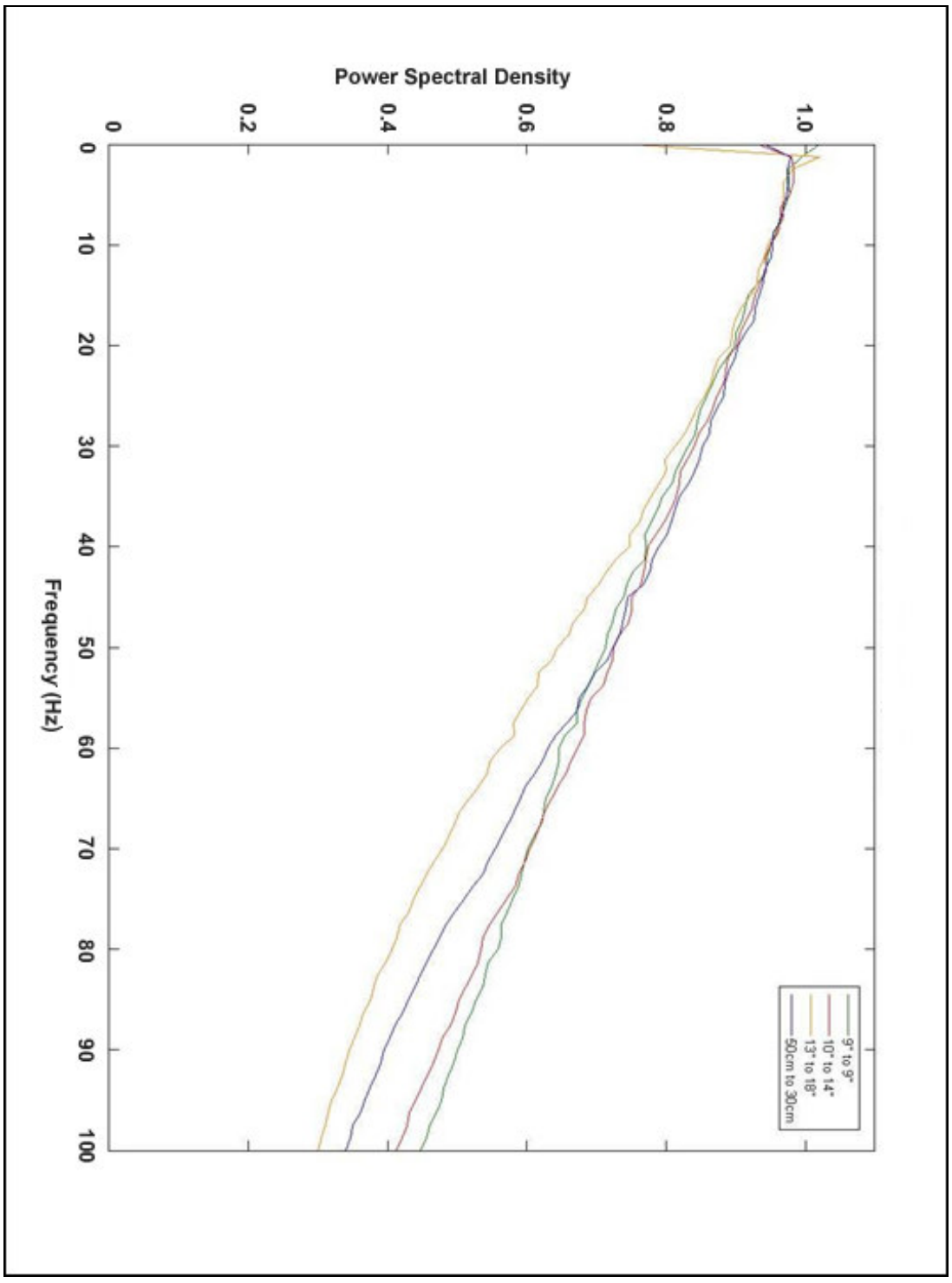

Figure F-4– Narrow-band power spectral density plot for NDR4 pressure measurement systems with various tubing configurations.

7.7 Appendix G - Example Calibration Curves

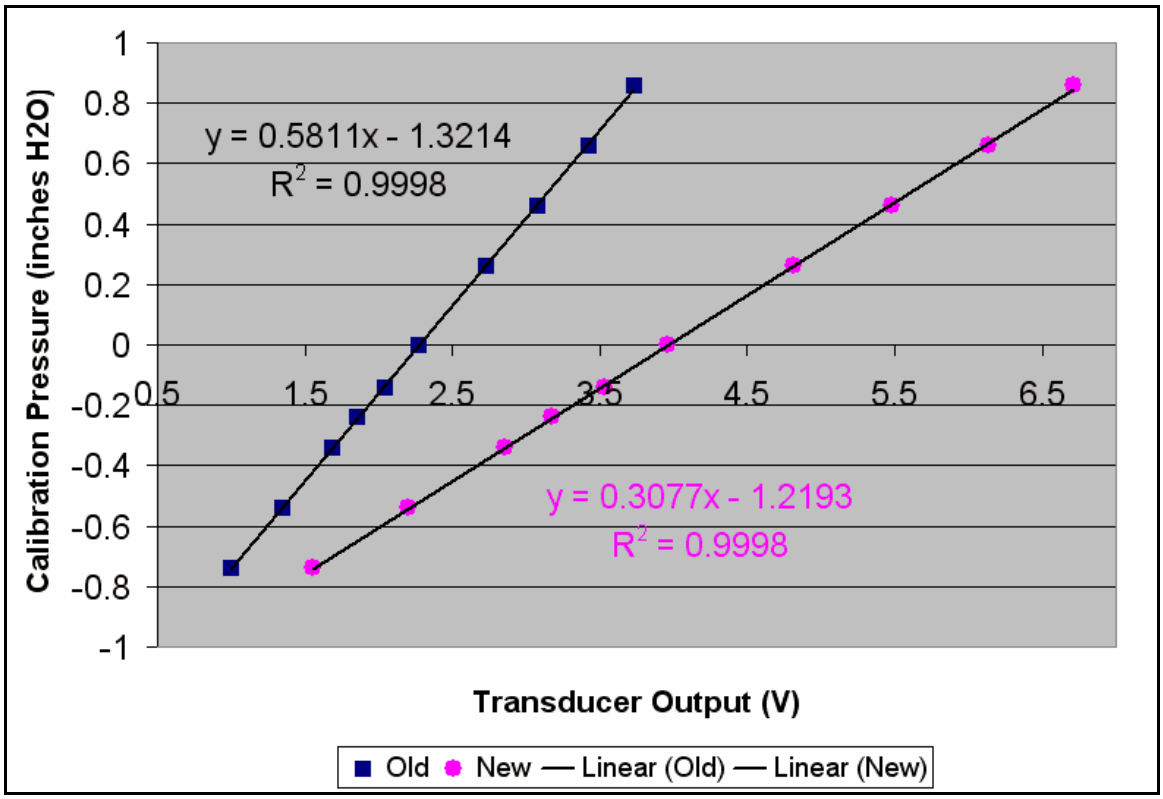

Figure G-1 – Example calibration curves for pressure transducers (DCAL4 model – blue square points and NDR4 model – pink circle points)

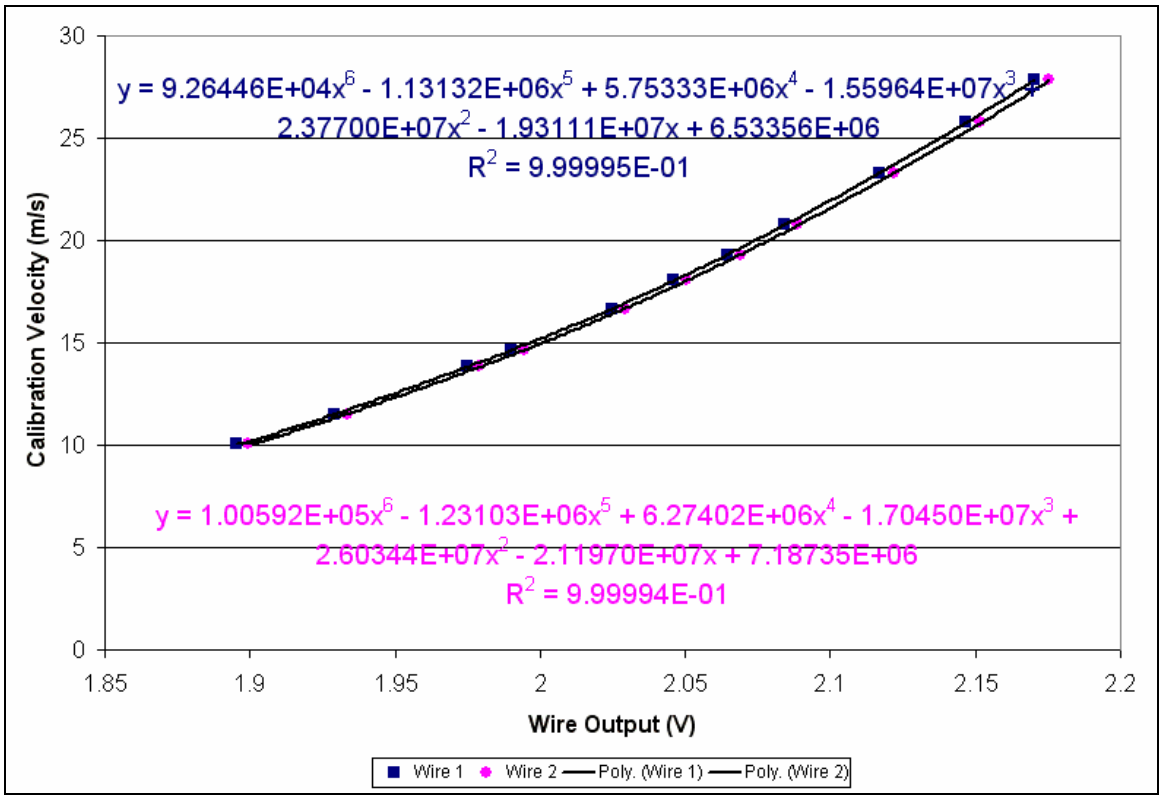

Figure G-2 – Example calibration curves for hot-wire probe (Wire 1 – blue square points and Wire 2 – pink circle points).

7.8 Appendix H - Detailed Investigation of the Tunnel Boundary Layer at Location of Measurements

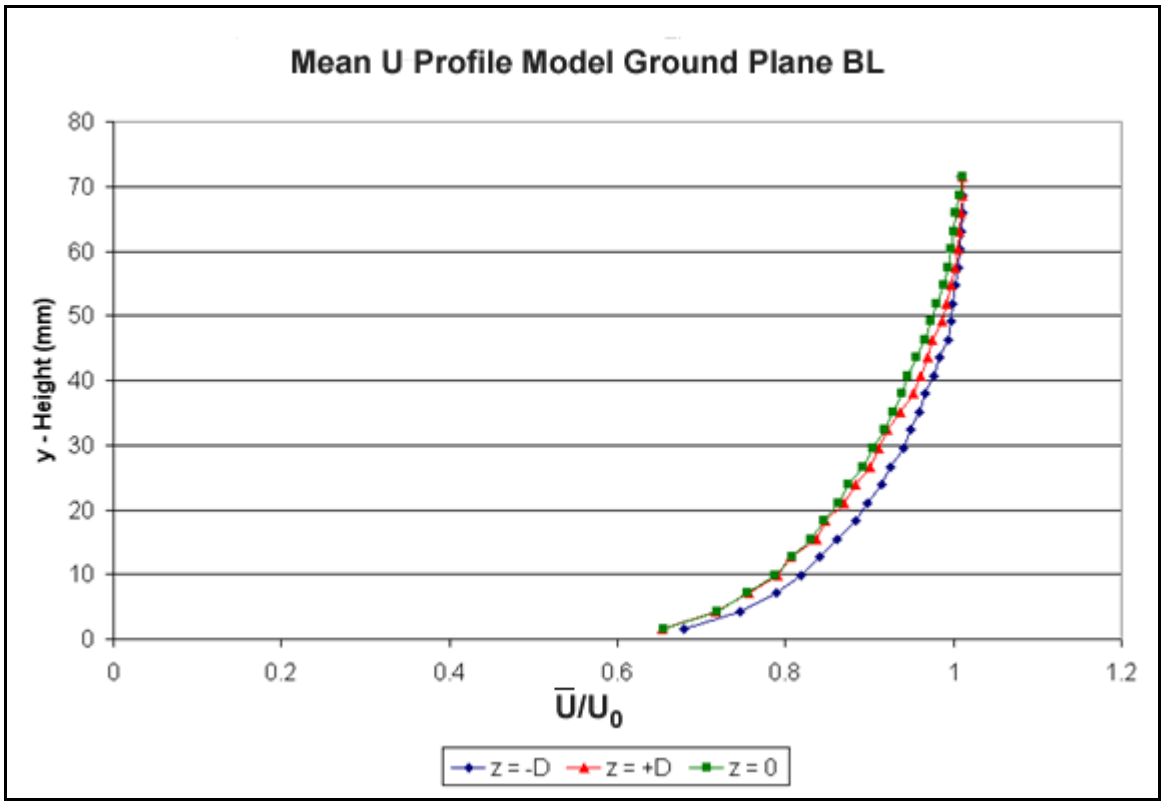

Figure H-1 – High point-density mean stream-wise velocity distributions at three span-wise locations: z = -D, 0 and +D.

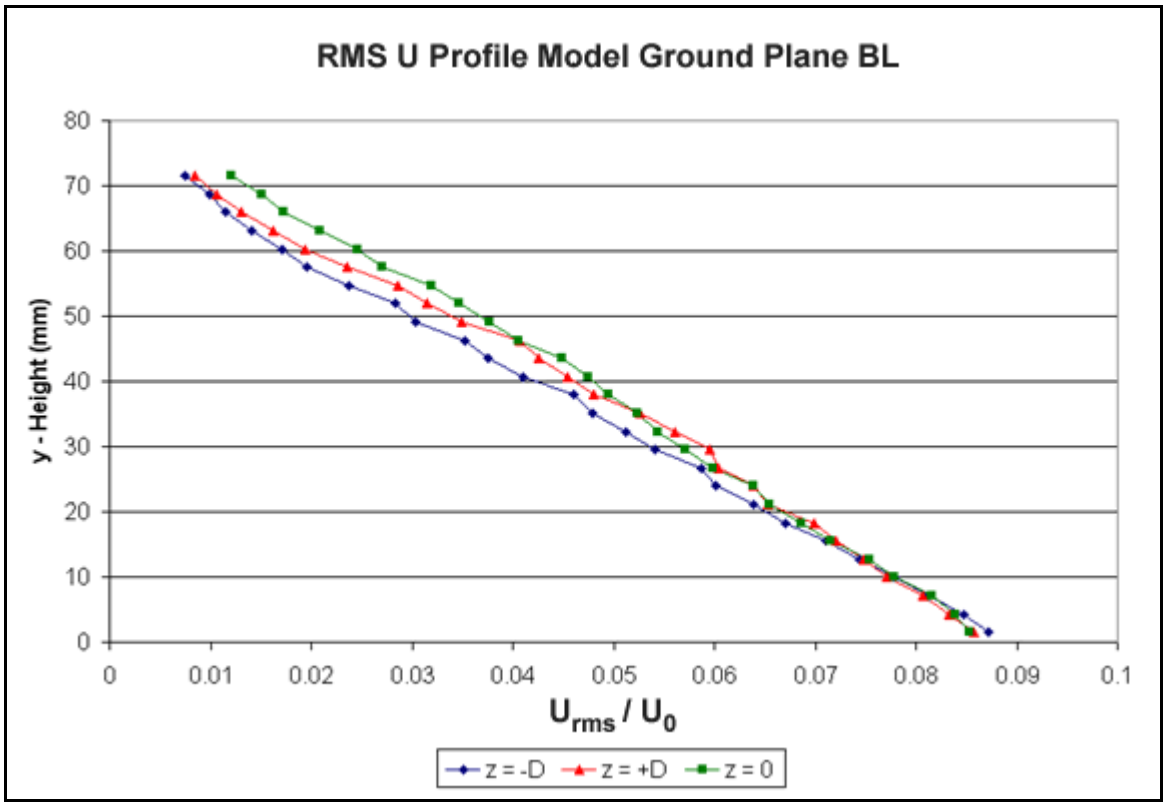

Figure H-2 – High point-density stream-wise RMS velocity distributions at three span-wise locations: z = -D, 0 and +D.

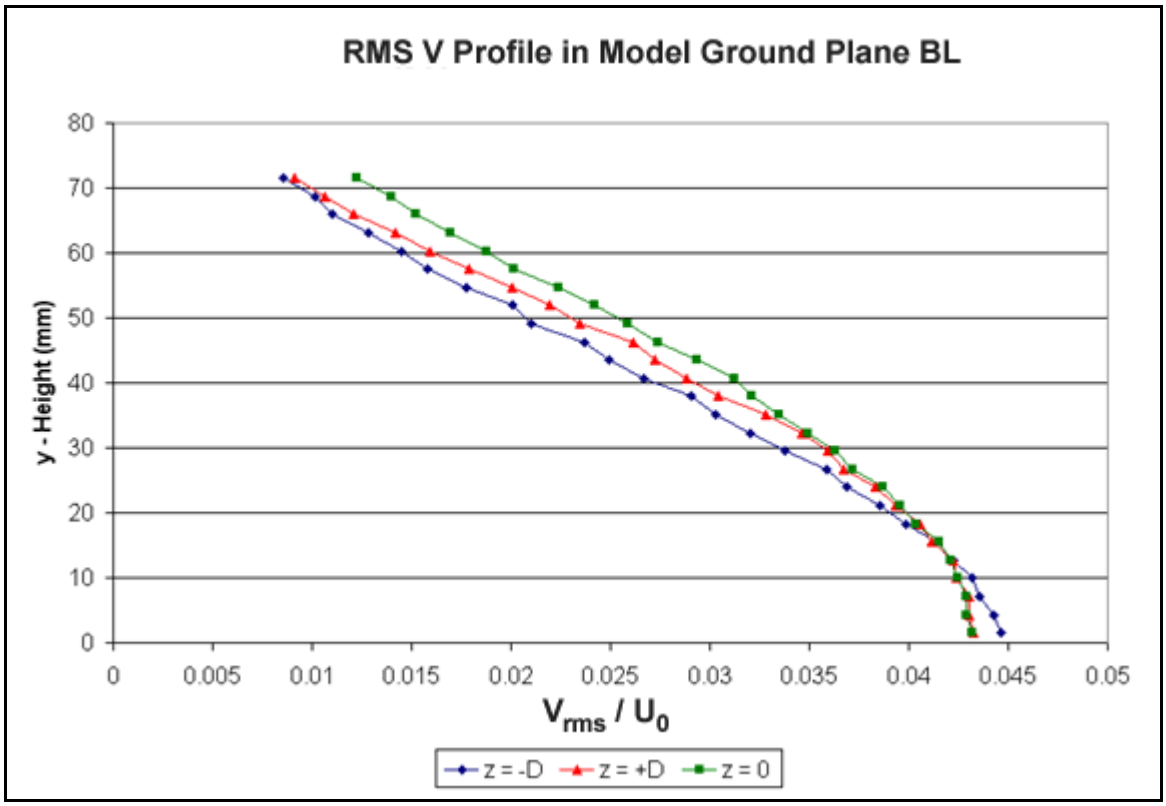

Figure H-3 – High point-density vertical RMS velocity distributions at three span-wise locations: z = -D, 0 and +D.

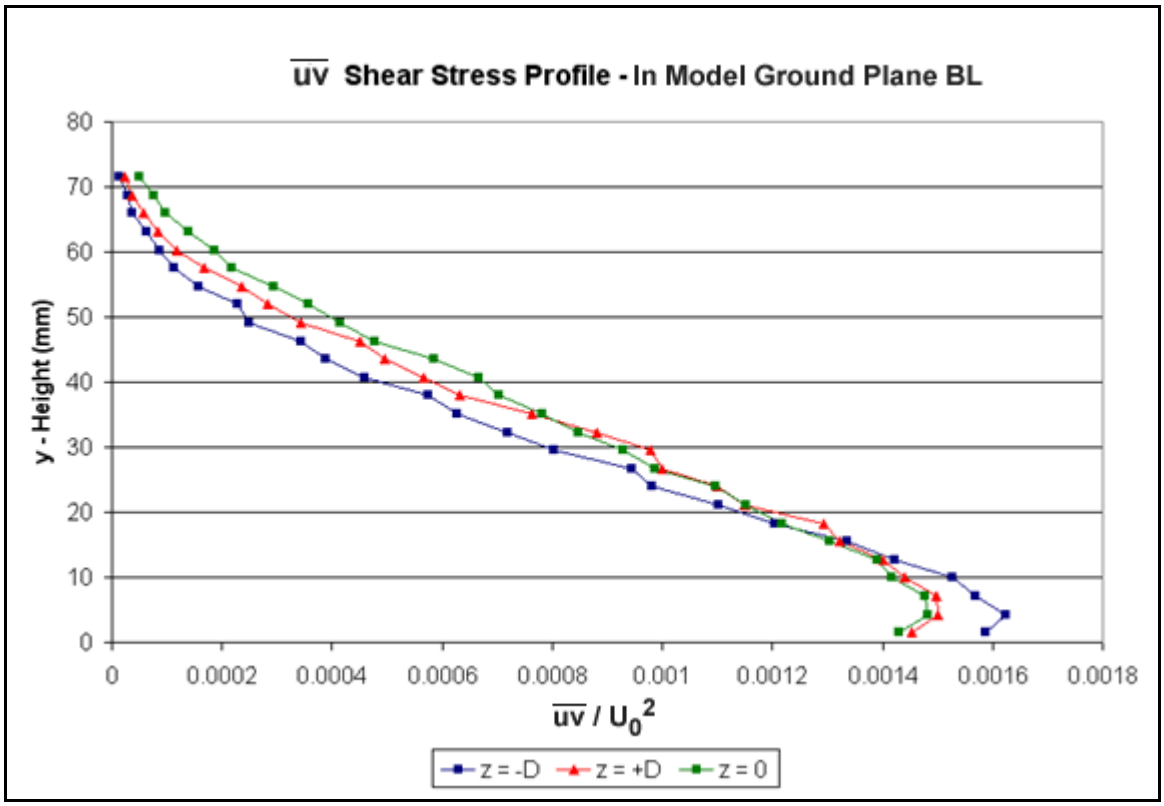

Figure H-4 – High point-density mean uv shear stress at three span-wise locations: z = -D, 0 and +D.

Figures H-1 to H-4 display the profiles generated using the data from this more detailed investigation. In all of these plots, the hot-wire probe started its measurement at 1.5 mm from the roof surface and subsequent measurements were separated vertically by 2.8 mm.

7.9 Appendix I - Tunnel Boundary Layer Flow Comparison at Location of Measurements to Law of the Wall approximation

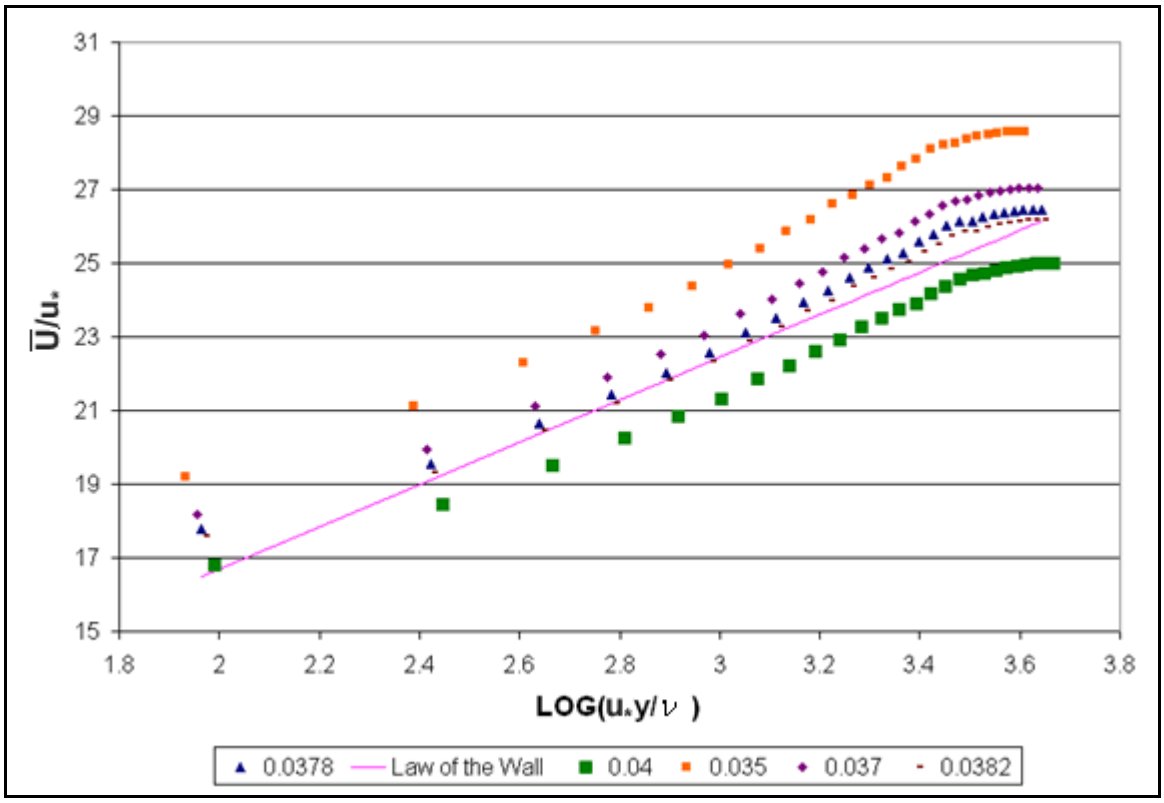

Figure I-1 – Comparing measured data to theoretical turbulent boundary layer flow using data measured at downstream location of cavity measurements at z = -D.

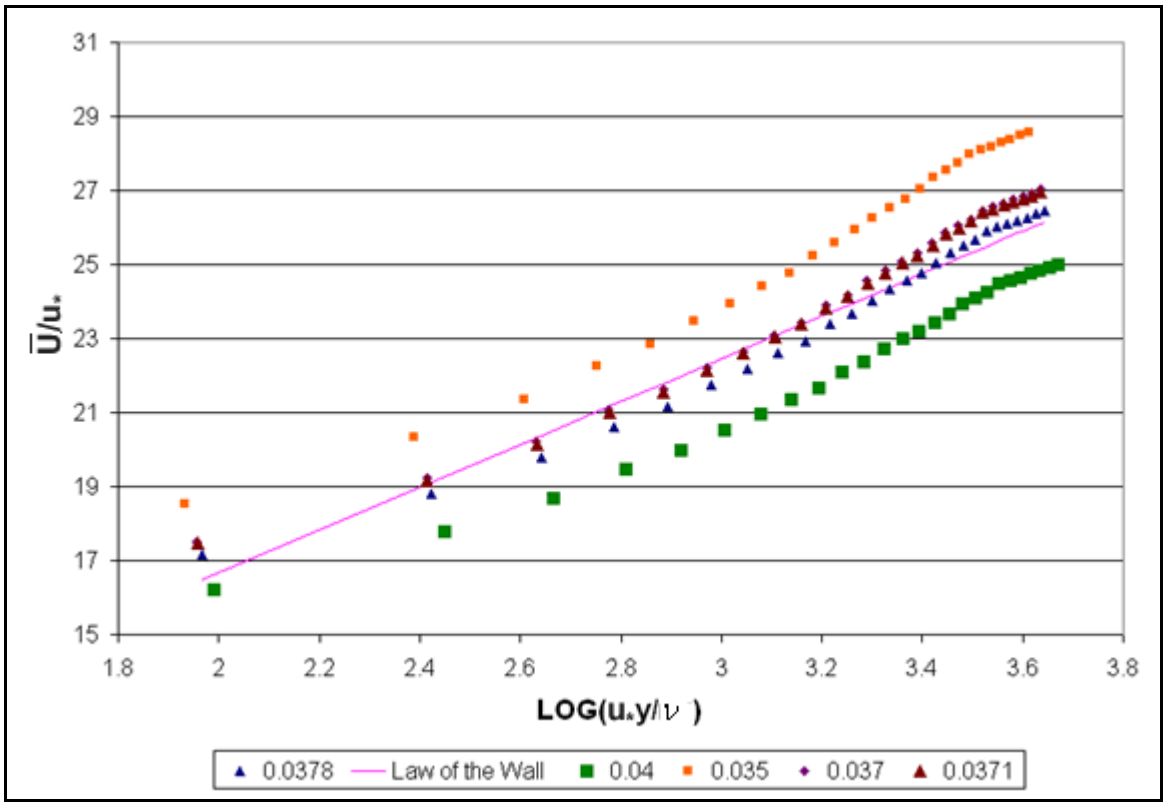

Figure I-2 – Comparing measured data to theoretical turbulent boundary layer flow using data measured at downstream location of cavity measurements at z = 0.

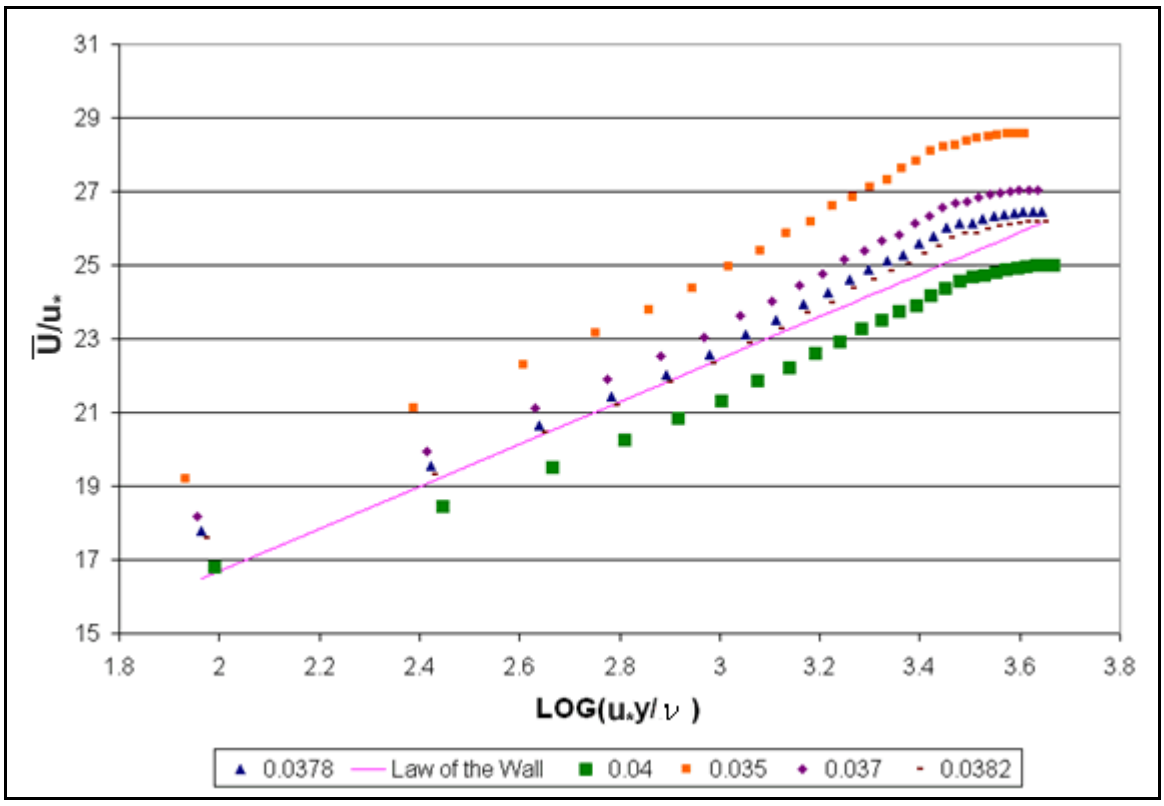

Figure I-3 – Comparing measured data to theoretical turbulent boundary layer flow using data measured at downstream location of cavity measurements at z = +D.

Figures I-1 to I-3 show comparisons of the Law of the Wall approximation, shown by the pink line of fit in the figures, to measured values of stream-wise velocity, $\overline{U}$, at various vertical points in the boundary layer. "Y"-axis co-ordinates in these plots are generated by dividing measured $\overline{U}$ values by an estimated value for the friction velocity u_* and "X"-axis co-ordinates were calculated by taking the base 10 logarithm of the product of the same estimated value for the friction velocity and the height from the wall at which the velocity $\overline{U}$ was measured at, divided by the kinematic viscosity, ν .

By varying the estimated friction velocity, a series of data sets were generated, and comparing the points to the Law of the Wall line calculated using the equation below, the value of the friction velocity used to generate the set of points that most closely matched this line, in terms of a least-squares fit, was deemed to be the friction

velocity approximated using this method. Values for the datasets of varying colour listed in the legends in Figures I-1 to I-3 are values of estimated u_* / U_0 used for generating the points in those particular sets.

$$\boxed{\frac{\overline{U}}{u_*} = 5.75 \log \frac{u_* y}{\nu} + 5.2}$$ (Monin and Yaglom, 1965)

The value for the friction velocity approximated using this method can be compared to the calculated friction velocity.

7.10 Appendix J - Investigating span-wise variability of tunnel flow at measurement location

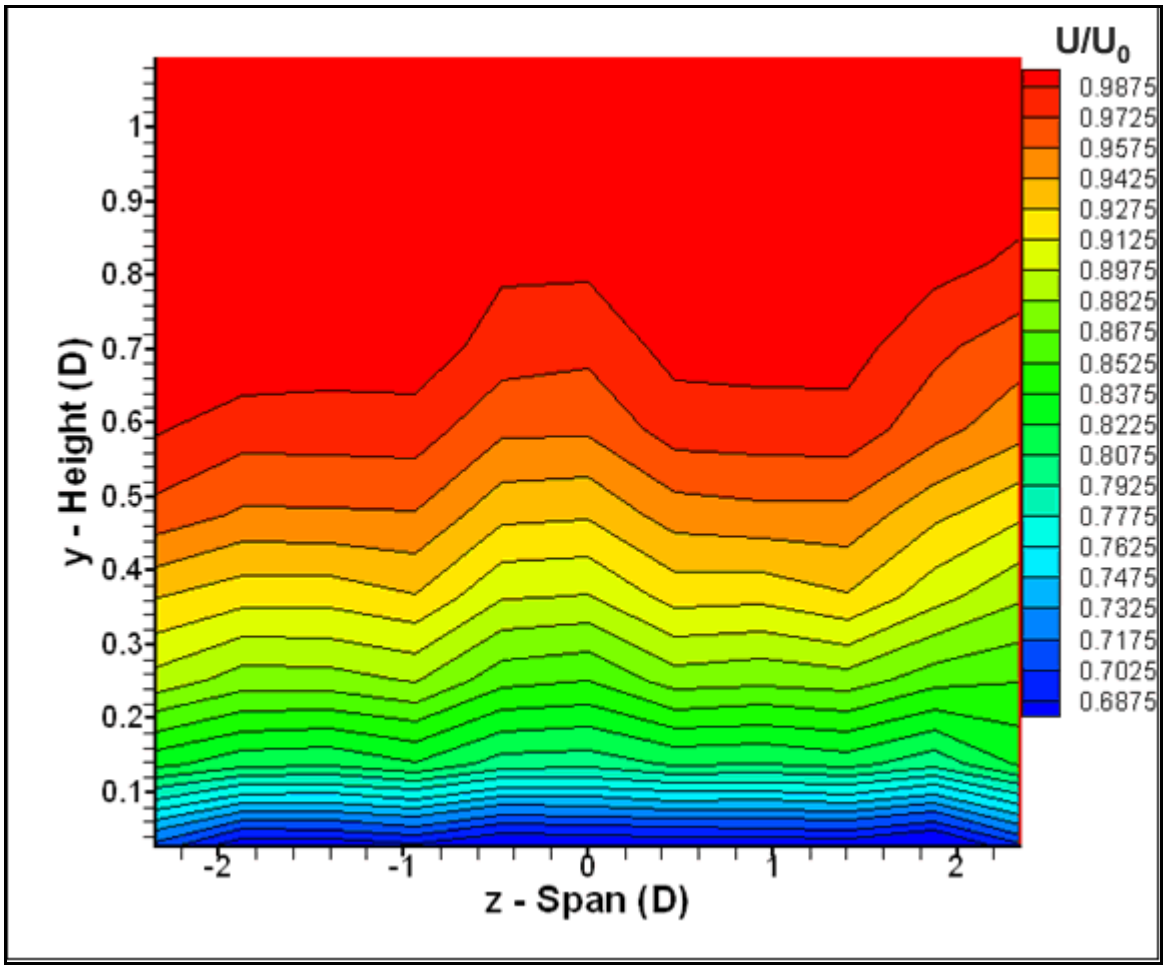

Figure J-1 – Normalized stream-wise velocity measured across ground plane boundary layer at downstream location of cavity measurements.

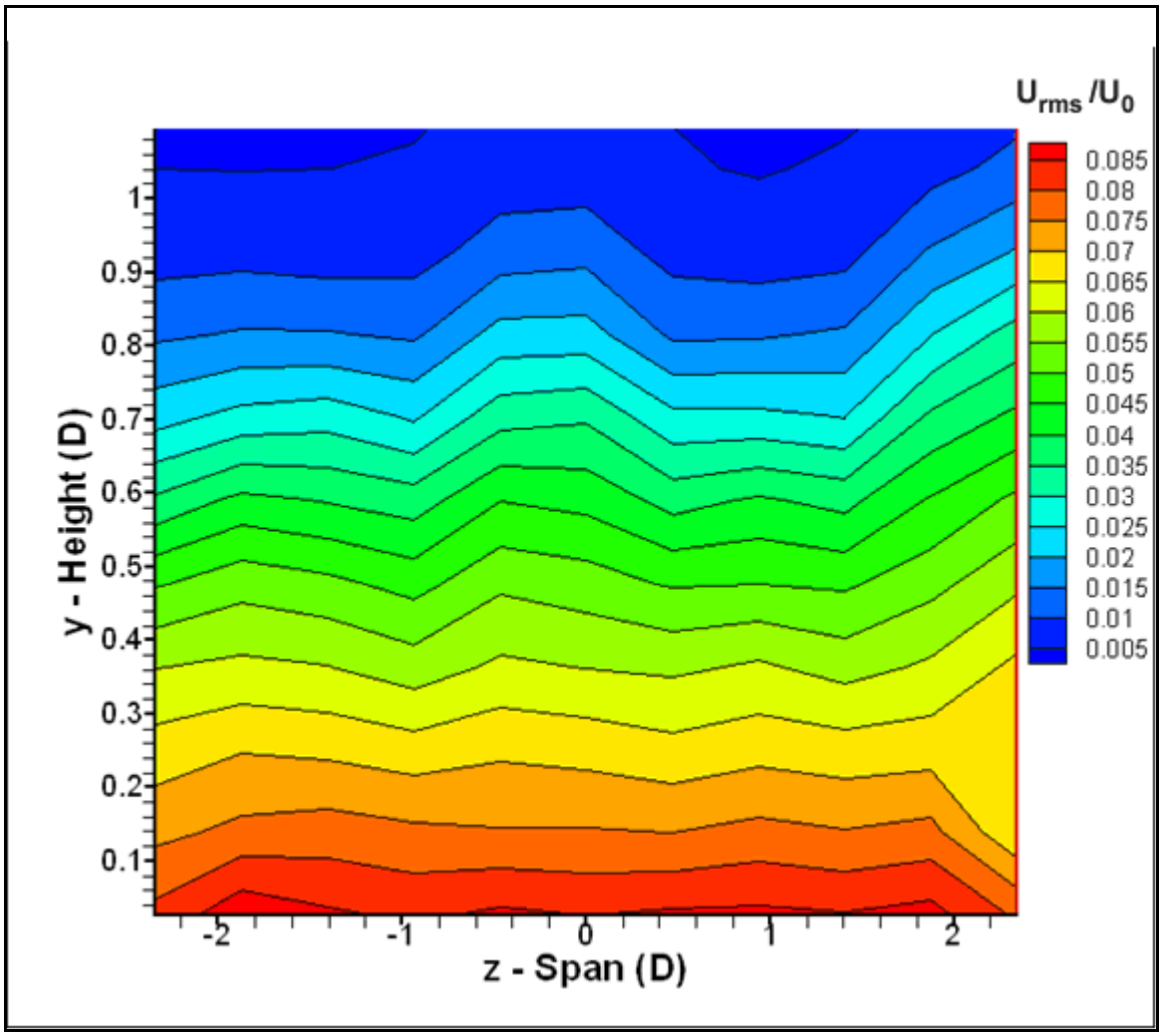

Figure J-2 – Normalized RMS of stream-wise velocity measured across ground plane boundary layer at downstream location of cavity measurements.

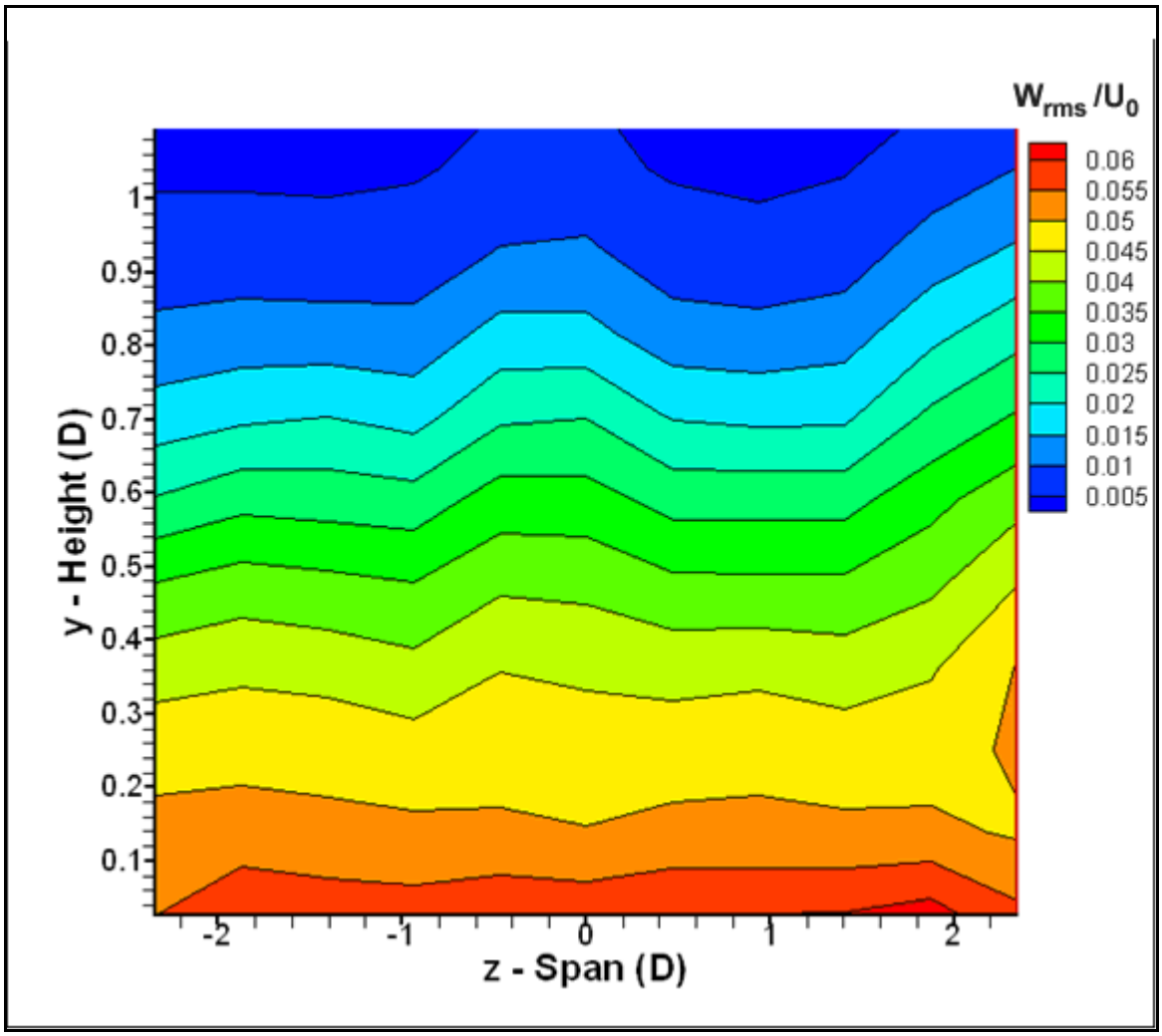

Figure J-3 – Normalized RMS of span-wise velocity measured across ground plane boundary layer at downstream location of cavity measurements.

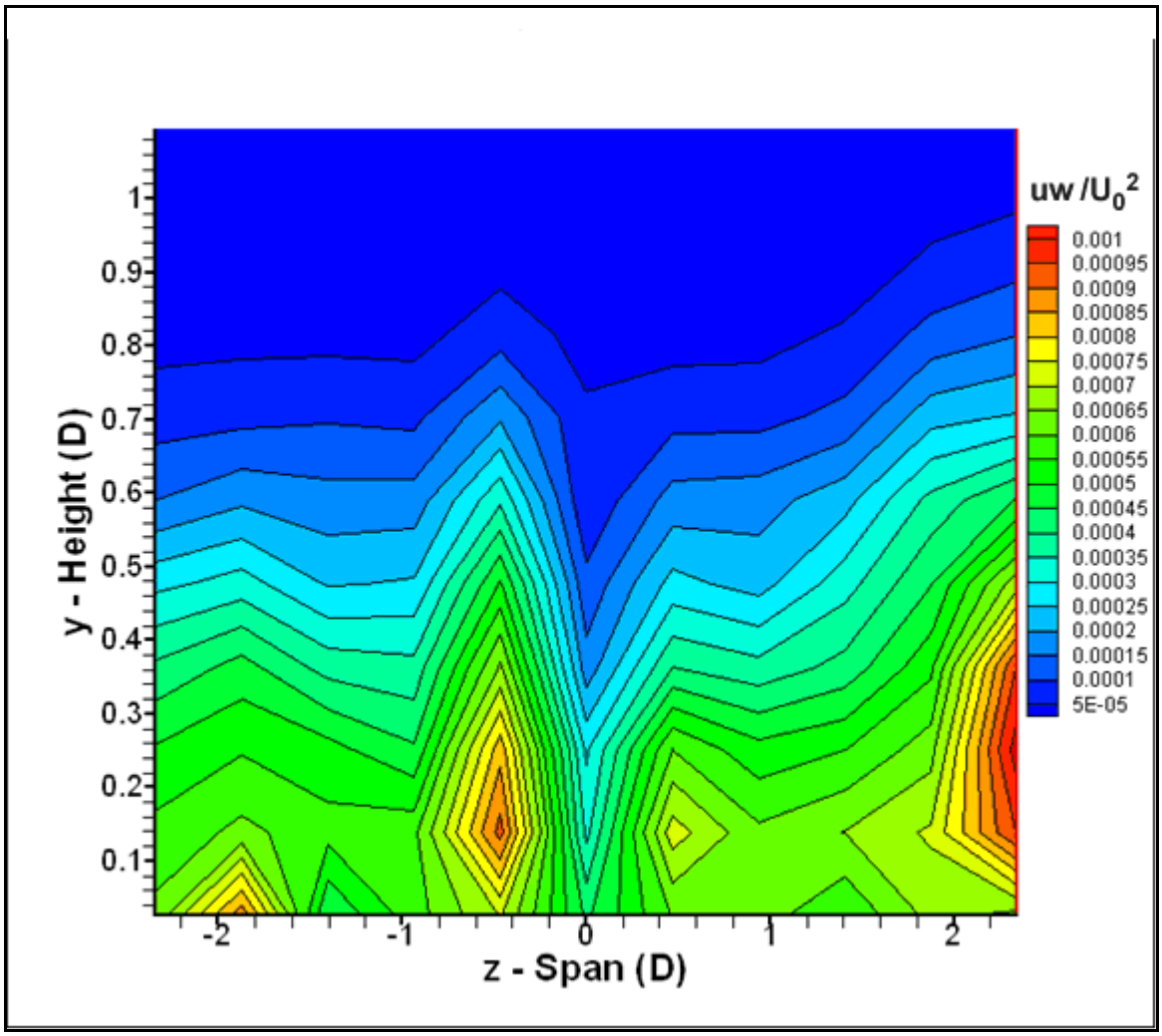

Figure J-4 – Normalized mean uw shear stress measured across ground plane boundary layer at downstream location of cavity measurements.

7.11 Appendix K - Surface Flow Diagram Feature Co-ordinates

Co-ordinates of features discerned from mean surface pressure patterns from cavity flow measurements are listed below in Table K-1.

	Cylindrical Co-ordinates (2r/D, θ, y/h)		
Index	h/D = 0.20	h/D = 0.47	h/D = 0.70
V_1	(1, 55°, 0.86)	(0.88, 30°, 1.0)	(1.0, 105°, 0.27)
V_2	(1, 105°, 0.72)	(1.0, 72°, 0.62)	(1.0, 255°, 0.25)
V_3	(1, 250°, 0.79)	*N/A*	(1.0, 345°, 0.46)
V_4	(1, 305°, 0.82)	*N/A*	*N/A*
A_1	(1, 200°, 0.13)	(1.0, 155°, 0.03)	(1.0, 162°, 0.023)
A_2	*N/A*	*N/A*	(1.0, 205°, 0.014)
C_1	*N/A*	(1.0, 240°, 0)	*N/A*

Table K-1 – Cylindrical co-ordinates of surface flow features for various cavity depth configurations.

Co-ordinates listed in this table are given in cylindrical co-ordinates with origin at the cavity centre at the height of the cavity lip. The radial co-ordinate is normalized by the cavity radius (D/2), thus features on the cavity sidewall carry a radial co-ordinate of 1.0, and the height co-ordinate is normalized by the cavity depth for the given depth configuration, such that a feature on the cavity base carries a height co-ordinate of 1.0.

7.12 Appendix L - Wide-band Power Spectral Density Example for Cavity Wake Velocity Measurements

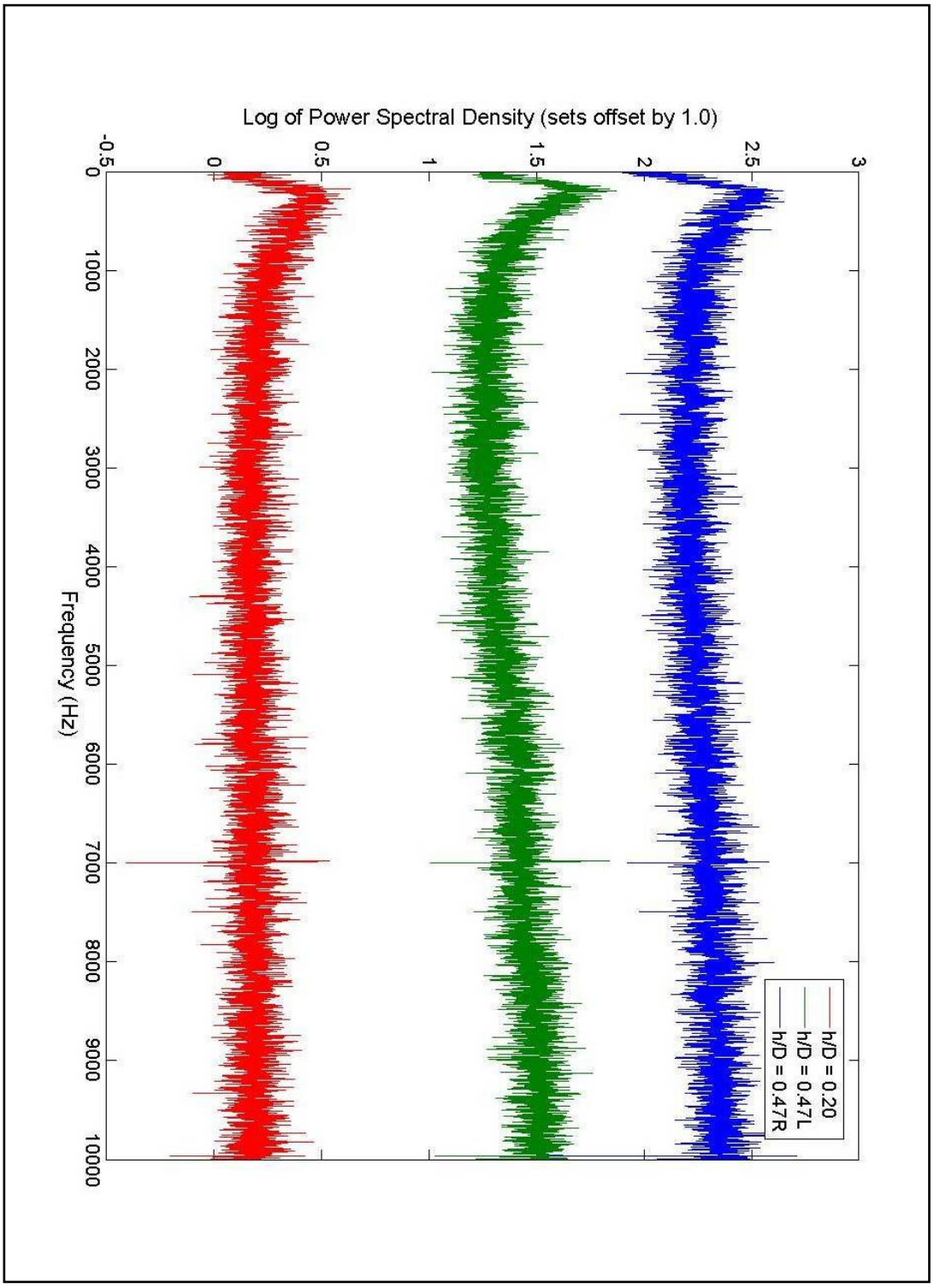

Figure L-1 – Wide-band power spectral density example for span-wise velocity fluctuations at Point 7 in the hot-wire measurement grid.

7.13 Appendix M - Frequency Response Comparison between Pressure Transducer and Microphone Systems

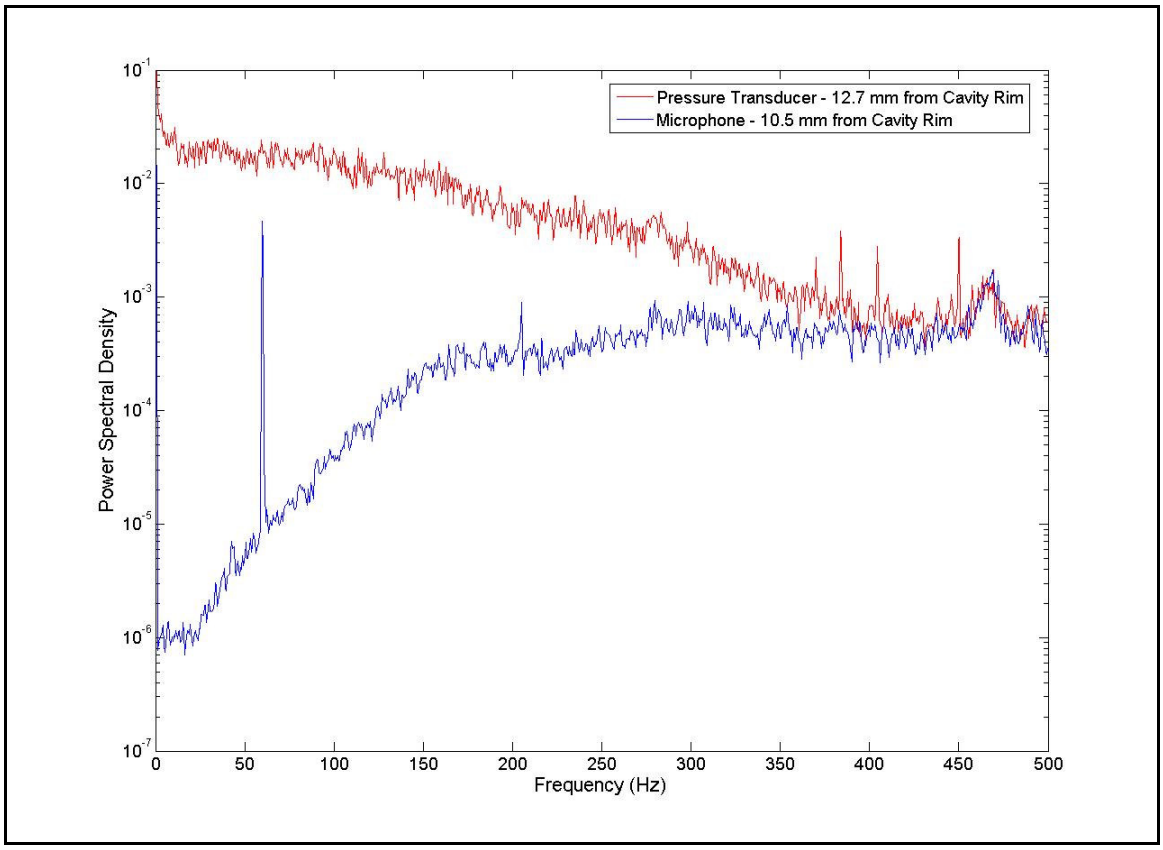

Figure M-1 – Comparison of Pressure Transducer and Microphone Power Spectral Density plots generated from data taken near the same location and configuration in the cavity model.

7.14 Appendix N - Identifying Fan-Related Noise Sources

The closed-loop wind tunnel used for experiments was powered by two 7-bladed axial fans, and, as is usual in wind tunnel experiments, certain noise sources are related to the blade-passing frequency of these fans.

An experiment was devised to determine which noise in the frequency spectrum was due to the fans. By sampling a surface-mounted microphone in the tunnel roof for various known tunnel speeds, fan-related peaks in the frequency spectra were discerned from other noise sources by dividing the peak frequencies by the measured free-stream speed for the given trial. Peaks found to have similar values for this quotient f/U_0 at different fan speeds were thus attributed to fan effects.

Power Spectral Density plots for various tunnel fan speeds are presented in Figure N-1.

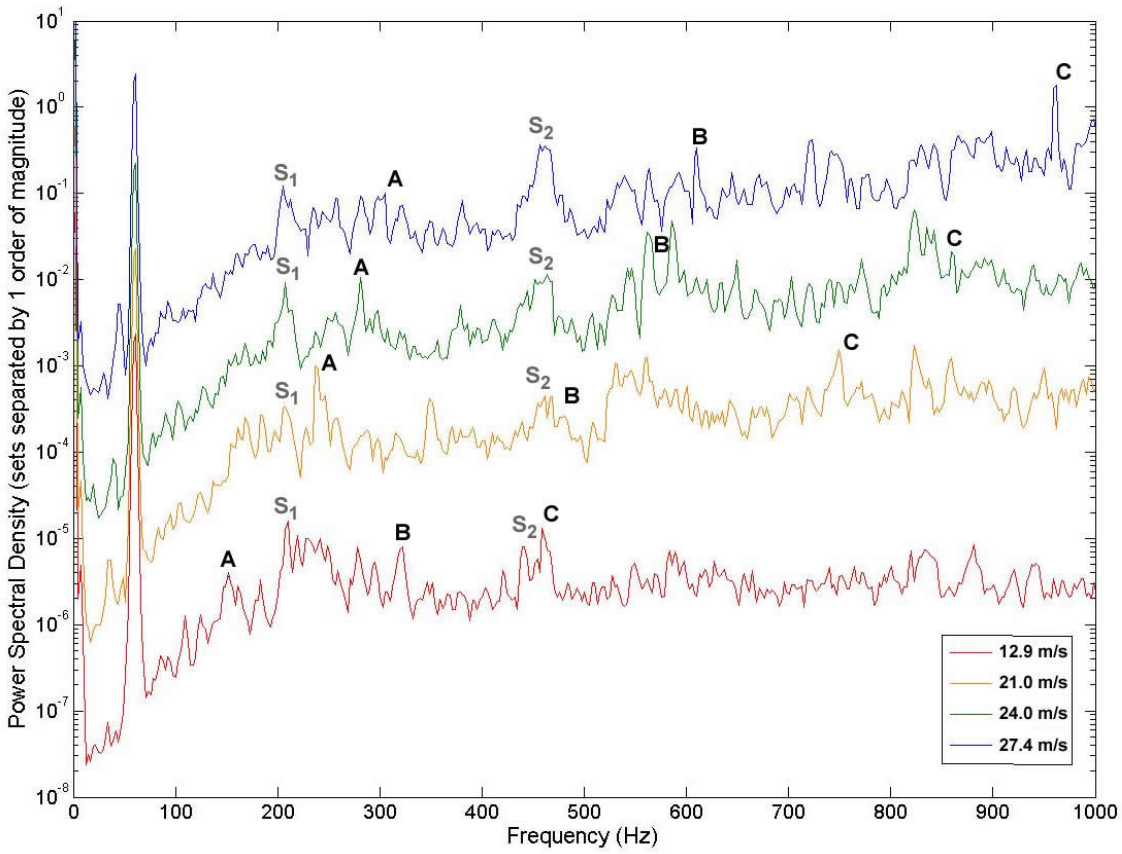

Figure N-1 – Power Spectral Density plots created from tunnel noise data for various tunnel fan speeds, separated by 1.5 orders of magnitude for clarity.

Figure N-1 displays peaks clearly related to the fan modes where A, B and C denote the first, second and third fan passing modes, respectively. Peaks which do not change frequency with changing fan speed are attributable acoustic sources such as ambient lab noise or geometrically-related resonances due to wind tunnel dimensions such as those labeled S_1 and S_2 in Figure N-1.

7.15 Appendix O - LabVIEW Program Description

Due to the awkward modular representation of LabVIEW vi programs, the program created to automate the movement of the two axis traverse and acquirement of hot-wire raw voltage data is briefly described rather than comprehensively listed.

This program was developed in conjunction with Velmex Inc. and allowed the data acquisition computer to communicate with the stepper motor controller (which controlled the motion of the two axes of the traverse) via the serial port using a built-in serial port communication vi in addition to allowing data from the hot-wire system to be acquired via the data acquisition card.

The program carried out the following steps illustrated in the block diagram, Figure O-1 below:

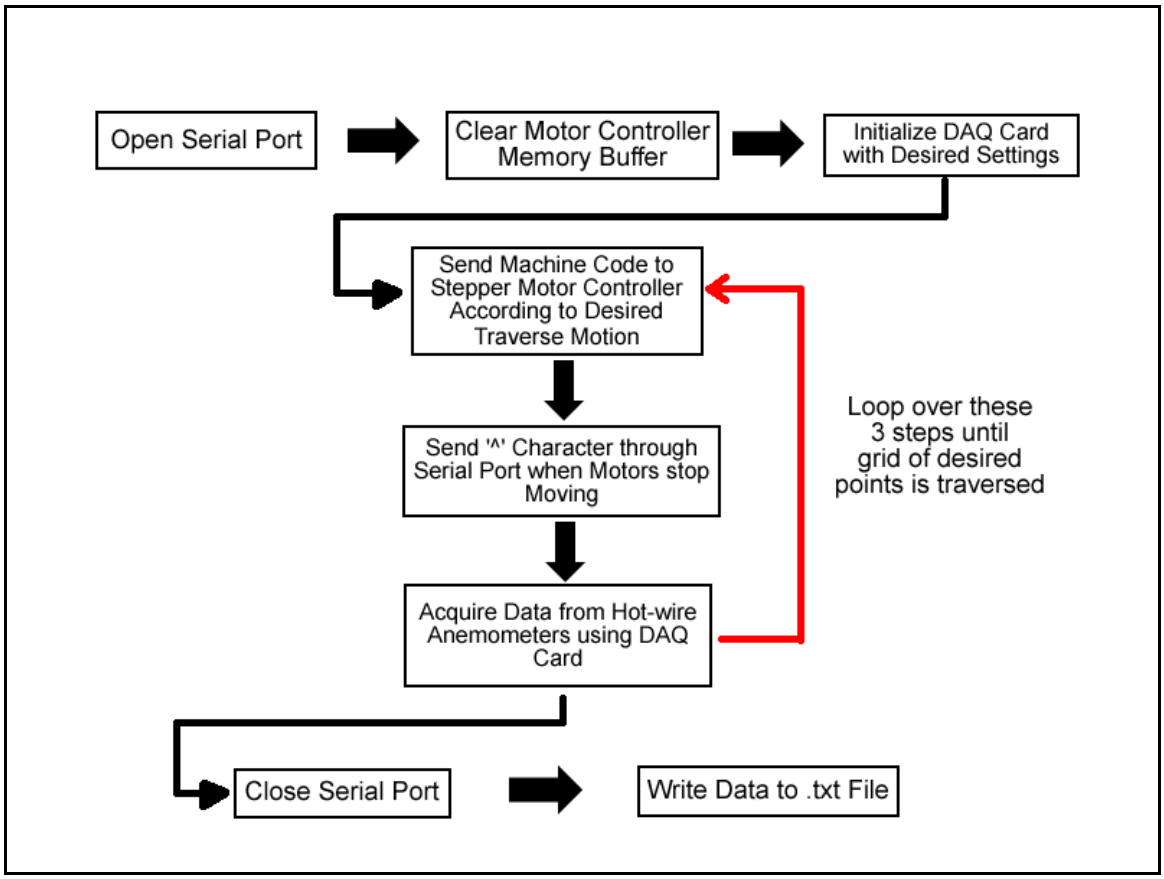

Figure O-1 – Block diagram summarizing functions carried out by LabVIEW program to allow a grid of hot-wire measurements to be carried out using the two-axis traverse and DAQ card.

7.16 Appendix P - MATLAB Command Line Calls used for Analysis

Frequency Analysis – Power Spectral Density Calculation

After reading the text file from the MATLAB 'work' folder into MATLAB using the load command:

```
load filename.txt;
```

Where 'filename' is the name of the data file containing time series data to be frequency analyzed. The power spectral density of the data was then calculated using:

```
[Pxx,F] = psd(filename,numFFTpts,sampleRate,windowOverlap);
```

Where 'filename' would be the default name for the workspace variable read in in the first step, numFFTpts is the number of points desired in the plot (effectively, the bin resolution), sampleRate is the rate at which the time series data was acquired in samples/s and windowOverlap is the number of samples desired to be used in overlapping signal windows in the psd calculation. Since a 50% overlap was used for the current analysis, windowOverlap = 0.5 * numFFTpts.

This call would create two one-dimensional arrays as workspace variables Pxx and F with Pxx being the relative amplitude data (or y-axis info) and F being the frequency bins (or x-axis info).

The base-10 log of Pxx was taken to make dominant peaks more pronounced relative to noise in the spectrum:

```
Pxx = log10(Pxx);
```

And finally, plotting the result:

```
plot(F,Pxx);
```

7.17 Appendix Q - Additional Cavity Model Pressure Contour Diagrams

Mean Surface Pressures

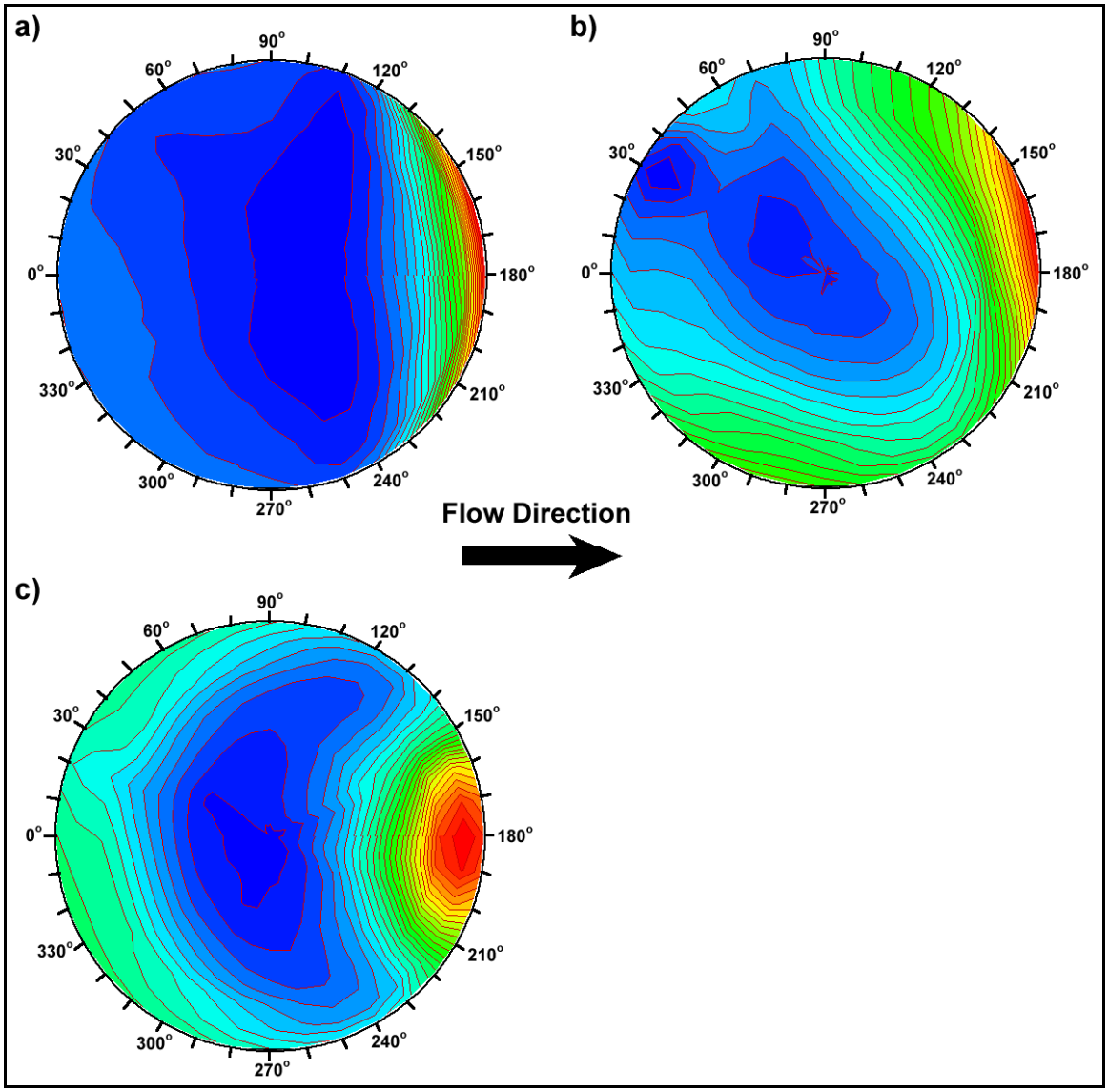

Figure Q-1 – High resolution mean pressure contours on cavity base.

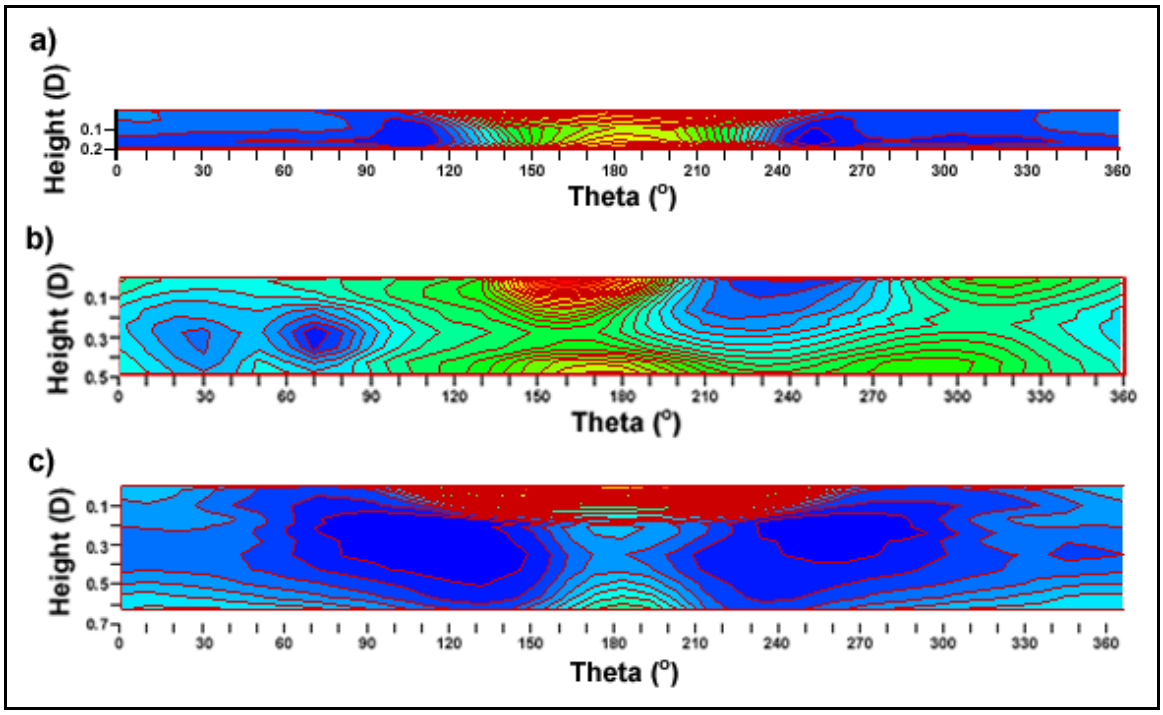

Figure Q-2 – High resolution mean pressure contours on unwrapped cavity sidewall.

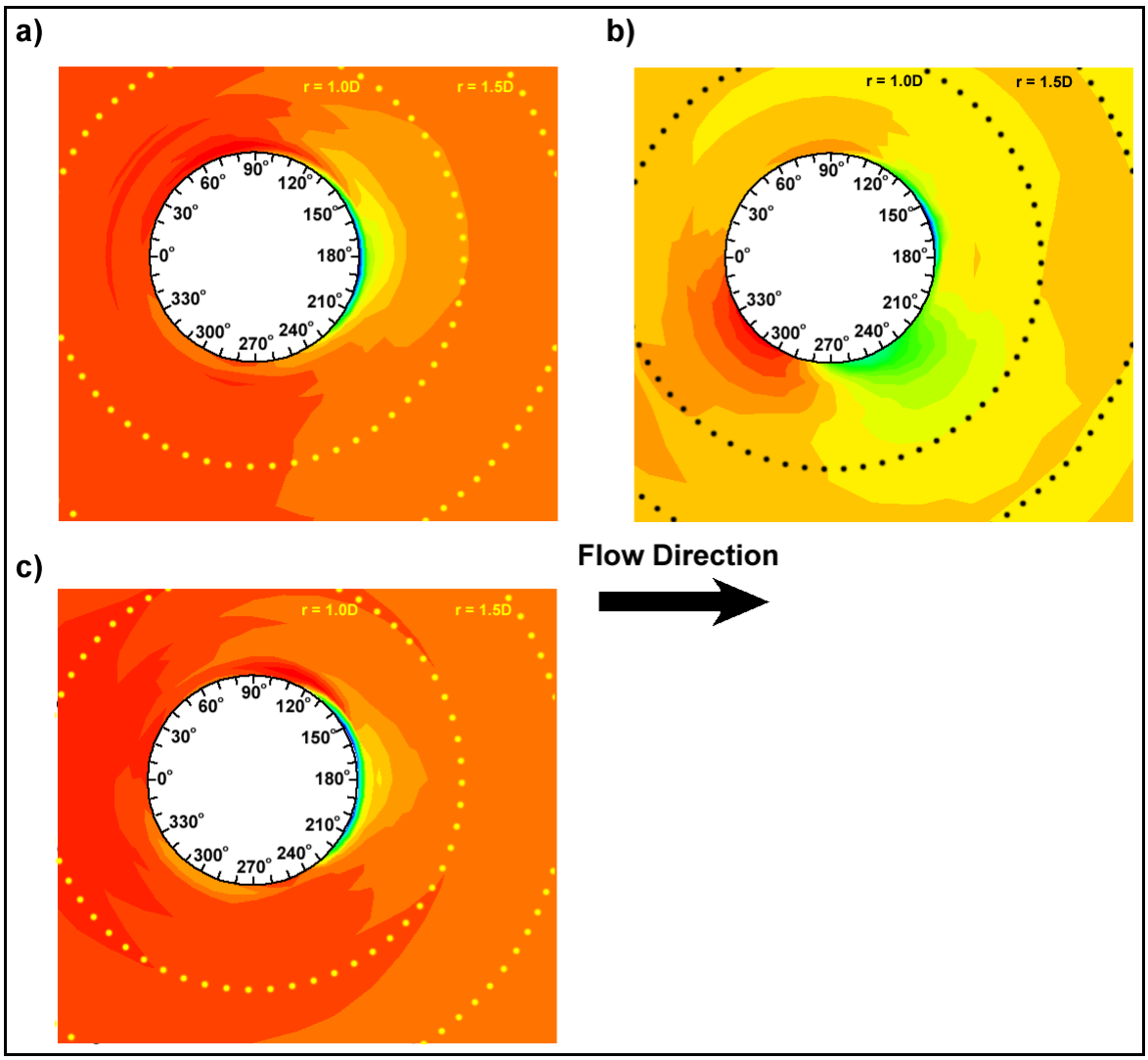

Figure Q-3 – High resolution mean pressure contours on unwrapped cavity turntable.

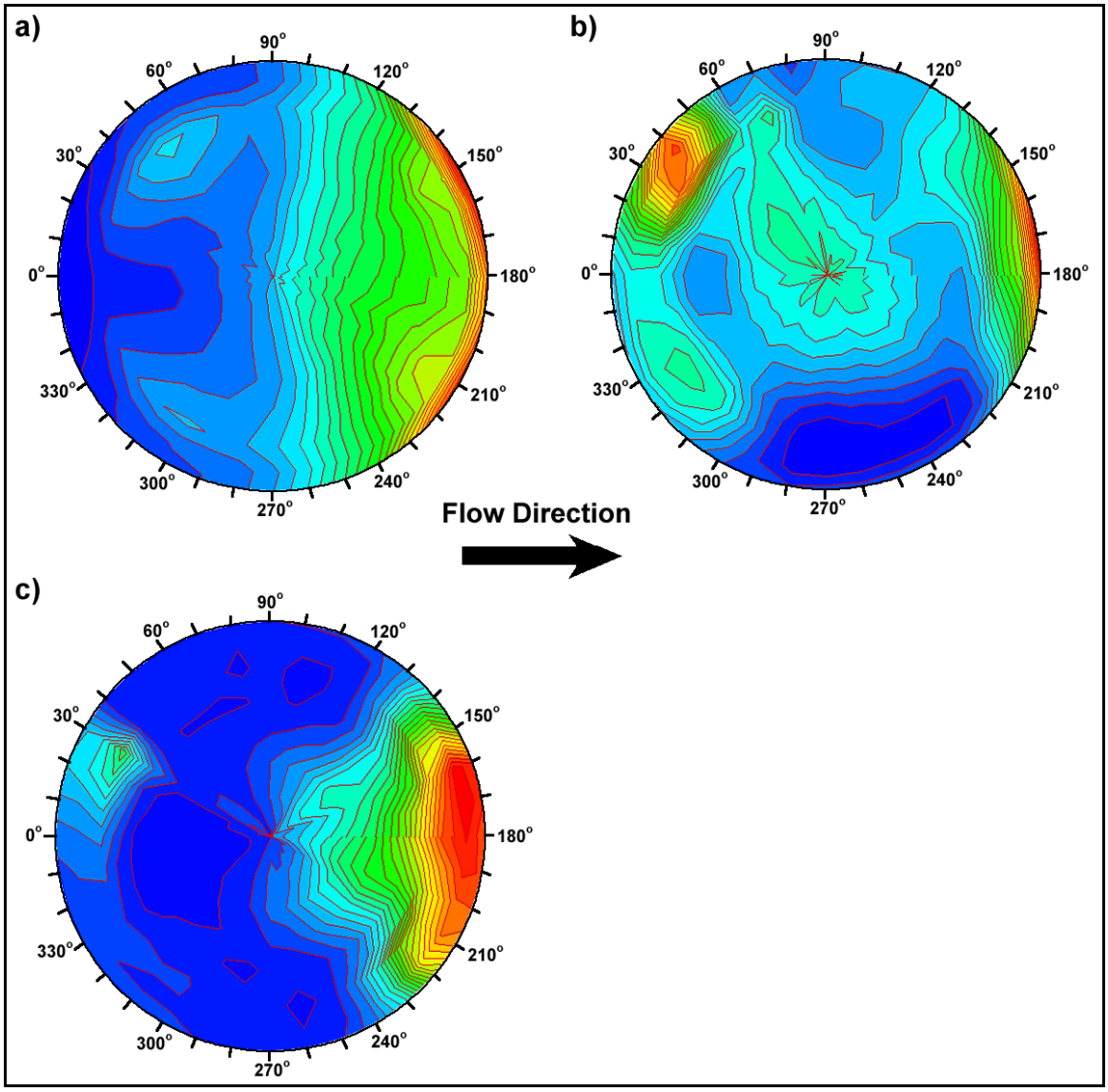

Figure Q-4 – High resolution rms pressure contours on cavity base.

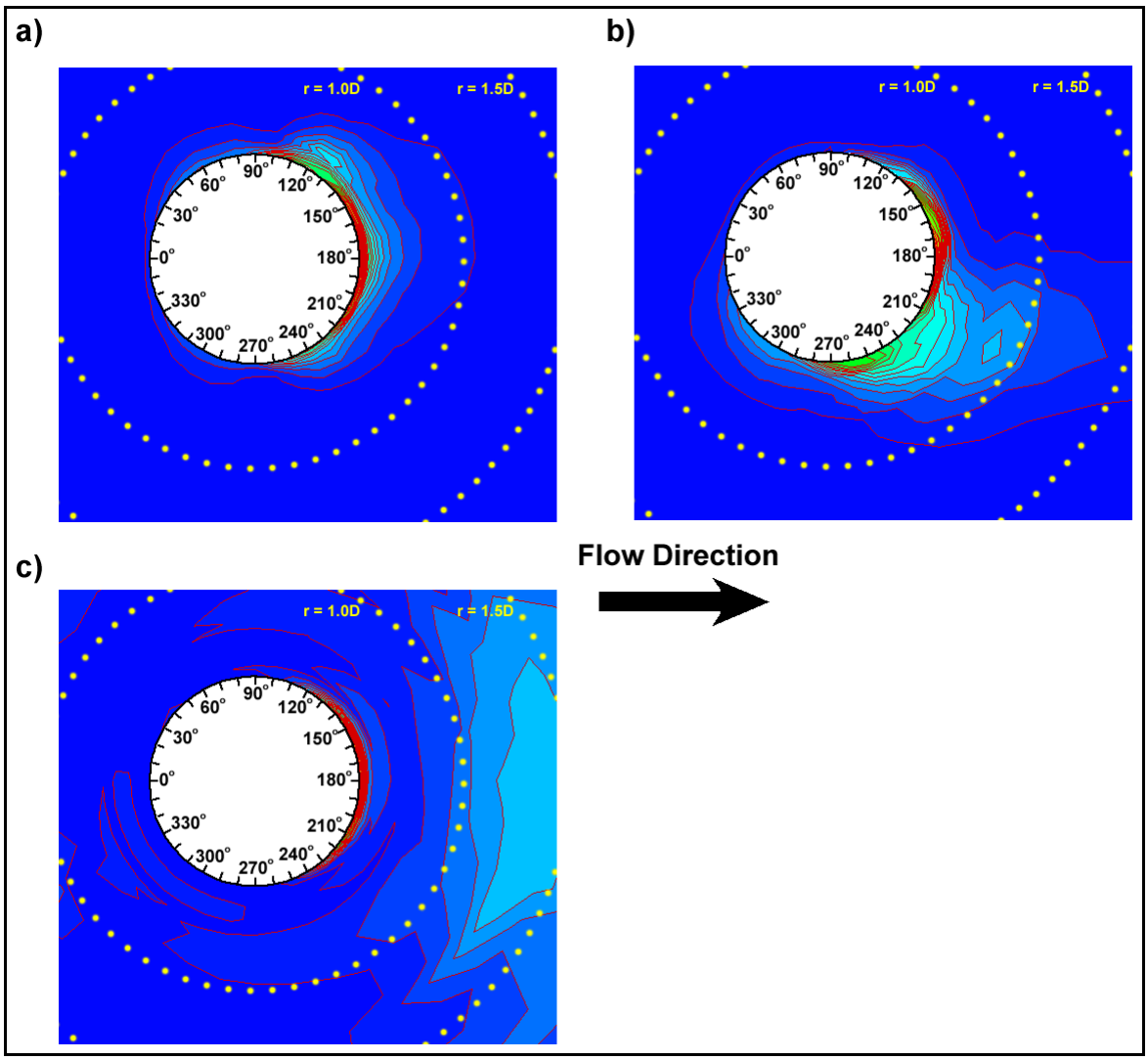

Figure Q-5 – High resolution rms pressure contours on cavity turntable.

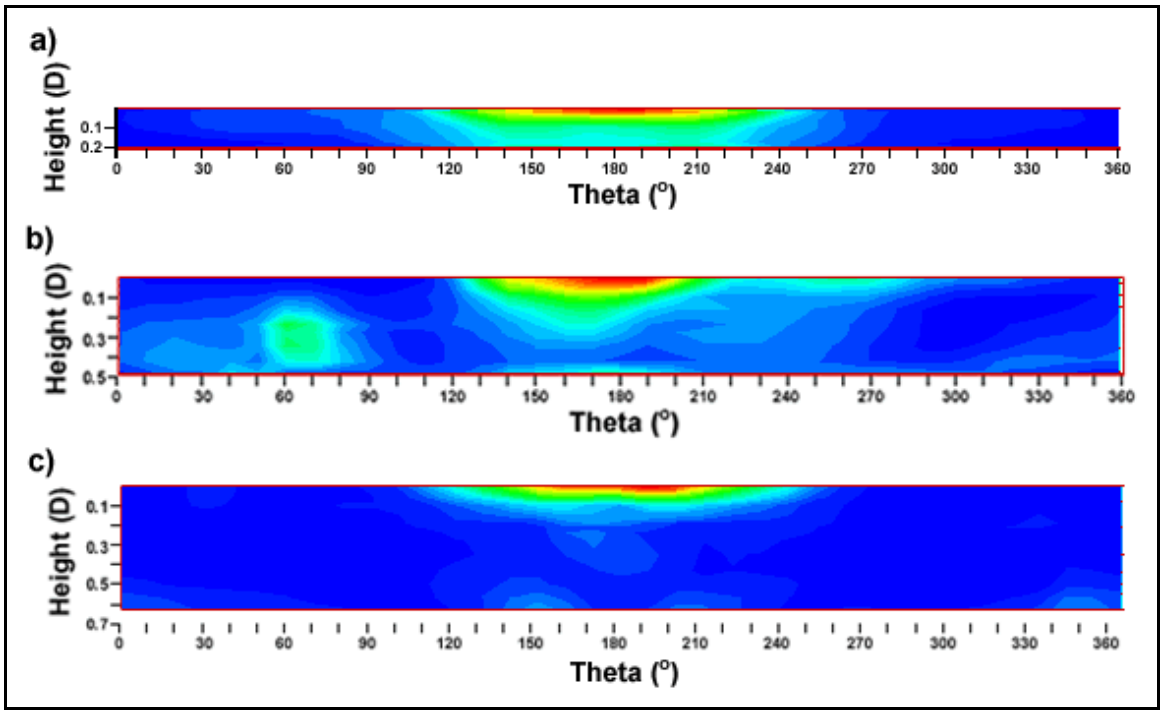

Figure Q-6 – High resolution rms pressure contours on unwrapped cavity sidewall.

7.18 Appendix R - Discussion of Microphone Fluctuating Pressure Measurements

Microphone Fluctuating Pressure Analysis

An array of model surface-mounted miniature microphones was also used to measure fluctuating pressures on the cavity model. Part of the intent of measuring with these devices was to have a check for the RMS pressures measured using the pressure transducer system, however, in terms of accuracy, these microphones did not allow for a reliable check of the data to be carried out.

The most significant problem with this system was the lack of availability of an adequate calibration system to carry out the frequently required calibrations for each microphone. A Sound Pressure Level Meter (SPL Meter) was borrowed from the UWO Audiology department on one occasion to calibrate the microphones, but some of the microphones were later broken and hence replaced between the time of calibration and the time of measurement. That, combined with the fact that some adjustments were made to the circuitry and wiring in this time to improve the microphone signal characteristics, effectively nullified the accuracy of the initial calibration. However, with the addition of an accurate SPL Meter along with the movement of the anti-drift circuit from a breadboard to the shielded, soldered circuit board on which the offset-removal circuit was connected it is believed that this system could become a more repeatable and accurate system.

Figure R-1 compares RMS measurements taken at various cavity configurations.

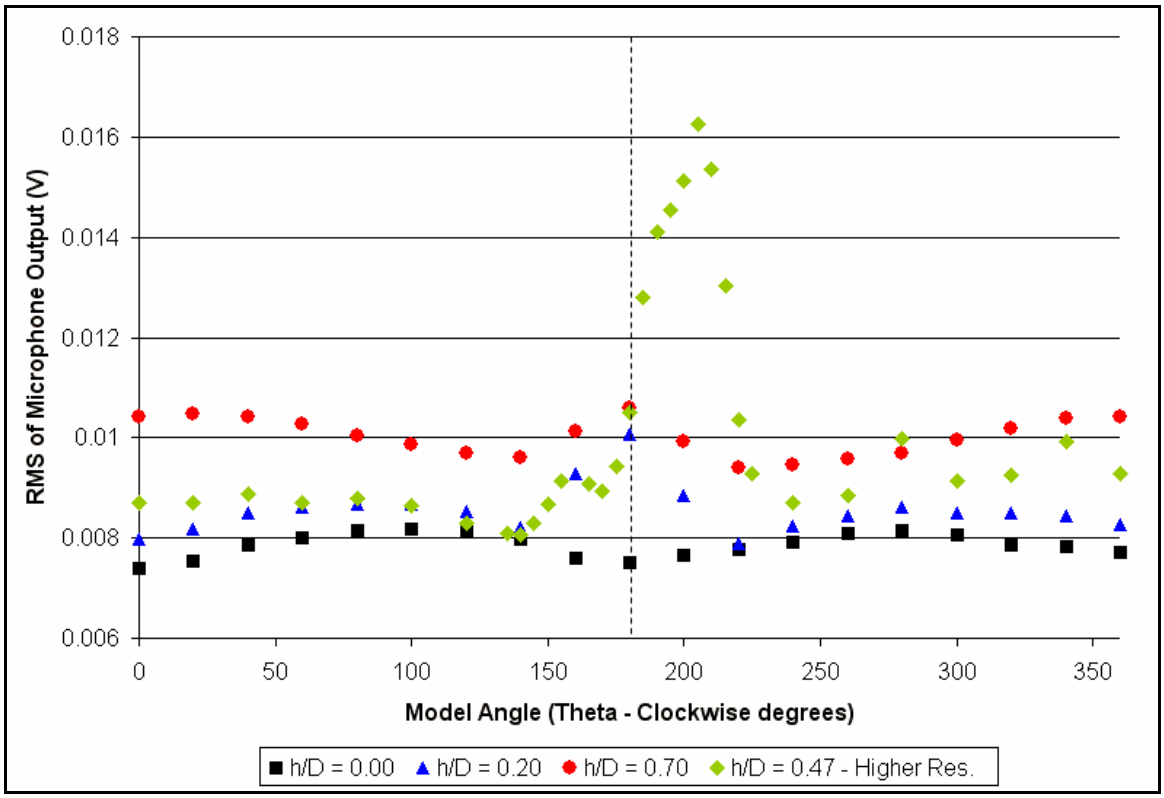

Figure R-1 – Microphone RMS Measurements taken at a point 88 mm from the cavity centre on the model turntable. Measurements for all cases except h/D = 0.47 were taken using a 20 degree rotation between points. For h/D = 0.47, measurements were spaced in 20 degree increments and 5 degree increments in regions of interest.

VITA

Name:	Jesse T. Dybenko
Post-secondary Education and Degrees:	Queen's University Kingston, Ontario, Canada 1999-2003 B.Sc.E. *The* University *of* Western Ontario London, Ontario, Canada 2003-2005 M.E.Sc.
Honours and Awards:	● Nominated for Graduate Student Teaching Award – *The* University *of* Western Ontario (2005) ● Special University Scholarship (SUS) – *The* University *of* Western Ontario (2004) ● OAC Physics Award – Mayfield Secondary School (1999) ● Winner of Mayfield Secondary School Science Fair (1998 and 1999)
Related Work Experience:	● Teaching Assistant, *The* University *of* Western Ontario, 2003-2005 ● Research Assistant, Engineering Field Experiment, Air Brands Incorporated, 2004-2005